THESIS FOR THE DEGREE OF DOCTOR OF PHILOSOPHY

# Superconducting Resonators for Hybrid Semiconducting and Magnetic Quantum Systems

IVO PETRONELLA CHRISTEL COOLS


CHALMERS

Quantum Device Physics
Department of Microtechnology and Nanoscience – MC2
Chalmers University of Technology
Göteborg, Sweden, 2026

**Superconducting Resonators for Hybrid Semiconducting and Magnetic Quantum Systems**

IVO PETRONELLA CHRISTEL COOLS



Chalmers University of Technology
Department of Microtechnology and Nanoscience – MC2
Quantum Device Physics
SE-412 96 Göteborg, Sweden
+ 46 (0) 31-772 1000

ISBN 978-91-8103-401-1
Doktorsavhandlingar vid Chalmers tekniska högskola
Ny serie nr 5858
ISSN 0346-718X

**Cover**
Schematic representation of the domains encompassed by hybrid quantum devices. Central to the figure is a semiconducting InAs nanowire, clad in Al and a rare-earth ferromagnet, EuS.

**Keywords:** Superconducting resonators, Hybrid quantum circuits, Andreev bound states, Andreev spectroscopy, spintronics, magnetism, magnons

Printed by Chalmers digitaltryck
Göteborg, Sweden 2026

# Abstract

As the field of superconducting quantum technology progresses beyond single-qubit control, scalable and multifunctional quantum architectures become increasingly vital. A central challenge is integrating fast, controllable superconducting circuits with components that offer longer coherence, rich physics, or new functionalities. Hybrid quantum systems, where superconducting microwave resonators interface with semiconducting or magnetic subsystems, have the capability to fulfil this need, yet they face significant engineering obstacles. Conventional superconducting resonator designs struggle under magnetic field biasing and electrostatic gating, both of which are essential for coupling to spin-based, semiconductor, or magnonic elements.

This thesis explores solutions to these bottlenecks through the development of magnetic-field-resilient coplanar stripline (CPS) resonators based on thin-film NbTiN. These resonators retain a stable resonance frequency in in-plane magnetic fields up to 1 T, can exhibit high kinetic inductance, and offer broad geometrical tunability, enabling strong and ultrastrong coupling to charge- and spin-based quantum systems. In the superconducting–semiconductor domain, we demonstrate high-impedance (up to 12 k$\Omega$) CPS resonators inductively coupled to Josephson junctions hosting Andreev bound states (ABSs), revealing both Andreev pair transitions and single-quasiparticle excitations near the ultrastrong coupling regime with maximal coupling strength $\frac{g_c}{2\pi} \approx 1.95$ GHz. This opens the door to fast, gate-tunable qubits based on microscopic ABSs, distinct from conventional macroscopic qubit architectures, and lays the groundwork for spin–photon hybridisation, non-perturbative light–matter interactions, and parity-based quantum logic.

In parallel, we investigate rare-earth iron garnet ferrimagnetic insulators as low-loss spin-wave media compatible with superconducting devices. In sputtered thin-film thulium iron garnet (TmIG) with perpendicular magnetic anisotropy, we observe deterministic spin-orbit torque switching at room temperature and multiple magnetisation polarity reversals at lower temperatures (respectively 81 K and 124 K). Furthermore, we show preliminary results on interfacing the TmIG with a superconducting waveguide to highlight the potential of TmIG for low-dissipation magnonic information transport, as a next-generation framework of quantum computing, and as magnetic substrates for superconducting hybrid devices.

Taken together, the thesis combines materials, device concepts, and measurement strategies for novel classes of hybrid quantum systems that combine robust superconducting circuitry, electrostatically tunable semiconductor excitations, and industry-scalable magnetic elements, thereby paving the way for next-generation hybrid quantum systems. More broadly, they provide routes to overcoming limitations of existing hybrid platforms and advance the development of versatile, low-dissipation quantum technologies.

# List of publications

## Appended publications

This thesis is based on the content in the following papers:

[A] I.P.C. Cools, R-M. López-Báez, V. Buccheri, O.O. Shvetsov, N Trnjanin, E. Hogedal and S.P. Dash, "Losses in magnetic field resilient coplanar stripline resonators for superconductor-semiconductor hybrid physics,"
*Journal of Physics D: Applied Physics*, vol. 58, no. 25, June, 2025.

[B] O.O. Shvetsov, A. Khola, V. Buccheri, I.P.C. Cools, N Trnjanin and A. Geresdi, T. Kanne and J. Nygård, "Approaching the ultrastrong-coupling regime between an Andreev level and a microwave resonator,"
*Physical Review Applied*, vol. 24, no. 4, October, 2025.

[C] R. Ngaloy, N. Yamashita, B. Zhao, K. Soojung, K. Yamashita, I.P.C. Cools, M.M. Agustrisno, L. Soobeom, Y. Kurokawa, Y. Chun-Yeol, H. Yuasa and S.P. Dash, "Deterministic spin-orbit torque switching of epitaxial ferrimagnetic insulator with perpendicular magnetic anisotropy fabricated by on-axis magnetron sputtering,"
*npj Spintronics*, vol. 3, no. 1, October, 2025.

[D] I.P.C Cools, J. Xu, L. Yan, D.P. Dubey, S.P. Dash and N. Yamashita "Observation of double anomalous Hall polarity reversals with temperature in an ultrathin ferrimagnetic insulator,"
*Submitted to: APL Materials, special issue: Low Dimensionality effects in Magnetic Materials*

# Other publications

The content of the following papers either partially overlaps with the appended papers or is out of the scope of this thesis.

[a] L. Nulens, N. Lejeune, J. Caeyers, S. Marinković, **I.P.C. Cools**, H. Dausy, S. Basov, B. Raes, M.J. Van Bael, A. Geresdi, A.V. Silhanek and J. Van de Vondel, "Catastrophic magnetic flux avalanches in NbTiN superconducting resonators," *Communications Physics*, vol. 6, no. 1, September 2023.

[b] F. Joint, A. Rafsanjani, **I.P.C. Cools** and S. Gasparinetti, "Dynamics of gate-controlled superconducting Dayem bridges," *Communications Physics*, vol. 125, no. 9, August 2024.

[c] L. Nulens, D.A.D. Chaves, S. Reniers, R. Dillemans, **I.P.C. Cools**, K. Temst, B. Raes, M.J. Van Bael and J. Van de Vondel, "Nonvolatile cryogenic phase-slip memory with single-shot readout," *Physical Review Applied*, vol. 24, no. 5, November 2025.

[d] S. Vervoort, L. Nulens, D.A.D. Chaves, H. Dausy, S. Reniers, M. Abouelela, **I.P.C. Cools**, A.V. Silhanek, M.J. Van Bael, B. Raes, J. Van de Vondel, "DC-operated Josephson junction arrays as a cryogenic on-chip microwave measurement platform," *Communications Physics*, vol. 8, no. 1, July 2025.

[e] N. Trnjanin, **I.P.C. Cools**, V. Buccheri, O.O. Shvetsov and T. Bauch, "Magneto-transport properties of thin Josephson junctions for spectroscopic applications in the presence of large magnetic fields," *Applied Physics Letters*, vol. 127, no. 7, August, 2025.

[f] N. Trnjanin, **I.P.C. Cools**, V. Buccheri, Y. Liu, J. Nygård and T. Bauch, "Magnetic-Field Anisotropy of the Josephson Diode Effect in Ferromagnetic Hybrid Nanowires," *Submitted to Phys. Rev. B.*

[g] J. Baumgarten, N. Lejeune, L. Nulens, **I.P.C. Cools**, J. Van de Vondel and A.V. Silhanek "Magnetic landscape of NbTiN superconducting resonators under radio-frequency excitation," *Submitted to Phys. Rev. Applied*

# Abbreviations & symbols

**Abbreviations**

| | |
|---|---|
| ABS | Andreev bound state |
| AFM | Antiferromagnet |
| AHE | Anomalous Hall effect |
| CPS | Co-planar stripline |
| cQED | Circuit quantum electrodynamics |
| CPW | Co-planar waveguide |
| DCM | Diameter-corrected (fitting) method |
| DW | Domain-wall |
| FiM | Ferrimagnet |
| FM | Ferromagnet |
| FWHM | Full-width at half maximum |
| GGG | Gadolinium gallium garnet |
| HM | Heavy metal |
| JJ | Josephson junction |
| ma | Metal-air interface |
| MPE | Magnetic proximity effect |
| ms | Metal-surface interface |
| mw | Microwave |
| OHE | Ordinary Hall effect |
| PCB | Printed circuit board |
| PMA | Perpendicular magnetic anisotropy |
| PT | Pair transition |
| REIG | Rare-earth iron garnet |
| rf | Radio-frequency |
| sa | Surface-air interface |
| SHE | Spin-Hall effect |
| SMR | Spin Hall magnetoresistance |
| SOT | Spin-orbit torque |
| SQPT | Single quasiparticle transition |
| TmIG | Thulium iron garnet |
| XRC | X-ray rocking curve |
| XRR | X-ray reflectivity |
| YIG | Yttrium iron garnet |
| $\phi$RM | $\phi$-rotation (fitting) method |

**Symbols**

| | |
|---|---|
| $B_c$ | Critical magnetic field |
| $f_r$ | Resonance frequency |
| $g$ | Coupling strength |
| $G$ | Resonator conductor spacing |
| $\langle n \rangle$ | Average photon number |
| $H_a$ | Applied external magnetic field |
| $\mathbf{M}$ | Magnetisation |
| $\mathbf{m}$ | Spin density |
| $R_Q$ | Quantum of resistance |
| $T_{\text{comp}}$ | Compensation temperature |
| $Q$ | Quality factor |
| $Q_C$ | Coupling quality factor |
| $Q_I$ | Internal quality factor |
| $Q_L$ | Loaded quality factor |
| $W$ | Resonator conductor width |
| $\phi$ | Impedance mismatch |
| $a$ | Amplitude in the IQ-plane |
| $\alpha$ | Phase offset in the IQ-plane |
| $\tau$ | Electrical delay time |
| $\varphi$ | Gauge-invariant phase |
| $\Phi$ | Flux |
| $\Phi_0$ | Quantum of flux |
| $\chi$ | Dispersive resonance shift |
| $g_c$ | Coupling strength |

# Contents

# Chapter 1

# Introduction

## 1.1 Quantum computing

The creation and use of the first semiconductor transistors marked a turning point in the history of computation. Classical computers operate on binary digits (bits) that exist in definite logical states (0 or 1, current or no-current), and their processors are built from transistor-based logic gates obeying Boolean algebra. Decades of engineering efforts have driven a reduction in transistor size to the nanometre scale, but as components approach atomic dimensions, quantum mechanical effects emerge that challenge the conventional binary framework [1]. Quantum computing offers a novel approach to information processing by inherently exploiting two-level quantum systems (quantum bits or "qubits") that can exist in superpositions of the basis states. A qubit can be in state $|0\rangle$, $|1\rangle$, or any coherent combination $\alpha|0\rangle + \beta|1\rangle$, enabling the existence of a quantum speed-up for certain problem classes [2, 3].

Many physical platforms for qubits have been explored, including the spin of electrons or nuclei [4], the polarisation of photons [5], and superconducting electronic circuits [6]. Superconductors are particularly attractive for building quantum processors [7]. A superconductor is a material that exhibits zero electrical resistance below a critical temperature $T_c$ [8], allowing persistent currents to flow without dissipation. In superconducting circuits, this property enables the creation of resonators and qubits with extremely low energy (and hence information) loss, with the downside of necessitating a cryogenic set-up and corresponding microwave wiring. A key component in many superconducting qubits is the insulator-based Josephson junction (JJ) [9], an electrical tunnel junction formed by two superconductors separated by a weak barrier (such as an insulator or a semiconducting channel). Cooper pairs of electrons can tunnel through the barrier, providing a non-linear, lossless inductive element. The non-linearity of a JJ allows it to behave as an artificial atom (with discrete energy levels of an anharmonic oscillator). Such junctions form the basis of qubit designs like charge, flux, and transmon qubits [10]. Moreover, superconducting qubits and resonators can be fabricated using lithographic integrated-circuit processes, making it seemingly feasible to scale up to large numbers of qubits on a single chip [11].

In recent years, superconducting qubit technology has advanced rapidly. For example, IBM has developed cloud-accessible quantum processors with their Condor processor,

including 1121 qubits [12], and a 105-qubit superconducting device (Willow) by Google was used to demonstrate a quantum computational advantage in 2024 [13]. These milestones underscore the viability of superconducting circuits as a platform for quantum computing.

Research to date has largely focussed on mitigating loss mechanisms in individual circuit elements, from qubits to signal lines. While these efforts have yielded incremental improvements, further progress towards practical quantum advantage requires a transition from component-level optimisation to a system-level engineering approach [14]. Bottlenecks to performance include fabrication methods, scalability, cross-talk between qubits and inherent Josephson junction losses:
(i) Existing fabrication is based on the shadow evaporation-technique, introducing potential loss-centres [15, 16].
(ii) Scalability is limited as each qubit needs its own drive line external to the chip.
(iii) Connecting more qubits inevitably leads to more cross-talk between signal lines (resonators), causing spurious excitation of adjacent qubits to the targeted one.
(iv) The Josephson junctions in the qubit cause losses due to the dielectric needed for the weak link.

Collectively, these limitations reduce qubit coherence times and thereby constrain the number of coherent operations that can be performed. Overcoming these challenges requires a shift towards scalable, low-loss architectures that integrate materials, device design, and control at the system level. In this thesis, we explore alternative approaches to both signal transmission and qubit design aimed at addressing these constraints.

## 1.2 Superconducting resonators and circuit QED

Microwave resonators are devices that support electromagnetic standing waves at specific resonant frequencies, where the stored field energy is greatly enhanced. In superconducting quantum circuits, on-chip microwave resonators play an essential role in enabling quantum interactions. They are used for high-fidelity qubit readout, for mediating coupling between qubits (serving as a quantum information bus), and even as their own quantum memory elements or filters [17]. A central framework in this field is circuit quantum electrodynamics (cQED), wherein a superconducting qubit acting as a two-level system is strongly coupled to the quantised electromagnetic field of a superconducting resonator [6]. In analogy to optical cavity QED, the resonator in cQED serves as a high quality factor ($Q$) microwave cavity on a chip. When the coupling strength $g$ between the qubit and resonator is comparable to the characteristic energy scales of the system, related to the resonance frequency $f_r$ of the resonator, the system enters the ultra-strong coupling regime [18]. In this regime, a single microwave photon can be exchanged coherently many times between the qubit and resonator before being lost, enabling entanglement and quantum state transfer between the two.

Because superconductors eliminate ohmic losses, superconducting resonators can achieve very high quality factors, meaning the photons inside persist for relatively long times. The photon lifetime $\tau$ in a resonator is related to $Q$ by $\tau = Q/(2\pi f_r)$ for a given resonance frequency. Thus, maximising $Q$ is crucial for storing quantum information and achieving strong coupling. In practice, one distinguishes between the

internal quality factor $Q_\mathrm{i}$ (limited by material and fabrication losses) and the external quality factor $Q_\mathrm{c}$ (due to coupling to the environment via input/output lines). By using superconducting materials and low-loss dielectrics, $Q_i$ can be made extremely high, while coupling capacitors or inductive couplers are used to set $Q_c$ to a desired value for efficient measurement access.

Among various resonator implementations, coplanar waveguide (CPW) resonators have become ubiquitous in superconducting quantum circuits [19–21]. A CPW resonator consists of a central conducting strip separated by narrow gaps from extended ground plane conductors on either side, all fabricated on a dielectric substrate. This planar transmission-line geometry offers excellent electric field confinement and is convenient for lithographic fabrication. Typical CPW resonators are designed to resonate in the microwave spectrum (GHz regime) and are made on the order of a few millimetres in length. Their impedance and mode volume can be engineered by adjusting the conductor width, gap, and length, allowing flexibility to optimise for specific applications [22]. Notably, CPW resonators with high kinetic inductance can achieve large zero-point field fluctuations (due to sub-wavelength mode confinement) which is advantageous for reaching strong to deep strong coupling with qubits [18, 23]. Superconducting CPWs are commonly fabricated from aluminium or niobium thin films on low-loss substrates like silicon or sapphire. This combination of design flexibility and low loss has made the CPW resonator a workhorse for quantum computing and quantum optics experiments on a chip [19, 24].

The first part of this thesis focuses on coplanar stripline (CPS) resonators, which offer critical advantages in hybrid environments. Unlike CPW geometries that rely on a continuous ground plane, our CPS resonators are differentially driven and do not require such a plane, enabling multiple local gate electrodes or magnetic substrates to be integrated without perturbing the microwave environment. Moreover, CPS resonators are inherently more resilient to applied magnetic fields, as they minimise vortex formation and energy loss in the absence of an extensive superconducting ground structure [25, 26]. This is essential when integrating materials like magnetic insulators or voltage-tunable devices, which require either static magnetic fields or local gating. Our experiments confirm that CPS devices maintain high internal quality factors and demonstrate stable resonance frequencies under applied fields, establishing them as a flexible and robust platform for next-generation hybrid quantum devices.

## 1.3 Hybrid quantum circuits with semiconductors

As superconducting quantum technologies mature, a key challenge emerges: how to combine fast gate operations with greater coherence, architectural flexibility, and richer functionality. One promising avenue lies in hybrid quantum circuits that couple superconducting resonators to semiconductor devices, particularly those supporting Andreev bound states (ABSs). After all, one way to implement a paradigm shift in superconducting quantum computing is by utilising the pre-existing CMOS semiconductor fabrication lines that enabled the exponential growth of conventional computing. Unlike qubits based on collective degrees of freedom (such as transmons), Andreev qubits leverage individual quasiparticle states confined to a nanoscale junction. This hybridisation strategy aims not only to leverage the benefits of both material platforms,

but also to unlock new types of qubits, coupling mechanisms, and control approaches. The field of hybrid quantum computing has recently gained a great deal of attention due to the controversial discovery of Majorana zero modes and the resulting preliminary industrial exploration of such states [27, 28].

At the core of this approach is the Josephson effect in semiconductor weak links. When a semiconductor nanowire [29] or two-dimensional electron gas is proximitised by superconducting leads, discrete ABSs form within the junction which carry the supercurrent [30]. These states arise from coherent Andreev reflections at the superconductor–semiconductor interfaces and can be engineered into two-level systems. Unlike transmons or flux qubits, Andreev-based devices are defined by microscopic degrees of freedom and are directly sensitive to material parameters such as spin–orbit interaction, electrostatic gating, and interface transparency. Crucially, many of their microscopic parameters are electrostatically gate-tunable, making them highly adaptable components within reconfigurable quantum circuits.
Coupling ABSs to superconducting microwave resonators enables high-resolution spectroscopic access to their energy structure and transition dynamics [31–33]. However, achieving strong and coherent coupling in such hybrid systems presents several challenges.

First, ABSs have inherently small electric dipole moments, requiring careful resonator design to amplify vacuum fluctuations, typically using high-impedance superconducting resonators. Second, the hybrid nature of the weak link introduces additional decoherence channels, such as quasiparticle poisoning and charge noise [34], which must be mitigated through fabrication, material choice, and shielding strategies. Finally, as mentioned above, conventional superconducting resonator geometries can be sensitive to magnetic fields and do not lend themselves well to (multiple) electrostatically gateable devices, limiting compatibility with electron mobility as a tunable parameter or spin-resolved ABS devices that require magnetic field biasing.

To address these issues, our experimental strategies have focused on utilising the characterised magnetic field resilient CPS resonators [35], fabricated from high kinetic inductance NbTiN and embedding semiconductors in flux-tunable loops for galvanic (inductive) coupling. These configurations increase the achievable coupling strength while preserving control over the ABS phase and parity. They also open the door to measuring transitions involving not only Andreev pairs, but also spin-split quasiparticle states, a feature inaccessible in insulator weak-link Josephson junction-based qubits [36]. Besides paving the way for new types of qubits, such a hybrid geometry allows one to study the ABS spectrum in detail [37].

Importantly, the coupling strength $g$ between the ABSs and resonator scales with the resonator's impedance, and can reach hundreds of MHz or even approach the GHz regime for resonator impedances exceeding the quantum of resistance $R_Q$. This enables the ultrastrong coupling regime, where the coupling strength $g$ becomes a significant fraction of the resonator frequency $f_r$ ($g/f_r \gtrsim 0.1$) and opens new physical regimes that transcend conventional cQED [38]. In this limit, light-matter interactions can no longer be described using the standard strong-coupling rotating-wave approximation, leading to hybridised eigenstates of the full system and enabling access to non-perturbative quantum electrodynamics. For Andreev-based devices, reaching this

regime provides new tools for ultrafast quantum control, non-adiabatic gate protocols, and novel ways to probe quasiparticle dynamics and parity switching at the quantum level [23]. Furthermore, it may allow simulation of exotic models of light–matter interaction, including quantum Rabi dynamics, within one solid-state platform. As such, pushing the coupling strength into the ultrastrong regime is both a technical milestone and a gateway to qualitatively new quantum functionalities.

Hybrid circuits based on Andreev physics are thus positioned to address some of the limitations of conventional superconducting qubits. Their high tunability, compatibility with spin–orbit coupling, and potential resilience to charge noise make them a compelling platform for next-generation quantum processors. Moreover, they can support both pair (even-parity) and single-quasiparticle (odd-parity) transitions, enabling complex control protocols inaccessible for standard superconductor (Al/$AlO_x$/Al) JJ based qubits. Thus, they provide a natural interface for exploring topological states of matter, Majorana physics, and parity-based qubit control, further enriching the quantum circuit landscape.

## 1.4 Hybrid quantum circuits with ferrimagnetic iron garnets

An alternative and particularly promising route towards hybrid quantum architectures is the integration of superconducting microwave circuits with magnetic insulators supporting collective spin excitations: magnons. These quasiparticles represent quantised spin waves in magnetically ordered systems and act as bosonic information carriers at microwave frequencies [39]. Unlike charge-based carriers, magnons propagate without net charge transport, suppressing Joule heating, and offer the potential for energy efficient, low dissipation signal transmission. In this context, ferrimagnetic insulators (such as rare-earth iron garnets, REIGs) form a compelling interface for coupling spin dynamics to superconducting microwave circuits. These ferrimagnets combine low magnetic damping with tunable anisotropy, multicomponent sublattice magnetisation dynamics, and strain sensitivity. In this thesis, we utilise thulium iron garnet ($Tm_3Fe_5O_{12}$, TmIG) [40, 41], a ferrimagnetic insulator that develops strong perpendicular magnetic anisotropy (PMA) when grown epitaxially on (111)-oriented gadolinium gallium garnet (GGG) substrates. The large negative magnetostriction ($\lambda_{111} \approx -5.2 \times 10^{-6}$) of TmIG makes it especially responsive to substrate-induced strain, stabilising uniform magnon modes. TmIG consists of three magnetic sublattices ($Fe^{3+}$ on octahedral and tetrahedral sites, $Tm^{3+}$ on dodecahedral sites) that interact via antiferromagnetic exchange, resulting in complex temperature-dependent magnetisation behaviour.

From an information-processing standpoint, magnons offer an elegant mechanism for coherent signal transport. As TmIG is an electrical insulator with exceptionally low damping constant, spin waves can propagate over micrometre to millimetre scales. Integrating such materials with superconducting resonators opens a pathway to hybrid devices in which microwave photons and magnons are coherently interfaced. Recent demonstrations with low-damping yttrium iron garnet (YIG) have shown strong coupling between superconducting resonators and magnon modes, enabling coherent

transfer and storage of quantum information [42–44]. TmIG, with similar magnetic damping and added benefits like tunable anisotropy, can thus serve as a high-coherence magnonic interconnect, functioning as a magnonic quantum bus, and enabling coherent transfer of quantum information between superconducting nodes without charge motion and associated loss.

An additional inherent property of ferrimagnetic systems like thin-film TmIG is the presence of a magnetisation compensation temperature ($T_{\mathrm{comp}}$). At this temperature, the opposing sublattice magnetisations cancel, rendering the net magnetic moment zero while retaining a population of free spins and strong exchange interactions. This produces antiferromagnet-like dynamics [45, 46], characterised by minimal stray magnetic fields, ultrafast spin dynamics, and sharp coercive transitions. These properties make them desirable in hybrid circuits: operating near $T_{\mathrm{comp}}$ minimises magnetic back-action on the superconducting resonator and supports enhanced magnon–photon coupling while maintaining high resonator quality factors.

The experimental results presented in this thesis thus serve a dual purpose. First, they demonstrate the controlled magnetic tunability of ultrathin TmIG films. Second, they lay the groundwork for future experiments targeting coherent magnon excitation and detection using high-$Q$ superconducting resonators. This coupling would form the basis of our long-term vision [39]: the development of hybrid superconducting–magnonic architectures in which microwave photons and magnons are coherently interfaced, opening a pathway toward low-loss, scalable information routing and novel quantum functionalities beyond purely charge-based superconducting circuits.

## 1.5 Thesis outline

In this thesis, we design and implement superconducting coplanar resonators for integrating with other quantum systems, as motivated above. The chapters of the dissertation are organised as follows:

- **Chapter 2: Superconducting resonators**
  This chapter will review the theoretical foundations of superconductivity and resonators, and present our results on a new type of resonator. We will see why the standard workhorse of cQED has to be adjusted to work with gate-tunable semiconductors, and in a magnetic field. Furthermore, we will provide a step-by-step description of microwave characterisation and warn for experimental pitfalls. Finally, we show the characterisation of the fabricated coplanar stripline resonators, including measurements of quality factors, microwave losses, and performance under applied magnetic fields.

- **Chapter 3: Semiconductor-superconductor hybrid system integration**
  In Chapter 3, we first describe the basic theory of Andreev bound state spectroscopy, and briefly why we aim for the ultra-strong coupling regime. Subsequently we demonstrate the practical implementation of the theory by presenting our results in devices consisting of semiconductor nanowires coupled to the novel resonator design. We characterise the coupling of the CPS resonators to Andreev levels, showcasing their potential for further super-semiconductor hybrid systems, and discuss the results in detail.

- **Chapter 4: Towards hybrid superconductor-magnetic quantum systems**
  We present our results on the characterisation of ultrathin TmIG films fabricated using an industry-compatible sputtering technique. To assess the viability of this approach for large-scale integration, we perform electrical characterisation across multiple samples at room temperature. Subsequently, a representative device is selected and studied as a function of temperature to investigate the underlying magnetic behaviour. These measurements provide insight into the temperature dependence of TmIG, which is essential for its integration with superconducting systems. We discuss the observed polarity reversals in the Hall signal in terms of an interplay between magnetic compensation phenomena and interfacial effects. The chapter concludes with preliminary results on coupling TmIG to a superconducting microwave circuit. Together, these results represent a first and promising step towards establishing rare-earth iron garnets as a compatible platform for current and next-generation quantum information architectures.

- **Chapter 5: Future progress and conclusion**
  The final chapter serves as a summary of the key findings of the work and provides an outlook on future directions and applications for superconducting resonators in hybrid quantum circuits.

# Chapter 2

# Superconducting resonators

*"Fortunately, I know enough about the processes of the mind not to let this block worry me too much. Instead of panicking and giving up (or what's even worse, pushing hard for answers that won't come) I've got to take my mind off the problem for a while and let it stew. I've gone as far as I can on a conscious level, and now It's up to those mysterious operations below the level of awareness. It's one of those inexplicable things, how everything I've learned and experienced is brought to bear on the problem. Pushing too hard will only make things freeze up. How many great problems have gone unsolved because men didn't know enough, or have enough faith in the creative process and in themselves, to let go for the whole mind to work at it?"*
— Daniel Keyes, *Flowers for Algernon*

The phenomenon of superconductivity, characterised by the simultaneous occurrence of zero electrical resistance and the active expulsion of magnetic flux, represents one of the most profound manifestations of quantum mechanics on a macroscopic scale. Its discovery in 1911 by Heike Kamerlingh Onnes [8], conjoint with the first successful liquefaction of helium, provided a paradigm shift in the classical understanding of electronic transport in metals. At the time, theoretical models for the temperature dependence of resistance varied wildly: it was thought there could be a finite residual resistance due to impurities, or that electrons would effectively freeze to their parent atoms, leading to an infinite resistance as temperature approached absolute zero [47]. The experimental observation of mercury's resistance dropping abruptly to a negligible value at 4.2 K provided the first evidence of a new thermodynamic state of matter (with nuclear magnetic resonance, follow-up experiments have sent a lower bound to the persistence of superconducting currents: they will keep running around for at least 100000 years without weakening much [48]). Further understanding proved that superconductivity is characterised by two main effects:

1. The vanishing of electrical resistance
2. The expulsion of magnetic flux, the Meissner-Ochsenfeld effect

both of which occur below a critical temperature, $T_c$, and a critical external magnetic field $B_c$. In a perfect classical conductor, the application of a magnetic field would induce eddy currents that oppose changes in flux, essentially freezing the magnetic state of the material to what it was before reaching the perfect-conduction temperature (following Faraday's law). After all, if resistivity is zero, Ohm's law dictates

that the electric fields $E = \rho \mathbf{J}$ must also be zero; then, following Maxwell's law, $\partial B/\partial t = -\nabla \times \mathbf{E} = 0$, and the magnetic field should not change in time (i.e. "freezes"). However, the discovery of the Meissner-Ochsenfeld effect in 1933 [49] demonstrated that superconductors are perfect diamagnets, actively *expelling* magnetic fields regardless of their initial state upon cooling below $T_c$, as schematically shown in Figure 2.1. This fundamental distinction implies that the superconducting state is an equilibrium state, necessitating a description that goes beyond classical Maxwell-electrodynamics.

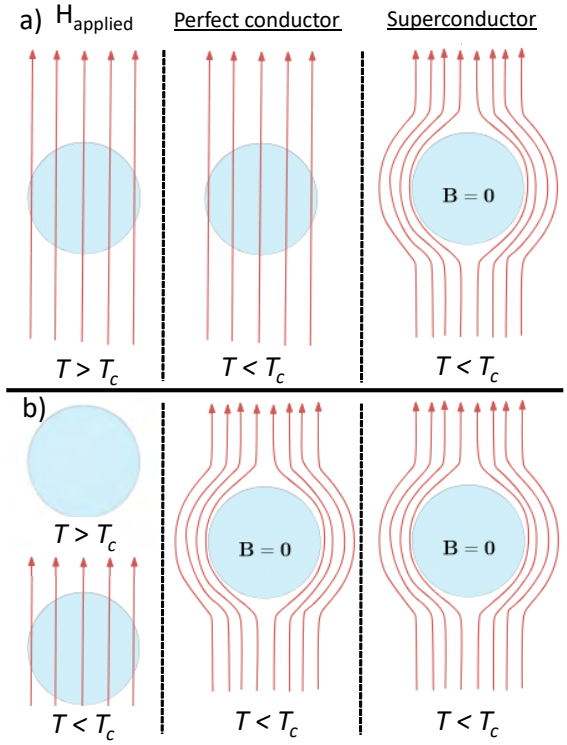


**Figure 2.1:** Schematic illustration of the Meissner–Ochsenfeld effect and the fundamental distinction between a perfect conductor and a superconductor in an external magnetic field. Left: applied magnetic field; middle: perfect conductor for $T < T_c$, the transition temperature; right: superconductor for $T < T_c$. **a**) If a magnetic field is present before cooling through the critical temperature ($T > T_c \rightarrow T < T_c$), a perfect conductor preserves the initial magnetic flux configuration; the magnetic field remains frozen inside the material. In contrast, a superconductor actively expels the magnetic field upon entering the superconducting state. **b**) If the external field is applied only after the system is already in the superconducting/perfect conducting state ($T < T_c$), for both cases the field is excluded from the interior. Image adapted from [50].

Modern circuit quantum electrodynamics (cQED) has leveraged these superconducting properties to develop high-performance microwave resonators. Traditionally, superconducting coplanar waveguide (CPW, Figure 2.2a) resonator geometries have been utilised due to their ease of fabrication and low losses in a variety of applications. However, CPW resonators suffer from two primary limitations in advanced hybrid systems: high susceptibility to external magnetic fields and poor (electrostatic) voltage gateability. The large ground planes of a CPW facilitate the trapping of magnetic vor-

tices, which move and dissipate energy under microwave excitation, thereby degrading the internal quality factor ($Q_i$). Furthermore, they act as an inhibiting factor that complicates the introduction of dc voltage gates required to tune coupled semiconducting devices - especially if multiple devices are involved. We addressed these challenges by moving to a coplanar stripline (CPS, Figure 2.2b) architecture, which omits the ground plane altogether to achieve magnetic field resilience and enhanced electrostatic control.

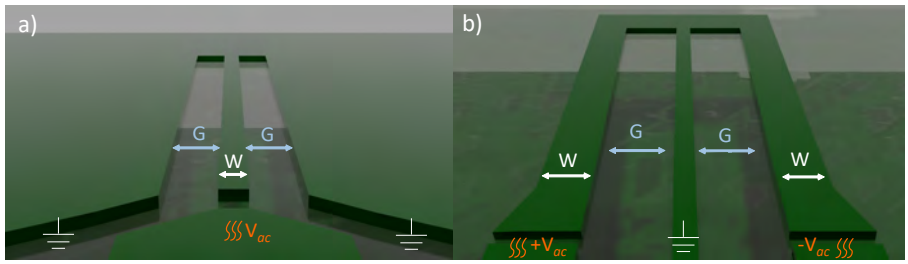


**Figure 2.2:** Schematic illustration of a coplanar waveguide (CPW, **a**) and coplanar stripline (CPS, **b**) resonator. The conductor width $W$, and conductor spacing to the ground $G$ are indicated in respectively white and light blue. The CPW consists of a central conducting line that flows into the ground plane(s). The CPS consists of two differentially driven conducting lines, shorted at a central dc-ground line; ac-excitation $V_{ac}$ is shown in orange.

In this chapter, first we give a brief theoretical overview of superconductivity and the relevant parameters (Section 2.1). Afterwards, we present our results on the characterisation of the superconductor niobium titanium nitride in Section 2.2, both fabrication wise as the kinetic inductance of these films. This is followed by a description of general superconductor resonators, including standard CPW geometries, and basic characterisation thereof to establish that our measurement chain (read-out and fitting procedure) works. To understand such data, we provide explanations on what are microwave losses, how to simulate resonators, best measurement practices, and how to fit the data, all in Section 2.3. Finally, we turn to our main results on CPS resonators in Section 2.4, where we delve deeper into why we use this new geometry and include the measurements of the power and temperature dependent losses, and the field related measurements.

## 2.1 Superconductivity

The superconducting state is defined by three interrelated critical parameters: the critical temperature $T_c$, the superconducting energy gap $\Delta$, and the critical magnetic field $B_c$. These parameters determine the phase boundary between the normal metallic state and the condensed superconducting phase. The critical temperature marks the second-order phase transition where the electronic system undergoes a spontaneous symmetry breaking into a bosonic state. Below $T_c$, the entropy of the electron gas decreases more rapidly than in the normal state, indicating a higher degree of order. The transition is characterised by an anomaly in the specific heat, where a jump is observed at $T_c$, followed by an exponential decay at lower temperatures. This exponential behaviour is a hallmark of an energy-gapped system, suggesting that the

lowest energy excitations are separated from the ground state by a finite energy interval.

According to the Bardeen-Cooper-Schrieffer (BCS) theory, this superconducting state emerges from the coherent pairing of electrons of opposite spin into Cooper pairs, which opens an energy gap $2\Delta$ in the quasiparticle excitation spectrum [51]. This pairing is mediated by the exchange of virtual phonons: an electron moving through the lattice creates a local polarisation that attracts a second electron, overcoming their mutual Coulomb repulsion. The pairing occurs between electrons with opposite momenta and spins ($\mathbf{k}\uparrow, -\mathbf{k}\downarrow$), resulting in a singlet state with a total spin zero. The gap represents the binding energy of the pair; to create a single-particle excitation (a Bogoliubov quasiparticle), a minimum energy of $\Delta$ must be supplied. Since excitations are always created in pairs by breaking a Cooper pair, the spectroscopic gap observed in tunnelling or microwave absorption experiments is $2\Delta$. In the weak-coupling BCS limit (e.g. for extremely dirty superconductors) [52–54], the zero-temperature gap $\Delta_0$ is proportional to $T_c$:

$$\Delta_0 = 1.764 k_B T_c \tag{2.1}$$

where $k_B$ is the Boltzmann constant. Strong-coupling materials, such as NbN, exhibit higher ratios (e.g., $\Delta_0 \approx 2.08 k_B T_c$), reflecting a more robust attractive interaction. The density of states, $N_s(E)$, in the superconducting state is drastically modified from the flat distribution of the normal metal near the Fermi level and exhibit Van Hove singularities near the gap. They are given by:

$$N_s(E) = N(0)\frac{E}{\sqrt{E^2-\Delta^2}} \quad \text{for} \quad |E| > \Delta \tag{2.2}$$

and $N_s(E) = 0$ for $|E| < \Delta$. This leads to the characteristic "coherence peaks" at the gap edges ($E = \pm\Delta$), which are frequently observed in scanning tunnelling spectroscopy. In the presence of disorder, these peaks get smeared out; hence, in physical materials there is no infinite density of states. We show such a theoretical smeared out spectrum in Figure 3.3(a, left and right).

The stability of the superconducting state is limited by the critical magnetic field $B_c$. When a superconductor expels a magnetic field, it increases its magnetic Gibbs free energy by $\frac{B^2}{2\mu_0}$ per unit volume. The superconducting phase remains stable as long as this energy cost is less than the condensation energy gained by forming Cooper pairs. The temperature dependence of $B_c$ broadly follows an empirical parabolic law:

$$B_c(T) = B_c(0)\left[1 - \left(\frac{T}{Tc}\right)^2\right], \tag{2.3}$$

where $B_c(0)$ is the field required to destroy superconductivity at absolute zero. The critical field behaviour is highly dependent on the geometry of the material and the direction of the applied magnetic field. In thin films where the thickness is significantly smaller than the magnetic penetration depth $\lambda$ (approximate depth until the field inside the superconductor is zero, or the range over which edge currents in the superconductor flow to expel or counteract an external field) and Ginzburg-Landau coherence length $\xi$ (broadly the distance between the electrons in a Cooper pair, or over which the superconducting order parameter $\psi$ varies), the application of an in-plane (parallel) magnetic field strongly suppresses magnetic vortex nucleation,

resulting in a substantially enhanced critical field; a vortex does not fit the layer. On the other hand, an out-of-plane (perpendicular) magnetic field easily penetrates the thin film, nucleating vortices at much lower field strengths. These vortices can move (as avalanches) and cause dissipative losses both in the dc and ac regimes [25, 26]. Related, superconductors are broadly classified into two categories based on the exact ratio of $\lambda$ and $\xi$. This is characterised by the Ginzburg-Landau parameter

$$\kappa = \frac{\lambda}{\xi}, \tag{2.4}$$

which is independent of both temperature and magnetic field close to $T_c$.

The distinction between Type I and Type II superconductors arises from the sign of the surface energy at the interface between a normal-conducting and a superconducting domain. In Type I superconductors (mostly pure bulk pure elements like Al, Sn, and Pb), the surface energy of the normal-superconductor interface is positive. This is where the Ginzburg-Landau parameter comes into play. If $\kappa < \frac{1}{\sqrt{2}}$, the energy required to suppress the superconducting order parameter over a distance $\xi$ outweighs the energy gain from allowing the magnetic field to penetrate over a distance $\lambda$. Consequently, the material maintains a complete Meissner state with no internal field until $B_c$ is reached, at which point it undergoes a first-order transition to the normal state. Thus, this transition is a competition between the energy gain from the condensation of Cooper pairs and the energy loss due to the magnetic field expulsion [55, 56].
These kinds of superconductors can be turned into Type II if the electron mean free path is reduced sufficiently [47]. In those Type II superconductors (including Nb(TiN) and many alloys and disordered films), the surface energy is negative, occurring when $\kappa > \frac{1}{\sqrt{2}}$. For these materials in bulk, the Meissner effect is only observed up to a lower critical field $B_{c1}$. Above $B_{c1}$, it becomes energetically favourable for the field to penetrate the superconductor in the form of discrete magnetic flux quantisations, known as Abrikosov vortices, up to a new critical field $B_{c2}$; the inter-phase regime is called the Shubnikov phase. Each vortex consists of a normal-state core of radius $\approx \xi$, containing a single flux quantum $\Phi_0 = h/2e$. Surrounding this core are circulating supercurrents that screen the flux from the rest of the superconducting bulk over a distance $\lambda$. As the external field increases, the density of these vortices grows, and they arrange themselves into a triangular or hexagonal Abrikosov lattice to minimise their repulsive interactions; the process of domain subdivision proceeds until they are limited by a spacing of $\xi$. Finally, at the upper critical field $B_{c2}$, the vortex cores maximally overlap, and the entire sample returns to the normal state.

This is the behaviour in bulk superconductors. However, in thin-film geometries, certain adjustments have to be made as the critical field behaviour is heavily modified by the relationship between the film thickness $d$ and the characteristic lengths $\lambda$ and $\xi$; a film is considered thin if $d \ll \lambda, \xi$ [57]. This is particularly important for coplanar resonators, where the superconducting leads are typically only 10-100 nm thick. When a magnetic field is applied perpendicular to a thin film, generally Type II, the large demagnetisation factor $N \approx 1$ ensures that flux penetrates already at low applied fields. For Type II films of isotropic nature (i.e. no strong dependence on crystallographical direction), the upper critical field in this orientation $B_{c2\perp}$ is essentially the same as the

bulk $B_{c2}$, defined by the coherence length:

$$B_{c2\perp} = \frac{\Phi_0}{2\pi\xi^2} \tag{2.5}$$

In this state, the film is filled with a dense array of vortices, and the internal quality factor of a resonator would be severely limited by vortex-induced dissipation. In practice, this provides a method to measure $\xi$ experimentally. However, as $B_{c2}$ reaches multiple Tesla in strength at cryogenic temperatures, a more easy-to-use formalism is given by the Werthamer-Helfand-Hohenberg formula [58, 59], where we extract the critical field at 0 K for a Type-II superconductor:

$$B_{c2}(0) = -\ln(2)\, T_c \left(\frac{\mathrm{d}B_{c2}}{\mathrm{d}T}\right)_{T=T_c}. \tag{2.6}$$

This remains an extrapolation from higher temperature-data to the field at 0 K, and is thus an approximate formula. It is valid for superconductors in the (very) dirty limit [60].

When the field is applied parallel to the film surface (in-plane), the behaviour changes significantly. If the film thickness $d$ is much smaller than $\xi$, the formation of vortices is suppressed because the geometric constraint prevents the circular current patterns necessary for a normal core. Instead, the transition is driven by the depairing of Cooper pairs. For a thin film in the limit $d \ll \xi$ and $d \ll \lambda$, Ginzburg and Landau showed that the parallel critical field $B_{c\parallel}$ is enhanced relative to the bulk value [61]. The formula for the parallel upper critical field is [56]:

$$B_{c2\parallel} = \frac{\sqrt{24}\, B_c\, \lambda}{d} \tag{2.7}$$

This indicates that $B_{c2\parallel}$ increases as $1/d$. For very thin films, this field can be orders of magnitude higher than $B_{c2\perp}$. This high in-plane resilience is the physical basis for our magnetic-field-resilient CPS resonators.

Now, we turn our attention to exactly these microwave frequencies for superconducting resonators. There, the alternating electric field accelerates the Cooper pairs. The inertial mass of these charge carriers produces a measurable reactance known as the kinetic inductance ($L_k$). It is a fundamental reactive property of superconductors that originates from the inertia of the Cooper pairs. In classical conductors, electrons undergo frequent scattering events, dissipating energy as heat. In a superconductor, however, the charge carriers move without resistance, and their response to an alternating electric field is purely inertial. The physical origin of kinetic inductance is understood via the Gorter-Casimir two-fluid model [62]. At $0 < T < T_c$, the total electron density $n$ is divided into a superconducting density $n_s$ and a normal density $n_n$. As temperature decreases, $n_s$ increases until $n_s = n$ at $T = 0$. Under a time-varying supercurrent density $\mathbf{J}_s e^{i\omega t}$, the electric $\mathbf{E}$ responds according to the first London equation [63]:

$$\mathbf{E} = \frac{m}{n_s e^2}\frac{\partial \mathbf{J}_s}{\partial t} = i\omega\left(\frac{m}{n_s e^2}\right)\mathbf{J}_s = i\omega\mu_0\lambda^2\mathbf{J}_s \tag{2.8}$$

This relationship is formally identical to the voltage-current relationship of an inductor, $V = L\frac{\mathrm{d}I}{\mathrm{d}t} = i\omega LI$, where the reactive component is defined by the mass and density

of the carriers. In ultrathin or highly disordered superconducting films, the reduced density of Cooper pairs causes this kinetic inductance to increase, often dominating the standard geometric inductance of the circuit. For a thin-film superconducting wire with uniform current density, and of length $l$, width $w$, and thickness $d$ (where $d \ll \lambda$), the total kinetic inductance $L_k$ is [64]:

$$L_k = \mu_0 \lambda^2 \frac{l}{wd}. \tag{2.9}$$

In the "dirty limit" [56] (where the mean free path $l_{\text{mfp}}$ is much smaller than the coherence length $\xi_0$), $\lambda$ is significantly enhanced: $\lambda_{eff} = \lambda(T)\sqrt{1+\xi_0/l_{mfp}}$. Standard values for thin film NbTiN are $\lambda \approx 300$ nm, $\xi_0 = 1-5$ nm and for the mean free path $l_{mfp} = 1$ nm [35, 54, 65–67]. We show some important parameters in Table 2.1 for a range of industrially or academically used superconductors. Naturally these parameters are a rough guideline, and depend heavily on deposition method, thickness, substrate, ambient conditions, exact stoichiometry, and more.

| Material | $T_c$ (K) | $\Delta_0$ (meV) | $\lambda$ (nm) | $B_{c2\perp}$ (T) | ref. |
|---|---|---|---|---|---|
| Al | 1.2 | 0.18 | 100 | 0.01 | [68, 69] |
| $\alpha$-Ta | 4.3 | 0.67 | 150 | 0.5 | [70, 71] |
| TiN | 4.5 | 0.7 | 600 | 3.5 | [72, 73] |
| Nb | 9 | 1.5 | 35 | 0.3 | [74, 75] |
| NbTiN | 12 | 1.5 | 350 | 10 | [54, 76, 77] |
| NbN | 15 | 2.75 | 350 | 20 | [78, 79] |

**TABLE 2.1:** COMPARISON OF APPROXIMATE SUPERCONDUCTING PARAMETERS FOR COMMON THIN-FILM SUPERCONDUCTORS. THESE PARAMETERS ARE ORDER-OF-MAGNITUDE, ROUGH, AVERAGED ESTIMATES.

Thus, the kinetic inductance is highly sensitive to the degree of disorder, the film structure and thickness and the energy gap: in the low-frequency limit ($\hbar\omega \ll \Delta$, i.e. dc) and at $T \ll T_c$, the Mattis-Bardeen theory provides a direct link between the normal-state sheet resistance per square $R_\square$ and the kinetic inductance per square [80]:

$$L_{k,\square} = \frac{\hbar R_\square}{\pi \Delta_0} \frac{1}{\tanh\left(\frac{\Delta}{2k_B T}\right)} \tag{2.10}$$

This implies that materials with high resistivity in the normal state, such as disordered TiN or Nb(Ti)N, will exhibit high kinetic inductance. Furthermore, the tanh-term tends to unity at low temperatures. These materials are superinductors [81] if their (microwave) impedance $Z = \sqrt{\frac{L}{C}} > R_Q \approx 6.45\text{k}\Omega$, and are essential for cQED applications as they allow for the realisation of high-impedance environments that suppress charge fluctuations in quantum circuits. While unattainable for geometrical inductors (limited by an unavoidable shunt capacitance to the free-space impedance $\approx 377\ \Omega$), the usage of the kinetic inductance makes this paradigm obtainable for specifically designed superconductors. The parameter of interest becomes the kinetic inductance fraction $\alpha = \frac{L_k}{L_k + L_{\text{geometry}}}$ that describes the fraction of the kinetic inductance to the total inductance in a superconducting device.

Thus, a certain degree of disorder is beneficial for increasing the kinetic inductance and the upper critical field. However, extreme disorder fundamentally alters the electronic transport. In the limit of very strong disorder, the material undergoes a phase transition from a superconducting state to an insulating state, known as the metal-to-insulator (or superconductor-to-insulator)transition. Then, the strong disorder either severely suppresses $\Delta$ or destroys the global phase coherence by localising the Cooper pairs, causing the material to behave as an insulator at low temperatures instead of the macroscopic superconductor. This transition in a normal metal occurs when the mean free path $l_{\mathrm{mfp}}$ becomes comparable to the Fermi wavelength, or more simply, to the interatomic distance. This is characterised by the Ioffe-Regel [82] parameter $k_F \times l_{mfp}$, where $k_F$ is the Fermi wave vector. When $k_F l_{mfp} \approx 1$, the electronic wave functions become gradually localised due to constructive quantum interference of backscattered paths, a process known as Anderson localisation [83]. For our 10 nm thick NbTiN films, we extract from Fig. 2.4 that $k_f = 12.9\ \mathrm{nm}^{-1}$ and $l_e = 0.74$ nm, and thus the Ioffe-Regel parameter is approximately $9.5 \gg 1$ (see below). In the context of superconductors, two primary scenarios for the transition are debated: the fermionic and the bosonic mechanisms. In the fermionic scenario, strong disorder and the resulting increase in Coulomb repulsion lead to a suppression of the attractive pairing potential. As the disorder increases, $T_c$ and the energy gap $\Delta$ gradually decrease and eventually vanish. In this model, the system becomes a normal metal or a weak insulator because the Cooper pairs themselves are destroyed before global coherence is lost. In the bosonic scenario, Cooper pairs (which are bosons) continue to exist as local entities even as global superconductivity is lost. The disorder causes the film to break up into superconducting islands where the pairing amplitude $\Delta$ remains finite, but the correlation between the quantum phases of the order parameter of each island fluctuates. The transition occurs when phase fluctuations become so strong that global phase coherence is destroyed. The resulting insulating state is peculiar: it may still exhibit a gap in the density of states (a pseudogap) and contain localised Cooper pairs, but it lacks the zero-resistance property. This transition is often associated with the Berezinskii-Kosterlitz-Thouless physics, where the unbinding of vortex-antivortex pairs leads to the onset of resistance [84–86].

## 2.2 NbTiN characterisation & fabrication

All the resonators discussed in this thesis are fabricated by dc-sputtering on a target of $Nb_{81.9}Ti_{18.1}$ in a near-UHV sputter dc-sputtering system from DCA instruments, a stoichiometrical ratio that leads to high $T_c$ and $B_c$ [76]. In a $N_2$ environment, this process leads to the formation of NbTiN. This material has shown considerable promise and results in the quantum (computing) community [26, 87–93] as a robust superconductor, which combines both low losses for resonators, significant potential for high $L_k$, all while maintaining a reasonably high critical temperature that facilitates operation in regimes where elemental superconductors like Al or Nb are non-superconducting, as shown in Table 2.1. We do note that the multi-element composition makes consistent and reproducible fabrication more challenging than e.g. conventional Nb superconductors. Nonetheless, the superconducting parameters of NbTiN are highly adjustable; depending on the exact deposition techniques, ambient conditions and sputtering parameters, it cab be tuned to applications ranging from low-resistive, high-$T_c$ thick

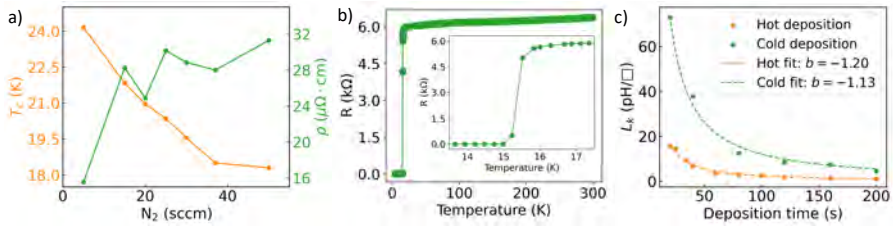


**Figure 2.3:** Basic superconducting characterisation of NbTiN thin films. **a**) Critical temperature $T_c$ and resistivity $\rho$ of 100s-deposition time films. The critical temperature is obtained from a measurement of decreasing temperature. **b**) Critical temperature measurements over a large range (with decreasing temperature) of a film grown with $N_2 = 37$ sccm, Ar = 60 sccm. *inset:* Finer scan (increasing temperature) around $T_c = 15.2$K. This films is fabricated with 35s sputtering time and is nominally 10 nm thick. **c**) The evolution of the kinetic inductance per square $L_{k,\square}$ with deposition time (as a proxy for thickness). Fits are shown to equation 2.9, with a thickness $t$ power-law ($t^b$) adjustment made as detailed in the text. The kinetic inductance is extracted from measurements of $T_c$ and $R_\square$ from Eq. 2.10.

layers to highly disordered thin-films. The primary control variables are the argon to nitrogen ratio, and the sputtering power. The former determines the exact stoichiometry of the resulting film, and hence many of the superconducting parameters. An increase of the latter leads to higher growth rates, which minimises impurity gas ation, a critical factor for active elements like Nb and Ti that readily form chemical bonds. Therefore, we always used the maximum sputtering power available (200 W). The substrate itself, target-substrate distance and substrate temperature also play significant roles; deposition at elevated temperature (upwards of at 450 °C) significantly improves $T_c$ and surface smoothness compared to unheated substrates [94–96]. The integrity of a superconducting thin film is fundamentally coupled to the quality of the substrate and the cleanliness of the growth interface. For the NbTiN films discussed herein, double-side polished C-plane ($Al_2O_3$) wafers with a thickness of $430 \pm 25\ \mu m$ serve as the substrate. Sapphire is selected not only for its low microwave loss tangent ($\tan\delta \sim 10^{-7}$ to $10^{-9}$ in the low-temperature regime) but also for its high thermal conductivity at millikelvin temperatures, which ensures that the superconducting leads remain thermalised to the mixing chamber plate of the dilution refrigerator [97–101]. To improve the surface, the sapphire substrates undergo a sequence of chemical treatments to eliminate organic and ionic contaminants, as detailed in Section 2.3.6. Then, the samples are loaded in the sputtering system. We worked with two recipes. For what we call "hot deposition", a pre-annealing step is performed and the substrate is heated in 30 minutes, to 660 °C which is held for another 30 minutes to facilitate the outgassing of adsorbed species and to promote surface reconstruction, ensuring optimal conditions for the subsequent growth of the NbTiN layer. For the "cold deposition", this annealing step is omitted and the substrate is clamped to an active water-cooled plate; empirically, it has been noted that this cooling is not very effective in this particular sputtering tool.

The sputtering occurs in a reactive atmosphere of Ar and $N_2$, where $Ar^+$ ions physically bombard the target, ejecting Nb and Ti atoms that react with $N_2$ molecules both in the plasma and on the substrate surface. The nitrogen partial pressure is the most critical control variable, as it determines whether the resulting film adopts a body-centred cubic metallic phase or the desired superconducting face-centred cubic rock-salt structure [102]. We thus performed a scan of the $N_2$/Ar carrier gas to

experimentally confirm the optimal growth conditions using cold deposition, shown in Figure 2.3a. We note that for these films, there is an exceptionally elevated $T_c$, likely due to cross-contamination with high-temperature superconductors that were grown in a system coupled to the sputtering chamber. The contamination was cleared afterwards, and "regular" critical temperatures of $\sim 15$ K were observed. From the gas(%) measurements, whose deposition occurred with a 60 sccm flow rate of Ar, we selected $N_2 = 37$ sccm as the optimal value that has acceptable resistivity (right graph axis), while maintaining a good superconductivity as shown in the $T_c$ measurements of Fig. 2.4b; a reasonable value of $T_c = 15.2$ K was obtained. These measurements, done in a Quantum Design DynaCool PPMS with 100 nA current bias, also gave a near-$T_c$ sheet resistance of $R_\square = 98.3\ \Omega/\square$. The critical temperate was extracted via a 1 $\Omega/\square$ cut-off in the averaged data of the temperature-decreasing sweep and the temperature increasing-sweep (inset), which overlap nearly exactly.

To further establish the superconductor fabrication process, we did measurements of the critical temperature and sheet resistance per square (not shown) in function of deposition time to extract the kinetic inductance with Equation 2.10, as shown in Fig. 2.3c. This relation is approximate in nature, and it was found that the (sheet) resistance in the measured deposition-time regime only marginally changes from room- to cryogenic temperature (increase of $\sim 10\%$). Hence, the $R_\square$ data was obtained at room temperature. We do this parameter sweep for both cold and hot deposition as detailed in the text above. Both deposition conditions exhibit a power-law scaling $L_k = at^b$, where $a$ and $b$ are fitting parameters characterising the deviance of the idealised geometric scaling of Eq. 2.9, i.e. $b = -1$. There, no account is taken for structural crystallographical changes with thickness. For both techniques $b < -1$; this indicates that the superfluid density increases with film thickness, consistent with a reduction in structural disorder (granularity) and improvement of film conductivity. The slightly more negative exponent observed for the hot-deposited films ($b_{\text{hot}} = -1.20$, $b_{\text{cold}} = -1.13$) suggests a stronger thickness-dependent evolution of superconducting properties, likely due to enhanced surface mobility during growth. We furthermore establish that, if a maximisation of $L_k$ is the prime goal, the cold deposition is a better option. On the other hand, the hot film provides a compromise between good film quality, while still maintaining a relatively large kinetic inductance potential.

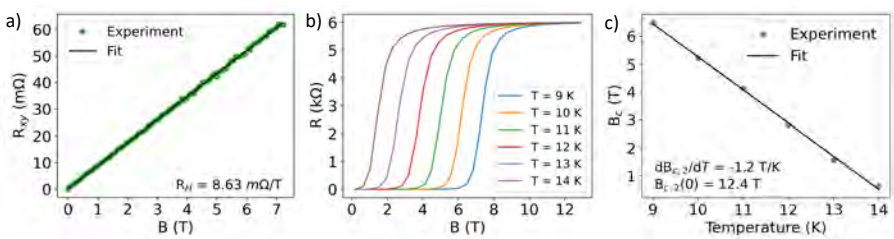


**Figure 2.4:** Direct-current measurement data of our nominally 10 nm thick (35 s deposition time) NbTiN films. **a**) Current biased (25 $\mu$A) ordinary Hall resistance in function of magnetic field taken at 30 K, just above $T_c$ for the thin film. Via a linear fit we extract $R_H = 8.63$ mΩ/T. **b**) The evolution of the (critical) magnetic field at elevated temperatures, close to $T_c$. **c**) The estimated critical fields $B_{c2}$ in function of the temperature near $T_c$. A fit to the Werthamer-Helfand-Hohenberg formula of Equation 2.6 yields $H_{c,2}(0) = 12.4$ T and $\frac{\mathrm{d}H_{c,2}}{\mathrm{d}T} = -1.2$T/K.

We now turn to the films that are used for later resonator fabrication: hot-style deposition of 34s deposition time (nominally 10 nm thick) on RCA cleaned sapphire. We performed out-of-plane magnetic field dependent characterisations of our NbTiN films in a four-point Hall bar geometry, with channel width 10 $\mu$m, length 595 $\mu$m and specifically fabricated out of the same film as the resonator with both conductor width and spacing 2 $\mu$m. These results are summarised in figure 2.4. The measurements are done at 30 K$\gg T_c$ to avoid potential interference of superconducting current screening. We use a current biased four-point measurement, with $I_{\text{bias}} = 25$ $\mu$A to measure the Hall-voltage $V_H$(B). We had to account for a small voltage offset of 1.2 $\mu$V, likely due to a misalignment of the arms, or a small in-plane field component due to the silver paint used to paste the sample to the puck. A linear fit to the data gives a Hall coefficient of $R_H = 8.63$ m$\Omega$/T. For one-charge carrier dominated transport, this coefficient is also defined as $R_H = \frac{1}{n_e e}$; hence from this measurement we obtain consecutively the electron carrier density $n_e = 7.23 \times 10^{28}$ m$^{-3}$ and the Fermi wave vector $k_F = (3\pi^2 n_e)^{\frac{1}{3}} = 12.9$ nm$^{-1}$. Subsequently, we derive the elastic electron mean free path $l_e = \frac{\hbar k_F}{n_e e^2 R_n d} = 0.74$ nm, a value similar to other NbTiN films reported in literature [66]. Including the limitations of data extraction, specifically for the film thickness, we estimate that the error on these values in first order is $\sim 20\%$. To extract the NbTiN coherence length, we first measure a B(T) diagram under a constant applied current bias of 25 nA, shown in Figure 2.4b. By scanning the magnetic field at fixed temperatures, we obtain the critical magnetic field $B_{c2}$ for each. Again, we use a 1 $\Omega/\square$ cut-of criterion. The close-to-$T_c$ tail-end of the $B_c$'s is shown in Figure 2.4c. Here, we extract the critical field at 0 K for a Type-II superconductor from fitting the data to the Werthamer–Helfand–Hohenberg formula of Eq. 2.6. Using our initially measured $T_c = 15.2$ K, this gives $B_{c2} = 12.4$ T. As the last step, we derive the Ginzburg-Landau coherence length as $\xi(0) = \sqrt{\frac{\Phi_0}{2\pi B_{c2}(0)}}$, giving $\xi(0) = 5.1$ nm, where $\Phi_0$ is the flux quantum.

As a final note on this Section, we want to highlight the multiple research articles that are either made, or have been directly inspired by this NbTiN sputtering recipe. These articles span the domains of superconducting resonators [35], Andreev state measurements [36], vortex physics [25, 26], phase-slip memory [89], superconducting computing [103], and cryogenic microwave generation with Josephson junction arrays [104].

## 2.3 Coplanar resonators

The engineering of superconducting microwave resonators has transitioned from basic circuit design to a matured discipline requiring an expert understanding of advanced material science, electromagnetic scattering theory, and (numerical) simulation. As central components in cQED, resonators serve as the primary mechanism for the readout and transmission of quantum information between different physical systems (e.g. qubits, optomechanical cavities, travelling-wave amplifiers, ...). The pursuit of high internal quality factors ($Q_i$) is driven by the necessity for long coherence times in superconducting qubits, high sensitivity in astronomical detectors and coherent quantum information transfer [105]. However, the emergence of hybrid quantum architectures which interface superconductors with semiconducting or magnetic struc-

tures, topological insulators, and ferrimagnetic insulators, introduces a new set of challenges, specifically the requirement for stable operation under high magnetic fields and the integration of local electrostatic gating. This Section reviews the state of the art in superconducting resonator research, with emphasis on the materials, device architectures, and analytical methods used in these quantum systems.

The fundamental performance of a superconducting resonator is determined by the (thin-film) superconductor and the dielectric substrate upon which it is deposited. While Al and niobium Nb have historically dominated the field due to their well-understood properties, documented characteristics and ease of integration into especially Josephson junction fabrication, their performance ceilings are increasingly challenged by emerging materials such as Ta, Nb(Ti)N, and granular aluminium (grAl). In essence, each of these materials have specific purposes and goals attached to them, with their own strengths and weaknesses. For example, Ta has recently emerged as

| **Material** | **Ox. Quality** | ***B*-resilience** | $F\delta_{LP,TLS}$ | **Uses** | Ref. |
|---|---|---|---|---|---|
| $\alpha$-Ta | High | Moderate | $1\times10^{-7}$ | Transmons, resonators | [106] |
| NbTiN | High | High | $3\times10^{-6}$ | Resonators | [35, 107] |
| grAl | - | Low | $1\times10^{-5}$ | Superinductors | [108] |
| Al | Moderate | Low | $1\times10^{-6}$ | Transmons, resonators | [109, 110] |

**TABLE 2.2:** BROAD OVERVIEW OF MATERIAL PROPERTIES AND CHARACTERISTIC TLS LOSS TANGENTS $F\delta_{LP,TLS}$ AT LOW POWER ($\langle n\rangle \approx 1$) FOR SUPERCONDUCTING QUANTUM CIRCUIT COMPONENTS. NOTE THAT THESE VALUES HIGHLY DEPEND ON EXACT GEOMETRIES, FILM STOICHIOMETRIES AND RESONATOR DESIGN.

a new material for high-coherence superconducting circuits [111]. The adoption of $\alpha$-tantalum has enabled a significant leap in transmon qubit lifetimes, with reported values exceeding 0.3 milliseconds [70] and approaching the millisecond regime in specialized architectures [112]. The primary advantage of tantalum lies in the structural and chemical stability of its native oxide, $Ta_2O_5$. Unlike the complex and often lossy sub-oxides of Nb, Ta's native oxide is thin, self-limiting, and hosts a low density of two-level system (TLS) fluctuators [111, 113]. An alternative approach is NbTiN, a material that due to the native nitrides also exhibits self-limiting oxide growth. It is a robust alternative for applications requiring high critical temperatures and substantial magnetic field tolerance. As shown in the previous section, the performance of NbTiN resonators is highly sensitive to the nitrogen partial pressure and the substrate temperature during growth; high-temperature deposition (660 °C) promotes surface reconstruction of the sapphire substrate, reducing the density of interface defects that contribute to TLS loss and generally improving the quality [112, 114]. Furthermore, thin film NbTiN is a "dirty" superconductor, with a high degree of granularity or disorder. This enables a large kinetic inductance, which is essential for reaching the strong coupling regime in hybrid circuits. Another emerging material is grAl, as a specialised material for the realisation of superinductors, which are circuit elements whose characteristic impedance need to exceed the resistance quantum ($R_Q = h/4e^2 \approx 6.45$ kΩ). Structurally, grAl consists of superconducting Al grains embedded in insulating amorphous $AlO_x$, forming essentially a three-dimensional network of Josephson junctions [108, 115]. This material-specific morphology leads to a kinetic inductance that can be several orders of magnitude larger than the geometric inductance, or than other related superconducting materials. Interestingly, the critical temperature $T_c \approx 2-4$ K is much larger than the non-disordered Al [116]! The reason

for this is outside the scope of this work, but speculations are found in [117]. On the other hand, grAl generally exhibits a relatively high loss factor, and quasiparticle domination at low temperatures. As the resistivity of the grAl increases (e.g. due to higher oxygen content during growth and thus smaller/more isolated grains), the internal losses also tend to increase, leading to a trade-off between the desired high kinetic inductance and the achievable quality factor. Furthermore, the high sensitivity of the film to oxygen content leads to reproducibility and homogeneity issues, further demonstrating the specificity of this material for applications [117]: the material's strong nonlinearity and high impedance make it uniquely suited for coupling to systems with small electric dipole moments, such as spin ensembles or isolated charge states, but not as a general resonator.

Thus, the trade-off between using Ta, NbTiN or grAl is a design consideration: Ta is a proven-true high quality resonator material, fit for many applications. NbTiN offers superior magnetic field resilience for hybrid cQED applications, and grAl is advantageous in low-field regimes [118, 119] requiring (very) large impedances and consequently large kinetic inductance. We summarise these parameters and the main use case of these materials in Table 2.2.

### 2.3.1 Basic resonator parameters

The characterisation of superconducting resonators relies on the measurement and interpretation of scattering (S) parameters, often obtained using a Vector Network Analyser (VNA). These parameters quantify the transmission and reflection of microwave signals at the resonator ports, providing the data necessary to extract the device's physical qualities and quantities. In a reflection-mode measurement, a single port is used to both excite the resonator and capture the reflected signal. The $S_{11}$ scattering coefficient is defined as the ratio of the reflected voltage wave to the incident voltage wave. For a resonator coupled to a transmission line, the $S_{11}$ response is characterised by a dip in the amplitude and a corresponding rotation in the phase at the resonance frequency, forming a circle in the complex (IQ) plane. The generalised model for the scattering coefficient of a reflection-type resonator [120] must account for the non-ideal microwave environment. This includes signal attenuation ($a$), an initial phase offset ($\alpha$), and an electronic delay ($\tau$) resulting from the finite length of the cryogenic microwave cables:

$$S_{11}(f) = ae^{i\alpha}e^{-2\pi i f\tau}\left(1 - \frac{2Q_l}{\widetilde{Q}_c}\frac{1}{1-2iQ_l(\frac{f_r-f}{f_r})}\right). \tag{2.11}$$

In this formulation, $f_r$ is the resonance frequency and $Q_l$ is the loaded quality factor. The coupling quality factor $\tilde{Q}_c$ is treated as a complex quantity, $\tilde{Q}_c = |Q_c|e^{-i\phi}$, where the phase $\phi$ (the so-called "phi factor" or fano factor) quantifies the asymmetry in the Lorentzian lineshape caused by e.g. impedance mismatches in the measurement chain. The efficiency of a resonator is defined by the quality factor ($Q_l$), which represents the ratio of stored energy to the energy lost per microwave cycle. This total or "loaded" quality factor is the inverse sum of the contributions from internal and external loss mechanisms, and is what is measured in a transmission measurement

(versus a reflection measurement):

$$\frac{1}{Q_l} = \frac{1}{Q_i} + \mathrm{Re}\left\{\frac{1}{\widetilde{Q}_c}\right\}. \tag{2.12}$$

Its value directly related to the phase-roll of the resonator around resonance:

$$\theta(f) = 2\tan^{-1}\left(2Q_l\left[\frac{f_r - f}{f_r}\right]\right) + \theta_{\mathrm{offset}}; \tag{2.13}$$

we see that at resonance, the phase roll exhibits a factor $2\pi$, independent of the phase offset $\theta_{\mathrm{offset}}$. Furthermore, from Eq. 2.12, it is seen that $Q_l$ is constituted from the internal quality factor and the coupling or external quality factor. The former, $Q_i$, is the primary metric for material performance, as it reflects energy dissipation within the superconducting film and the surrounding dielectrics. The latter, $Q_c$, represents the rate at which energy escapes the resonator into the external measurement circuit. For material research, it is often desirable to have $Q_c \approx Q_i$ (critical coupling) or $Q_c < Q_i$ (the overcoupled-regime) to ensure faster pulse-speeds for qubit gating and good state-discernibleness; in the undercoupled regime, most of the mw-signal gets reflected at the input capacitor and hence the visual drop in phase and amplitude are small. In the heavily overcoupled regime, the amplitude is still small, but the phase roll is maximal and at least the resonator's resonance frequency can accurately be measured or traced (albeit not easily the quality factors, besides $Q_l$) [121, 122].

### 2.3.2 Introduction to microwave losses

The energy dissipation in superconducting resonators originates from multiple primary channels: two-level system fluctuators, non-equilibrium quasiparticles, radiative losses, disorder, substrate losses, vortex motion in the presence of magnetic fields and more. These losses are related to the internal quality factor as $\tan(\delta) = \frac{1}{Q_i} \approx \delta$, and can be written in the form of

$$\frac{1}{Q_i} = \frac{1}{Q_{i,\mathrm{TLS}}(T,P)} + \frac{1}{Q_{i,\mathrm{QP}}(P,T)} + \frac{1}{Q_{i,\mathrm{rad}}} + \frac{1}{Q_{i,\mathrm{disorder}}(t)} + \frac{1}{Q_{i,\mathrm{sub}}} + \frac{1}{Q_{i,\mathrm{vortex}}(B)} + \frac{1}{Q_{i,\mathrm{environment}}(T,P)} + \frac{1}{Q_{i,\mathrm{cosmic\,rays}}} \ldots \tag{2.14}$$

Immediately it is clear that the internal quality factor (and hence, the losses) will be limited by the largest loss mechanism in the structure, which depends on power $P$, temperature $T$, thickness or material structure $t$, environment and magnetic field $B$. Furthermore, these parameters are not independent - for example, an increase in disorder is often due to increase in film oxidation, leading to more TLS. However, it also changes the superconducting gap, and hence the distribution of quasiparticles in the superconducting film.

At millikelvin temperatures, low microwave powers, no magnetic field and a well-isolated device, the dominant loss mechanism in high-$Q_i$ resonators is *often* the resonant absorption of photons by TLS, some mechanisms of which are shown in Figure 2.5. These fluctuators are microscopic defects, e.g. polar molecules, dangling bonds, hydrocarbons or atomic tunnelling states [22], that exist in the amorphous native oxides present around the device and at the (disorderous) interfaces. The internal

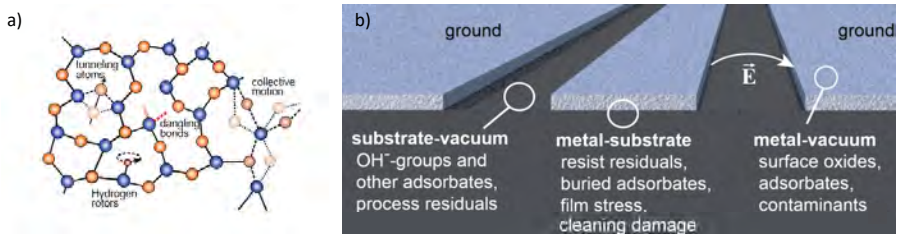


**Figure 2.5: a**) A schematic overview of (some) mechanisms of TLS formation in amorphous materials: tunnelling of single atoms, collective motion of small atomic groups, dangling bonds, and hydrogen defects. **b**) Typical mechanisms underlying TLS formation at the different interfaces of coplanar waveguide resonators. Images both adapted from [123].

loss due to TLS follows a characteristic power and temperature dependence. As the microwave power (and hence the average internal photon number $\langle n \rangle$) increases, the TLS ensemble becomes saturated. In this state, the population of the excited state increases until the TLS no longer absorb additional photons, leading to an effective increase in $Q_i$, as the loss-factors no longer participate in transport above a characteristic power threshold $n_c$. These power-dependent losses are also called the "*narrow-band*" losses as they only probe a narrow frequency band around the resonance [124, 125], and are modelled at cryogenic temperatures as [126, 127]:

$$\frac{1}{Q_i} = \frac{F\tan(\delta_{\text{tls}}^0)}{\left(1+\frac{\langle n \rangle}{n_c}\right)^{\beta}} + \delta_{\text{other}}\,, \tag{2.15}$$

where $F$ is the geometric filling factor (the fraction of the electric field energy stored in the lossy dielectric), $\tan(\delta_{tls}^0)$ is the intrinsic TLS loss tangent, $\delta_{\text{other}}$ the next-largest loss factor from Equation 2.14, $n_c$ is the characteristic photon saturation number that depends on the TLS dipole moments, zero point energy and the TLS coherence times [128], and $\beta$ describes the interaction strength within the TLS ensemble [129, 130]: $\beta = 0.5$ for non-interacting TLS, and $\beta < 0.5$ for planar resonators with interacting TLS due to oxide interfaces or processing residues. While this equation is oft-used, it is an approximation that neglects the effect of quasiparticle-loss due to increased microwave power [131, 132]. To derive the average photon number $\langle n \rangle$ that circulates in the resonator due to an applied power at the chip $P_{in}$, we use a general form of $S_{11}$, given by Equation 2.16 [133, 134]:

$$|S_{11}| = \left| \frac{1-\frac{Q_i}{Q_c}}{1+\frac{Q_i}{Q_c}} \right| . \tag{2.16}$$

Under steady-state conditions, the average photon number circulating in the resonator is [135]

$$\langle n \rangle = \frac{P_{\text{abs}}\, Q_i}{\hbar \omega_R^2} . \tag{2.17}$$

In a pure reflection-type resonator (i.e. without coupling to a central transmission line), we also relate the dissipated energy per resonance cycle $P_{abs}$ to the input power at the chip by [136]:

$$P_{abs} = P_{in} - |S_{11}|^2 P_{\text{in}} \tag{2.18}$$

which means that

$$\langle n \rangle = \frac{4Q_l^2}{\hbar\omega_R^2 Q_c} P_{\text{in}} \tag{2.19}$$

as $Q_l = \frac{Q_i Q_c}{Q_i + Q_c}$. To account for reflections due to impedance mismatch between the input feedline impedance $Z_0$ and a resonator impedance $Z_R$, the final result becomes

$$\langle n \rangle = \frac{Z_0}{Z_R} \frac{4Q_l^2}{\hbar\omega_R^2 Q_c} P_{\text{in}} \,, \tag{2.20}$$

where $Q_c = |Q_c|\cos(\phi)$. We note that it seems that at $\phi = \frac{\pi}{2}$, the photon number would diverge, which is an unphysical scenario as it implies an infinite coupling capacitance, leading to all the photons escaping the resonator. In simulation, this shows as a minimal phase roll associated with resonance, as is seen in Figure 2.6. We stress that experimentally most of these values are an approximation, especially without cryogenic in-situ calibration and hence $\langle n \rangle$ can vary by an order of magnitude compared to the "real" physical value.

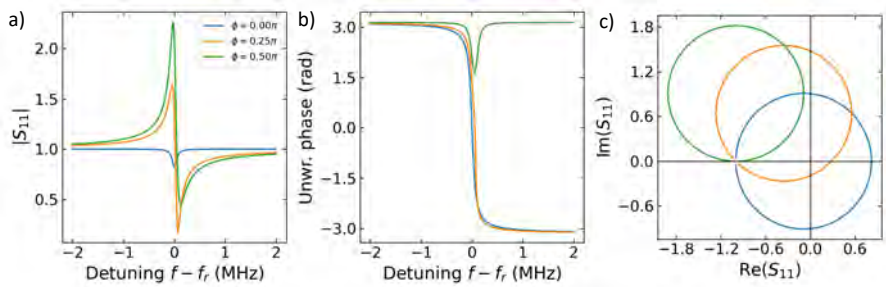


**Figure 2.6:** Simulated reflection response $S_{11}$, generated using Eq. 2.11 of an isolated overcoupled resonator for different values of the asymmetry parameter $\phi$; $Q_i = 6 \times 10^5$, $Q_c = 6 \times 10^4$, $f_r = 6$ GHz.
**a**) magnitude response as a function of frequency detuning from resonance. **b**) corresponding unwrapped phase response. **c**) trajectory in the complex IQ plane. A non-zero $\phi$ produces an asymmetric resonance line shape and rotates the resonance circle in the complex plane, illustrating the effect of e.g. impedance mismatch in the measurement environment.

An exemplary fit for Equation 2.15 is shown in Figure 2.7a for the CPS resonator with conductor widths 2 $\mu$m and gap spacing 2 $\mu$m. In our films, even though optimised for measurements using high kinetic inductance, we still use a comparatively non-disorderous film with corresponding "low" $L_k$ [115] as high kinetic inductance (i.e. ultra thin) films are prone to low fabrication reliability. Furthermore, quasiparticles and are more readily excited for highly disordered superconductors and are mainly generated by high-frequency radiation which more easily enters the device at higher drive powers (e.g. due to higher harmonic/frequency components that become more pronounced). As shown in Section 2.3.6, we avoid this using specially designed copper powder filters that filter away this radiative component, similar to [137].

A further characterisation technique for superconducting resonators is temperate dependent loss measurements. As temperature increases, the real part of the dielectric constant of the TLS medium changes, causing $f_r$ to shift. This wide-band effect (and hence, *wide-band* losses) is nearly power-independent because off-resonant TLS,

which span a broad spectral range, remain unsaturated. Due to this, it is possible to gather data at higher powers which speeds up measurements. We used $\langle n \rangle = 1e5$, which for each characterised resonator in this thesis is in the high-power saturated regime [125] of Eq. 2.15. The relative frequency shift is modelled by the complex digamma function ($\Psi$), valid for approximately $T \lesssim 0.1T_c$, where quasiparticle losses generally take over [130, 138, 139]:

$$\delta f = \frac{\Delta f}{f_0} = \frac{k}{\pi}\left(\mathrm{Re}\left[\Psi\left(\frac{1}{2}+\frac{1}{2\pi i}\frac{hf_r(T)}{k_BT}\right)\right]-\ln\left(\frac{hf_r(T)}{k_BT}\right)\right). \tag{2.21}$$

In this equation, $\Delta f = f_r(\mathrm{T}) - f_0$ is the temperature-dependent resonance frequency referenced at low temperature (in our data at the lowest point of 10 mK). furthermore, the factor $k = F\delta_{\mathrm{tls}}^{0,i}$ contains the intrinsic temperature dependent TLS-loss component, $\delta_{\mathrm{tls}}^{0,i}$, sensitive to thermally varying TLS for a wide spectrum [22], and the filling factor $F$, a geometric parameter representing the fraction of the electric field energy stored in the TLS-hosting medium. At higher temperatures, the onset of quasiparticles dominates the resonator's frequency shift and losses [72, 140]. For this reason we constrained all our later fits to data up to $\sim 450$ mK, still well below the superconducting energy gap of NbTiN (with $T_c$ in the range of 15 K). A representative fit of the temperature dependent frequency shift is shown in Figure 2.7b. The presence of a universal dip in the relative frequency shift at $T \approx \frac{\hbar\omega_R}{2k_B}$ supports the validity of Equation 2.21 for these resonators, and confirms that quasiparticle loss is not a dominant factor in the total loss of the resonator [115, 139]. The observed discrepancy between fit and experimental data at very low temperatures has similarly been observed for TLS-dominated CPW resonators [141, 142]. Primarily, this occurs as Eq. 2.21 is an approximation that ignores the presence of strong long-range TLS-TLS interactions [123, 128, 143]. Due to the high-power allowance, the frequency shift provides a generally fast method for extracting the TLS loss tangent compared to power-dependent measurements; furthermore, if one simply tracks the change in derivative *phase* around resonance, instead of the full resonator $S_{11}$ amplitude, this method becomes even faster without losing much accuracy at the cost of extraction of the $Q$-factors.

The impact of TLS loss is highly sensitive to the resonator geometry. Because TLS fluctuators are concentrated at interfaces, the total loss is a summation of the participation ratios ($p_i$) of the different dielectric regions: metal-air (ma), metal-substrate (ms), and substrate-air (sa). The total loss tangent is expressed as $\sum p_i \tan(\delta_i)$, where surface type $i$ has a loss tangent $\delta_i$. Numerical simulations using finite element methods, e.g. with COMSOL or Ansys HFSS, indicate that the participation ratios of the lossy surface layers decrease as the width ($W$) of the resonator leads and the gap spacing between the leads ($G$) increase. This is because wider leads distribute the electric field over a larger volume of the low-loss substrate, thereby reducing the relative influence of the interface oxides. The participation ratio $p_i$ for a given volume or interface $V_i$ with dielectric constant $\varepsilon_i$ is defined as the fraction of the electric field (energy) $E$ in that volume to the total electric energy stored in the electric field (energy) threading the resonator. Generally, there are 5 such interfaces participating in loss-calculations: the metal-air interface ($p_{ma}$), the metal-surface interface ($p_{substrate}$) , the surface-air interface ($p_{sa}$), the substrate ($p_{air}$) and the air/vacuum. The participation ratio of a TLS-host volume is then defined as

$$p_i = \frac{\frac{1}{2}\int_{V_i}\varepsilon_i|E|^2\mathrm{d}V}{\frac{1}{2}\int_V \varepsilon|E|^2\mathrm{d}V}\ . \tag{2.22}$$

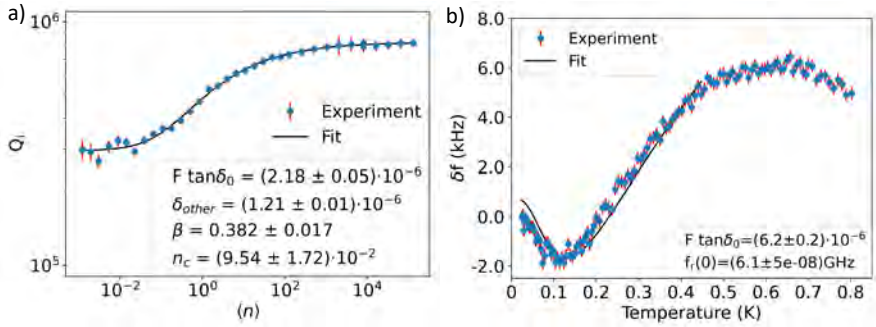


**Figure 2.7:** Representative fits of the losses of the coplanar stripline resonator with conductor widths $W = 2\ \mu$m and gap spacing $G = 2\ \mu$m.
**a**) A representative power-dependent evolution of the internal quality factor . The experimentally determined internal quality factor $Q_i$ values (blue), including error bar (red), are fitted to Equation 2.15 (black). **b)** Low-temperature dependent resonance shift at zero magnetic field at high average internal photon level. The experimentally determined frequency shift $\delta f$ values (blue), including error bar (red), are fitted to equation 2.21 (black).

Here, $\varepsilon$ is the effective permittivity of the entire volume $V$ [144, 145].

### 2.3.3 Simulation

The design and optimisation of high-$Q$ superconducting resonators relies on accurate electromagnetic modelling. For planar circuits used in circuit quantum electrodynamics, Sonnet Software [146], which is based on a method-of-moments (MoM) solver, is particularly well suited. Most simulations in this thesis were done using Sonnet 19.52. In the case of high-kinetic-inductance superconductors such as NbTiN, the film should be modelled using the surface impedance loss type, in which the surface kinetic inductance is included as an input parameter in units of pH/□. Prior to low-temperature characterisation, this quantity is generally not known precisely. Instead, it must be estimated from the sheet resistance and superconducting energy gap within the thin-film superconductor model at base temperature using Eq. 2.10, and subsequently refined by comparison between simulated and measured resonance frequencies. In practice, an iterative calibration of the effective $L_k$ is often required, since estimates based on room temperature dc transport deviate by several percent due to film non-uniformity, thickness variations, or fabrication-related disorder.

#### Meshing

Within an MoM solver, the circuit geometry is discretised into subsections over which the surface current distribution is calculated. Sonnet provides two principal meshing strategies: staircase meshing and conformal meshing. Staircase meshing uses rectangular subsections aligned with the simulation box and is computationally efficient during matrix construction, but it requires a very large number of cells to represent curved or oblique geometries accurately. Since the computational cost (generally: the matrix-fill and solve time $t$) of matrix inversion scales steeply with the number of subsections $N$, namely as $t \sim N^3$, this leads to long simulation times for complex layouts. Conformal meshing instead adapts the subsection boundaries to

the underlying polygonal geometry, thereby providing a more faithful representation of current flow with fewer elements. This is especially advantageous for meandered structures and high-impedance nanowire resonators, where geometric details strongly influence the impedance and current density distribution. Even for comparatively simple CPS resonators, the use of a refined mesh near conductor edges is important, because the microwave current density is strongly enhanced at the edges. The current profile in Figure 2.8a shows this for a reference simulation using mesh sizes $\Delta x, \Delta y = 0.1\ \mu$m. Capturing this non-uniform current distribution is essential for accurately understanding and extracting the kinetic inductance contribution. This importance is further clarified in Figure 2.9.

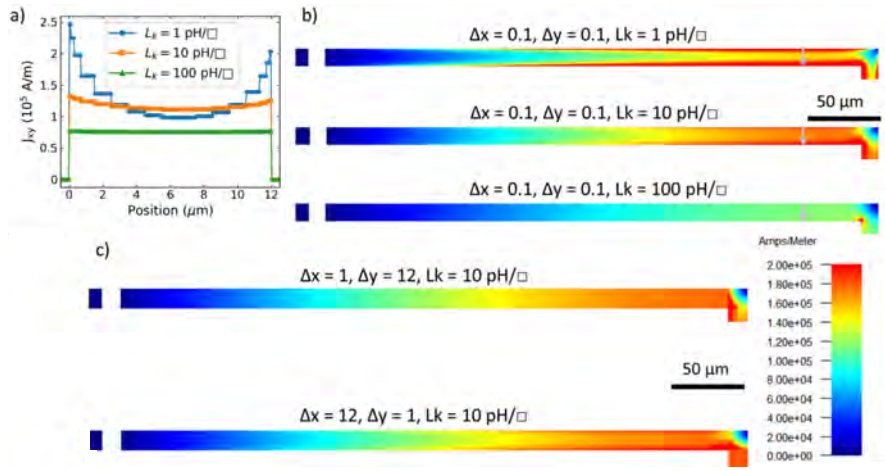


**Figure 2.8:** Simulated current density $J_{xy}$ as a function of location on the conductor line, and in function of smallest mesh step $\Delta x, \Delta y$ .
**a**) Current profile with respect to position as indicated with black arrows in subfigure b; direction and position on the conducting line correspond to the position $0 \rightarrow 12\ \mu$m. The low-kinetic inductance $L_k$ resonator has more pronounced edge currents. **b**) Simulation of current density at the smallest mesh sizes of $\Delta x, y = 0.1\ \mu$m. **c**) Effect of current crowding due to large finite mesh sizes. The scale bar is shared over the current density plots.

Naturally, one would like to use the smallest meshing size available; however, as noted above, this leads to an exponential increase of discretised polygons and hence computation time. Thus, a trade-off has to be made, especially when including the kinetic inductance. The importance of meshing and its relation to the $L_k$ of the superconducting film is further summarised in Figure 2.8b. Here, we show the current density flowing through the superconductor of the reference simulation at $L_k = 1, 10, 100$ pH/□. For the CPS resonator structure, simulated using a perfect differential drive, we varied both the horizontal axis ('$x$'-axis) and vertical axis ('$y$'-axis) meshing using minimal step $\Delta x, \Delta y = 0.1\ \mu$m. All critical parameters of the resonator are 12 $\mu$m: conductor line width, capacitance gap and ground-conductor spacing. For low kinetic inductances the current is constrained to the edges of the resonator, while for very high $L_k$, the profile is much more uniform. Phenomenologically this is understood via the definition of $L_k$, Equation 2.9, which scales with the London penetration depth. For large kinetic inductances, $\lambda \gg w$, the width of the conducting line and thus the current density is uniform over the entire width. We notice in Fig 2.8a that $J_{xy}$ is also asymmetric over

the width of the resonator due to the differential drive. Indeed, this is a core tenet of the differentially driven CPS resonators, as the lower current density, and hence electric field, will intuitively lead to lower losses as will be seen later.

The evolution of the simulated resonance frequency shift compared to the reference simulation-resonance frequency, exhibits a clear trend of increasing offset as the meshing density decreases. The scaling with x-meshing ($\Delta y = 1\ \mu$m) of Figure 2.9a is comparatively small. Since the resonator structure is elongated in this direction, the only real parameters that changes in this case is $Q_c$. However, at large meshing sizes ($\Delta x = 12\ \mu$m), we see seemingly improved behaviour, with the resonance frequency nearing that of the reference simulation. As the current reaches the final bend of the resonator, flowing into the ground plane, there is current crowding. We show this in Figure 2.8c for parameters $\Delta x/y = 1/12$ and $12/1\ \mu$m and $L_k = 10$ pH/□. Ideally, this is mitigated by a more rounded, or even subdivided corner, respectively a fillet or a chamfer. Such chamfering of the corners leads less current reflections on the sharp edges, and provides a method to compensate for both parasitic capacitance as well as bend reactance [147]. Due to the non-negligible step when the meshing is nearing the critical parameter size, likely this crowding is not taken into account in simulation, leading in this specific case to 'improved' simulation. Conversely, when varying the $y$-mesh ($x$-mesh $= 1\ \mu$m) in Figure 2.9b, we see an order-of-magnitude larger change in the extracted resonance frequency due to similar reasoning. Furthermore, in both cases of meshing, the shift is much smaller with large kinetic inductances. Both the current-density and resonance frequency shift simulations point towards a same underlying cause, as earlier touched upon. The apparent improved accuracy in $f_r$ of especially the $L_k = 1$ pH/□ simulation at larger mesh sizes is due to current crowding at the final bend, chiefly. At low kinetic inductances, the result of *not* including this effect is largest, as the current landscape is more intricate compared to e.g. the $L_k = 100$ pH/□ simulation. Hence, aberrations to the "expected" behaviour are more pronounced.

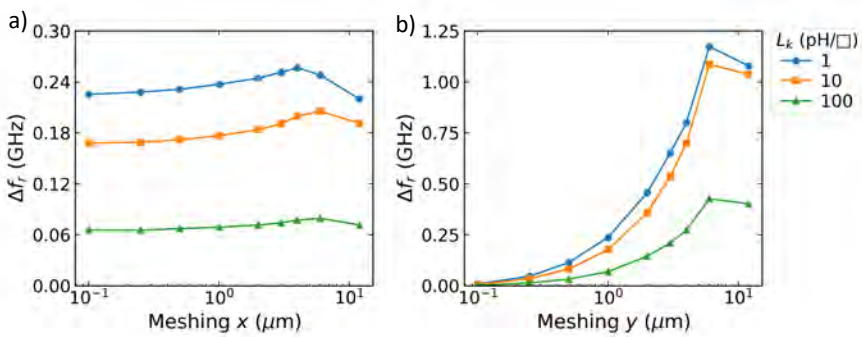


**Figure 2.9:** Dependence of the simulated resonance-frequency shift $\Delta f_r$ on the simulation meshing density for different values of the kinetic inductance $L_k$. **a**) Variation of $\Delta f_r$ with the mesh size in the $x$ direction, showing a relatively weak dependence over the investigated range. **b**) Variation of $\Delta f_r$ with the mesh size in the $y$ direction, for which the simulated resonance becomes markedly more sensitive, especially for smaller $L_k$. This highlights the importance of accurate choice of mesh-size when simulating superconducting resonators, particularly across the transversal conductor width.

### Coupling capacitance and coupling quality factor

Correct simulation of the coupling quality factor $Q_c$ also requires careful treatment of the coupling capacitance and of the impedance environment surrounding the resonator. In principle, one would like to incorporate the physical thickness of the relevant material layers explicitly. However, Sonnet is fundamentally a planar solver. Nevertheless, it provides reliable capacitance estimates through its surface-impedance description of the metal layers. In this approach, the finite conductivity and thickness of the conductor are incorporated into an effective surface impedance assigned to an idealised zero-thickness sheet. This treatment captures much of the relevant electromagnetic response of planar capacitor structures, including fringing fields and shunt capacitance to ground. In Sonnet, the quantity *Capacitance1*, derived from the input admittance $\mathrm{Im}(Y_{11})$, includes the effect of the shunt capacitance, whereas *Capacitance2*, derived from $\mathrm{Im}(Y_{21})$, more closely represents the series capacitance with the shunt contribution removed. For thin superconducting films and moderate trace spacing, this planar approximation is often sufficient. However, when the metal thickness becomes comparable to the trace width, or when the gaps are very small, the standard *General Metal* model may underestimate the physical capacitance of the fabricated device. In such cases, the *Thick Metal* model provides a more realistic representation by approximating the conductor as a finite-thickness structure with separate top and bottom sheets connected around the polygon perimeter. This improves the accuracy of capacitance extraction for conventional metallic structures, but comes at the expense of a straightforward inclusion of superconducting surface inductance. As a result, simulations of superconducting resonators often involve a trade-off between accurately capturing finite-thickness capacitance effects and including the kinetic inductance contribution self-consistently, although newer implementations of the software may mitigate this limitation [148].

In addition to direct capacitance extraction from the simulated admittance matrix, the coupling capacitance is also estimated from the (measured or simulated) coupling quality factor. Using the expression

$$Q_c = \frac{\pi}{4(2\pi f_r)^2 C_c^2 Z_0 Z_R}\,, \tag{2.23}$$

one may determine the coupling capacitance $C_c$ once $Q_c$ is known. In practice, this can be done very accurately by exploiting the fact that the resonance reflection minimum is deepest near critical coupling, where $Q_i = Q_c$. Thus, by sweeping the internal quality factor in simulation and identifying the point at which the absolute resonance features (phase and amplitude) are maximised, one can get a very accurate estimate of $Q_c$ and readily extract $C_c$. In our CPS resonators, generally $C_C = 5.09$ fF.
To derive Equation 2.23, we followed the same procedure as Ref. [149], adapted here to pure reflection type $\lambda/4$-resonators. The input impedance of a shorted $\lambda/4$ line near resonance is given by [133]

$$Z_{in} = \frac{2Z_R}{\frac{\pi}{2Q_i} + \frac{i\pi\Delta\omega_0}{\omega_0}} \tag{2.24}$$

where $Z_R$ is the resonator's characteristic impedance and $\Delta\omega_0$, the drive frequency $\omega$ offset to the bare resonator resonance frequency $\omega_0$. Coupling the resonator to the

environment is usually done via $C_c$ which modifies the impedance

$$\begin{aligned} Z_{\text{tot}} &= Z_{in} + \frac{1}{i\omega C} \\ &= 2Z_R \frac{\frac{2Q_i}{\pi} - i\left[\frac{4Q_i^2}{\pi}\frac{\Delta\omega_0}{\omega_0} + \frac{1}{2\omega Z_R C_c}\left(1+4Q_i^2\frac{\Delta\omega_0}{\omega_0}^2\right)\right]}{1+4Q_i^2(\frac{\Delta\omega_0}{\omega_0})^2} \,. \end{aligned} \tag{2.25}$$

The resonance frequency is correspondingly shifted to a new value $\omega_R$:

$$\frac{\Delta\omega_0}{\omega_0} = \frac{2}{\pi}\omega_R Z_R C_c \,. \tag{2.26}$$

Here, we used the fact that $\text{Im}(Z_{\text{tot}}) = 0$ at resonance. Furthermore, we assume that $\frac{Q_i^2}{\pi^2} \gg \frac{1}{4\omega_R^2 C_c^2 Z_R^2}$ which is valid for most high-impedance mw resonators with $Q_i \gtrsim$ 1e5. Under these conditions, the total impedance at resonance becomes:

$$\begin{aligned} Z_{tot} &= \frac{4Z_R Q_i}{\pi}\frac{1}{1+\frac{1}{\pi^2}16Q_i^2\omega_R^2 Z_R^2 C_c^2} \\ &= \frac{\pi}{4Q_i Z_R \omega_R^2 C_c^2} \,. \end{aligned} \tag{2.27}$$

Finally, equating the general impedance expression for the reflection coefficient with a standard resonator form (Eq. 2.16) gives [133, 134]:

$$|S_{11}| = \left|\frac{1-\frac{Z_0}{Z_{tot}}}{1+\frac{Z_0}{Z_{tot}}}\right| = \left|\frac{1-\frac{Q_i}{Q_c}}{1+\frac{Q_i}{Q_c}}\right| \,, \tag{2.28}$$

from which Eq. 2.23 follows directly by inspection.

### Impedance

In addition to resonance frequency and coupling, impedance extraction in Sonnet requires some care in interpretation. In particular, the quantity reported as `Line Z0` should not be understood as the total impedance of the full resonator structure seen from a port. Rather, it corresponds to the characteristic impedance of the transmission-line cross section defined locally at the box-wall reference plane, as determined from the port de-embedding calibration standards. Notably, in the case that the full resonator (including coupling capacitance) is simulated, it is the impedance of the feedline in conjunction with the resonator that is seen. In Sonnet, these calibration standards are constructed from the geometry attached to the box wall and are used to define quantities such as `Line Z0` and effective permittivity at the reference plane. By contrast, the physically relevant impedance seen by the excitation port is the `Input Impedance`, which is derived from the simulated reflection coefficient with respect to the specified port impedance (typically 50 Ω). For non-uniform or composite superconducting transmission lines, these two quantities differ substantially: `Line Z0` primarily reflects the local line section at the port, whereas the `Input Impedance` captures the frequency-dependent response of the entire downstream structure, including impedance transformations, discontinuities, and resonant loading. Consequently, when analysing high-impedance superconducting resonators or structures with significant

or spatially varying kinetic inductance, the input impedance is the more meaningful quantity for comparison with experiment, while `Line Z0` is best viewed as a local reference-plane property rather than a global device impedance. For this reason, impedance simulations in Sonnet should be carried out with fine meshing and carefully chosen coupling capacitance, since the locally extracted line parameters retain sensitivity to the exact construction. In the specific case of CPS resonators, we suggest to just implement the resonator conductor line (and potential ground line), without the coupling capacitance, and using the `Input Impedance` close to resonance.

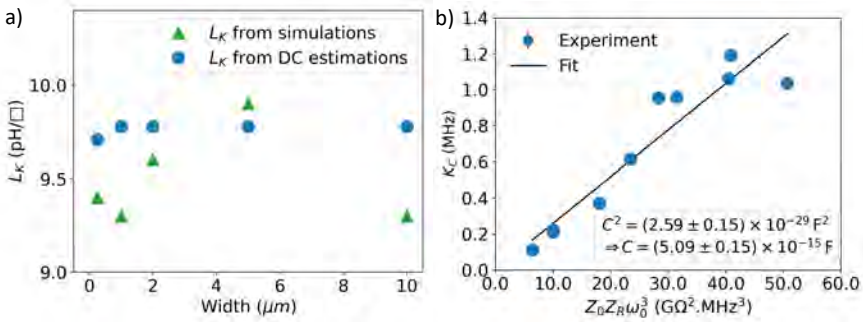


**Figure 2.10: a**) The estimated kinetic inductance $L_k$ of each sample from dc measurement of bulk films at room temperature, compared to the estimated kinetic inductance from simulations of the resonance in the mK regime for varying conductor width $W$. Green triangles are the simulated $L_k$, blue circles are the estimated $L_k$ from dc measurements. **b**) Validity test of the simulation and fitting procedures. The external quality factor $Q_c$ is plotted versus the rescaled simulated impedance of the resonators. A fit is performed using Equation 2.23.

### Verification

Since the coplanar stripline geometry is a new design, uses a differentially driving technique and exists of a relatively high kinetic inductance material, we needed to be certain that standard mw resonator simulation techniques work. We present this verification in Figure 2.10. When fabricating a sample, we measure the dc-sheet resistance of the NbTiN film which enables us to estimate the kinetic inductance via Equation 2.10, where we use the superconducting energy gap of NbTiN via the BCS theory for extremely dirty superconductors, Equation 2.1 [52–54, 80]. The critical temperature $T_c$ is estimated from dc-measurements on similar NbTiN films of the same thickness and is $\sim 15$ K, while the normal state resistance $R_N$ is ideally measured right above $T_c$. As the resistance of disordered metals does not change appreciably with temperature, we estimate it from measurements at room temperature. All dc-parameters of a representative film are shown in Section 2.2. We correspond the resulting inductance value to the kinetic inductance we obtain from a comparison between a simulated resonance frequency in Sonnet to the fitted resonance frequency from measurements [140]. This data is shown in Figure 2.10a. We attribute deviations to fabrication tolerances, a slight non-uniformity of the film thickness and the crude estimation of the kinetic inductance using only the room temperature sheet resistance. A good correspondence is obtained.

A second check of simulations versus measurements is shown in Figure 2.10b. From

fitting resonator data we obtain the external quality factor $Q_c$ while from resonator simulations we obtain its impedance $Z_R$, as detailed above. The relation between $Q_c$ and $Z_R$ is given by Equation 2.23. Large discrepancies would show in case the simulations are not realistic; luckily, these are absent. This lets us to derive the coupling capacitance $C_c$. In the resonator designs, this capacitance was kept approximately constant. However, deviations cause discrepancies between data and fit, e.g. due to the increasing width of the conductor which minimally changes $C_c$ but was unaccounted for. Furthermore, a constant $f_r$ was assumed, but here a natural variation due to slightly differing kinetic inductances was also observed. Finally, at smaller resonator conductor width, fabrication errors become relatively more pronounced (i.e. at higher $Z_R$). We use Equation 2.23 to do a linear fit to the coupling rate $\kappa_c = \frac{2\pi f_r}{Q_c}$ in function of $Z_R f_r \times Z_0 f_r^2$ to obtain the coupling capacitance directly, and we get a reasonable value of $C_c = (5.09 \pm 0.15) \times 10^{-15}$ F. We find the correspondence enough to conclude that standard industry CPW simulation and fitting routines are applicable to CPS resonators.

### 2.3.4 Fitting algorithm

Extracting the quality factors and resonance frequency from noisy VNA data requires a robust fitting algorithm. The methodology developed by Probst *et al.*, based on prior work by Khalil *et al.* [134, 150] has become the gold standard for this analysis due to its robustness against the presence of noise and its handling of experimental non-idealities. It's generally called the algebraic "circle-fit", or more accurately, diameter-corrected method (DCM): the complex reflection coefficient, $S_{11}$, for a pure reflection-type resonator is described by a Lorentzian-like lineshape that traces a circle in the complex IQ-plane. Unlike traditional fitting routines that often struggle with convergence or accuracy in low-power regimes or asymmetric signal profiles, the circle-fit method used an algebraic circle fit technique of the real and imaginary data that is computationally fast and physically intuitive. Furthermore, it is not reliant on initial parametrisation; iterative fitting techniques often suffer from poor convergence if the initial parameter guesses are inaccurate or if the signal-to-noise ratio is low. Moreover, a common pitfall in resonator fitting is the handling of asymmetry due to impedance mismatch. Early analysis methods often employed a simple rotation of the resonance circle back to the real axis [21, 139], a technique known as the $\phi$-rotation method ($\phi$RM). A fit to the IQ-plane circle is used to determine a guess of parameters, to be used in direct fitting to the standard (or equivalent) form of Equation 2.11. However, research by Khalil *et al.* demonstrated that this empirical approach is flawed, especially in the presence of impedance imbalances. Asymmetry in the resonance circle is a distortion caused by reactive components in the coupling, mismatches in the transmission line impedances or a fano-like phase addition due to a superposition with a shorted input signal (e.g. a signal that passes through the circulator isolation ports). When an impedance mismatch is present, the resonance circle is both rotated by an angle $\phi$ and increased in diameter by a factor of $1/\cos(\phi)$. Hence, since the $\phi$RM does not account for this, it overestimates the relation $\frac{Q_l}{Q_c}$ by $\frac{1}{\cos(\phi)}$, naturally leading to incorrect results. Alternatively, the inverse $S_{21}$ method [151] does include the environmental variables, with a complex coupling factor, but it is unable to fully capture $Q_c$ without prior calibration of the environment impedance.

This is because in a real experimental set-up, this ideal response is adapted by the

| Parameter | Symbol | Geometrical effects in complex plane |
|---|---|---|
| Loaded Q | $Q_l$ | Frequency spacing of points along the circle |
| Coupling Q | $Q_c$ | Circle diameter through the coupling strength |
| Internal Q | $Q_i$ | Extracted from the relationship between $Q_l$ and $Q_c$ |
| Impedance mismatch | $\phi$ | Tilt/rotation of the circle relative to the real axis |
| Resonance freq. | $f_r$ | Point on the circle opposite the off-resonant point |
| Cable delay | $\tau$ | Twists the resonance circle into a spiral or loop |
| Initial phase | $\alpha$ | Shifts $f_r$ to the imaginary axis |
| Amplitude | $a$ | Circle diameter |

**TABLE 2.3:** PHYSICAL FIT PARAMETERS OF A RESONATOR AND THEIR GEOMETRICAL REPRESENTATION IN THE COMPLEX IQ PLANE.

microwave environment, which includes the effects of cable attenuation, amplifiers, and the finite speed of light through the measurement chain. The generalised model for the measured scattering data is expressed by Eq. 2.11. The equation is divided into two distinct physical contributions: the environment, and the resonator's response. The prefactor $ae^{i\alpha}e^{-2\pi i f\tau}$ accounts for the environment outside the sample holder. Parameter $a$ represents the net amplitude scaling due to gain and loss in the system, $\alpha$ is a constant phase offset, and $\tau$ is the electronic delay caused by the microwave cables. In cryogenic set-ups, where cables may be several meters long and span temperature gradients from 300 K to 10 mK, the electronic delay $\tau$ becomes an important factor that leads to data distortion. Indeed, especially for modes where $Q_i \gg Q_c$, it is difficult to see an amplitude signal; luckily, there is still a full $\sim 2\pi$ roll in the phase signal. However, without subtracting electrical delay, this phase roll remains hard to observe because of the transmission line delay. Subtracting the slope of the electrical delay accurately leads to a very flat phase, with only resonator features remaining. Since the environmental variables are largely independent of power and temperature, a recent adjustment to the DCM has arisen: the parameter-corrected DCM [152]. Here, the underlying physics and fitting concepts are generally the same as the regular DCM, but the environmental parameters are extracted first at high powers, where noise is less than at $\langle n\rangle = 1$. These parameters are then fed in as fixed variables for the low-power regime fitting, leading to a better fit of the resonator characteristics when taking a power spectrum. The effects of all parameters to the circle in the IQ-plane are summarised in Table 2.3, and a step-by-step schematic view of the fitting routine is shown for simulated data in Figure 2.11.

It is furthermore essential that the fit takes the full data of the IQ-plane, and not just, say, the amplitude as still sometimes is the in literature, e.g. for $|S_{21}|$ resonance extraction. With just the $|S_{11}|$-data, the internal and external coupling factors, the amplitude scaling and the impedance mismatch factors are correlated parameters; one thus cannot extract them independently. Indeed, the diameter of the ideal resonator's resonance circle is $\frac{Q_l}{|Q_c|}$, but without calibration of the environmental parameters, there is still an initially arbitrary amplitude scaling originating from the attenuation and amplification in the measurements system, so that a fit to the amplitude would give $Q = a\frac{Q_l}{|Q_c|}$. Using Eq. 2.13 one could extract $Q_l$ theoretically, but that is not sufficient to also get $Q_c$ and $a$.

The off-resonant point, $P$, defined as the limit where $f \to \pm\infty$, is the main parameter

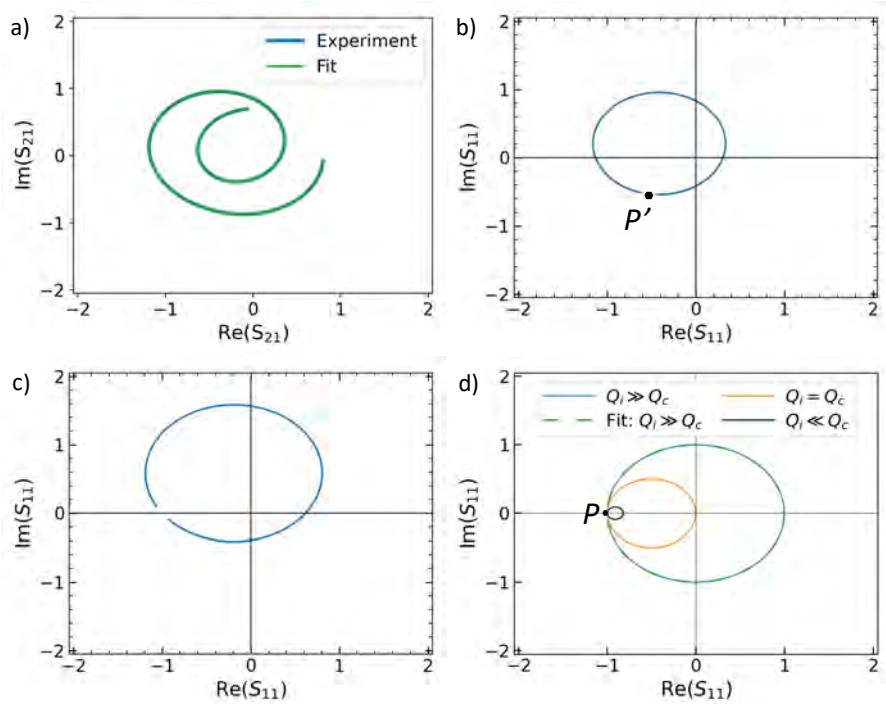


**Figure 2.11:** Simulations and corresponding fits of the resonator in the IQ-plane for an overcoupled resonator. The simulations have parameters as shown in Table 2.4. Blue is simulated data, green is fit. **a**) The pure imperfect resonator case of a resonator with $f_r = 6$ GHz, including finite cable delay $\tau = 75$ ns, amplitude scaling $a = 0.75$, global phase rotation $\alpha = \frac{\pi}{4}$ and impedance mismatch $\phi = \frac{\pi}{5}$. **b**) The electrical delay removed, opening up the extraction of the observed position $P'$ of the off-resonant point $P$. **c**) The resonance circle with only the impedance mismatch term $\phi$ remaining. **d**) A "perfect" resonator, impedance-matched and without environmental effect. The resonance frequency $f_r$ is at coordinates $(1,0)$, and $P$ is at $(-1,0)$, as expected when $Q_i \gg Q_c$ (blue - $Q_i = 5\times10^6$, $Q_c = 5\times10^4$)). Other simulated data is shown, with $Q_i = Q_c$ (orange - $Q_c = 5\times10^6$), and $Q_i \ll Q_c$ (black - $Q_c = 5\times10^7$)).

to find in this analysis. In an ideal, calibrated system, for a pure reflection type resonance with $Q_i = Q_c$, the value of $P$ is located at $(Re, Im) = (-1,0)$ in the complex plane; the resonance is at $(0,0)$. The resonance circle always intersects this point, and its diameter thus extends toward positive real values. If $Q_i \gg Q_c$, the resonator is overcoupled, and the circle is large, creating a deep amplitude dip and moving the resonance frequency point towards larger positive real values, up to maximally $(1,0)$. Conversely, if $Q_i \ll Q_c$, the resonator is undercoupled, resulting in a small circle that remains close to the off-resonant point: $\lim_{Q_i\to0,Q_c\to\infty} Coord.(f_r) = (-1,0)$.

Thus, before the intrinsic resonator parameters can be extracted, the environmental prefactors must be accurately determined and removed. This process is often referred to as "calibrating" the data, though it differs from a traditional thru-reflect-line calibration in that it is performed on the measurement data itself [153–155]; the physical calibration is difficult for pure reflection resonators. Because the phase shift $-2\pi i f\tau$ is frequency-dependent, it causes the resonance circle to rotate as the frequency is swept. This results in the "twisting" of the resonance circle into a loop or a spiral. To remove this effect, one must find the value of $\tau$ that "untwists" the data back into

| Case | $Q_i(10^6)$ | $Q_c(10^4)$ | $f_r$ (GHz) | $\tau$ (ns) | $a$ | $\alpha$ | $\phi$ |
|---|---|---|---|---|---|---|---|
| Imperfect sim. | 5.0 | 1.0 | 6.0 | 75 | 0.75 | $\pi/4$ | $\pi/5$ |
| Imperfect fit | $5.0\pm10^{-5}$ | $1.0\pm10^{-3}$ | $6\pm10^{-6}$ | 75.0 | 0.75 | 0.7854 | 0.6283 |
| Ideal sim. | 5.0 | 1.0 | 6.0 | 0 | 1 | 0 | 0 |
| Ideal fit | $5.0\pm10^{10}$ | $1.0\pm10^{-8}$ | $6.0\pm10^{-12}$ | $10^{-13}$ | 1.0 | $10^{-6}$ | $10^{-9}$ |

**TABLE 2.4:** COMPARISON BETWEEN INPUT SIMULATION PARAMETERS AND EXTRACTED FIT PARAMETERS OF THE GRAPHS OF FIGURE 2.11A AND D FOR SYNTHETIC RESONATOR DATA. THE IMPERFECT CASE INCLUDES FINITE CABLE DELAY, AMPLITUDE SCALING, GLOBAL PHASE ROTATION AND IMPEDANCE MISMATCH, WHEREAS THE IDEAL CASE SETS THESE EXTRA DISTORTIONS TO ZERO. THE FIT IS EXCELLENT.

a closed circular shape; it is done by a nonlinear least square fit, that minimises the deviation from an ideal circular shape with central points $x_c$ and $y_c$ in the complex plane, obtained from an algebraic circle fit to the data (including the phase delay). A general circle parametrisation, which avoids divergences, is given by [156, 157]

$$A(x^2+y^2)+Bx+Cy+D=0. \tag{2.29}$$

The parameters $A,B,C,D$ must satisfy an inequality $B^2+C^2-4AD>0$ in order to define a non-trivial curve. Without loss of generality, we impose an arbitrary constraint $B^2+C^2-4AD=1$. Then, after fitting the data to this, the radius and central coordinates are extracted as $x_c=-\frac{B}{2A}, y_c=-\frac{C}{2A}$ and $r_0=\frac{1}{2|A|}$. Alternatively, empirically a linear fit of the phase in frequency can work well or even better in certain situation, as is shown in Section 2.3.6, if for example $\tau$ is large; then, the data in the complex plane deviates too much from a circle due to rotations and twists. With the extracted $\tau$, we multiply the data by $e^{-2\pi i f\tau}$.
Once the delay is removed, the data forms a circle, but its position and size are still arbitrary due to the factors $a$ and $\alpha$. These parameters represent the total system gain/loss and the constant phase offset, respectively. Because the off-resonant point $P=(-1,0)$ is an invariant of the resonator model, its observed position $P'$ in the delay-corrected data defines the remaining prefactors; its only dependence is on these! To find both $P$ and $P'$, one first translates the resonance circle to the origin using the determined $x_c$ and $y_c$. Then, a fit to Eq. 2.13 gives $f_r, Q_l$ and $\theta_{\text{offset}}$.

Geometric relations then allow for the calculation of the complex position of $P'$ relative to the circle's centre. The magnitude $|P'|$ gives the scaling factor $a$, while the argument $\arg(P')$ gives the phase offset $\alpha$. Normalising the raw data by $ae^{i\alpha}e^{-2\pi i f\tau}$ places the resonance circle in its canonical,standard position, where $P$ is at $(-1,0)$, allowing the subsequent analysis to focus on extracting the remaining intrinsic parameters: $Q_i, Q_c$, and $\phi$.
To summarise, we now have obtained the environmental parameters $a,\alpha$ and $\tau$, the circle parameters $P,P',x_c,y_c$ and related the radius $r_0$, and some of the resonator parameters: $f_r$ and $Q_l$. We directly determine the impedance mismatch $\phi=-\sin^{-1}(\frac{y_c}{r_0})$. By knowing this, we readily extract the coupling quality factor as $Q_c=\frac{Q_l}{2r_0e^{-i\phi}}$; this directly leads to the internal quality factor as $\frac{1}{Q_i}=\frac{1}{Q_l}-\mathrm{Re}(\frac{1}{Q_c})$, as it has to be a real parameter.

### 2.3.5 Non-ideal Lorentzian behaviour

We found that the complex coupling factor $Q_c = |Q_c|e^{-i\phi}$ describes the asymmetry in the Lorentzian line shape of $|S_{11}|$ and is attributed to either an impedance mismatch at the coupling ports [21], an extra series inductance from the wire bond connections [151, 158], phase imbalances in the differential drive lines (for CPS architectures), reflections/standing waves in the resonator's feedline [159] or a general Fano factor [160]. For the data in the IQ-plane, this mismatch exhibits itself as non-circular behaviour near the off-resonance point. In this Section, we perform circuit simulations using the open-source software package QUCS [161] to demonstrated that imperfections in the 180° hybrid component with added impedance mismatches in the wire bonds create this typical "shoulder-like" features in the magnitude spectrum. We start the simulations by first simulating a perfectly matched "ideal" sample to establish a baseline, whose parameters are shown in Figure 2.12a. Subsequently, controlled perturbations were introduced to various parameters to investigate potential sources contributing to the shoulder-like features observed in the Lorentzian profile governing the magnitude spectrum of the resonator. Finally, we attempt to recreate a $\phi$-value corresponding to measurement. The hybrid $S_{11}$ file is custom made. All the resonator parameters $f_r$, $Q_i$, $Q_c$ and $\phi$ have been obtained from fits to simulated data, using the same fitting algorithm as mentioned in Section 2.3.4.

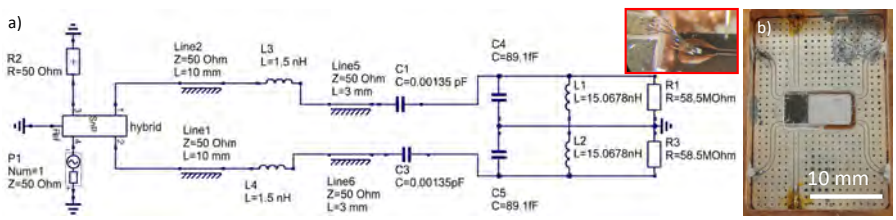


**Figure 2.12:** **a**) QUCS simulation parameters for the "idealised" device. Varying parameters, and their effects, are shown in Tab. 2.5. The hybrid was adjusted by changing the parameters in a separate "hybrid $|S_{11}|$-model. **b**) The general PCB used in measurements, with a sample silver-pasted to it. The PCB exists out of a copper box, with sapphire substrate. An on-chip CPW feedline (not a resonator!) routs the signal from the PCB to the CPS resonator to minimise bondwire-lengths. *Inset*: picture of the wirebonding, showcasing an extensive amount.

The first aspect investigated is the phase mismatch in the transmission lines between hybrid and sample (*H-S leads*). Here, we varied the cable lengths to induce a phase difference (attributable to electrical length) between the signals emerging from the -3dB ports of the 180° hybrid. This also includes any on-chip or on-PCB feedlines. There is only a minimal effect on $\phi$ in first order. Experimentally, we measured the transmission spectrum of the SMA cables using room temperature VNA characterisation, as shown in Figure 2.13, to optimise this parameter in measurements. Secondly, we asses the impact of an impedance mismatch in the wirebonds (*Wirebonds*, length and impedance). Notably, this introduces a very large shoulder behaviour in the Lorentzian lineshape, as shown in Figure 2.14a, which aligns with the results from Deng *et al.* who found the wirebonds a likely cause of $\phi$ [162]. As seen in Figure 2.12b, the feedlines on our PCB do not necessarily match the contacts on our CPS resonator on-chip, and long bondwires would have to be used. To avoid this, we used a large large CPW feedlines (impedance matched to 50 Ω)to route the mw signal from the PCB to the actual CPS resonator. We stress that this was a specific case, due

| Variation | hybrid [°] | H-S leads [mm], [Ω] | Wirebonds [mm], [Ω] | $C_{couple}$ [fF], [fF] | $R_R$ [MΩ] | $f_r$ [GHz] | $Q_i$ [1e5] | $Q_c$ [1e4] | $\phi$ [rad] |
|---|---|---|---|---|---|---|---|---|---|
| Ideal | 180 | 100, 50<br>100, 50 | 4, 50<br>4, 50 | 5<br>5 | 100 | 5.964 | 10.03 | 1.14 | 1.54e-6 |
| Ideal, high $Q_i$ | 180 | 100, 50<br>100, 50 | 4, 50<br>4, 50 | 5<br>5 | 10e3 | 5.964 | 1.003e3 | 1.14 | 3.948e-08 |
| phase mismatch | 180 | 98.3, 50<br>100, 50 | 4, 50<br>4, 50 | 5<br>5 | 100 | 5.964 | -968.1 | 1.13 | 1.952e-4 |
| Wirebonds.a | 180 | 100, 50<br>100, 50 | 4, 90<br>4, 30 | 5<br>5 | 100 | 5.964 | -4.921 | 1.16 | 5.89e-2 |
| Wirebonds.b | 180 | 100, 50<br>100, 50 | 2.3, 50<br>4, 50 | 5<br>5 | 100 | 5.964 | -1.003e3 | 1.13 | 1.71e-4 |
| Hybrid.a | 167.5 | 100, 50<br>100, 50 | 4, 50<br>4, 50 | 5<br>5 | 100 | 5.964 | -154.1 | 1.13 | 2.264e-4 |
| Hybrid.b | 167.9 | 100, 50<br>100, 50 | 4, 50<br>4, 50 | 5<br>5 | 100 | 5.964 | 3040 | 1.13 | 2.118e-4 |
| Hybrid.c | 170 | 100, 50<br>100, 50 | 4, 50<br>4, 50 | 5<br>5 | 100 | 5.964 | 3.103e6 | 1.14 | 1.443e-4 |
| Hybrid.d | 175 | 100, 50<br>100, 50 | 4, 50<br>4, 50 | 5<br>5 | 100 | 5.964 | 1.205 | 1.14 | 3.690e-5 |
| Hybrid.e | 185 | 100, 50<br>100, 50 | 4, 50<br>4, 50 | 5<br>5 | 100 | 5.964 | 1.025 | 1.14 | 3.689e-5 |
| R resonator.a | 170 | 100, 50<br>100, 50 | 4, 50<br>4, 50 | 5<br>5 | 10 | 5.964 | 1.076 | 1.14 | 1.582e-4 |
| R resonator.b | 170 | 100, 50<br>100, 50 | 4, 50<br>4, 50 | 5<br>5 | 146 | 5.964 | 121.9 | 1.13 | 1.438e-4 |
| R resonator.c | 170 | 100, 50<br>100, 50 | 4, 50<br>4, 50 | 5<br>5 | 250 | 5.964 | -36.26 | 1.14 | 1.434e-4 |
| Coupling C.a | 170 | 100, 50<br>100, 50 | 4, 50<br>4, 50 | 1.575<br>1.575 | 100 | 5.983 | 10.73 | 11.3 | 4.671e-5 |
| Coupling C.b | 170 | 100, 50<br>100, 50 | 4, 50<br>4, 50 | 6.046<br>6.046 | 100 | 5.958 | 79.72 | 0.7783 | 1.736e-4 |
| Combination | 170 | 100, 50<br>100, 50 | 7, 10<br>4, 90 | 5<br>5 | 10 | 5.964 | 1.511 | 1.704 | 6.016e-1 |

**TABLE 2.5:** TABULATED SIMULATION DATA OF VARIOUS RESONATORS TO UNCOVER THE CAUSE OF THE NON-IDEAL LORENTZIAN SHAPE OF SOME RESONATOR PROFILES. THE PARAMETERS $f_r$, $Q_i$, $Q_c$ AND $\phi$ ARE DERIVED FROM FITTING OF SIMULATION.

to the available PCB, and not a necessary limitation of the design. We then model the non-ideal behaviour of the hybrid by directly altering the phase relation between its output ports (*Hybrid a-e*). This modification did not lead to large changes in the $\phi$-factor when using realistic values for a functioning component, with a for the rest perfect circuit. However, we found that while the hybrid itself does not lead to phase mismatch, in these simulations it serves as an amplifying factor to existing mismatch from other sources! Thus, further simulations were performed using a 170°hybrid set-up. In the worst case, there is no effect; in the best case, a stronger signal is obtained.

Subsequently, to exclude the influence of the internal quality factor, we vary the resonator's $R_R$ (which directly defines $Q_i$ in QUCS simulations) under these largest imperfect hybrid conditions. This is shown in *R resonator a-c*. Even over many orders of magnitude, we observe no appreciable difference in $\phi$, indicating that non-ideal Lorentzian behaviour primarily stems from the imperfections introduced in the 180° hybrid component. However, we observe the occurrence of a negative $Q_i$ for the higher $R_R$ value, indicating that it may be the ratio between $Q_i$ and $Q_c$ that is of importance, as also shown in [163]. This only occurs when imperfections in the system are present, as shown in the *ideal, high* $Q_i$ resonator behaviour.

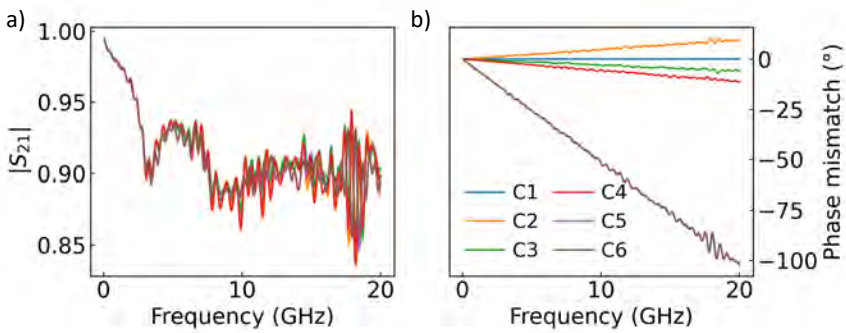


**Figure 2.13:** Experimental study of 6 SMA-connectors to find the perfect phase-matched cables for post-hybrid signal transmission. These cables are nominally the same, as provided by the supplier (50Ω handformable Johnson / Cinch Connectivity Solutions SMA connectors). **a**) $|S_{21}|$ spectrum as measured by the VNA in transmission. No distinguishable features are present. **b**) Referenced (to Cable 1) phase spectrum. Form this data, it was concluded that the pairs C1-C2 and C3-C4 are best matched.

To verify this effect of changing coupling factor $g = \frac{Q_i}{Q_c}$, we altered $Q_c$ of two resonators by changing their coupling capacitances (*Coupling C.a-b*), keeping their coupling rate $g$ consistent with respectively the resonators *R resonator.a* and *R resonator.b*. We conclude that, under similar circumstances, a higher $g$ increases $\phi$, which is attributed to a lower coupling to external impedance mismatches. We could not do the same simulations for *R resonator.c* as it is not possible to define a $g$ for a negative $Q_i$. We stress that this is because negative $Q_i$s are not physical values (without external pumping, it violates the first law of thermodynamics), but have to be seen as a convolution of environment and resonator that includes constructive interference between the incoming and outgoing signals. This is a purely unphysical algorithmic artefact. Even then, there is the excellent agreement between fit and

simulated data as shown in Figure 2.14 for the simulation *Wirebonds.a*. This confirms in part that especially without a well-known background, getting an accurate value of $Q_i$ for pure reflection type resonators is difficult and leads to inaccuracies not present in hanger-mode resonator fitting [21]. The root cause is that with a pure reflection type of resonator, one essentially probes the entire microwave structure in which the resonator is embedded, which can cause constructive interference between the ingoing and outgoing signal. However, since this environment is only minimally power and temperature dependent, while the absolute value of $Q_i$ may be inaccurate in such cases, that the methodology of using *relative shifts* of $Q_i$ (or $f_r$ for that matter) as a function of power or temperature remains valid.

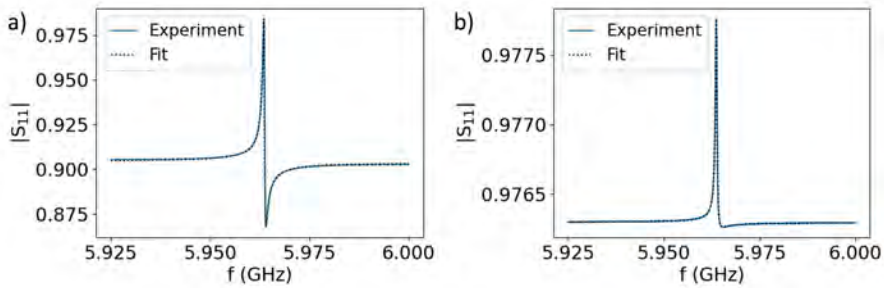


**Figure 2.14: a**) and **b**) The simulation of respectively samples *Wirebonds.a* and *Hybrid.a*, showcasing the excellent fit even with a virtual negative internal quality factor.

Finally, we combine all potential contributing factors to replicate a similar $\phi$ as to the measured resonators. Especially the wirebonding impedance mismatch is of prime importance to achieve a realistic result. In practice, such mismatch occurs by e.g. having wirebonds go loose during sample cooldown, or differing wirebonding lengths. Hence, to avoid non-ideal Lorentzian behaviour in these resonators, we suggest to add multiple wirebonds per contact pad. Furthermore, we conclude that the occurrence of a negative $Q_i$ is not directly related to a high $\phi$-factor, yet does require a non-symmetric environment. It will only occur at a higher coupling factor.

Summarising, to minimise all environmental effects leading to a significant $\phi$-factor in a differentially driven CPS resonator, best practices include:

- Using multiple wire bonds per contact pad to reduce stray inductance
- Ensuring the phase matching of cables between the 180° hybrid and the sample
- Utilising impedance-matched CPW feedlines on the sample PCB to route signals to the CPS resonator leads

### 2.3.6 Step-by-step resonator measurement

We now have all ingredients to do resonator characterisation measurements. In this section, we outline the practical steps required to go from resonator design to experimental measurement, including important nanofabrication considerations and common caveats encountered in the laboratory. These steps are not specific to our CPS resonators.

### Fabrication

The first step towards measuring superconducting resonators is their design and fabrication. The design process has been discussed extensively in Section 2.3.3, typically employing electromagnetic simulation tools such as Sonnet. To keep the fundamental (odd) resonance frequency at a desired value, the total length of each resonator is adjusted, and, as necessary for impedance considerations, also the geometrical parameters (resonator lead width $W$ and lead spacing $G$,). Via similar simulations, one can estimate the external quality factor $Q_C$ by simulations of the resonance frequency bandwidth using a lossless dielectric [21]. In practice, however, the realised resonance frequency may deviate from the designed value due to uncertainties in material parameters, most notably the kinetic inductance. It is therefore advisable to perform a prior dc characterisation of the film and use Eq. 2.10 to refine the design.

Following design, the resonators are fabricated on double-side polished C-plane $Al_2O_3$ (sapphire) wafers with a thickness of $430 \pm 25$ $\mu$m, chosen for their low microwave losses. An alternative substrate is intrinsic Si; however, this is less suitable for hybrid superconductor-semiconductor devices. Empirically, Si exhibits a lower dielectric breakdown voltage under gating, limiting the maximum applicable gate voltage. In addition, dry etching of Si leads to ion implantation effects, which are undesirable. These advantages of sapphire come at the cost of increased fabrication complexity (e.g. charging, and the optical transparency of the sample).

The fabrication process begins with a standard RCA cleaning procedure (5:1:1 mixture of deionised water, ammonia water $NH_4OH$, and hydrogen peroxide $H_2O_2$), performed at 80°C for 10 minutes. This process removes organic or metallic residues through complex modification of the surface layer [164]. The solution is heated to 80°C for a duration of 10 minutes, initiating a reaction that repels particles from the substrate surface. We omit the oxide-removing HF cleaning step that is used in Si substrates, as it is not beneficial for sapphire; it is an oxide of itself, and using HF increase the surface roughness [98]. This RCA cleaning step is critical, as surface contaminations (such as any residual carbon or metallic ions at the interface) contribute significantly to dielectric loss, particularly in coplanar stripline resonators where metal-surface participation is high as will be discussed later. Within approximately 15 minutes after cleaning, $Nb_{81.9}Ti_{18.1}N$ is deposited on both sides of the wafer using a near-UHV sputtering system [76], with an Ar:$N_2$ partial pressure ratio of 60:37. Approximately 100 nm of NbTiN is deposited on the backside with 'cold' sputtering, while the wafer is actively cooled. After a brief *ex-situ* cleaning step using isopropyl alcohol, an additional NbTiN deposition is performed on the sample side. Prior to this, the wafer is pre-annealed at 660°C for 30 minutes, followed by sputtering for 34 s. The pre-deposition annealing further improves the sapphire smoothness [165]. This double-layered design does *not* mean the resonator includes a ground plane; the superconducting backside layer has only a limited effect on the microwave current distribution. Nevertheless, we observe a modest improvement in $Q_i$ for resonators containing it, and therefore retained this layer. The resonator structures are subsequently defined using electron-beam lithography with hydrogen silsesquioxane (HSQ) as a negative resist, pre-baked at 90°C. To mitigate substrate charging during exposure, and to improve EBL surface detection, an Espacer 300Z conductive layer is applied. The design is written using small main-field sizes, which averages out potential misalignments. After development for 60 s in

MF-319, the unprotected front-size NbTiN is removed using anisotropic inductively coupled plasma etching with an Ar/Cl gas mixture (4:50 sccm) [22, 166]. While reactive, the main etching process happens due to Ar ion bombardment especially as we use a relatively high pressure process ($\sim$ 20 mTorr). Dry etching is preferred over wet etching, as it has been shown to reduce resonator losses and offers better industrial reliability and hence scalability [112]. Following patterning, the HSQ mask is removed by immersing the sample in a 2% HF solution for 30 s. This step is essential, as residual HSQ forms disordered $SiO_x$ bonds that host TLS, which are known sources of microwave loss [22]. However, it also induces surface roughness in the sapphire. Later designs thus transitioned to maN-resist instead, that is readily removable by solvents. The wafer is then diced, and individual chips are mounted onto oxygen-free copper sample boxes using silver paint to ensure good thermalisation at low temperatures [167]. Finally, aluminium/silicon bond wires connect the resonators to a printed circuit board (PCB), which interfaces with 50 $\Omega$ microwave lines for measurement.

**Measurement set-up**

The devices are then ready to be measured in a BlueFors LD dilution refrigerator, with base temperature $\sim$10mK, using a set-up as shown in Figure 2.15a. The VNA, a Keysight P5004A, is protected from dc signals by a high-pass filter (Mini-Circuits BLKD-183-S+ dc block) on both input and output sides. The probing signal is attenuated at the different temperature stages to achieve an upper bound of $10^{-3}$ noise photon number at the mixing chamber plate [168]. Besides the cryogenic attenuators, we assume an extra 6dB attenuation from the CuNi coaxial microwave cabling [168, 169]. To further minimise stray infrared radiation causing quasiparticle generation [170], two in-house fabricated copper powder filters [171, 172] are mounted at the mixing chamber plate, both on the input and output side, with cut-off frequency at $\sim$18 GHz. A picture of such filters is shown in Fig. 2.15d, for a length of 30 mm. Our group (under lead of V. Buccheri) developed these based on similar devices as [172, 173]. In essence, they consist of a wire, surrounded by a lossy copper-powder epoxy. By variation of the copper-powder concentration, or by varying the length of the copper housing, different filtering characteristics are achieved. For example, as shown in Fig. 2.15c and brown-inducated inset, we show how the cut-off frequency varies with length for a filter with 83%-mass concentration copper powder in the epoxy. This has a direct effect on the measured resonator spectrum in temperature, shown in Figure 2.15b: before the filter installation, we see a characteristic loss spectrum in temperature for quasiparticle dominated loss. However, installing the filter leads to the a curve as expected from Eq. 2.21; these data-sets were taken on different resonators, but using the same geometry and nominally the same film. The difference is likely due to the high-frequency radiation that gets filtered, which is prone to induce quasiparticles in the disordered superconducting film. Additionally, the filters are magnetic field resilient and do not vary significantly in their filtering capabilities up to 9 T. Finally, the cut-off frequency is tuned by the mass-percentage of the copper powder (lower percentage leads to a higher $-3$ dBm point). Afterwards, a dual circulator-isolator (LNF-CIISC4_12A) routes the signal first from a 6-port microwave switch (Radiall Cryogenic SP6T switch) to the $\Delta$-port of a 180°-hybrid (Krytar 4060200) which splits the signal, allowing to differentially drive the resonator through two short phase-matched SMA cables between hybrid and sample. This phase-matching was checked

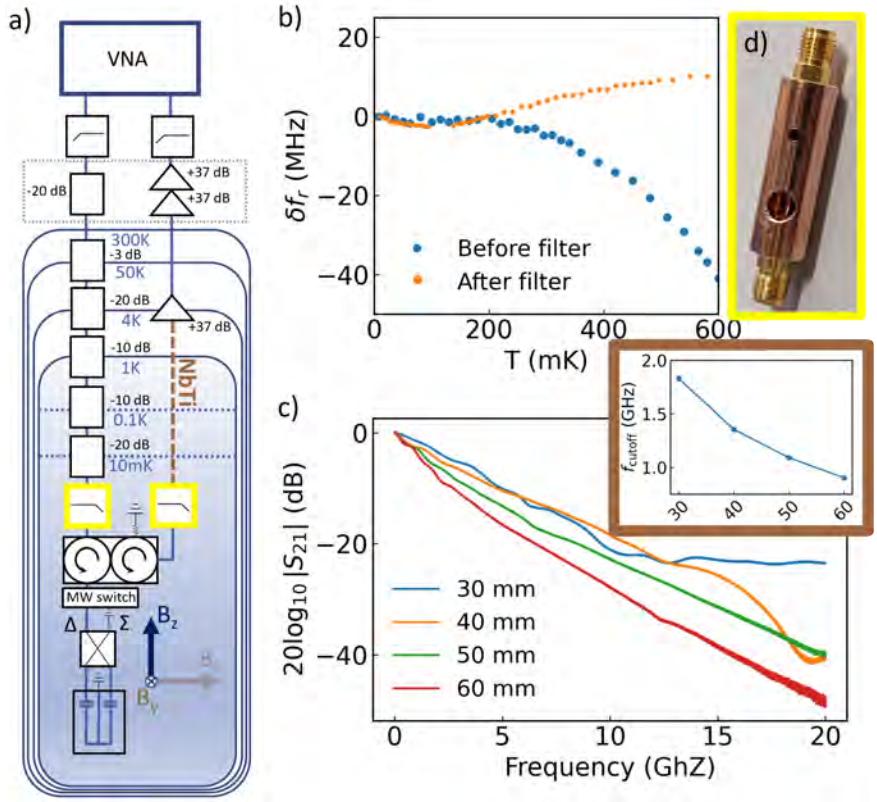


**Figure 2.15:** Experimental set-up and filtering. **a**) The dilution refrigerator and room temperature microwave set-up for the experiments. Elements enclosed in the yellow-dashed lines are only used for low-power measurements (below -30dBm) to avoid resonator bifurcation at high powers. **b**) Effect of including the filter on mw-loss measurements (in temperature). The effect of quasiparticles due to high-energy radiation disappears, and the data can be fitted with Equation 2.21. **c**) Frequency dependence of the copper-powder filters of different lengths. *Inset, brown:* cut-off frequency in GHz (-3 dBm point) in function of length of the filter. **d**) Picture of the filter with length 30 mm. The powder is encased in a copper box. The locations in the fridge are indicated by a yellow box, right before and after the circulator, thermalised to the mixing chamber plate.

at room temperature, and is shown in Figure 2.13. The reflected signal from the resonating sample is then routed through a second copper powder filter to an output line where a cryogenic low noise amplifier (LNF-LNC4_16B mounted at the 4K stage) and two room temperature HEMT low noise amplifiers (LNF-LNR4_14B) amplify the outgoing signal. Physically the resulting measurement is between ports 1 and 2 of the VNA ($S_{21}$-spectrum), yet due to the presence of the circulator in the measurement set-up has to be seen as a reflection measurement of the resonator ($S_{11}$-spectrum). Magnetic field reliant data is measured in a similar dilution refrigerator but containing a vector magnet (AMI Cryogen-free MAxes Vector Magnet).

### Microwave measurement and parameter extraction

After fabrication, cooldown, and proper shielding from stray infrared radiation, the resonator can be characterised. As a first step, we recommend performing a broad frequency sweep to identify resonance features. In strongly overcoupled resonators, a clear dip in the $|S_{21}|$ amplitude may be absent. However, the resonance can often still be identified in the unwrapped phase response, provided that the electrical delay is properly accounted for. In practice, this delay is typically obtained via iterative estimation.

Once the resonance frequency is located, a more narrow sweep is performed using optimised parameters (see Sec. 2.3.7). The resulting dataset is then fitted to extract the resonator parameters. In this work, we primarily employ the diameter correction method (Section 2.3.4), which provides reliable results but becomes sensitive to large phase rolls associated with finite electrical delay. To systematically assess fitting performance, we compare two approaches to extracting the electrical delay $\tau$:
(i) a circular fit to the phase response, following the standard fitting protocol outlined by [134], and
(ii) a linear fit to the phase difference between the highest and lowest probed frequencies.
These correspond to the first and second rows in Table 2.6, respectively. We simulate

| | | No prior delay | | Circular delay fit | |
|---|---|---|---|---|---|
| Fit | Condition | $\tau = 0$ | $\tau > 0$ | $\tau = 0$ | $\tau > 0$ |
| Circular, for column 2 | $Q_i < Q_c$ | ✓ | × | × | ✓ |
| | $Q_i = Q_c$ | ✓ | × | ✓ | ✓ |
| | $Q_i > Q_c$ | ✓ | × | × | × |
| Linear | $Q_i < Q_c$ | × | × | – | – |
| | $Q_i = Q_c$ | × | × | – | – |
| | $Q_i > Q_c$ | ✓ | ✓ | – | – |

**TABLE 2.6:** PERFORMANCE OF DIFFERENT ELECTRICAL DELAY EXTRACTION METHODS FOR RESONATOR FITTING AS A FUNCTION OF COUPLING REGIME ($Q_i/Q_c$) AND ELECTRICAL DELAY $\tau$. CHECKMARKS (✓) INDICATE SUCCESSFUL AND RELIABLE FITS, WHILE CROSSES (×) DENOTE FAILURE OR POOR CONVERGENCE; DASHES (−) ARE NOT APPLICABLE, AS THE LINEAR FITTING METHOD DOES NOT USE A CIRCULAR DELAY FIT. TWO APPROACHES ARE COMPARED: (I) CIRCULAR PHASE FITTING (FOLLOWING REF. [134]) AND (II) LINEAR PHASE FITTING. THE RESULTS SHOW THAT LINEAR PHASE FITTING IS ROBUST IN THE OVERCOUPLED REGIME ($Q_i > Q_c$), WHEREAS CIRCULAR FITTING IS REQUIRED FOR ACCURATE DELAY EXTRACTION WHEN $Q_i \leq Q_c$ AND FINITE ELECTRICAL DELAY IS PRESENT.

resonators with varying coupling regimes while keeping $Q_c = 10^5$ fixed, and evaluate performance for both negligible and finite (100 ns) electrical delay. The results reveal a clear dependence on the ratio $Q_i/Q_c$:

- For $Q_i > Q_c$ (overcoupled regime), a linear phase fit provides the most robust extraction of $\tau$.
- For $Q_i \leq Q_c$, the optimal method depends on the magnitude of $\tau$:
  - If $\tau \approx 0$ (e.g., pre-corrected in the VNA), omitting delay correction yields the best results.

- For finite $\tau$, a circular phase fit is required to accurately capture the phase roll.

Based on these observations, we implement two practical fitting strategies:

1. **Pre-calibrated approach:** The VNA is calibrated such that the electrical delay is minimised ($\tau \approx 0$). While this simplifies fitting, it is generally undesirable, as it alters the raw data and reduces flexibility in post-processing.

2. **Adaptive fitting approach:** A two-step fitting routine is employed. First, a linear phase fit is attempted. If this fails (e.g., due to insufficient phase roll), the algorithm automatically switches to a circular phase fit. In practice, such failures predominantly occur in the regime $Q_i < Q_c$, where the circular method is indeed required.

### 2.3.7 Notes on $Q_i$

During the course of this thesis, it became clear that the internal quality factor $Q_i$ is often reported from so-called "hero" samples. While this is commonplace, recently it has become clear that $Q_i$ is a systems-wide efficiency metric, while it is the losses that are the dissipation metric. The former conflates design, material, set-up and more, while the latter decouples material intrinsic properties, especially when reported in conjunction with filling factors and participation ratios. The main reason for this is that $Q_i$ depends on a multitude of parameters, as is seen in Eq. 2.12 which are not all resonator-material dependent. To highlight this, we recall the definition of $Q_i$ as

$$\frac{1}{Q_i} = \sum_i p_i \tan(\delta_i) \ . \tag{2.30}$$

This relationship highlights the fundamental flaw in using $Q_i$ as a benchmark for material quality. A researcher can "improve" the $Q_i$ of a device by an order of magnitude simply by increasing the width of the conducting lead or the gap between lead and ground of the resonator (changing the ratios of the $p_i$s). By widening the gap, the electric field is diluted over a larger volume of vacuum (which is essentially lossless), thereby reducing the participation ratio of the lossy surface oxides at the metal-substrate and substrate-air interfaces. Consequently, a "hero" device reporting a $Q_i$ of several million may actually be using inferior materials compared to a smaller, more integrated device with a lower $Q_i$ but higher participation. Without reporting the $p_i$s and extracting the underlying $\tan(\delta)$, $Q_i$ measurements are irreproducible across different designs, materials and even cryogenic set-ups. This can lead to a "geometric bias" in the literature, where improvements in reported $Q_i$ values over time may be more reflective of a trend toward larger, more diluted geometries rather than actual breakthroughs in material synthesis or surface treatment advances. Transitioning to losses as the primary metric requires researchers to simulate their geometries and report the intrinsic loss tangent of the material, which is a more universal benchmarking tool. Note that this is not to dismiss $Q_i$ as a useful parameter; it remains physically meaningful and is, for example, directly relevant for estimating qubit coherence times through $T_1 = \frac{Q_i}{2\pi f_{10}}$. However, standardised reporting of loss tangents extracted from resonator measurements would allow qubit designers to estimate device-specific $T_1$ limits prior to fabrication. Such predictive capability is important for the maturation of the development of large-scale quantum processors, where sources of decoherence

must be accurately determined. In this sense, a focus on $Q_i$ tends to favour an trial-and-error approach, whereas a focus on intrinsic loss supports a more predictive design strategy. We stress here that while $Q_i$ as an inherent parameter to report may be of lesser usefulness, the evolution of $Q_i$ with external parameters $(P,T,B)$ *is not*, assuming fitting scripts, material and measurement protocol remain the same, during the same cooldown.

**Fitting inaccuracies**

The extraction of $Q_i$ from vector-network-analyser data is itself subject to systematic uncertainty, as touched upon in Section 2.3.4. In an ideal measurement, the complex resonator response traces a simple circle in the complex plane and yields $Q_i$, $Q_c$, and $f_r$ from a Lorentzian line shape. In practice, however, cable delay, gain and attenuation in the microwave chain, impedance mismatch, standing waves, and other background features distort this ideal response and introduce asymmetry into the measured resonance [21, 134]. A commonly used fitting protocol, the $\phi$-rotation method, systematically overestimates $Q_i$ in the presence of asymmetric line shapes, whereas the more advanced diameter-correction method removes this bias by accounting for the fact that asymmetry changes not only the orientation but also the effective geometry of the resonance circle [150]. Probst *et al.* demonstrated that robust complex-plane fitting substantially improves parameter extraction under noisy conditions, but also emphasised that accurate calibration of delay, amplitude, and phase requires sufficiently high signal-to-noise ratio, while sparse or noisy data still compromises the reliability of the extracted quality factors and other resonator parameters [134]. This becomes especially important as usually the parameter reported is $Q_i$ at $\langle n \rangle \approx 1$, where generally noise is a significant factor, leading to potentially large uncertainties in the fitted $Q_i$. The different fitting algorithms applied to the same data yields $Q_i$ values that differ by 20% to 50%! Here, we will not discuss amplitude-based fitting methods that are still sometimes used and are often off by orders of magnitude due to the lack of taking into account the environment; there, it is assumed that $Q_i = \frac{Q_l}{|S_{21}|}$. However, we admit that as far as we know, it is the only way to characterise transmission-mode '$\lambda/2$'-resonators [174, 175].

Accurate determination of $Q_i$ requires thus not only an appropriate fitting model, but also careful background normalisation and a measurement geometry in which $Q_c$ is reasonably matched to $Q_i$: when $Q_c \ll Q_i$, the measured line shape is dominated by the coupling, whereas for $Q_c \gg Q_i$ the resonance contrast becomes too small for accurate fitting. More recently, it was shown that even apparently symmetric resonance line shapes conceal systematic errors due to Fano interference with background microwave paths, implying that a unique extraction of $Q_i$ may be impossible without additional assumptions or in-situ calibration; importantly, the associated uncertainty increases strongly in the overcoupled regime [163]. These problems are all be mitigated by reporting loss contributions instead. They add linearly, and they can be interpreted more naturally in combination with participation-ratio analysis and interface-specific loss extraction [21]. Ultimately, the most reliable assessment of intrinsic material performance does not come from a single fitted $Q_i$ value, but from the scaling of measured loss across resonators with varied geometry, coupling strength, and measurement conditions.

### Material and fabrication insights

A shift from reporting resonator performance solely in terms of $Q_i$ towards reporting loss-based quantities is essential if one wishes to compare materials and processes in a physically meaningful way. As emphasised in Eq. 2.30, the total loss of a superconducting resonator is not set by the material alone, but by the product of the intrinsic loss of each dielectric or interface and its electromagnetic participation ratio [21]. Consequently, a larger measured $Q_i$ does not by itself imply a lower-loss material: two resonators fabricated from different superconductors or subjected to different surface treatments may have very different participation factors because of differences in conductor width, gap spacing, trench depth, or capacitor layout, even if the underlying interface loss tangents are unchanged [21, 176]. In that sense, reporting only $Q_i$ obscures the actual materials physics, whereas reporting quantities such as $\delta_{\mathrm{LP}}$, $F\tan\delta_{\mathrm{TLS}}$, or extracted interface loss tangents is far more transferable across device geometries. This distinction is especially important for materials optimisation and fabrication development. Surface and interface losses at the metal-substrate, substrate-air, and metal-air boundaries are now widely understood to be among the dominant limits in planar superconducting resonators, and their contribution depends strongly on both processing history and field concentration near edges and corners [21, 176, 177]. Accordingly, fabrication steps such as substrate cleaning, native-oxide removal, passivation, etching, and post-patterning residue removal should be viewed as interface-engineering tools rather than optional steps for optimal resonator performance. Treatments such as RCA cleaning, HF oxide removal, and annealing improves resonator performance, while more aggressive ion cleaning may instead damage the substrate and increase dielectric loss [178]. Likewise, the TiN study of Ohya *et al.* [179] illustrates why raw $Q_i$ alone is misleading as a materials metric: room temperature sputtered TiN films displayed improved resonator performance as film strain was reduced, even though oxygen contamination increased, while the same oxygen uptake also changed resistivity and kinetic inductance uniformity across the wafer.

The transition to loss-based reporting is thus essential for evaluating the success of new materials and surface treatments. Superconducting materials such as Nb, Al, TiN, NbTiN and Ta each have distinct chemical properties that affect loss, indicated in Table 2.2. Al, for example, forms a very thin, self-limiting native oxide ($AlO_x$) [180], while Nb forms a complex mixture of sub-oxides ($NbO, NbO_2, Nb_2O_5$) that can be several nanometres thick [181–183]. If a researcher reports, say, a $Q_i$ of $1\times10^6$ for an Al resonator and $1\times10^5$ for a TiN resonator, one might conclude that Al is the superior material. However, if the Al resonator has a participation ratio five times smaller than the TiN device due to its geometry, the TiN is actually the lower-loss material! Likely causes of this discrepancy are the exact applied power, dilution refrigerator shielding or magnetic field remnant (vortex) effects. Furthermore, surface treatments like hydrofluoric acid etching or oxygen plasma cleaning affect specific interfaces differently. HF etching is known to reduce losses specifically at the substrate-air interface by removing native silicon oxide and passivating the surface with hydrogen. The impact of such a treatment leads to a change in the interface loss tangent ($\Delta\tan\delta_{sa}$), but its effect on the total $Q_i$ will depend entirely on the participation ratio of that interface in the chosen resonator design. If focusing purely on $Q_i$, the field misses the opportunity to build a universal database of interface loss tangents that could be used to predict the performance of any arbitrary resonator (or qubit) design.

### Measurement protocol

After addressing fitting artefacts and the material-dependent considerations, we next consider the data-acquisition procedure itself, which also contributes to variations in the extracted internal quality factor. To investigate this systematically, we measured a fabricated CPS resonator ($W = 1\ \mu$m, $G = 2\ \mu$m) at a fixed VNA output power of $P = -10$ dBm, while varying one experimental parameter at a time and keeping all others constant. The parameters studied were the number of averages, the number of frequency points, and the measurement window (or span) around the resonance. Whereas varying the number of points or the level of averaging produced little change in the extracted $Q_i$ value, provided a sufficient realistic threshold was chosen, the frequency span exhibit a clear dependence (under fixed amount of points). This dependence is shown in Figure 2.16.

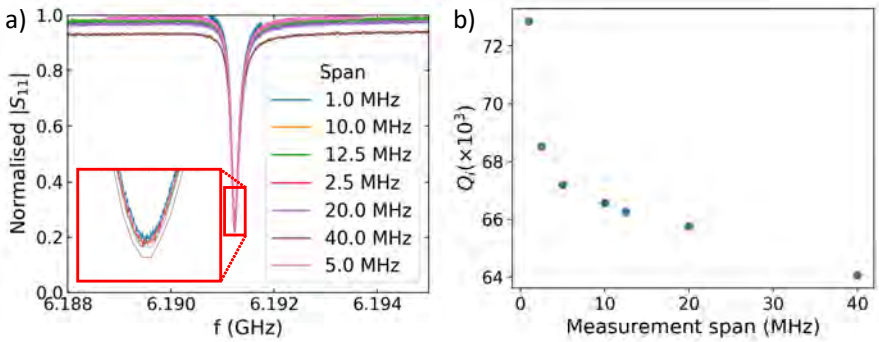


**Figure 2.16:** Extracted internal quality factor $Q_i$ as a function of the frequency span used in the resonator measurement and fitting routine.

As discussed by Baity *et al.*, both the fit uncertainty and a possible systematic bias depends on the ratio between the total measurement span $\Delta F$ and the resonance linewidth $\Delta f_r$, since the off-resonant data points influence the weighting of the background and the baseline model used in the fit [135]. This behaviour is consistent with our own measurements, done before the results of the Baity paper: fitting the same resonance using the Probst circle-fit algorithm over different spans yields slightly different values of $Q_i$ (and $Q_c$), even though the extracted resonance frequency remains unchanged. Physically, a span that is too narrow may insufficiently constrain the background response, while a span that is too wide introduces additional sensitivity to slow baseline drifts, impedance mismatch, or residual asymmetries in the measurement chain, or just not capture the full resonator characteristics given the same amount of points. The error to this grows as $\sqrt{\frac{\Delta F}{f_r}}$ For this reason, $Q_i$ should be corroborated against reasonable variations in the fitting span, with any remaining spread included as a systematic uncertainty. One way to do this is by using a so-called homophasal measurement point distribution which is more uniformly distributed around the resonance circle in the IQ-plane [135]. Note that this does require an approximate preliminary determination of $Q_l$, $f_r$, and $\theta_{\text{offset}}$, for use in Eq. 2.13, and is often difficult to implement in practice. A practical compromise is to use sparse sampling in the tails of the Lorentzian and increased sampling density in the vicinity of $f_r$.

**Cooldown to cooldown variations**

Besides all of the above points, there is one more key variation in $Q_i$: the measurement-to-measurement variation. Repeated measurements of the same resonator across multiple thermal cycles have revealed significant variation in the high-power quality factor $Q_{HP}$. Calusine et al. [176] observed that for a set of TiN resonators, but general for every material, the mean $Q_i$ at high power $Q_{HP}$ shifted from $5.5 \times 10^6$ in the first cooldown to $2.9 \times 10^6$ in the second, a reduction of nearly 50%. However, they also found that this can be mitigated. When the power-independent loss (representing $1/Q_{HP}$) was subtracted to isolate the TLS-limited quality factor $Q_{TLS}$, the results were stable across cooldowns within statistical uncertainty ($3.4 \times 10^6$ versus $3.3 \times 10^6$). This indicates that while the TLS distribution at the interfaces is relatively robust to thermal cycling, the mechanisms governing $Q_{HP}$ are not. Probable causes are trapped magnetic flux vortices (in the superconducting ground planes) or non-equilibrium quasiparticles from stray radiation which are highly sensitive to the specific conditions of the cooldown procedure. Empirically, we experienced this variation by measuring in our two different dilution refrigerators; we observed an order of magnitude difference due to enhanced filtering, wirebonding changes and sample ageing (oxidation).

## 2.4 Coplanar stripline resonators

### 2.4.1 Why a new geometry

So far, this thesis chapter was rather general: we have focussed on the main points involving the measurement of superconducting resonators, how to extract relevant parameters and what are the losses involved with microwave physics. In high-end research, and industry, there is what can be called a workhorse of cQED measurements: the coplanar waveguide resonator, CPW [6, 19, 24]. These types of resonators have a central conducting line of width $W$, separated from ground planes by a gap $G$ and are well-suited for low-noise operations. Moreover, their ease of fabrication and high internal quality factors only builds on these strengths [21, 184]. Usually, they are fabricated from one of the superconducting materials in Table 2.2. The geometrical parameters $W$ and $G$, including the length of the resonator, and the kinetic inductance of the film determine the resonance frequency and impedance of the resonator unambiguously. However, CPWs are not without their drawbacks: their susceptibility to an external magnetic field limits their general functionality as the large ground areas readily trap magnetic vortices under applied fields [26]. In an external magnetic field, such vortices entering the ground plane experience Lorentz forces due to the microwave (return) currents that drive them across the film and dissipate energy, reducing the resonator's internal quality factor [185], and leading to resonance frequency jittering [25]. In addition, the CPW design is not well suited to be coupled to superconductor-semiconductor heterostructures. Such applications often require electrostatic gating, which necessitates the interruption of the ground plane particularly when gating multiple devices per resonator. This alteration changes the characteristics of a CPW as it disturbs the return current flowing through the ground plane [132, 186]. It leads to electromagnetic interference problems, such as the appearance of parasitic slotlines [187] or crosstalk between devices, a major issue for e.g. qubits [188]. To mitigate this requires significant alterations to the microwave environment or design [189].

In light of these challenges, we fabricated and measured quarter wavelength differentially driven coplanar stripline resonators (CPS) made of NbTiN. A CPS transmission line geometry uses two identical parallel conductors, under a differential drive where each conductor has an ac-voltage $\pm\frac{V_{ac}}{\sqrt{2}}$ and omits the coplanar ground plane entirely. To allow for accurate gate-levelling, we made the choice of adding one ground line, symmetrically centred to the middle between the conducting line; this gives a dc-ground to any voltage gating we apply to coupled devices, and ensures no dc-voltage charging of the resonator occurs. The combined set-up and geometry has the downside that both odd- and even-modes of the resonator could appear; however, the differential drive, phase-matching of the different microwave conductors and clever resonator design with the grounding stripline (which does not affect the odd-mode, but does affect the even-mode) make this readily avoidable, and only the odd-mode is probed. We note that similar designs to our developed CPS have already been used to measure millisecond coherence in on-chip superconducting quantum memories [190].

In the context of cQED, CPS resonators thus bring several key advantages over CPWs particularly for electrostatic gating integration, high-impedance circuits, and operation in magnetic fields:

1. **Electrostatic gating:** In a CPS geometry, no large ground plane obstructs the sample region. In cQED, the coupling strength between resonator and the dipolar moment of hybrid superconductor-semiconductor structures (such as electrons in single or double quantum dots [191–193], electronic spins [194,195] or quasiparticles in semiconductors [32]), and the physical device characteristics (such as band spectrum for semiconductors) are tunable via electrostatic gating. Due to the design, gate electrodes can be brought close to the two stripline conductors without creating microwave discontinuities; only gate-leakage (which is omnipresent) has to be taken into account. In practice, this means one can integrate multiple gate lines and dc contacts alongside the CPS itself while leaving the resonator mode structure intact, opening up multiple devices coupled to a single resonator. The differential nature of CPS also provides (some) common-mode rejection of voltage noise as noted above, aiding device stability.

2. **High-impedance integration:** The coupling between superconducting resonator and semiconductor-superconductor heterostructure is further mediated by the zero point voltage fluctuations $V_{ZPF} \sim \omega_R\sqrt{Z_R}$ in the resonator [196], where $\omega_R$ is the angular fundamental resonance frequency and $Z_R = \sqrt{\frac{L_R}{C_R}}$ is the characteristic impedance of the resonator as defined by the total inductance, $L_R$, and capacitance, $C_R$. Hence, to achieve the strong coupling regime it is typically necessary to fabricate the device from a superconducting material with high kinetic inductance, and to minimise the resonator capacitance. The latter effect is limited up to the vacuum impedance. The CPS strips, which has a high design versatility, can be made extremely narrow and from a disordered material to maximise kinetic inductance $L_k$, while even $C_c$ can be minimised by spacing between the conducting or ground line. High $L_k$ leads to high characteristic impedance and a large zero-point voltage, which enhances coupling to charge-dipole systems and suppresses charge-noise sensitivity [22], while maintaining high internal quality factors. For example, high-$L_k$ TiN films grown by atomic layer deposition [197] have been shown to support resonator impedances on the order of tens of k$\Omega$, all the while maintaining $Q_i \sim 10^6$ (TLS-limited) at $\langle n\rangle = 1$.

Similarly, grAl films exhibit nearly unity kinetic inductance fraction (where $L_k \approx 2\frac{\text{nH}}{\square} \gg L_{\text{geometrical}}$) and still achieve $Q_i \sim 10^5$ [115]. In each case, the high $L_k$ of disordered superconductors in a CPS circuit yields high impedance and strong dipole coupling, enabling strong sensitivity and novel qubit designs.

3. **Magnetic field resilience:** With no extended ground plane, the available area for Abrikosov vortex trapping is reduced by orders of magnitude. Moreover, by patterning the strips with width $w$ smaller than or comparable to the Pearl or effective penetration depth ($\Lambda_P = \lambda^2/d$ for film thickness $d$), one energetically prohibit vortex entry up to high critical fields. Experimentally, this improves performance in large fields. Narrow NbN stripline resonators (width $\lesssim \Lambda_P$) exhibit almost unchanged resonance frequency and quality factor up to the vortex threshold, far outperforming wider CPWs [175]. CPS resonators made from thin films (which exploits the enhanced in-plane critical field $B_{c\parallel}$, Eq. 2.7) similarly show only mild degradation in quality factor in Tesla-scale fields. In short, CPS designs essentially "turn off" vortex losses by using minimal superconducting cross-section and thus remain highly coherent under strong magnetic bias.

### Magnetic field effects on CPW

Together with collaborators, we did studies on the effect of the magnetic field has on the ground-planes of CPW, how vortices form and how to mitigate their nucleation [25,26]. To develop those mitigation strategies, we first go over the physical mechanisms of vortex formation and how they compromise the performance of CPW resonators.

| Parameter | Impact | Physical Origin |
|---|---|---|
| $Q_i$ | Sharp decrease | Joule heating from vortex core motion |
| $f_r$ - value | Stochastic noise / discrete jumps | $L_k$ change from avalanches |
| $f_r(P)$ | Larger but less jumps at low $P$ | Vortex charging |
| $f_r(\pm H_a)$ | Butterfly-like loops | Trapping of (anti-)flux during $H_a$-cycling |

**TABLE 2.7:** IMPACT OF VORTEX PENETRATION ON SUPERCONDUCTING RESONATOR PERFORMANCE.

In a microwave resonator, the resonator's behaviour is not determined only by the number of vortices, but also by their location relative to the radio-frequency current and magnetic-field distribution: vortices located in regions of large rf current density are particularly harmful, since the oscillatory Lorentz force drives vortex motion (so-called 'vortex shaking') which converts stored electromagnetic energy into heat [25, 26] as the vortex core is normal. In CPW geometries this issue is amplified by the large superconducting ground planes, which not only provide a large area for vortex entry and trapping, but also enhances demagnetisation and flux-focusing effects under a perpendicular field. As a result, the local field at the outer rim of the ground plane and at the CPW gaps exceed the nominally applied field $H_a$ by a factor $\simeq \mu_0 H_a \sqrt{\frac{W}{t}}$ where $W$ is the groundplane width and $t$ its thickness, so that flux penetration may occur at small external fields [198, 199].

The onset of vortex penetration is governed by the competition between energetically favourable vortex nucleation in the Shubnikov phase (with the onset of screening currents), and an energy barrier against vortex entry due to the material surface. For

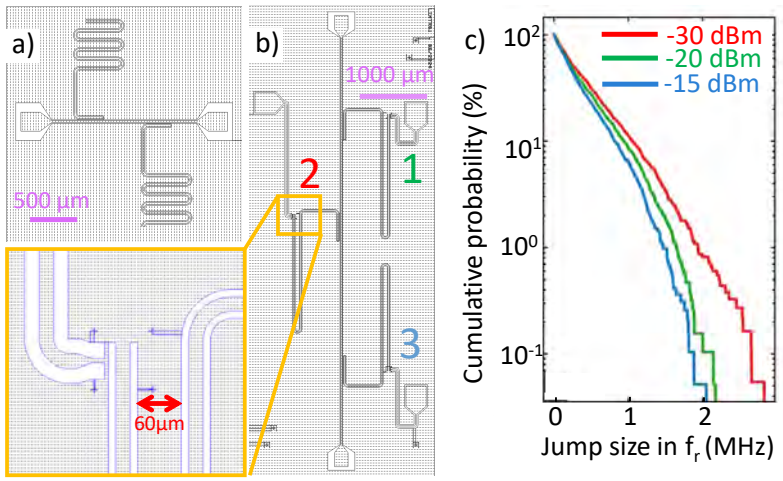


**Figure 2.17:** Design of the resonators discussed in this section, and the power-dependent resonance fluctuations. Resonators are all made of thin-film NbTiN with $L_k \approx 1\ \frac{\text{pH}}{\square}$). **a**) Design of the main sample as described in Ref. [25]; chiefly related to the results of Figure 2.18. **b**) Design of the main sample as discussed in Ref. [26]; chiefly related to the results of Figure 2.19. **c**) Cumulative probability of resonance frequency jump sizes for the three rf-powers applied at $T = 3.2$ K. Image adapted from [26]. Note that the colour schemes here are not joint between the subfigures.

an ideal, bulk, defect-free Type-II superconductor, this barrier is first discussed by the Bean-Livingston theory [200]. It resulted in the conclusion that the Meissner state remains metastable even above $B_{c1}$, until a superheating field $H_s$ [201]. However, in thin films and strips, the situation changes. Then, the magnetic response is strongly non-local, because the screening currents extend over the full strip width and the vortex interaction is governed by the Pearl length rather than by the bulk penetration depth alone [201, 202]. For example, in finite NbTiN strips, the field for first-vortex entry depends sensitively on strip width and edge morphology, and pinning defects substantially lower the experimentally observed threshold field below the ideal Bean-Livingston $H_s$ [203].

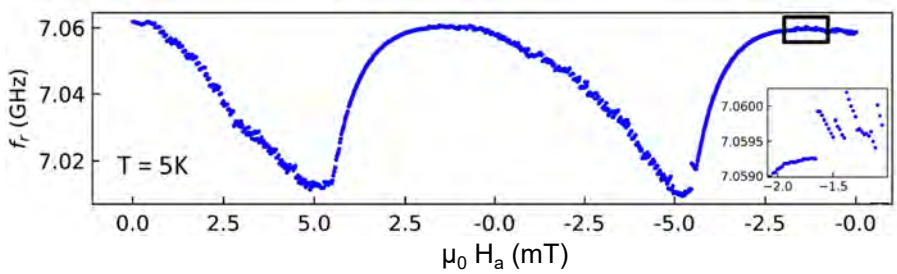


**Figure 2.18:** Fluctuation of the resonance frequency due to **a**) an applied magnetic field, showcasing the hysteresis at $T = 5$ K for a NbTiN resonator. *Inset* a zoom-in of the framed region. Image adapted with permission from L. Nulens [25].

In real devices, such as shown in Figure 2.17a and b for the used devices by Nulens [25] and Baumgarten [26], edge and border defects are therefore essential to take

into account if the goal is to mitigate vortex effects on superconducting resonators. The shown resonators have nominally the same material and geometrical parameters. Lithographic roughnesses, notches, material defects, contamination sites, or any local suppression of the order parameter perturb the screening-currents and cause current crowding. In thin superconducting films this perturbation is long-ranged, so a local defect modifies the current distribution over distances far larger than the defect itself [26]. Furthermore, the defects cause local energy minima, creating preferred nucleation points for vortices to grow. In CPW resonators, where strong screening currents already crowd near conductor and ground-plane edges, these border imperfections are especially detrimental. The situation becomes more pronounced at cryogenic temperature, typically below about $\frac{T_c}{2}$, where thermo-magnetic instabilities trigger flux avalanches over a timescale of $\sim 100$ ns or $v_{\text{vortex,max}} \sim 100$ km/s [204]. These are a runaway effect: the motion of one vortex (i.e. a small amount of flux) produces local heating, which reduces the local critical current and facilitates flux penetration and motion, leading to further vortex nucleations. Magneto-optical imaging combined with microwave measurements have shown directly that such avalanches manifest as stochastic downwards jumps in the resonance frequency (Figure 2.18) due to a local lowering in kinetic inductance, which in itself is due to a local lowering of the magnetic field after or during an avalanche event. Additionally, upwards jumps in $f_r$ are understood by an increase of kinetic inductance due to the extended normal vortex core. These avalanches originate in the ground plane, the feedline environment, or the spaces between neighbouring resonator-meanders, i.e. not necessarily within the resonator conductor itself. Furthermore, in extended CPW geometries with multiple resonators coupled to a central feedline ("notch-type resonator"), vortex movement at one device can be sensed at another, spatially ($\sim$ mm distance) remote device, thus on a range much larger than the coherence length, even with the central conductor separating them. It is because the magnetic field at a given position is a function of the distribution of critical current over the whole film [202]. This is best shown in Figure 2.19, where individual vortex nucleation and avalanching are associated with individual frequency jumps [26].

This non-locality is particularly important for measurements: a resonator suffers a semi-stochastic frequency shift or additional losses due to a flux event that occurs some distance away from the currently probed resonance, albeit that early measurements have pointed towards the possibility of a temporary *increase* in $Q_i$ due to magnetic strain relaxation. Paradoxically, at higher rf powers, the stochastic jump size of $f_r$ decreases compared to low powers, although less frequent jumps are observed for the latter, as shown in Figure 2.17c. This suggests that rf induced effects such as vortex shaking or localised heating may inhibit the formation of large-scale avalanches by triggering smaller avalanches more easily. On the other hand, at low rf powers, larger jumps are more likely, which are characteristics of abrupt, large scale magnetic flux avalanches, as more magnetic field builds up before an event is triggered.

These considerations suggest several mitigation strategies. First, if the goal is parallel field measurements, one should reduce the perpendicular field component as much as possible by sample alignment (think: silver paste uniformity), since even a small out-of-plane component can dominate vortex nucleation in otherwise field-compatible devices [199]. Second, the local field enhancement at the CPW perimeter should be minimised by reducing or segmenting the ground plane, thereby suppressing flux

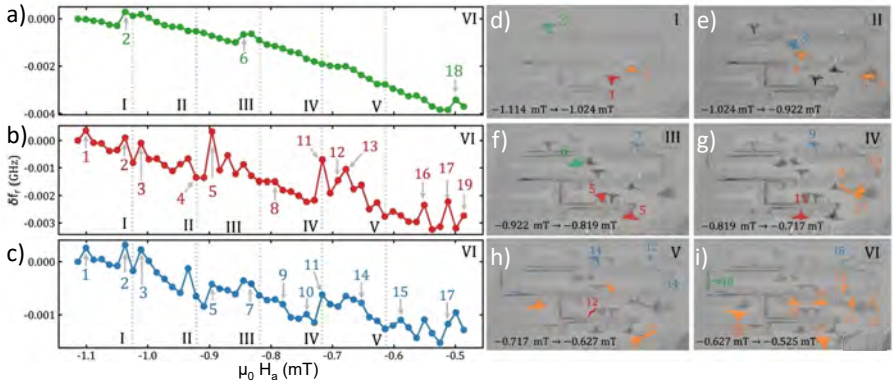


**Figure 2.19:** Long-distance correlations of vortex physics. **a) - c)** Shift in resonance frequency $\delta f_r$ as a function of applied magnetic field $H_a$ of three resonators, coupled with a central feedline: a 'notch-type' geometry. **d) - i)** Magneto-optical images related to the intervals of magnetic field I-VI. Each new avalanche is coloured with respect to the nucleation position. Resonators 1,2 and 3, indicated in Figure 2.17b, are respectively green, red and blue. Avalanches forming at the feedline and the border edges are coloured in orange. Image adapted from [26].

focusing and delaying magnetic perforation. Third, thin and narrow superconducting traces are beneficial because they raise the vortex-entry threshold and reduce the available area for trapping flux; this is one of the main reasons why narrow high-kinetic-inductance resonators outperform conventional wide CPWs in field [203, 205]. Fourth, engineered pinning can be advantageous when used carefully. Hole arrays and flux-trap patterns in the ground plane inhibit vortex motion and improve cooldown-to-cooldown reproducibility, provided they are placed away from the regions of strongest microwave current crowding [185, 199, 206, 207]. However, one must be cautious: pinning landscapes that reduce vortex motion at intermediate temperatures also promote thermo-magnetic avalanches at lower temperatures, so artificial pinning is not universally beneficial [201]. Finally, improving border quality, through e.g. anisotropic etching, smoother edges, and the avoidance of sharp defects, directly increases the robustness of the Meissner state by suppressing local current concentration and raising the effective penetration field. A trade-off has to be made here as a larger ground plane circumference also enhances the local field at the sample borders, enhancing vortex formation in turn.

Taken together, vortex nucleation in CPW resonators is controlled by several factors acting on different length scales: the demagnetisation by the ground-plane geometry, the thin-film edge barrier determined by $d$, $\lambda_{(\mathrm{Pearl})}$, and $\xi$, and the local current crowding arising from (unavoidable) edge and border defects. The magnetic-field resilience of a resonator is therefore not set just by the intrinsic critical field of the superconductor, but by an interplay between device geometry, material properties, and nanofabrication quality. This is what makes the alternative layout of CPS attractive: by removing most of the vortex-vulnerable ground-plane and inter-conductor line areas, it strongly reduces the susceptibility to vortex entry and thereby provide a particularly promising route towards magnetic-field-compatible microwave circuits.

### Electrostatic gating effects on CPW

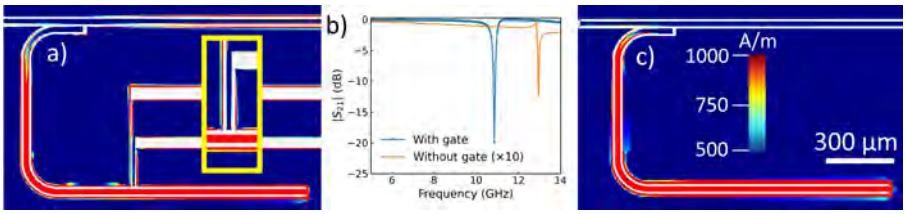


**Figure 2.20:** Effect of electrostatic gating on a CPW resonator obtained from Sonnet simulations. The simulations illustrate how ground-plane modification required for gating perturbs the CPW boundary conditions, alters current paths, and strongly modifies the microwave response. The scale bars are identical for panels (a) and (c). **a**) Surface current density distribution of the gated CPW resonator at its fundamental mode ($\sim$ 11 GHz). The yellow box highlights the gated region where the ground plane is interrupted and re-routed. **b**) Simulated transmission $|S_{21}|$ for the gated (blue) and un-gated (orange) geometries, showing a pronounced resonance shift. The latter signal is enhanced 10 times for visibility. **c**) Surface current density distribution of the un-gated CPW resonator at its fundamental mode ($\sim$ 13 GHz).

To illustrate the effect of electrostatic gating in CPW resonators, we performed simplified Sonnet simulations, shown in Figure 2.20. We note that the gate layouts considered in panel (a) is intentionally simple and is not intended as an optimised design; in practice, more careful gate placement and mode-mitigation strategies substantially reduce their impact. Nevertheless, these simulations provide a view of the main physical consequences of incorporating gate structures into a CPW geometry.
The point is that electrostatic gating in a CPW is generally not just an easy modification of the layout, since it often requires interrupting or re-routing the ground plane that carries the microwave return current, especially in the presence of multiple devices that are coupled to the central conductor. This perturbs the CPW boundary conditions and modifies the current distribution, so that the measured response no longer corresponds to that of an ideal single-mode CPW resonator. In particular, disturbing the ground-plane currents enhances radiation loss, change $g$ and promote the appearance of parasitic slotline-like modes or coupled-slotline modes, especially in the presence of structural asymmetries and discontinuities [35, 187, 189]. Moreover, if the ground planes are not effectively grounded, the addition of a gate voltage can charge the ground planes (and hence change the resonator's capacitance), leading to gate-dependent resonance effects. As shown schematically in Figure 2.20b and the current distribution at respective fundamental resonance in Fig. 2.20a and c, the resulting spectrum may exhibit a shift in the resonance frequency $f_r$, changed $g$, strong asymmetry, and the emergence or enhancement of spurious spectral features. Beyond these spectral distortions, the altered current paths also influence the non-local magnetic-field response discussed in Section 2.4.1. Finally, the current is essential in galvanically coupling the resonators to semiconductor structures; an adjusted current distribution changes thus the coupling. This sensitivity of CPW resonators to ground-plane modification is one of the principal motivations for exploring alternative geometries, such as CPS resonators, in experiments that require local electrostatic control [35, 189].

Summarising these last two sections, the magnetic-field-resilient CPS geometry is a natural successor for CPWs for hybrid cQED experiments that require strong magnetic bias, electrostatic gating, or both. By eliminating the extended ground planes of a

CPW, CPS designs suppress parasitic slotline behaviour and reduce the available area for vortex trapping, while the differential-drive layout allows for gate electrodes in close proximity to the active device region.

### 2.4.2 Loss-measurements

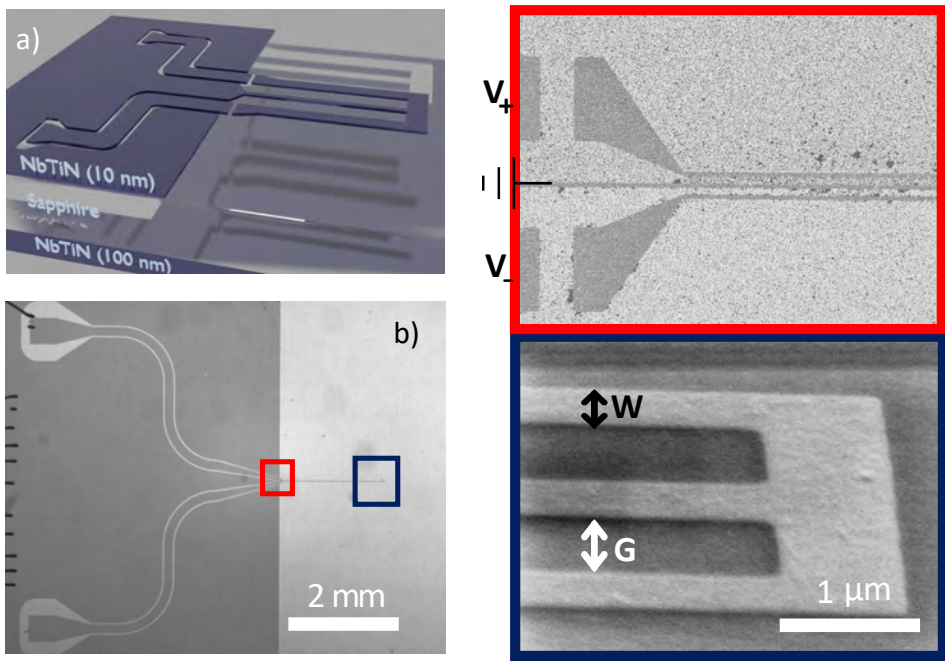


**Figure 2.21: a)** Schematic view of the sample stack of ultra-thin (∼ 10 nm )NbTiN/sapphire. **b)** Optical image of one resonator. Right panels are SEM images of the capacitative gap coupler (red) and a tilted image of the resonator's end (dark blue), the latter visualising the definition of lead width $W$ and gap $G$.

Now, we turn to the main point of this thesis chapter: the loss-measurements in CPS resonators. We measured multiple devices with varying geometrical parameters in these novel resonators and analyse changes in their internal quality factor and two-level system losses. Furthermore, we establish the resilience of the resonators to an applied magnetic field by tracking the resonance frequency shift, without further optimisation of the resonator geometry or adding vortex-pinning structures. Due to their flexible design and high magnetic field resilience, coplanar stripline resonators are particularly well-suited to study superconductor-semiconductor heterophysics where voltage gating or a magnetic field are necessary.

Both dependence on the width of the resonator conductor lines $W$ and the evolution of loss under an increasing conductor-spacing $G$ are investigated; these geometrical parameters determine partially the losses in the resonator [144]. A mock-up, and optical/SEM images of a device is shown in Figure 2.21. We included a pre-resonator CPW feedline structure to minimise the effect of long bondwires; we expanded on this idea in Section 2.3.5. These resonators are differentially driven using the set-up

of Figure 2.15; using clever design (chiefly: the ground line), only the odd-mode is probed (n$\lambda/4$-mode) in reflectance, and not the even-mode (n$\lambda/2$), where $n \in \mathbb{N}$. By examination of the power dependence of $Q_i$ of each resonator together with a temperature dependence of the resonance frequency, insight is provided into the spectral distribution of TLS losses. This large variation in parameter space enables us to characterise resonators with impedances ranging from 81 to 681Ω, using a film with a relatively low kinetic inductance compared to similar measurements from high-impedance resonators in literature [140, 149, 208].

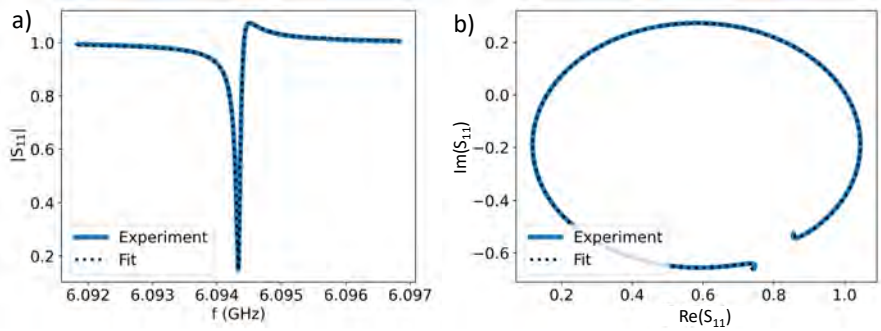


**Figure 2.22:** Representative fits and plots of the losses of coplanar stripline resonators with conductor width $W = 1$ $\mu$m and spacing $G = 10$ $\mu$m.
**a)** Normalised $|S_{11}|$ versus frequency. Experimental data (blue) is fitted to equation 2.28 using the methods detailed in Section 2.3.4 (black dashed line). The presence of an impedance mismatch between sample and feedline is shown in the deviation from an ideal Lorentzian shape in the magnitude plot. **b)** The resonator of a), plotted in the IQ-plane, showing the effect of the impedance mismatch near the off-resonance point.

We use this set-up to investigate the effect on the resonator losses in both power and temperature. Figure 2.22a and b show representative data in a small frequency window around the resonance frequency $f_r$ of the resonator with $W = 1$ $\mu$m and $G = 10$ $\mu$m. Both a representative normalised $|S_{11}|$ plot and the normalised data represented in the IQ-plane are shown. Reflection data is fitted around the fundamental odd resonance using the diameter-correction method [134, 150], thoroughly detailed in Section 2.3.4, taking into account the fact that the resonators are purely reflectively measured (and thus not hanger-type). In that case, we describe $S_{11}$ with Eq. 2.11. We remind the reader of the important parameters in this relation. There are the resonance frequency $f_r$ and the probe frequency $f$. Then there is the prefactor $ae^{i\alpha}e^{-2\pi i f_r \tau}$ due to the resonator's environment: $a$ is the attenuation factor of the signal, $e^{i\alpha}$ acts as a phase prefactor and $e^{-2\pi i f_r \tau}$ is due to the electrical delay in the refrigerator's microwave lines. Finally, $Q_l$ is the total quality factor, combining both $Q_i$, the internal and the complex external quality factor $\widetilde{Q_c} = |Q_c|\exp(-i\phi)$ as $Q_l^{-1} = Q_i^{-1} + Q_c^{-1}$. This complex $Q_c$ describes originates generally from a resonator-feedline impedance mismatch, the mechanism and qualities described more in detail in Section 2.3.5. For the dataset shown in Figure 2.15a and b, the mismatch is $\phi = -0.43$. The exact fitting scripts are published online [209].

To understand the behaviour of TLS losses on the resonator, the evolution of $Q_i$ on input power is studied at base refrigerator temperature $\sim 10$ mK. As input power varies depending on the exact attenuation [127, 210], the unitless quantity of average photon

number $\langle n \rangle$ is used instead, defined and derived in Eq. 2.20. Both the characteristic impedance of the input feedline, $Z_0$, as that of the resonator $Z_R$ play a role, as well as the input power $P_{\text{in}}$ at the resonator's feedline. At low temperature, we fit [126, 127] the power-dependent $Q_i$ to Equation 2.15. The parameters there are $F$, a material dependent filling factor of the electric field [127], $\tan(\delta^0_{\text{tls}})$, the intrinsic TLS loss tangent of the same material, and $\delta_{\text{other}}$, dominated by the next-largest loss channel of the resonator. Furthermore, the amount of photons needed to saturate the TLS is given by $n_c$, while $\beta$ is determined by the interacting strength between individual TLS. We neglect the effect of quasiparticles with increasing $\mu$w-power [131, 132] due to the comparatively low kinetic inductance fraction in these resonators [115] and the presence of low-pass copper powder filters filtering away high energy radiation. A representative fit of the power spectrum is shown in Figure 2.7a. In this plot, the difference between high and low power saturation values is attributed to the TLS losses. Since this power-dependence approach only probes a narrow window of TLS around the resonance, they are called the *narrow-band TLS losses*. [124, 125]. At higher power, the intrinsic kinetic inductance of the resonator causes a bifurcation, a Duffing nonlinearity [211], complicating the fitting procedure while not adding much to the physics that we probe. We do not include these points in any of our fits, as a full description is outside the scope of this thesis. On the other hand, the *wide band TLS losses* are uncovered by the temperature dependence of the real part of the dielectric constant, usually measured via the relative resonance frequency shift up until $\sim 1$ K$\approx \frac{T_c}{10}$ [130, 138]. It is given by Eq. 2.21. Here is $\Delta f = f_r(\text{T}) - f_0$ the temperature-dependent resonance frequency referenced at low temperature (in our data at the lowest measurable temperature, $\sim 10$ mK) while $\Psi$ is the complex digamma function. The factor $k = F\delta^{0,i}_{\text{tls}}$ contains the intrinsic temperature dependent TLS-loss component, $\delta^{0,i}_{\text{tls}}$, which is sensitive to thermally varying TLS for a wide spectrum [22]. As these off-resonant TLS are not saturated, the frequency shift is nearly power independent and it is possible to gather data at higher powers which speeds up measurements. We used $\langle n \rangle = 1\text{e}5$, which for each resonator is in the high-power saturated regime [125]. At higher temperatures, the onset of quasiparticles dominates the resonator's frequency shift and losses [72, 140]; this deviation from the $\frac{T_c}{10}$-behaviour as predicted by Gao *et al.* is uniquely be attributed to the higher kinetic inductance, absent in their derivation. For this reason we constrained our fits to data up to 450 mK, naturally well below the superconducting energy gap of NbTiN. A representative fit of the temperature dependent frequency shift is shown in Figure 2.7b. The presence of a universal dip in the relative frequency shift at $T \approx \frac{\hbar\omega_R}{2k_B}$ supports the validity of equation 2.21 for these resonators, and confirms that quasiparticle loss is, while present, not a dominant factor in the total loss of the resonator [115, 139], partially due to exact the presence of the filtering stages.

Using the established fitting and simulation procedure from earlier in the thesis, we quantify the losses depending on resonator conductor lead geometry using the aforementioned methods (power and temperature dependence). As shown in Figure 2.23, we observe decreasing losses with both $W$-dependence of the lead as with $G$, which is on the same order of magnitude as results of similar geometric dependences of CPW resonators [21, 138, 145, 212]. We show the data of all measured resonators (the combined measurement, and simulated $Z_R$) numerically in Table 2.8. We report the narrow-band (power-dependent) loss tangent $\tan(\delta_P)$, the wide-band (temperature dependent) losses $\tan(\delta_T)$, and the high-power loss tangent ($\delta_{\text{other}}$).

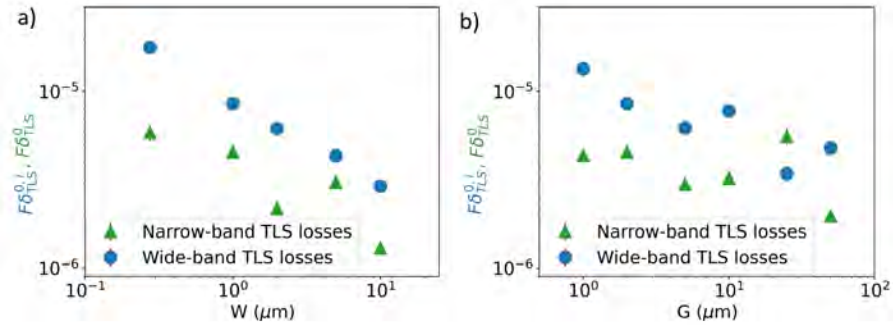


**Figure 2.23:** The evolution of the geometrically dependent loss tangent of the narrow-band losses $F\delta^0_{\text{tls}}$ (green triangles) and the wide-bands losses $F\delta^{0,i}_{\text{tls}}$ (blue circles) **a)** decreases with increased width $W$ of the resonator leads (for constant gap spacing $G = 2\ \mu$m) and **b)** decreases with an increasing $G$ of the leads (for constant $W = 1\mu$m).

| W [$\mu$m] | G [$\mu$m] | $L_K$ [$\frac{\text{pH}}{\square}$] | $f_R$ [GHz] | $Z_R$ [$\Omega$] | $Q_i$ [$\times 10^4$] | $Q_c$ [$\times 10^4$] | $\tan(\delta_P)$ [$\times 10^{-6}$] | $\tan(\delta_T)$ [$\times 10^{-5}$] | $\delta_{\text{other}}$ [$\times 10^{-6}$] |
|---|---|---|---|---|---|---|---|---|---|
| 1 | 1 | 9.9 | 5.98 | 287 | 40.3 | 6.09 | 4.362 | 13.43 | 1.33 |
| **1** | **2** | **9.3** | **6.19** | **310** | **6.35** | **4.07** | **4.547** | **8.564** | **15.0** |
| 1 | 5 | 9.8 | 6.11 | 359 | 65.6 | 4.01 | 2.996 | 6.243 | 0.748 |
| 1 | 10 | 9.7 | 6.09 | 389 | 7.87 | 11.3 | 3.231 | 7.766 | 11.3 |
| 1 | 25 | 8.8 | 6.36 | 411 | 25.8 | 3.76 | 5.583 | 3.437 | 2.89 |
| 1 | 50 | 9.5 | 6.17 | 454 | 4.53 | 3.27 | 1.983 | 4.789 | 21.6 |
| 0.275 | 2 | 9.4 | 5.79 | 681 | 47.9 | 3.50 | 5.870 | 17.76 | 1.66 |
| **1** | **2** | **9.3** | **6.19** | **310** | **6.35** | **4.07** | **4.547** | **8.564** | **15.0** |
| 2 | 2 | 9.6 | 6.10 | 208 | 46.9 | 10.3 | 2.184 | 6.181 | 1.21 |
| 5 | 2 | 9.9 | 5.96 | 123 | 87.8 | 16.9 | 3.074 | 4.326 | 0.285 |
| 10 | 2 | 9.3 | 5.91 | 81 | 44.0 | 33.6 | 1.303 | 2.923 | 1.19 |

**TABLE 2.8:** MEASURED AND INFERRED VALUES OF ALL RESONATORS DATA. THE DEVICE WITH WIDTH $W = 1\ \mu$M AND GAP $G = 2\ \mu$M (BOLDED) IS USED AS THE REFERENCE DESIGN AND IS MENTIONED TWICE. BOTH THE REPORTED INTERNAL AND EXTERNAL QUALITY FACTORS $Q_i$ AND $Q_c$ ARE EXTRACTED AT AVERAGE INTERNAL PHOTON NUMBER $\langle n \rangle = 1$. ALSO $W$ AND $G$ COUNT AS MEASURED PARAMETERS.

We explain the geometric behaviour by the fact that the current density (and hence electric field) is highest on the inner edges of the differentially driven resonators [213, 214], also shown in simulations in Section 2.3.3 for lower $L_k$-resonators. This means that the interaction of the field with the TLS is enhanced there, efficiently exciting them, and thus TLS losses are higher for resonators with a relatively larger contribution of conductor-edge to total-resonator-surface. These are the narrower resonators, as the data shows. In a similar vein, an increased gap to lead-width ratio decreases the current density at the inner edge and improves the TLS losses.

We support this conclusion by the simulations of interface participation ratios $p_i$ shown in Figure 2.24. This entity, as detailed in Section 2.3.2, describes how much of the electrical field is threaded through each individual volume in the resonator. As electric field couples to the dipolar TLS, a higher participation ratio under constant loss-factor leads to a relatively larger loss for a given volume. We describe these ratios by the

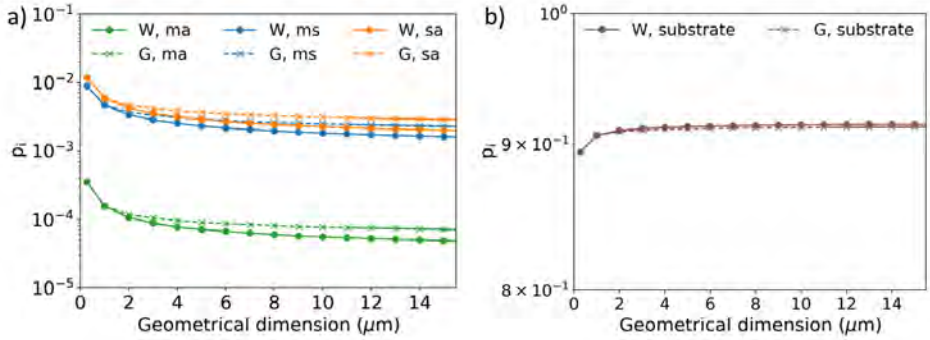


**Figure 2.24:** Simulation of the participation ratios of different dielectric volumes of the resonators. **a**) Simulation of the metal-air (ma), metal-surface (ms) and surface-air (sa) interfaces, threaded by the electric field and their evolution with geometrical parameter (resp. $W$, width, in full line and circle, and $G$, the gap, in dashed line and cross). **b**) Simulation of the participation ratio of the substrate and its evolution with geometrical parameter.

| Property | thickness (nm) | dielectric constant $\varepsilon_i$ |
|---|---|---|
| Metal-air | 1.2 | 54 |
| Metal-substrate | 3 | 11.35 |
| Substrate-air | 3 | 11.35 |
| Substrate | $280 \times 10^3$ | 11.35 |
| Air/vacuum | $10^6$ | 1 |

**TABLE 2.9:** SIMULATION PARAMETERS OF THE RESONATOR FOR DIFFERENT INTERFACES: METAL-AIR, METAL-SUBSTRATE, SUBSTRATE-AIR, SUBSTRATE AND AIR. NOTE THAT THE REAL SUBSTRATE THICKNESS USED IN EXPERIMENTS WAS 430 $\mu$M - THIS SHOULD NOT GIVE A MEASURABLE DIFFERENCE [187, 215, 216].

penetrating of the field through four dielectric regions: metal-air (ma), metal-substrate (ms), substrate-air (sa) and substrate. Here, we neglect the influence of the participation ratio of the perfect vacuum volume. More details on the simulation are given in Table 2.9. A unique advantage of the differentially driven CPS resonator is that, when constraining the data to the conductor leads themselves, the metal-substrate interface has the largest contribution to TLS-losses, which is a parameter that can be improved using enhanced fabrication methods. The metal-air interface has two orders of magnitude less contribution to loss participation than both the ms and the sa interfaces, including at higher dimensions of both width and gap. As the participation ratio of the lossy dielectric interfaces drop for larger geometrical dimension, the relative contribution of the substrate related losses increase as shown in Figure 2.24b. This is because the total electrical field penetrating the ms and ma interfaces scale as approximately respectively $W$ or $G$ while the total field in the substrate scales as approximately $W^2$ and $G^2$. Since the losses of bulk sapphire are negligible compared to those in the resonator surfaces (the bulk average losses of sapphire are in the range of $10^{-7} - 10^{-9}$, while those of the resonator surfaces are around $10^{-3} - 10^{-4}$), the overall internal quality factor decreases with increasing width and gap as observed [97, 107, 217].

### 2.4.3 Magnetic field dependence

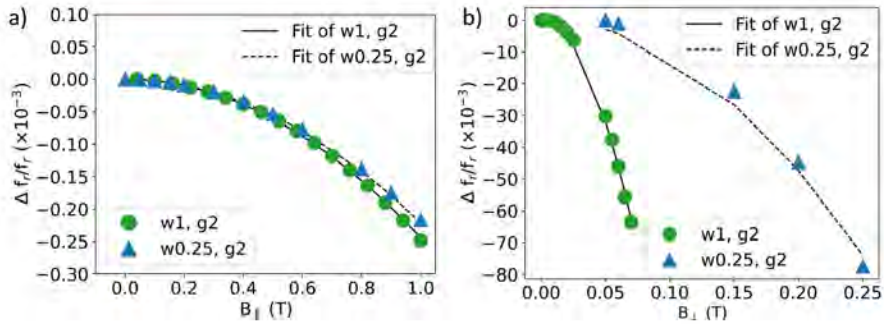


**Figure 2.25:** The relative shift of the resonance frequency of the resonator with width $W = 0.25$ $\mu$m and 1 $\mu$m (gap spacing $G = 2\mu$m) when sweeping an external magnetic field. Error bars are smaller than the data points. **a)** Evolution under an in-plane applied field ($B_\parallel$). A best fit of the data to $\frac{\Delta f_r}{f_r} = -k_{\perp,\parallel}B^2$ gives respectively $k$-values of **b)** An perpendicular applied field ($B_\perp$). Using a similar fit, we get respective $k$-values of The relative shift of the resonance frequency of the resonator with width $W = 0.25$ $\mu$m and 1 $\mu$m (gap spacing $G = 2\mu$m) when sweeping an external magnetic field. Error bars are smaller than the data points. **a), b)** Evolution of the frequency shift under an in-plane (perpendicular) applied field. Data is fit to $\frac{\Delta f_r}{f_r} = -k_{\parallel(\perp)}B^2_{\parallel(\perp)}$.

The behaviour of the resonance frequency to a magnetic field is shown in Figure 2.25. These measurements were taken at an average photon number of $\langle n \rangle \sim 10^4$, for the CPS resonators with nominal $W = 0.25$ $\mu$m and $W = 1$ $\mu$m, with $G = 2$ $\mu$m. The thick substrate effectively shields the resonator current distribution from the effect of vortex nucleation on the superconducting plane on the sample's backside [213]. Hence, the magnetic field behaviour is fully due to the currents circulating in the resonator leads. In general, the relative frequency shift due to the supercurrent depairing by a parallel magnetic field is well approximated by a quadratic relation of the form

$$\frac{\Delta f_r(B)}{f_{R,0}} = -k_\parallel B_\parallel^2 \tag{2.31}$$

$$= \frac{-\pi}{48}\frac{De^2}{\hbar k_B T_c(0)} B_\parallel^2 t^2, \tag{2.32}$$

valid for thin films where the $t$ is much smaller than the *effective* London penetration depth, $\lambda_{\text{eff}} = \lambda(1 + \frac{\xi_0}{l})^{\frac{1}{2}}$, around 1 $\mu$m for these films [54,56,65,66,218]. Here, $\lambda$, $\xi_0$ and $l$ are respectively the London penetration depth, the coherence length of NbTiN and the elastic electron mean free path, for which representative values are shown in Section 2.2.

We extend this formalism to a perpendicular magnetic field. In that case [219], as $t \ll \lambda_{\text{eff}}$, the screening distance takes the form of $\lambda_\perp = \frac{\lambda_{\text{eff}}^2}{t} \approx 100$ $\mu$m $\gg W$. This validates our approach to use $W$ instead of $t$ for perpendicular fields in Equation 2.31. For the data shown in Figure 2.25, we get $k_{0.25\mu\text{m},\perp} = 1.18 \pm 4.81 \times 10^{-2}$ T$^{-2}$ and $k_{1\mu\text{m},\perp} = 1.28e1 \pm 1.37 \times 10^{-1}$ T$^{-2}$. In this approximation, we derive directly the electron diffusion coefficient $D$ of the NbTiN films. We obtain diffusion coefficients of $D_{1\mu\text{m}} = 1.55$ cm$^2$s$^{-1}$ and $D_{0.25\mu\text{m}} = 2.29$ cm$^2$s$^{-1}$ from the perpendicular field data, which is in line with earlier reported results on NbTiN [66, 149, 199, 208].

We use these derived diffusion coefficients of the material to recreate the effective electronic thickness of the film. For this, we determine the $k$-values of the devices under an in-plane applied magnetic field parallel to the resonator direction with Equation 2.31. We extract respective $k$-values of $k_{0.25\mu\mathrm{m},\parallel} = 2.23 \times 10^{-4} \pm 4.0 \times 10^{-7}$ T$^{-2}$ and $k_{1\mu\mathrm{m},\parallel} = 2.47 \times 10^{-4} \pm 3.74 \times 10^{-7}$ T$^{-2}$, which results in calculated electronic film thicknesses of 4.39 nm and 3.44 nm for the 1 micrometer and 250 nanometre wide resonators, respectively. We attribute the difference to the physical layer thickness (which is around 10 nm) to the rough granular structure of the NbTiN, especially near the substrate surface, and the suppression of shielding currents within one coherence length from the surfaces. Finally, we stress the resonator's reliability in magnetic field from the consistent and low relative resonance frequency shift up to 1 T for a parallel field and up to 250 mT for a perpendicular field.

**Summary**

In conclusion, this Chapter described general effects on resonators and why we transition to a new resonator type. It continued by presenting the characterisation of these new, differentially driven CPS superconducting resonators with varying geometrical parameters, made from a 10 pH/□ NbTiN. By varying the width of the conductor leads and the spacing between the conductor pair, we achieved impedances ranging from 81 to 681 Ω. This stresses the flexibility of the CPS as its impedance is proportional to the coupling strength with a dipolar moment of e.g. Andreev bound states in semiconducting nanowires [36]. Moreover, the lack of groundplane makes these resonators an ideal platform for the next generation of superconductor-semiconductor heterostructure coupled devices, as they enable electrostatic gating without compromising resonator characteristics. Through the use of standard fitting techniques, we determined that losses are dominated by TLS in the zero-field regime. Furthermore, magnetic field indicates a high electronic diffusion constant of the NbTiN films, suggesting a high film quality. The films are especially resilient to parallel magnetic fields, which are paramount for cQED Majorana research.

# Chapter 3

# Andreev spectroscopy

*"Intuition or mathematics? Do we use models to find the truth? Or do we know the truth first, and then develop the mathematics to explain it?"*
— Arthur C. Clarke & Gentry Lee, *Rama II*

The historical evolution of quantum electrodynamics has transitioned from the study of light-matter interactions in natural atomic systems to the highly engineered environment of superconducting circuits. In this context, the interaction between artificial atoms and microwave photons has enabled the exploration of quantum mechanics in regimes previously unattainable. Central to these developments is the concept of circuit quantum electrodynamics (cQED), where the role of the atom is played by a superconducting qubit and the role of the cavity is played by a microwave resonator. As the field matures, the demand for higher degrees of control and faster operational speeds has pushed research toward the ultrastrong coupling (USC) regime, where the coupling strength $g$ becomes a significant fraction of the bare transition frequencies of the system. Simultaneously, the integration of semiconductor nanostructures into superconducting circuits has given rise to hybrid devices that leverage the unique properties of both platforms. At the heart of many of these hybrid systems lie Andreev bound states (ABS), which are discrete electronic states that emerge within the superconducting energy gap of a weak link due to the proximity effect. These states provide a microscopic degree of freedom that is tuned by both electric and magnetic fields, making them ideal candidates for the next generation of tunable quantum bits. The coupling of these Andreev bound states to superconducting resonators in the ultrastrong coupling regime represents a new paradigm in quantum physics, offering a window into non-perturbative light-matter interactions and the potential for topologically protected quantum information processing.

This chapter introduces our experimental results in using the CPS resonators, developed in Chapter 2, to couple to ABS in an aluminium-capped InAs semiconducting nanowire, etched in a Josephson junction (JJ) geometry. We begin with an experimentalist's summary of key concepts, such as Josephson junctions, Andreev bound states and their microscopic origin, particularly in semiconducting nanowires. Then, we take a more holistic approach and discuss their use cases. Since these nanowires are coupled to a cQED structure, also standard spectroscopy terms are covered. A small part will be dedicated to the ultrastrong coupling regime as well, and why it is a milestone to have reached this in these coupled heterostructures. Finally, we outline our main results.

In dc measurements, one fixes the junction phase (e.g. with a flux-biased SQUID) or measure switching currents. In cQED, phase is often controlled by an external flux in a loop; each approach offers complementary information. First, we show typical dc measurements on the InAs nanowire device platforms and the fabrication thereof, followed by our results on microwave spectroscopy.

## 3.1 The Josephson equations

This section covers the basics of the Josephson effect, one of the most striking macroscopic quantum phenomena of superconductivity. In 1962, Brian D. Josephson [9] predicted that in between two superconducting banks, sufficiently closely spaced by a thin barrier, a tunnelling current will flow that has two main characteristics: at zero voltage, a dc-supercurrent runs between the two superconducting banks, and that a finite dc voltage leads to an alternating current with frequency $\frac{2e}{h}V$. The former effect has been formally named the dc-Josephson effect, while the latter is called the ac-Josephson effect. This barrier, the weak link, was originally an oxide but could in principle be any material that reduces the superconducting order parameter. Indeed, Josephson junctions have been made of oxides (S*I*S-junctions [220]), superconductors with weaker order parameter (S$S'$S-junctions [221]), ferromagnets (S$F$S-junctions [222]) and normal metals or semiconductors (S$N$S [223]). For the SIS junction, the insulating barrier is generally on the order of nanometres thick; other junctions, such as the SNS-junction, can show dissipationless current on the order of hundreds of nanometres, simply because the Cooper pairs penetrate much deeper into a normal metal or gated semiconductor than into an oxide layer. In such an SNS junction, Cooper pair decay length depends on, among others, the electron mean free path [47].

The Josephson relations to first order are

$$\begin{aligned} I &= I_c \sin(\delta), \\ \frac{\partial \delta}{\partial t} &= \frac{2e}{\hbar} V \, . \end{aligned} \tag{3.1}$$

These expressions detail how the phase difference, $\delta = \varphi_1 - \varphi_2$ of the order parameters of the two superconducting banks, $\Delta_1 e^{i\varphi_1}$ and $\Delta_2 e^{i\varphi_2}$ leads to a sinusoidal current $I(\delta)$ through the junction, dissipationless up to a critical current density $I_c = A\frac{4Ke}{\hbar} n_{s,0}$, a value determined by the area $A$, shape and structure of the junction. The constant $\frac{2e}{\hbar}$ is known as the Josephson constant, $K = \frac{1}{\Phi_0}$, which is the inverse quantum of flux $\Phi_0$, and $n_{s,0}$ is the equilibrium density of Cooper pairs. The first Josephson relation depends on the exact type of weak link, and can exhibit higher harmonics, leading to a general form [224]

$$I(\varphi) = \sum_{n=1}^{\inf} \left[ I_{n,1} \sin(n\delta) + I_{n,2} \cos(n\delta) \right] \, , \tag{3.2}$$

where the second term is present only in systems violating time-reversal symmetry. This current-phase relation furthermore depends on the weak link geometry, or temperature. The two Josephson equations are intimately related: a time-dependent current

applied to the junction leads to a voltage over the junction. Thus, one associates a phase-dependent inductance with each junction:

$$L(\varphi) = \frac{L_J}{\cos(\delta)}, \tag{3.3}$$

where $L_J = \frac{\Phi_0}{2\pi I_c}$ is the so-called Josephson inductance. Up to now we have assumed that the phase difference $\varphi$ is constant in the entire junction. However, we run into a problem. The values of $\varphi_{1,2}$ are not gauge-invariant and hence do not have a uniquely determined value, but the current $I$ is well-defined. We solve this by replacing $\delta$ by

$$\varphi = \varphi_1 - \varphi_2 - \left(\frac{2\pi}{\Phi_0}\int \mathbf{A}\cdot \mathrm{d}\mathbf{l}\right) \tag{3.4}$$

where the integral is taken from one superconductor to the other over the magnetic potential $\mathbf{A}$. This gauge-invariance strengthens the fact that the Josephson relations are valid for many different types of junctions. Furthermore, it tells us that the phase across the junction is a function of an external magnetic field (potential), and hence is tunable without a dc-current or voltage application [225].

## 3.2 Andreev bound states

In the SIS Josephson junction, the weak link is an insulator, typically a thin $AlO_x$ tunnel barrier. In that case, the original picture says that the Josephson current arises from the coherent tunnelling of Cooper pairs between two superconducting electrodes, provided that phase coherence is maintained across the barrier. A natural question is then what happens when the insulating barrier is replaced by a normal metal or a semiconductor, such as InAs. In such SNS junctions, superconducting correlations leak into the non-superconducting region through the proximity effect [225, 226]. As a result, the weak link may support a dissipationless supercurrent even though it is not itself intrinsically superconducting. When such a normal conductor is brought into good contact with a superconductor, electron-hole correlations are induced in the normal region. These correlations decay over a characteristic normal-metal coherence length, denoted $\xi_N$, which in the clean limit scales approximately as $\xi_N \sim \hbar v_F / k_B T$ [227]. For sufficiently short junctions, or more generally when the junction length is smaller than the relevant coherence length, the induced superconducting correlations extend across the entire weak link, allowing phase-coherent transport between the two superconducting banks.

The microscopic origin of this phase-coherent transport is Andreev reflection [228], which as it turns out is also valid for insulating weak links [229]. Consider an electron incident from the normal region with excitation energy $E < \Delta$ onto a superconductor. Since no propagating quasiparticle states are available inside the superconducting gap, the electron cannot enter the superconductor as a single particle. Instead, it is converted into a Cooper pair in the condensate by combining with a second electron of opposite spin and momentum, while a hole is reflected back into the normal region. This reflected hole retraces, in the simplest limit, the path of the incident electron, and its phase is determined by both the incident electron and the superconducting phase of the electrode. In this way, Andreev reflection couples electron and hole amplitudes and transfers superconducting phase information into the weak link. In an SNS junction,

the two NS interfaces act together: an electron incident on one superconducting interface is Andreev-reflected as a hole, which propagates to the opposite interface and is there converted back into an electron. Repeated coherent Andreev reflections between the two superconductors quantise the allowed subgap states in the weak link; it is analogous to a particle-in-a-box problem. These discrete phase-dependent states are the Andreev bound states, and these discrete fermionic excitations, spatially confined in the weak link, are the microscopic origin of the Josephson supercurrent in a short, coherent junction. Their energies depend on the superconducting phase difference $\varphi$ across the junction, so that the supercurrent follows directly from the phase dispersion of the bound-state spectrum. For a short, single-channel junction of normal-state channel transmission $\tau$, the ABS energies are given by [230, 231]

$$E_{\pm}(\varphi) = \pm\Delta\sqrt{1-\tau\sin^2\left(\frac{\varphi}{2}\right)}, \tag{3.5}$$

which reduces to the familiar tunnel-junction limit for small transmission and evolves towards highly dispersive subgap states as $\tau \to 1$. Equation 3.5 provides physical insight in the junction. For a perfectly transparent channel ($\tau = 1$), the energy levels $\pm\Delta\cos(\varphi/2)$ cross at zero energy when the phase difference is $\pi$. However, for a realistic junction with backscattering ($\tau < 1$), an avoided crossing opens at $\varphi = \pi$ with a size of $2\Delta\sqrt{1-\tau}$. This mini-gap is a signature of the finite transparency and is fundamental to the deviations from pure $\sin(\varphi)$-current-phase relations observed in hybrid junctions [224, 232, 233].

Besides generating bound states in equilibrium, Andreev reflection also governs transport under finite bias. When a voltage $V$ is applied across a superconducting weak link, a quasiparticle gains an energy $eV$ during each traversal of the junction. Repeated Andreev reflections therefore stepwise increase their energy until it exceeds the superconducting gap, giving rise to characteristic conductance features (multiple Andreev reflections) at voltages

$$V_n = \frac{2\Delta}{ne}, n \in \mathbb{N} \tag{3.6}$$

known as the sub-harmonic gap structure. This mechanism is distinct from Shapiro steps, which arise when the Josephson effect is driven by external microwave irradiation. Nevertheless, both phenomena reflect the phase-coherent dynamics of superconducting weak links. The ABS also directly relate to the Josephson supercurrent. The essential point is that the superconducting phase difference $\varphi$ acts as a generalised coordinate, while the current is its conjugate response. Using energy conservation,

$$\frac{dE}{dt} = \frac{\partial E}{\partial \varphi}\frac{\partial \varphi}{\partial t} = IV, \tag{3.7}$$

together with the ac Josephson relation,

$$\frac{d\varphi}{dt} = \frac{2e}{\hbar}V, \tag{3.8}$$

one finds that the supercurrent associated with a phase-dependent energy level is given by [30, 234]

$$I(\varphi) = \pm\frac{2e}{\hbar}\frac{\partial E}{\partial \varphi}, \tag{3.9}$$

where either positive or negative energy branches are considered. In other words, each ABS carries a current set by the derivative of its energy spectrum with respect to the superconducting phase difference. In a long or multi-channel junction, several transport channels contribute, each characterised by its own phase-dependent ABS energy spectrum $E_n(\varphi)$. The total supercurrent is then obtained by summing the contributions of the occupied states [235],

$$I(\varphi) = \pm\frac{2e}{\hbar}\sum_n \frac{\partial E_n(\varphi)}{\partial \varphi} = \pm\frac{e\Delta}{2\hbar}\sum_n \frac{\tau_n \sin(\varphi)}{\sqrt{1-\tau_n \sin^2(\frac{\varphi}{2})}}, \tag{3.10}$$

or, more generally at finite temperature, by weighting each contribution with its occupation $\sum_n f(E_n)$; at zero temperature, only the negative-energy branches are occupied. For a tunnel junction, where $\tau_n \ll 1$, we find the familiar dc-Josephson effect at zero temperature with $I_c = \frac{\pi\Delta}{2eR_N}$ where $R_N$ is the junction's normal state resistance. Thus, the Josephson current follows directly from the phase dispersion of the bound states themselves.

The classification of a junction as "short" or "long" is determined by the ratio between the length of the normal region $L_N$ and the ballistic superconducting coherence length $\xi_0 = \frac{\hbar v_F}{\Delta}$ [236]. In the short junction limit ($L_N \ll \xi_0$), the transit time of quasiparticles across the normal region is negligible compared to the superconducting gap timescale $\frac{\hbar}{\Delta}$. Consequently, the energies of the ABS are governed primarily by the phase difference across the junction and the transparency of the individual conduction channels. For a single conduction channel with a normal-state transparency $\tau$, the energy of the ABS pair is then described by Eq. 3.5.
In contrast, the ballistic long junction limit ($L_N \gg \xi_0$) accommodates multiple ABS pairs. The relevant energy scale is defined by the ballistic Thouless energy $E_T = \frac{\hbar v_F}{L_N}$, which represents the inverse of the time required for a quasiparticle to travel across the normal region $\tau_f = \frac{L_N}{v_F}$. The states in this regime are more densely packed; for energies $E \ll \Delta$, the spectrum is approximated as [237–239]:

$$E_n = \frac{\hbar v_F}{2L_N}\left(\pi(2n+1) \pm \varphi\right) , \tag{3.11}$$

where the sign corresponds to the direction of the quasiparticle trajectory right-moving electron/left-moving hole (+) or vice-versa (−). As $L_N$ increases, these discrete levels converge to form a quasi-continuum of subgap states [240]. Unlike the states in the continuum above the gap, which consists of propagating quasiparticles that escape into the superconducting leads, these states remain localised within the nanowire due to successive Andreev reflections at the superconductor-nanowire interfaces [241]. This high density of states marks the transition from a discrete quantum system to a regime approaching the classical limit of a 1D ballistic conductor.

### 3.2.1 Semiconducting nanowire heterostructures

Hybrid semiconductor-superconductor nanowires provide an experimentally versatile route to engineer low-dimensional superconductivity with *in situ* tunability. As described above, a superconducting proximity effect occurs when a narrow band-gap III-V semiconductor (such as InAs) is brought into good contact with a superconductor, inducing superconducting correlations and an energy gap in the semiconductor [227].

| Regime | JJ length | Dominant energy scale | ABS # |
|---|---|---|---|
| Short Junction | $L_N \ll \xi$ | Superconducting gap ($\Delta$) | One pair per channel |
| Intermediate | $L_N \approx \xi$ | $\Delta$ and $E_T$ comparable | Few pairs |
| Long Junction | $L_N \gg \xi$ | Thouless energy ($E_T$) | Many pairs (continuum-like) |

**TABLE 3.1:** CLASSIFICATION OF ANDREEV BOUND STATES IN BALLISTIC WEAK LINKS AS A FUNCTION OF JUNCTION LENGTH.

In the modern InAs/Al platform, an epitaxial aluminium shell can be deposited by molecular beam epitaxy *in situ* on an InAs nanowire core, strongly reducing interfacial disorder and enabling high transparency at the semiconductor-superconductor interface [242]. Junctions are defined by selectively removing a segment of the Al shell, creating a bare InAs weak link of length $L$ akin to a SNS junction. A half-shell or partial-shell geometry (Al covering only some facets of the hexagonal nanowire) leaves part of the InAs exposed, enabling efficient electrostatic gating with minimal etching. Normal-metal or superconducting contact electrodes (e.g. Ti/Au, Ti/Al) are used to interface the nanowire to external circuitry, often combined with surface preparation (oxide removal or sulphur passivation) to maximise contact transparency. Electrostatic gates (global backgate or local side/top gates) tune carrier density, the chemical potential and the spin-orbit coupling (SOC) in the weak link [243, 244], all related to channel transparency $\tau$. For clean interfaces, the induced gap $\Delta'$ approaches the parent Al gap (hard gap regime); in the ballistic limit the coherence length becomes $\xi_0 = \hbar v_F/(\pi\Delta')$, while in the diffusive limit one uses $\xi \sim \sqrt{\hbar D/\Delta'}$ [245,246].

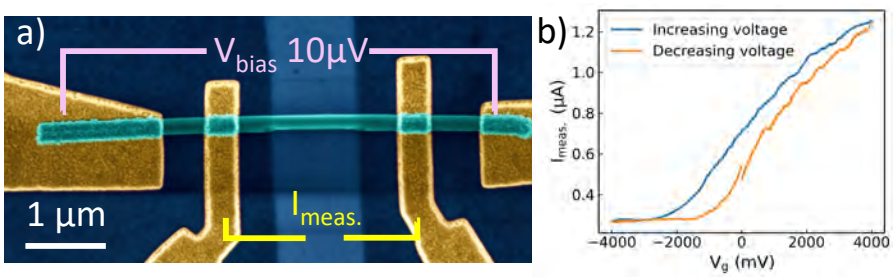


**Figure 3.1: a**) False-colour scanning electron micrograph of a InAs (teal) nanowire partially covered by epitaxial aluminium on three facets. Additional contacts are Al (yellow). A long junction ($L \approx 1$ $\mu$m) is etched. The device is configured in a four-terminal geometry: a bias voltage $V_{bias} = 10$ mV is applied across the outer contacts (pink), while the voltage drop is measured between inner probes to obtain the four-point resistance. The scale bar corresponds to 1 $\mu$m. **b**) Measured current $I_{meas}$ as a function of gate voltage $V_g$ at fixed large bias $V_{bias} = 10$ mV to reach the non-superconducting regime, showing forward (increasing gate voltage) and backward (decreasing gate voltage) sweeps. The discrepancy at $V_g = 0$ V for the decreasing voltage is due to gate-limitations and corresponds to continuation via a new measurement. The hysteresis reflects charge trapping and electrostatic drift in the nanowire.

In practice, electrostatic tuning in InAs/Al SNS devices (see false-coloured image in Fig. 3.1a) has multiple intertwined effects. Gate voltages modify the carrier density and chemical potential in the weak link, thereby controlling the number of occupied one-dimensional modes as well as their Fermi velocity and mean free path, particularly near depletion. At the same time, they influence interface barrier strengths, the magnitude of Rashba spin–orbit coupling, the set of transmission probabilities

$\tau_n$, and the effective coupling to the superconducting leads. As a consequence, the device accesses qualitatively different transport regimes depending on gate voltage and disorder. These range from quantum-dot-like behaviour with localised states, to a few-mode regime, and ultimately to a highly transmissive multi-mode regime. In the normal state, the gate response is typically characterised using current–voltage traces, from which threshold and pinch-off voltages are extracted. These quantities depend sensitively on device geometry, dielectric environment, surface states, and the intrinsic surface accumulation layer of InAs [247].

Representative dc measurements are shown in Fig. 3.1b for a long junction ($L \sim 1\ \mu$m) that does not exhibit a measurable Josephson effect: in this long-junction limit, the device effectively behaves as a normal semiconductor. A similar suppression of superconducting transport is achieved by applying a large bias ($I > I_c$ or $V > 2\Delta/e$) or an external magnetic field exceeding the critical field ($H_a > B_c$). The observed hysteresis between forward and reverse gate sweeps is indicative of charge trapping and slow electrostatic drift, which complicates the definition of a unique threshold voltage. With superconductivity present, additional junction characteristics become relevant, including the critical current, normal-state resistance, induced gap, and subgap hardness. In sufficiently short and clean junctions, one may further observe conductance quantisation and discrete Andreev bound state spectra.

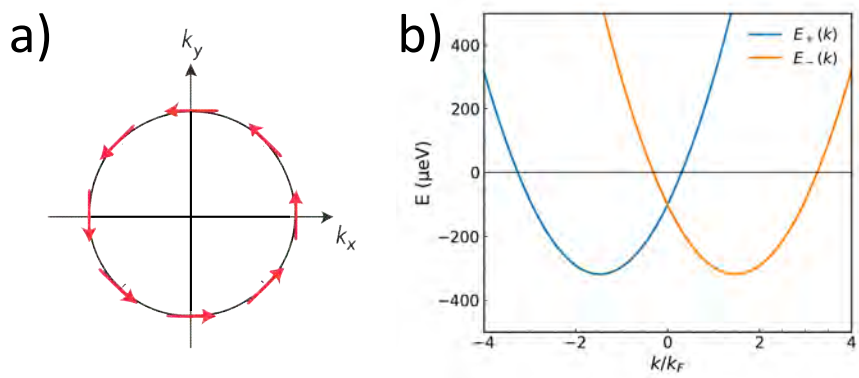


**Figure 3.2:** Rashba spin–orbit coupling in a quasi-one-dimensional nanowire. **a**) Momentum-space representation in a 2D-device (with corresponding Hamiltonian $H = \alpha(\sigma_x p_y - \sigma_y p x)$ [248]). The circular constant-energy contour in the $(k_x, k_y)$ plane illustrates spin–momentum locking: the spin orientation (red arrows) is perpendicular to the electron momentum and tangential to the Fermi contour, reversing direction for opposite momenta. **b**) Corresponding simulated normal-state band dispersion in a one-dimensional nanowire oriented along $x$. Rashba spin–orbit coupling lifts spin degeneracy and splits the parabolic band into two branches $E_\pm(k) = \frac{\hbar^2 k^2}{2m^*} \pm \alpha k$, shown here as a function of the normalised momentum $k/k_F$. The splitting shifts the band minima away from $k = 0$ and is characterised by the Rashba coupling strength $\alpha$; here $\alpha = 38 \times 10^3\ \mu$eV·nm, characteristic for InAs nanowires [249].

Beyond interface quality and gateability, a defining characteristic of narrow-gap III-V nanowires is their strong SOC, which couples an electron's momentum to its spin. In solids, the SOC effect arises from different symmetry-breaking mechanisms. Crystal/bulk inversion asymmetry leads to Dresselhaus SOC [250] whereas structural inversion asymmetry, common at interfaces and in electrostatically confined systems,

gives rise to the relativistic Rashba SOC [251]. The former happens in crystals that lack a centre of inversion, while the latter occurs when the potential environment of the electron is asymmetric along a specific direction (usually the growth direction of a heterostructure or the surface normal). The physical reason is that if a charged particle with a momentum $\mathbf{p}$ moves in a magnetic field $\mathbf{B}$, it will both experience a Lorentz force perpendicular to its motion, $F = -\frac{e}{m_e}\mathbf{p} \times \mathbf{B}$, and possess a Zeeman energy $E_{\text{Zeeman}} = \mu_B \sigma \cdot \mathbf{B}$, where $\sigma$ are the Pauli-matrices. Furthermore, the laws of electrodynamics are symmetric with respect to electric and magnetic fields. Hence, if the electron instead moved in an electric field $\mathbf{E}$, then it experiences an effective magnetic field, which in turn couples to the electron's spin via the Zeeman energy [252]. For Dresselhaus SOC, it is the crystal itself that has an intrinsic electrical field. For Rashba SOC, an external confining potential, which could also be crystal interfaces, lead to the field.

In gate-defined low-dimensional systems such as quantum wells and nanowires, Rashba SOC is often the dominant contribution because external gating and confinement generate strong transverse electric fields. Crucially, this SOC strength is electrostatically tunable, which makes it particularly relevant in hybrid superconducting devices where the gate simultaneously controls carrier density, transmission, and spin physics. We write the Rashba interaction as [253]

$$H_{\text{SO}} = -\alpha \cdot (\mathbf{k} \times \boldsymbol{\sigma}) \,, \tag{3.12}$$

where $\alpha$ is the Rashba coupling strength that is gate-tunable and $\mathbf{k}$ is the electron's wave vector. In a quasi-one-dimensional nanowire oriented along $\hat{x}$ (with a dominant transverse electric field defining $\hat{z}$), transverse confinement freezes out (or strongly quantises) motion in two directions and the Rashba term reduces to an effective 1D form:

$$H_{\text{SO}} = -\alpha \, p_x \, \sigma_y, \tag{3.13}$$

illustrating that the spin quantisation axis becomes locked to the momentum direction $p_x$: so-called spin-momentum locking. As a consequence, the electronic dispersion splits into two branches of opposite spin momentum,

$$E_{\pm}(k) = \frac{\hbar^2 k^2}{2m^*} \pm \alpha k, \tag{3.14}$$

corresponding to opposite spin orientations in momentum space. This lifts the degeneracy of the bands and splits them horizontally and symmetrically around $k = 0$. This is made more visible by rewriting Eq. 3.14 as shifted parabolas

$$E_{\pm}(k) = \frac{\hbar^2}{2m^*}(k \pm k_{\text{so}})^2 - E_{\text{so}}, \qquad k_{\text{so}} = \frac{m^* \alpha}{\hbar^2}, \qquad E_{\text{so}} = \frac{m^* \alpha^2}{2\hbar^2}, \tag{3.15}$$

which makes explicit that Rashba SOC displaces the band minima horizontally in $k$-space by $\pm k_{\text{so}}$ and sets a characteristic SOC energy scale $E_{\text{so}}$. We show the effect of Rashba spin-momentum locking, and on the energy bands in Figure 3.2. In the hybrid InAs/Al context, this Rashba-induced splitting, together with Zeeman splitting from an external magnetic field and proximity-induced pairing, provides the microscopic ingredients that enable unconventional superconductivity, Josephson diodes [254] and topological devices [244, 255].

The natural question is now: how do Andreev bound states respond to spin–orbit coupling in the nanowire? In the short-junction limit ($L \ll \xi$), the answer is: only weakly. In this regime, quasiparticles traverse the weak link without accumulating a significant dynamical phase, and the ABS spectrum is governed primarily by the interface transparency $\tau$. Spin–orbit coupling modifies the spin texture of the propagating states, but since the junction length is negligible, there is little spatial extent over which SOC-induced phase differences build up and both electrons and holes acquire the same phase in a round-trip. As a result, the conventional short-junction dispersion, Equation 3.5, remains intact as the spin-degeneracy is not lifted.

The situation changes qualitatively once the junction is of finite length. In this case, the ABS energies are determined not only by Andreev reflection at the interfaces, but also by the phase accumulated during propagation through the normal region. Spin–orbit coupling further enriches the finite-length picture. Because SOC splits the normal-state spectrum into modes with different velocities, the transport is no longer characterised by a single Fermi velocity $v_F$, but effectively by two velocities $v_1$ and $v_2$. This naturally introduces two coherence lengths

$$\xi_j = \frac{\hbar v_j}{\Delta}, \qquad j = 1,2, \tag{3.16}$$

which allows us to introduce two corresponding dimensionless length parameters

$$\lambda_j \equiv \frac{L}{\xi_j}, \tag{3.17}$$

which relates the ballistic superconducting coherence length to the junction length $L$. Physically, $\lambda_1$ and $\lambda_2$ quantify how rapidly each SOC-related mode accumulates phase while traversing the junction. Due to this, the particles in the long quasi-1D junction regime acquire different phases at the junction boundaries:

$$\pm\delta - 2\arccos(\varepsilon) + 2\lambda_{i,j}\varepsilon = 0 \mod 2\pi, \qquad \varepsilon = \frac{E}{\Delta}, \tag{3.18}$$

where the additional term $2\lambda_{i,j}\varepsilon$ represents this energy-dependent dynamical phase acquired by traversing the weak link. Once $L$ is not negligible, this term reshapes the $\varphi$-dispersion of the ABS and cannot be ignored.

Including backscattering within the wire adds another adjustment to the spectrum. A localised scatterer of transmission $\tau$ placed at position $x_0$ along the junction is parametrised by the reduced coordinate

$$x_r = \frac{2x_0}{L}, x_r \in [-1,1]. \tag{3.19}$$

The subgap ABS energies then follow from a transcendental equation of the form [249, 256, 257]

$$\begin{aligned}\tau\cos\Big[(\lambda_1-\lambda_2)\varepsilon \mp \varphi\Big] + (1-\tau)\cos\Big[(\lambda_1+\lambda_2)\varepsilon x_r\Big] \\ = \cos\Big[2\arccos(\varepsilon) - (\lambda_1+\lambda_2)\varepsilon\Big].\end{aligned} \tag{3.20}$$

normalised with $\varepsilon = E_A/\Delta_{sc}$. We show a possible spectrum, containing three ABS in Figure 3.3a. Equation 3.20 makes the physical structure a bit more transparent:

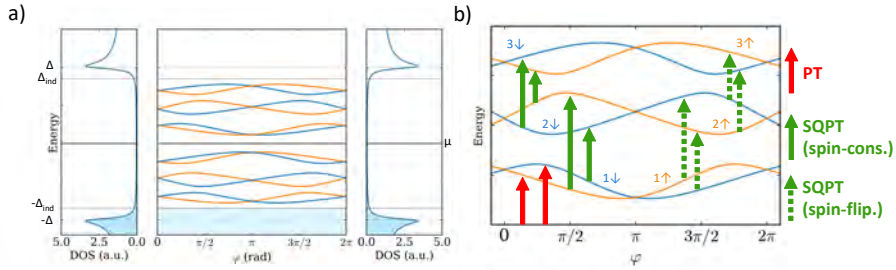


**Figure 3.3:** Effect of Rashba spin-orbit coupling on the Andreev bound state spectrum in the semiconductor picture normalised to the superconducting Al gap Δ. **a**) *Left, right*: BCS-like density of states (DOS) of the superconducting banks, where energy is rescaled compared to Eq. 2.2 with a disorder parameter Γ to smoothen the Van Hove singularities. The weak link is characterised by an induced gap $\Delta_{ind}$ [232]. Band filling is represented by solid light blue colour, up to the chemical potential $\mu$. *Central:* In a finite-length ('long') weak link, multiple ABS doublets squeeze into the spectrum. Three levels are shown here of equal transparency $\tau$ for a scatterer at $x_r$. Spin-orbit interaction lifts the spin degeneracy, splitting each of the states. These are solutions to Eq. 3.20. Parameters for simulation: $\Delta_{ind} = 0.85\Delta$, $\Gamma = 0.03\Delta$, $\mu = 1.2\Delta$, $\lambda_1 = 4.5$, $\lambda_2 = 2.0$, $\tau = 0.7$, $x_r = 0.5$. Parameters are reused for **b**), possible transitions in the excitation picture of a long weak link with spin-orbit interaction. In this specific case, three ABSs are present in the spectrum, each of them is split into a doublet of states with the opposite pseudo-spin, denoted by ↑ and ↓. Microwave photons induce pair transitions (PT, red arrows) and single-quasiparticle transitions (SQPT, green arrows), where for the latter spin-conserving (solid) and spin-flipping (dashed) processes can be distinguished. The energy scale is normalized to the superconducting induced gap. The time-reversal symmetry preserves degeneracy at $\varphi = 0$ and $\varphi = \pi$.

- $\tau$ controls the strength of backscattering.
- $x_r$ determines where along the junction this scattering occurs.
- $\lambda_1, \lambda_2$ encode the propagation phases of the two SOC-split modes, and are related to the junction length.
- $\Delta_{sc}$ remains the parameter that renormalises the spectrum.

The main point of the effect of SOC on the Andreev bound states is the appearance of two distinct propagation phases, rather than a single one. The ABS spectrum therefore becomes sensitive to the difference $\lambda_1 - \lambda_2$, i.e. to the Fermi velocity asymmetry induced by spin–orbit coupling. From an experimental perspective, this parametrisation provides a direct bridge between the theory, and the nitty-gritty of electrostatic tuning and spectroscopy. Gate voltage modifies the chemical potential $\mu$, thereby changing the velocities $v_j$ and shifting $\lambda_1$ and $\lambda_2$. At the same time, gating alters the effective scattering strength $\tau$ and even the dominant scattering location $x_r$. Consequently, SOC in finite-length nanowire junctions directly controls the dynamical phase accumulation of multiple modes and thus reshapes the ABS dispersion as a function of phase bias $\varphi$. This explains why ABS spectroscopy in gated InAs/Al junctions often cannot be captured by a single short-junction transparency $\tau$ alone. Finite-length propagation and SOC-induced multi-mode dynamics enter on equal footing through the parameters $\lambda_1$, $\lambda_2$, $\tau$, and $x_r$, which together determine the experimentally observed phase-dependent subgap structure; this is especially valid for long junctions where multiple ABS squeeze in the spectrum as seen from the earlier particle-in-the-box picture: a larger box pushes the levels down in absolute energy, and more states thus squeeze in. We furthermore note that the degeneracies in Figure 3.3b at $\varphi = 0 \mathrm{mod} \pi$

are only be lifted under an external magnetic field.

## 3.3 Microwave Spectroscopy

The integration of an ABS-based junction into a cQED architecture requires a mechanism to translate microwave photons in a resonator into transitions between Andreev levels. Unlike transmons, which couple primarily via the electric field (capacitive coupling), Andreev bound states are most effectively coupled galvanically. Inductive coupling is typically achieved by embedding the Josephson junction into a superconducting loop that is shared with a portion of a microwave resonator. This "shared inductance" geometry ensures that the zero-point fluctuations of the magnetic flux in the resonator ($\Phi_{zpf}$) modulate the phase difference across the junction. To characterise light-matter interactions, specifically those of a single-mode resonator coupled with strength $g_c$ to a two-level system, the Jaynes-Cummings (JC) Hamiltonian is often the starting point [19, 258]:

$$H_{\mathrm{JC}} = \hbar\omega\left(a^\dagger a + \tfrac{1}{2}\right) + \frac{\hbar\Omega}{2}\sigma_z + \hbar g(a^\dagger\sigma_- + a\sigma_+)\,, \tag{3.21}$$

where the constant term $\frac{\hbar\omega}{2}$ is just a constant offset, the zero-point energy of the field, and $\sigma_\pm$ are the ladder operators. This equation describes a two-level system ("atom") with a ground state $|-\rangle$ and excited state $|+\rangle$ (whose energy difference is given by $\hbar\Omega$) under a drive of frequency $\omega$. Importantly, the JC Hamiltonian is an approximation [259], and is valid for weakly coupled systems, and under assumption that $|\omega-\Omega| \ll \Omega+\omega$ if the probing frequency is near the transition frequency $\Omega$. In that case, the first term, the resonant (detuning) term oscillates at $\omega-\Omega \approx 0$, while the counter-rotating term oscillates at $\omega+\Omega \approx 2\Omega$. In other words, the detuning term varies little over one cycle; the counter-rotating term completes many periods. This defines the rotating-wave approximation (RWA); over the timescale of a standard qubit measurement under moderate resonator-qubit coupling, the counter-rotating terms will cancel out. In the limit of large detuning, where $\hbar|\Delta_\omega| = \hbar|\omega-\Omega| \gg g_c$, the coupling between field and artificial atom will renormalise the energy spectrum of the system, and atom and field cannot efficiently exchange excitations. Then, under perturbation of $\frac{g_c}{\Delta_\omega}$, the resulting damping-free dispersive JC Hamiltonian becomes [19]

$$H_{\mathrm{JC,disp}} = \frac{\hbar}{2}\left(\Omega + \frac{g_c^2}{\Delta_\omega}\right)\sigma_z + \hbar\left(\omega + \frac{g_c^2}{\Delta_\omega}\sigma_z\right)a^\dagger a \tag{3.22}$$

$$\tag{3.23}$$

$$= \frac{\hbar\Omega'}{2}\,\sigma_z + \hbar\omega\, a^\dagger a + \hbar\chi\,\sigma_z a^\dagger a \tag{3.24}$$

valid up to second order of $\chi = \frac{g_c^2}{\Delta_\omega}$. The term $\Omega'$ is the shifted qubit frequency under coupling that depends on the mean photon number $\langle a^\dagger a\rangle$: $\Omega' = \Omega + 2\chi\langle n\rangle$ [260]. Moreover, the qubit also shifts the resonator's resonance frequency by $\pm\chi$ depending on the qubit's state, allowing for non-demolition discrimination of its state. Note that this derivation is only valid for the linear dispersion regime of small photon number

$n_{critical} = \frac{1}{4}\frac{\Delta_0^2}{g_c^2}$ [261].

The next question we then naturally ask is how does a cQED system, such as a resonator, couple to the microscopic degrees of freedom in an ABS? The exact nature of the coupling between the resonator and the ABS is an engineering challenge and the details depend on geometry. However, certain general cases are identified by what resonator coordinate couples to what operator. In ABS(-qubits), this coupling will depend on the variables of the superconducting condensate [262]. We follow the derivation of a single-level ABS-qubit by [122, 262, 263], itself based on the proposal of the Andreev pair qubit by Zazunov [196]. First, let us discuss the Hamiltonian. The entire Hamiltonian of the system (resonator, Andreev qubit, coupling) is given by the coupling of the Andreev states to the resonator:

$$H = H_R + H_A + H_{AR} \, . \tag{3.25}$$

The resonator's Hamiltonian is treated in the single-mode regime, providing

$$H_R = h f_r (a^\dagger a + \frac{1}{2}) \, . \tag{3.26}$$

In the Andreev state basis, assuming high-transparent contacts under stationary conditions, $\frac{\partial \varphi}{\partial t} = 0$, the Andreev Hamiltonian is given by:

$$H_A(\varphi) = -E_A(\varphi)\sigma_z(\varphi) \, , \tag{3.27}$$

where $E_A$ is the previous defined Andreev energy spectrum 3.5. The final term, that described the coupling Hamiltonian between Andreev states and the resonator is given in first order by

$$H_{AR} = M \hat{I}_R \hat{I}_A(\varphi) \, , \tag{3.28}$$

where $M$ is the shared inductance between a flux loop and resonator in an inductively coupled system, $\hat{I}_R = \sqrt{\frac{\pi h f_r^2}{2 Z_R}}(a^\dagger + a)$ is the resonator current operator, and the current operator of the Andreev system is

$$\hat{I_A}(\varphi, \tau) = \frac{\Delta_{\mathrm{sc}}}{4\Phi_0} \frac{\tau \sin(\varphi)}{\sqrt{1 - \tau \sin^2(\frac{\varphi}{2})}} \, . \tag{3.29}$$

This includes the bare superconducting gap $\Delta_{\mathrm{sc}}$ (in our case that of Al), the resonator's impedance $Z_R$ and notably a strong phase dependence. In total, this means the coupling Hamiltonian becomes:

$$\begin{aligned} H_{AR} = \sqrt{z} \frac{E_A(\pi)}{2} & \left( \frac{\Delta_{\mathrm{sc}}}{E_A(\varphi, \tau)} - \frac{E_A(\varphi, \tau)}{\Delta_{\mathrm{sc}}} \right) \\ & \times (a^\dagger + a) \\ & \times \left( \frac{1}{\sqrt{1 - \tau} \tan\left(\frac{\varphi}{2}\right)} \sigma_z + \sigma_x \right) . \end{aligned} \tag{3.30}$$

The first term in this equation is the coupling term, $g_c$, with the prefactor $z = \pi \frac{M^2 Z_R}{L^2 R_Q}$. This coupling peaks at $\varphi = \pi$, and smoothens out for low-transparency channels. From

here, we derive a JC-like Hamiltonian. First, basic quantum information says that $\sigma_x = \sigma_+ + \sigma_-$. Then, we apply the RWA to obtain:

$$H = \hbar\omega_r(a^\dagger a + \frac{1}{2}) - E_A\sigma_z + \hbar g_c(a\sigma_+ + a^\dagger\sigma_-) \ . \tag{3.31}$$

The dispersive form thus follows Eq. 3.24.
This derivation is based on a system that involves coupling via a mutual inductance $M$; it is also valid in our case of a coupling to a *mutually shared* inductance, where we replace $M$ by $\ell$, a shared inductance. To see that such a structure allows for coupling to ABS, first, we apply a static, external flux bias $\Phi$. This causes the phase inside the junction to change as $\varphi \approx 2\pi\frac{\Phi}{\Phi_0}$ in first order. Then, we send a perturbative microwave drive either in, or coupled to the ABS. This, in turn, leads to an oscillating flux $\varphi e^{i\omega t}$. In first order, the Hamiltonian that governs the Andreev bound state spectrum changes as:

$$H \sim \varphi e^{i\omega t}\frac{\partial H_a}{\partial\Phi} \ . \tag{3.32}$$

This means the Hamiltonian scales with the current operator, analogous to Eq. 3.9, and given by Equation 3.29. We see thus immediately that the resonator current couples to the Andreev spectrum via an induced phase, either directly or via such a phase-drop over a mutually shared inductance.

This can be quantised: the flux due to the resonator is $\Phi_r = p\Phi_{zpf}$, where $p$ is the voltage participation ratio between junction and resonator; in our geometries, the ratio of the shared inductance to the total inductance of the resonator $\frac{\ell}{L_{tot}}$. The zero-point fluctuations are given by $\Phi_{zpf} = \sqrt{\langle 0|\hat{\Phi}^2|0\rangle} = \sqrt{\frac{\hbar Z_r}{2}}$ at low temperature and frequencies, with $Z_r$ the differential impedance of the resonator. These fluctuations are present even in the ground state: the resonator can be modelled as a quantum harmonic oscillator, where even in the vacuum state, the conjugate variables flux $\hat{\Phi} = \Phi_r(a^\dagger + a)$ and charge $\hat{Q}$ exhibit non-vanishing variances due to the Heisenberg uncertainty principle, resulting in $\Phi_{zpf}$.

This intuitive picture allows us to derive an equivalent coupling Hamiltonian to Eq. 3.28. Assume we have a small external flux of the form $\Phi_r$ as defined above. Then a Taylor expansion leads to [229]

$$\begin{aligned}
H =& \hbar\omega_r\left(a^\dagger a + \frac{1}{2}\right) + H_A(\Phi + \mathrm{d}\Phi) \\
=& \hbar\omega_r\left(a^\dagger a + \frac{1}{2}\right) + H_A\big(\Phi + p\Phi_{\mathrm{zpf}}(a + a^\dagger)\big) \\
\approx& \hbar\omega_r\left(a^\dagger a + \frac{1}{2}\right) + H_A(\Phi) + p\Phi_{\mathrm{zpf}}\frac{\mathrm{d}H_A}{\mathrm{d}\Phi}(a + a^\dagger) + (p\Phi_{\mathrm{zpf}})^2\frac{\mathrm{d}^2H_A}{\mathrm{d}\Phi^2}(a + a^\dagger)^2 + \dots \\
\approx& H_R + H_A(\Phi) + p\Phi_{\mathrm{zpf}}J_A(a + a^\dagger)
\end{aligned} \tag{3.33}$$

In the RWA and the Andreev state basis, this current operator is given by [229]

$$J_A = I_A\left(\sigma_z(\varphi) + \sqrt{1-\tau}\tan(\frac{\varphi}{2})\sigma_y(\varphi)\right) \ , \tag{3.34}$$

where $I_A$ is given by Eq. 3.9. This current operator includes off-diagonal terms that allow us to couple the ground and excited states of the Andreev spectrum. Furthermore,

since we used the RWA, it is valid for when the ABS resonance frequency $\omega_A$ and $\omega_r$, the resonator's resonance frequency, are detuned. Writing Eq. 3.33 in a more suggestive form gives

$$H = H_R + H_A(\Phi) + g_c(\varphi)(a^\dagger \sigma_- + a\sigma_+) \,, \tag{3.35}$$

where

$$g_c(\varphi) = p\Phi_{zpf}\sqrt{1-\tau}\frac{I_A}{\hbar}(\varphi)\tan(\frac{\varphi}{2}) \,, \tag{3.36}$$

with $p = \frac{l}{L_{tot}}$ Thus, we recover the phase-dependent coupling from the earlier model which used a mutual inductance. We now found that the coupling is dependent on both the zero-point fluctuations, and on the shared inductance between resonator and Andreev state hosting device. In the dispersive regime, this again leads to a frequency pull of $\chi = \frac{g_c^2}{\omega_r - \omega_{\text{ABS}}}$. We will use this to our advantage later.

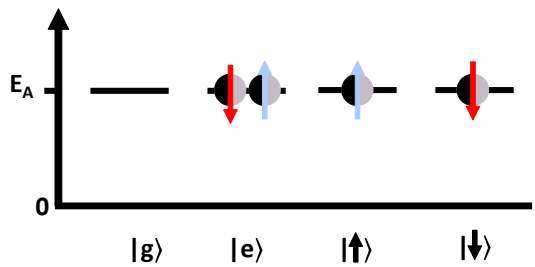


**Figure 3.4:** The four possible configurations of the ABS filling by fermionic quasiparticles. The ground and excited states (even-parity, left) have energies $2E_A$, while the odd-parity single-quasiparticle states (right) have energy $E_A$ [229].

How does this all show in the spectrum? For pair transitions, occurring between $|g\rangle$ and $|e\rangle$ where pairs of quasiparticles are created and destroyed (as shown in Figure 3.4, left-most two states), Cooper pairs are excited from the bosonic ground state and hence we observe an average of a spin-split Andreev doublet. In the short junctions regime, we neglect SOC and thus $\lambda_1 \approx \lambda_2 = \lambda$. Then, in the case of near-ballistic transport $\tau \approx 1$, close to $\varphi = \pi$, and for a single Andreev pair, the energy diagram of the two-tone spectrum becomes a renormalised version of Eq. 3.5:

$$\frac{hf_{PT}}{2} = E_A(\Delta) = \Delta_{eff}\sqrt{1-\tau\sin^2(\frac{\varphi}{2})} \tag{3.37}$$

where the effective induced gap is

$$\Delta_{eff} = \frac{\Delta_{sc}}{\sqrt{(1+\lambda)^2 + (x_r\lambda\sqrt{1-\tau})^2}} \,, \tag{3.38}$$

which is what is observed in two-tone spectra.
In single tone measurements, we use a second-order perturbative model [264, 265]. We expand the Hamiltonian of Eq. 3.30 in $\frac{\Phi_{zpf}}{\Phi_0}$ to derive the frequency shift when

coupling to a single occupied ABS level. This becomes:

$$\delta f_r = -2\left(\frac{\pi\Phi_{\text{zpf}}}{\Phi_0}\right)^2 \frac{\partial^2 f_A}{\partial\varphi^2} + \left(\frac{g_c(\varphi)}{2\pi}\right)^2 \left(\frac{2}{f_A} - \frac{1}{f_A - f_r} - \frac{1}{f_A + f_r}\right), \tag{3.39}$$

with again the phase-dependent coupling rate alike to Eq. 3.36:

$$\frac{g_c(\varphi)}{2\pi} = \frac{p\Phi_{zpf}}{\Phi_0}\sqrt{(1-\tau)}\left(-\frac{\partial f_A}{\partial\varphi}\right)\tan(\varphi/2), \tag{3.40}$$

where the pair transition frequency is expressed through its energy as $f_A(\varphi) = \frac{2E_A(\varphi)}{h}$. This model is generally only applicable to single-channel ABS and neglects all the possible higher energy states, including the continuum of states above the superconducting gap, which is known to contribute to the inductive response of a finite-length weak link [266, 267]. We also neglected the inductive energy of the shared inductance, which is generally true only when the supercurrent in the weak link is sufficiently small; however, as this is a second-order perturbation, the model still holds even in our case of high-coupling regimes. To avoid fitting divergences, we usually multiply the data by $f_A - f_r$. We found that this model still adequately describes the data.

Additionally, as shown in Fig. 3.3b, theoretically we can also excite single quasiparticle transitions, either spin-conserving or spin-flipping; both are shown as the right-most two states in Figure 3.4. Then, again in second-order perturbation theory [32, 268], the dispersive shift due to the state of the quasiparticle becomes

$$\chi_{\text{SQPT}} = \delta f_r^{\text{SQPT}} \approx \left(\frac{g_c}{2\pi}\right)^2 \frac{2f_{SQPT}}{f_{SQPT}^2 - f_r^2}, \tag{3.41}$$

where the coupling rate is spin-dependent. There are no off-diagonal spin-mixing terms in the Hamiltonian governing the system, and hence in first order, only the spin-conserving transitions contribute to the dispersive shift [32].

## 3.4 A brief word on ultra-strong coupling

In cQED, the interaction strength is characterised by a dimensionless normalised coupling

$$\eta \equiv \frac{g_c}{\omega_{\text{ref}}}, \tag{3.42}$$

here $\omega_{\text{ref}}$ is a relevant bare frequency scale (typically $\omega_r$ for the resonator mode or $\omega_q$ for the qubit transition). For general qubit-state measurements, $\eta$ is small; in the ultra-strong coupling (USC) regime, this is no longer true: the interaction energy is a comparable fraction of the bare transition frequencies, and perturbative or rotating-wave treatments become unreliable.

In standard strong coupling, as often used in superconducting qubit measurements, a two-level system and a single resonator mode is modelled with the dispersive Jaynes–Cummings Hamiltonian as shown in Eq. 3.24, obtained by discarding counter-rotating terms; the RWA. In USC, that step fails because the counter-rotating terms oscillate at frequencies that are no longer large compared to $g_c$ [269]. A system is generally said to enter the ultrastrong coupling regime when $g_c/\omega_r > 0.1$ [270]. For even higher coupling, the system enters a deep-strong coupling (DSC) regime; a

summary of these regimes is given in Table 3.2. A minimal model to still describe the experiments is the quantum Rabi Hamiltonian [271]

$$\hat{H}_{\text{Rabi}} = \hbar\omega_r a^\dagger a + \frac{\hbar\omega_q}{2}\sigma_z + \hbar g_c(a + a^\dagger)(\sigma_+ + \sigma_-), \tag{3.43}$$

whose defining features in the USC regime are [272, 273]:

(i) The breakdown of excitation-number conservation due to counter-rotating terms, with only parity remaining a symmetry.

(ii) The ground state can contain *virtual* photons, entangled light-matter excitations.

(iii) Non-perturbative renormalisation of the spectrum and observables occurs: the system must be described by hybrid modes (i.e. the spectrum is reshaped and becomes non-linear with parameter tuning)

These qualitative changes are the experimental hallmarks of USC. While in our experiments we nearly reached this regime, modifications to the above theory of Section 3.3 were not necessary to adequately capture the data.

| **Regime** | **Ratio** $g_c/\omega_{\text{ref}}$ | **Ground State** |
|---|---|---|
| Weak | $\ll 0.01$ | Vacuum |
| Strong | $0.01 - 0.1$ | Vacuum |
| Ultrastrong | $0.1 - 1.0$ | Entangled |
| Deep strong | $> 1.0$ | Degenerate / hybrid |

**TABLE 3.2:** CLASSIFICATION OF LIGHT-MATTER COUPLING REGIMES IN TERMS OF THE NORMALISED COUPLING STRENGTH $g_c/\omega_{\text{ref}}$.

The question becomes now: why do we want to achieve the USC regime? Besides the interesting new physics, it provides several advantages for quantum technologies [38]. Simply said, it enables more efficient interactions [273]:

- Ultrafast quantum gates: the speed of operations in cQED is fundamentally limited by the coupling strength. In the USC regime, it becomes possible to perform quantum gates on sub-nanosecond timescales, potentially faster than the decoherence processes inherent to solid-state systems [274]

- Hardware protection: systems in the USC and DSC regimes can be used to engineer Hamiltonians that are intrinsically protected against noise. For example, it has been shown that in a system of multiple coupled qubits, the coherence times decreases with increasing coupling [275]. Furthermore, protected quantum memories are theoretically proposed in the USC regime [276, 277].

- Deterministic non-linear optics: in the ultrastrong-coupling regime, the breakdown of excitation-number conservation in the quantum Rabi model enables higher-order, non-perturbative processes to occur deterministically [269]. This allows, for example, multi-particle transitions such as the excitation of two atoms by a single photon or the generation of photon pairs from a single qubit transition with appreciable efficiency [278].

- Quantum metrology: virtual excitations in the USC regime can be used as a resource for sensing. By leveraging the renormalised frequency shifts of the hybridised light-matter modes, sensors achieve higher precision, surpassing the standard quantum limit [279].

## 3.5 Results of the experiment

### 3.5.1 Sample fabrication and set-up

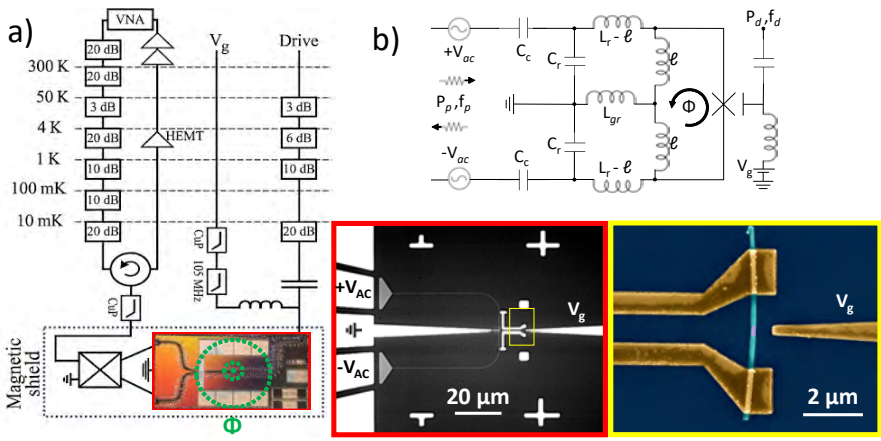


**Figure 3.5:** Experimental set-up of the dilution refrigerator and device architecture for the Andreev bound state spectrum measurements. **a**) Experimental set-up, similar to Figure 2.15. The gate and drive lines are connected via a bias-Tee. A coil on top of the copper box containing the sample PCB generates an external flux Φ (green circle). **Red box:** Scanning electron microscopy (SEM) picture of the used resonators, illustrating the compact footprint of the resonator structure. The resonator itself consists of a U-shaped structure patterned from a thin NbTiN film with high kinetic inductance (grey). It is capacitively coupled to a pair of feedlines made of thick NbTiN, where a voltage $\pm V_{ac}$ is applied due to the 180 °hybrid coupler. A weak link in an InAs-Al nanowire is defined close to the mirror line of the device and coupled to the resonator by *ex-situ* evaporated Al contacts. **Yellow box:** False-coloured SEM picture of the nanowire and gate. Gold colour is *ex-situ* evaporated Al, cyan is epitaxially MBE-sputtered Al, and magenta where the nanowire is etched and the weak link is defined. Dark blue is the sapphire substrate. **b**) Circuit design of the CPS resonator coupled to a weak link, driven differentially with pump-tone $(P_p, f_p)$ and drive tone $(P_d, f_d)$.

We now describe the devices investigated in our work. The nanowires are grown at the centre for Quantum devices at the University of Copenhagen [242] by T. Kanne and lead by J. Nygård. After arrival in our lab, they are picked up using a nanomanipulator, and deposited on the chip where they are embedded in a superconducting loop with a high-impedance lumped-element resonator, in the style of the resonators of Section 2.4 and as shown in Figure 3.5. Three devices were successfully fabricated and measured, where the resonator geometry and the weak link length vary. Their parameters are listed in Table 3.3. The resonator itself is patterned on a sapphire substrate with a thin (around 6 nm) sputtered film of a highly disordered NbTiN superconductor used cold sputtering, as detailed in Section 2.2. The use of highly disordered NbTiN maximises the kinetic inductance and thereby enhances both the resonator impedance and the zero-point flux fluctuations. However, it comes at the cost of device reproducibility and fabrication success. Figure 3.5, red box, shows a scanning electron micrograph of the

| Device | $l$ ($\mu$m) | $w$ (nm) | $Z_{r,\mathrm{diff}}$ (k$\Omega$) | $L_{k,\square}$ (pH) | $f_r$ (GHz) | $\Phi_{\mathrm{zpf}}$ ($10^{-3}\Phi_0$) | $l_{\mathrm{wl}}$ (nm) |
|---|---|---|---|---|---|---|---|
| 1 | 48.3 | 130 | 12.28 | 320 | 8.223 | 16 | 250 |
| 2 | 38.3 | 130 | 12.76 | 400 | 8.619 | 21 | 320 |
| 3 | 53.3 | 130 | 13.27 | 345 | 7.469 | 15 | 450 |

**TABLE 3.3:** DEVICE PARAMETERS: RESONATOR ARM LENGTH $l$ (LENGTH OF ONE ARM OF THE DIFFERENTIALLY DRIVEN CPS RESONATOR), CONDUCTOR WIDTH $w$, DIFFERENTIAL IMPEDANCE $Z_{r,\mathrm{diff}}$, SHEET KINETIC INDUCTANCE $L_{k,\square}$ (MAY VARY SLIGHTLY DUE TO AGEING AND FABRICATION VARIATIONS), BARE RESONANT FREQUENCY $f_r$, GEOMETRICALLY ESTIMATED ZERO-POINT FLUX FLUCTUATIONS $\Phi_{\mathrm{zpf}}$ ACROSS THE WEAK LINK DUE TO THE SHARED INDUCTANCE, AND WEAK-LINK LENGTH $l_{\mathrm{wl}}$.

resonator of Device 2. The circuit is a compact differential lumped-element resonator comprising two symmetric NbTiN arms (width 130 nm, length 38.3 $\mu$m) separated by a grounded strip. Each arm terminates in a triangular capacitor plate that couples capacitively to a 50 $\Omega$ feedline. The differential geometry supports two resonant modes. In the odd mode (differential excitation) the currents in the two arms flow with opposite phase, producing a finite current through the shared inductive section and thereby enabling coupling to the weak link. The current density is maximised in the shared inductance. In the even mode (common excitation) the arm currents are in phase and largely cancel through the shared inductance, rendering this mode comparatively insensitive to the state of the weak link. Both modes are still routinely observed experimentally. The even mode appears several hundred MHz below the odd mode and produces a nearly gate-independent feature around 8.1 GHz for device 2. Simulations in Sonnet confirm that the common mode frequency is affected, as per design, by the increased effective inductance associated with the grounding strip, $2\pi f_r^{\mathrm{even}} = \frac{1}{\sqrt{\left(L_r+2L_{\mathrm{gr}}\right)C_r}}$ where $L_{\mathrm{gr}} \approx 10$ nH is the inductance of the central grounding connection. The occurrence of the even mode is thus a design aspect that can easily be mitigated in future devices by changing the length of the ground line.

To characterise the ultra-thin, high-kinetic inductance NbTiN film, we performed dc transport measurements on a test resonator structure, obtaining a normal-state sheet resistance $R_{N,\square} = 1.46$ k$\Omega$ and a critical temperature $T_c \simeq 6$ K following the procedure described in Sec. 2.2. We use the standard dirty-limit estimate for the sheet kinetic inductance, Eq. 2.10. This gives an estimated $L_{k,\square}^{\mathrm{dc}} \approx 320$ pH/$\square$, consistent with the order of magnitude required to reproduce the measured microwave response. For the actual devices, we additionally performed microwave-domain simulations using the as-fabricated geometries. To emulate the *bare* resonator response we replaced the nanowire weak link by a short interruption of the NbTiN film, while retaining all aluminium structures, which contribute appreciably to the total stray capacitance. We then extracted $L_{k,\square}$ by fitting the simulated response to the experimental spectra at low $V_g$, where the nanowires are fully depleted and effectively decoupled from the resonator. Since all resonators were patterned from the same NbTiN batch and thickness, we attribute the device-to-device variations in $L_{k,\square}$ mainly to ageing, non-uniform NbTiN growth at these thicknesses and small differences in processing conditions during nanowire integration (e.g. resist bake temperature), which were empirically found to affect the inferred kinetic inductance. Generally, only high-temperature annealing (partially) resolves this issue, but is not a viable option with nanowires present.

Owing to the large sheet kinetic inductance of the ultra-thin NbTiN film ($L_{k,\square} \approx$ 400 pH), the structure realises a large total inductance despite its small footprint ($50 \times 50\ \mu\text{m}^2$), and therefore operates as a lumped-element resonator. We denote the inductance and capacitance of the *differential* (odd) mode by $L_r$ and $C_r$, respectively. The corresponding differential impedance is then $Z_{r,\text{diff}} \equiv 2\sqrt{\frac{L_r}{C_r}}$, and using $f_r = \left(2\pi\sqrt{L_r C_r}\right)^{-1}$ one may equivalently write

$$Z_{r,\text{diff}} = 4\pi f_r L_r. \tag{3.44}$$

For Device 2, microwave simulations yield $L_r \approx 118$ nH per arm and $Z_{r,\text{diff}} \approx 12.76\ \text{k}\Omega$, and the odd-mode resonance is measured at $f_r = 8.619$ GHz.

The resonators themselves are fitted using the algorithm described in Section 2.3.4, which yields the internal quality factor $Q_i \approx 3800$ and the coupling quality factor $Q_c \approx 1000$ when the ABSs are far detuned. In this set-up, the large coupling magnitude results in a significant magnetic flux dependence of the internal quality factor when the Andreev level energy approaches the bare resonator frequency. At $\varphi = \pi$ the nanowire introduces maximum losses to the system, and $Q_i$ usually drops to around 1000. As shown in Figure 3.5b, for the single tone spectra resonators are excited using a probe tone at frequency $f_r$ with power $P_p$. Then, the phase is biased using the external coil-current $I$ that leads to a changing magnetic flux $\Phi$. As the nanowire junction behaves as a rf-SQUID, this leads to a change in phase $\varphi$ over the junction. The relation between current and phase is done by realising that the phase is $2\pi-$periodic, as shown in Appendix A.

### 3.5.2 Initial considerations

The weak link is defined in a 150 nm-diameter MBE-grown InAs nanowire with an *in situ* epitaxial aluminium shell covering three facets. A segment of the 27 nm thick Al shell is removed by wet etching, defining a bare InAs section of length $l_{\text{wl}} \approx$ 250-450 nm depending on device, as illustrated in Fig. 3.5, yellow box. With the Al coherence length in similar wires being $\sim 150$ nm [280,281], this puts us in the regime where $\lambda \approx 1$, so neither definite short nor long junction regime. Wet etching is known to introduce surface roughness and potential disorder in the nanowire surface [282]. While shadow-evaporated alternatives were available, we did not obtain sufficiently strong dc or microwave gate response in those samples to justify their use here.
Coupling between the resonator and the nanowire is achieved by embedding the weak link in a superconducting loop formed by thin Al contacts, such that the resonator shares an inductance $2\ell$ with the loop, in our case, $2\ell \approx 12.3$ nH, obtained from the microwave simulations. This design couples selectively to the odd mode: as mentioned, in the even mode the currents through the shared inductance cancel, suppressing flux modulation of the junction phase. In this geometry, the coupling strength is set by the zero-point flux fluctuations across the shared inductance,

$$\Phi_{\text{zpf}} = \frac{\ell}{L_r}\sqrt{\frac{\hbar Z_{r,\text{diff}}}{2}} \approx 0.021\,\Phi_0\ . \tag{3.45}$$

The shared inductance was designed to be large, yet comparable to the weak-link Josephson inductance, ensuring that the junction phase $\varphi$ remains a single-valued

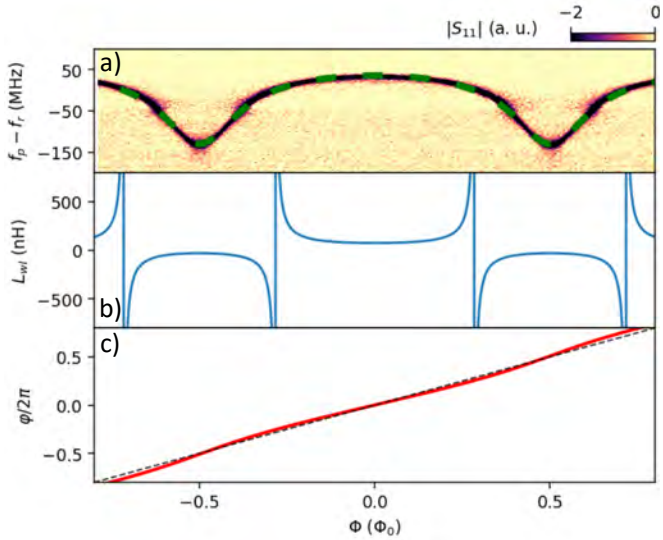


**Figure 3.6: a**) Single-tone spectrum measured of Device 3 at $V_g = 1.5034$ V offset to the bare resonator frequency $f_r = 7.4685$ GHz. The frequency shift fit as a function of applied flux is denoted by the green dashed line. **b**) Corresponding weak link inductance, derived from the combination of Equations 3.47 and 3.48. **c**) The red line represents the phase across the weak link $\varphi$ as a function of the applied flux $\Phi$. For comparison, the black dashed line is plotted in the absence of self-screening, $2\ell = 0$.

(non-hysteretic) function of the applied flux $\Phi$. In practice, we find that $\varphi \approx 2\pi\Phi/\Phi_0$ is a good approximation for our device parameters. In our devices, the loop inductance comprises the highly inductive NbTiN film with a total inductance of $2l \approx 10$ nH. When external flux is applied, part of the phase drops across the loop inductance, causing the self-screening effect [283]:

$$\varphi = \frac{2\pi}{\Phi_0}(\Phi - 2\,l\,I_{screen}) \,, \tag{3.46}$$

where the supercurrent through the weak link is given by the Andreev current of Eq. 3.9, summing over all present ABS with different transmissions; we generally used a single-channel as it adequately captured the data. It is then possible to estimate the self-screening effect in the dispersive regime. Considering the circuit diagram shown in Figure 3.5b, classically, we approximately obtain the resonator frequency shift $\delta f_r$ that arises from shunting the $2\ell$ part of the resonator inductance with the phase-dependent Josephson inductance $L_{wl}(\varphi)$, assuming bare resonance frequency $f_r$:

$$\begin{aligned} f_r(L+\delta L) &= f_r(L) + \delta f \\ &\approx f_r(L) + \frac{\partial f_r(L)}{\partial L}\delta L \\ &= f_r(L) - \frac{2f_r(L)}{2L}\delta L \\ \Rightarrow \frac{\delta f}{f_r} &= -\frac{\delta L}{2L} \end{aligned} \tag{3.47}$$

and where $L$ is the total resonator inductance, twice the inductance of one branch $L_r$. Furthermore, the effective change in the total inductance due to the weak link is

$$\delta L = 2L_r - 2l + \frac{2\ell L_{wl}}{2\ell + L_{wl}} - 2L_r = -\frac{(2\ell)^2}{2\ell + L_{wl}} \,. \tag{3.48}$$

Thus, the weak link inductance is directly retrieved from the single-tone spectra in dispersive regime. The total supercurrent is related to the weak link inductance as [284]:

$$L_{wl}(\varphi)^{-1} = \frac{2\pi}{\Phi_0}\frac{\partial I_{screen}}{\partial \varphi}. \tag{3.49}$$

We analyse the self-screening effect, using the single-tone spectroscopy data obtained for Device 3 at $V_g = 1.5034$ V, as shown in Fig. 3.6a. In this regime, no avoided crossing is observed, but the resonator shift is reasonably large (about 150 MHz), consistent with the presence of one or a small number of ABS channels with intermediate transmission in the weak link, resulting in a relatively large supercurrent. The frequency shift fit is obtained by introducing one channel with $\Delta'/h = 17$ GHz, $\tau = 0.68$, $\Phi_{zpf} = 0.025\Phi_0$. Using Eq. 3.47 and Eq. 3.48, we extract $L_{wl}$ as a function of the applied flux, see Figure 3.6b. Further, under the assumption of negligible self-screening $\varphi \approx 2\pi\Phi/\Phi_0$, the supercurrent is calculated by numerically integrating Equation 3.49. In turn, it is plugged into Eq. 3.46 to estimate the full effect of self-screening. Fig. 3.6c shows that $\varphi \approx 2\pi\Phi/\Phi_0$ is indeed a reasonable approximation, and self-screening can be neglected in first order over a large range of fluxes.

Another essential element for the working of the Andreev state measurements is the gate-tunability of the ABS. The change in the absolute value of the resonator reflection $\delta|S_{11}|$ as a function of the probe frequency $f_p$ and side-gate voltage $V_g$ is shown in Figure 3.7, where the gate-independent background is subtracted using featureless concatenated data. For example, in Fig. 3.7a, it is a concatenation of the data at $-2$ V for $f_p > 8.7$ GHz and at 8 V for $f_p < 8.7$ GHz. The difference between the left and right sub-panels is the phase: in **a, c, e**, the phase across the weak link $\varphi$ is fixed at zero, while for **b,d,f**, it is $\varphi = \pi$. The junction is fully pinched off below $V_g \approx 1 - -4$ V, depending on device, where the resonance approaches the bare resonator frequency. The data obtained at $\varphi = \pi$ in sub-panels **b,d,f** demonstrates multiple avoided crossings, signifying that the ABSs are strongly coupled to the resonator mode.

### 3.5.3 Pair transition spectroscopy

A pair transition corresponds to exciting a Cooper pair from the condensate into the ABS doublet, which in the simplest case shifts two quasiparticles from the ground state to the lowest excited state of each ABS branch. In contrast, a single-particle transition requires a quasiparticle already present, exciting it to the higher ABS level (spin-conserving or spin-flipping). Pair transitions preserve the overall fermion parity and hence only occurs from the even ground state, whereas single-quasiparticle transitions occur from the odd state. In practice, pair transitions produce a parabolic dispersion $f_{PT}(\varphi)$ with minimum at $\varphi = \pi$, while single transitions appear at different energies and flux dependence (often observed as two or four lines due to spin splitting, depending on $\varphi$). In this Section, we describe the signatures of Cooper-pair-like transitions

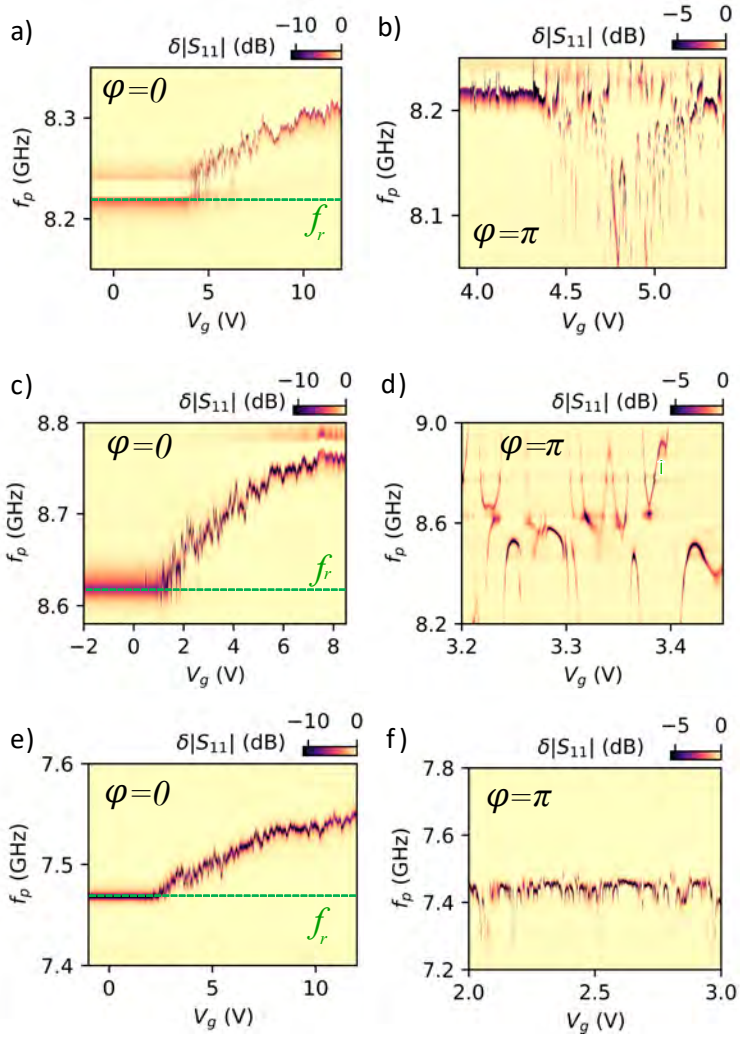


**Figure 3.7:** Change in the absolute value of the resonator reflection, $\delta|S_{11}|$, as a function of probe frequency $f_p$ and gate voltage $V_g$ for Device 1 (a,b), Device 2 (c,d), and Device 3 (e,f). The left column shows measurements at $\varphi = 0$, while the right column shows measurements at $\varphi = \pi$, where the coupling between the resonator and the ABS is maximal. A gate-independent background was subtracted as described in the main text. The respective bare resonance frequencies, extracted from the fully pinched-off nanowire, are **a**) $f_r = 8.223$ GHz; **c**) $f_r = 8.619$ GHz; **e**) $f_r = 7.470$ GHz. Additionally, **d**) shows the corresponding spectrum for Device 2 at $\varphi = \pi$; the green arrow marks an extremum at $V_g = 3.39$ V.

between ABSs. Two-tone microwave spectroscopy reveals avoided level crossings between the pair-transition line and the resonator mode, indicating ultra-strong coupling to a nearly ballistic ABS channel, with $g_c/2\pi$ up to $\sim$2 GHz. Fitting the flux dispersion of these transitions to the short-junction formula yields transmissions $\tau$ of order unity (e.g. $\tau \approx 0.96$–$0.999$), confirming the presence of highly-transmissive channels.

We performed spectroscopy to characterise the devices. To mitigate charge noise and

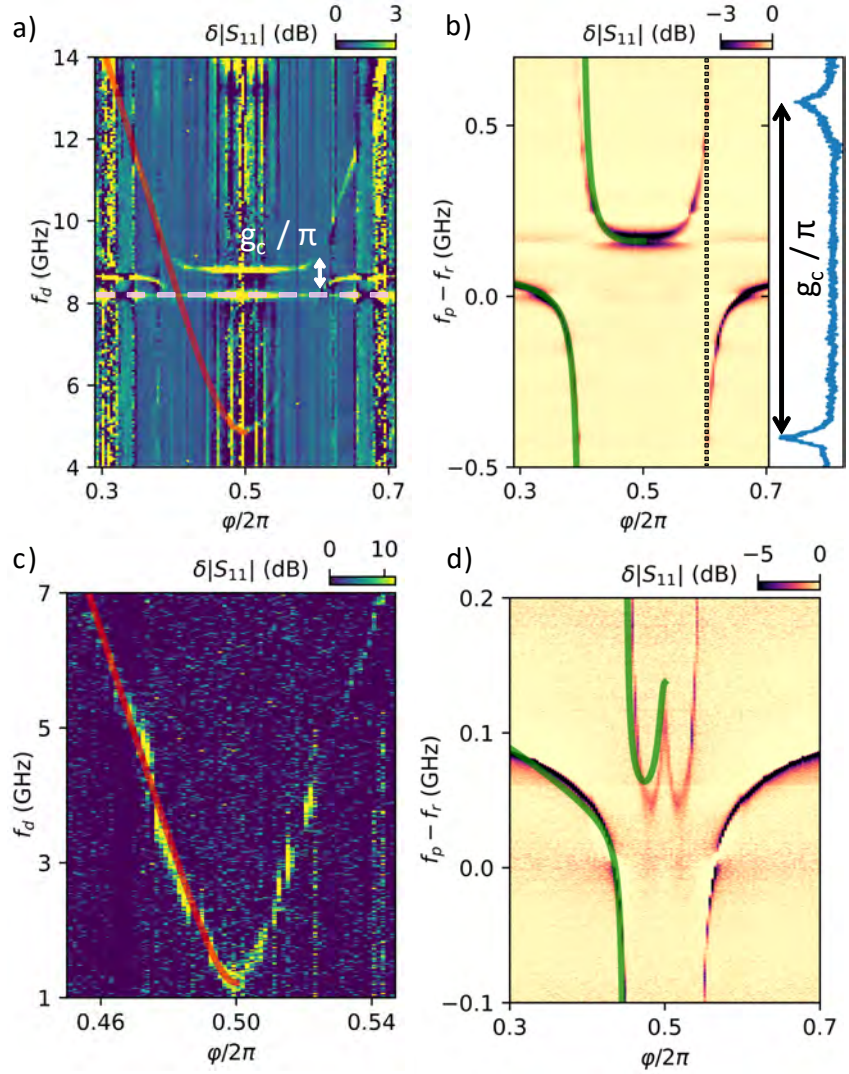


**Figure 3.8:** Spectra measured in Devices 2 (**a,b**) at $V_g = 3.39$ V, and Device 1 (**c,d**) at $V_g = 14.5$ V.
**a**) The fit of the PT frequency as a function of phase is shown by the red line in the two-tone spectrum. The spectrum reveals avoided crossings at $\varphi/2\pi = 0.4$ and $\varphi/2\pi = 0.6$ with the coupling at the crossings $g_c/2\pi \approx 490$ MHz, denoted by the white arrow. A flat line seen at around 8.1 GHz, in dashed pink, corresponds to the resonator's even mode, which is insensitive to the state of the weak link.
**b**) Corresponding single-tone spectrum. The probe frequency $f_p$ is offset to the bare resonator frequency at zero flux $f_r = 8.619$ GHz. The green line represents the fit of the resonator shift. The line-cut on the right side confirms $g_c/2\pi \approx 490$ MHz at the avoided crossing (along the grey dotted line).
**c**) The PT frequency fit plotted as a function of phase is denoted by the red line in the two-tone spectrum.
**d**) Corresponding single-tone spectrum. The probe frequency $f_p$ is offset to the bare resonator frequency $f_r = 8.223$ GHz. The green line denotes the fit of the resonator shift.

electrostatic resonance drift, we fix the gate voltage $V_g$ at one of the points where the resonator gate response has a local extremum, such as one of those observed in Fig. 3.7b, green arrow. Single-tone spectra are taken by sweeping the probe frequency $f_p$ of power $P_p$ and measuring complex parameters $S_{11}$ at various applied fluxes. To

identify pair versus single-quasiparticle transitions, we also employ two-tone spectroscopy: for each point, we first perform a single-tone frequency sweep to define the resonance position at a certain phase (flux). Then, a continuous wave probe tone was fixed at this frequency and $S_{11}$ was measured as a function of the drive tone with frequency $f_d$ and power $P_d$. To reference the signal measured in two-tone spectra, we subtracted a drive frequency-independent background.

Figure 3.8a and b shows the spectroscopy data of Device 2. Data were acquired at $V_g = 3.39$ V and at the nominal powers $P_p \approx -130$ dBm and $P_d \approx -100$ dBm, which is close to $\langle n \rangle \approx 1$. The left panel illustrates the two-tone spectrum, which reveals a PT arising from a highly transmissive ABS. It crosses the odd mode of the resonator, forming a pair of avoided crossings at $\varphi/2\pi = 0.4$ and $\varphi/2\pi = 0.6$, where the coupling is directly extracted from the level splitting on resonance $g_c/2\pi \approx 490$ MHz. We also observe the even mode at $f \approx 8.1 GHz$, indicated as a dashed pink line. Additional microwave simulations point towards the shared ground line as the culprit. We also note that this mode does not interact with the ABS, as expected. In the vicinity of $\varphi = \pi$, the PT frequency is fitted to the dispersion relation valid for a short weak link, Eq. 3.37, where we use the induced gap parameter, as the effective gap value in a finite-length weak link is smaller than the gap in the epitaxial Al $\Delta' < \Delta_{Al}$. A least-squares fitting yields $\Delta'/h = 11.69 \pm 0.03$ GHz and $\tau = 0.9569 \pm 0.0005$. The resulting fit is represented as a red line in the figure. Phase-independent features are from the microwave background and do not constitute actual physics; they are a measurement artefact.

Fig. 3.8b shows the corresponding single-tone spectrum (where we remind that it was taking ahead of the two-tone spectrum). The coupling at the avoided crossings $g_c/2\pi \approx 490$ MHz is extracted from the line-cut along the grey dotted line, shown on the right side of the plot. The green line denotes the fit that was obtained from the model described of Equation 3.39. The fit relies on a single ABS observed in the two-tone spectrum in sub-figure a. To confirm this, we checked over a wide frequency range, and no higher-energy states are observed up to $f_d = 21$ GHz, shown in Appendix A. In the fit, the zero-point flux fluctuations across the shared inductance is the only fitting parameter. A least-squares fit to the experimental data yields $\Phi_{zpf} = (0.0282 \pm 0.0002)\Phi_0$, which slightly overshoots the value obtained from the geometrical analysis of Table 3.3. To validate the fit, we extract the magnitude of the coupling at the avoided crossings $g_c/2\pi = 495 \pm 4$ MHz, which is in good agreement with the observed energy splitting. The maximum coupling is extracted at $\varphi = \pi$: $g_c/2\pi = 968 \pm 7$ MHz.

Fig. 3.8c,d provides the spectroscopy data, obtained for Device 1 with the shortest 250 nm weak link at $P_p \approx -130$ dBm and $P_d \approx -100$ dBm, and at $V_g = 14.5$ V. Here, the gate voltage is higher due to the increased distance between weak link and gate electrode. We follow the same fitting routine. The two-tone spectrum in Fig. 3.8c is fitted by Eq. (3.37) describing a PT arising from a single high-transmission channel. The best fit reveals $\tau = 0.99942 \pm 0.00006$ and $\Delta'/h = 25.2 \pm 0.2$ GHz. The occurrence of ABS with a very large transmission in single-tone spectroscopy in Fig. 3.8d is a sharp peak at $\varphi = \pi$ [264]. This feature is described with the model of Eq. 3.40, where $\Phi_{zpf} = (0.0247 \pm 0.0002)\Phi_0$ is now the only remaining fitting parameter, and we extract the maximum coupling $g_c/2\pi = 1.95 \pm 0.02$ GHz at $\varphi = \pi$. We note that

the extracted coupling indicates that the system could be beyond the applicability of the perturbative approach. This explains a noticeable fit deviation. At this level of consideration, the extracted coupling should be perceived as an approximate value, accurate to order of magnitude.

In our analysis, we made certain assumptions. We have employed the single-channel short-junction formula (Eq. 3.37), but if residual quasiparticles are present, or if multiple channels contribute, the spectroscopy becomes more complex. The extracted couplings are taken from level splittings; beyond the perturbative regime the standard equations used may underestimate the true coupling: it would require a non-perturbative, full treatment, which is unavailable theoretically as of writing this thesis. In addition, charge noise or photon population induces line broadening, which we mitigate by low drive power. Alternative interpretations (e.g. multiple low-transmission modes) are unlikely given the quantitative fits to a single-channel model, but cannot be ruled out entirely.

### 3.5.4 Single-quasiparticle transition spectroscopy

Single quasiparticle transitions (SQPTs) associated with spin-orbit split ABSs were observed for Devices 2 and 3 with longer weak links. Fig. 3.9a,d provides the spectroscopy data obtained for Device 3 at $V_g = 1.498$ V and for Device 2 at $V_g = 2.44$ V around the degeneracy points $\varphi = 0$ and $\varphi = \pi$, respectively. Panels **a** and **b** illustrate two-tone spectroscopy data that reveal bundles of 4 lines, which we assign to spin-conserving SQPTs, as schematically indicated in Fig.3.3b. The spectroscopic lines in Fig. 3.9a are fitted with the transitions between the two lowest Andreev doublets ($1\uparrow \Rightarrow 2\uparrow$ and $1\downarrow \Rightarrow 2\downarrow$). Parameters which provide the best fit were obtained by the least-squares method applied to transitions between the ABSs given by Equation (3.20). These parameters are listed in Table 3.4, column A. The fit is shown by the red dotted line.

**TABLE 3.4:** FIT PARAMETERS FOR THE SUPERCONDUCTING QUANTUM PHASE TRANSITION (SQPT) FITS SHOWN IN FIG. 3.9(A,B). THE SUPERCONDUCTING GAP WAS FIXED TO $\Delta_{\mathrm{Al}}/h = 52$ GHz. UNCERTAINTIES DENOTE ONE STANDARD DEVIATION FROM THE FIT.

| Parameter | A | B | C |
|---|---|---|---|
| $\lambda_1$ | $5.7 \pm 0.3$ | $2.44 \pm 0.07$ | $2.8 \pm 0.1$ |
| $\lambda_2$ | $1.5 \pm 0.3$ | $3.06 \pm 0.09$ | $3.2 \pm 0.1$ |
| $\tau$ | $0.35 \pm 0.04$ | $0.243 \pm 0.009$ | $0.265 \pm 0.006$ |
| $x_0$ | $0.489 \pm 0.005$ | $0.2615 \pm 0.0001$ | $-8.4 \times 10^{-4} \approx 0$ |

In Fig. 3.9b, for Device 2, two bundles of lines are observed. Each of those take place at relatively large frequencies above 19 GHz and have an upward curved shape, implying that the transitions occur between the upper doublets ($2\uparrow \Rightarrow 3\uparrow$ and $2\downarrow \Rightarrow 3\downarrow$). The parameters provided by the least-squares method are again listed in Table 3.4, where respectively B corresponds to the lower, red dotted line, and C to the upper, orange line. The coupling between the resonator and a spinful ABS is estimated from the line shape of a SQPT. Fig. 3.9e shows the phase of the reflected signal as a function of the drive frequency at a minimum of the lower SQPT, marked in Fig. 3.9 by a

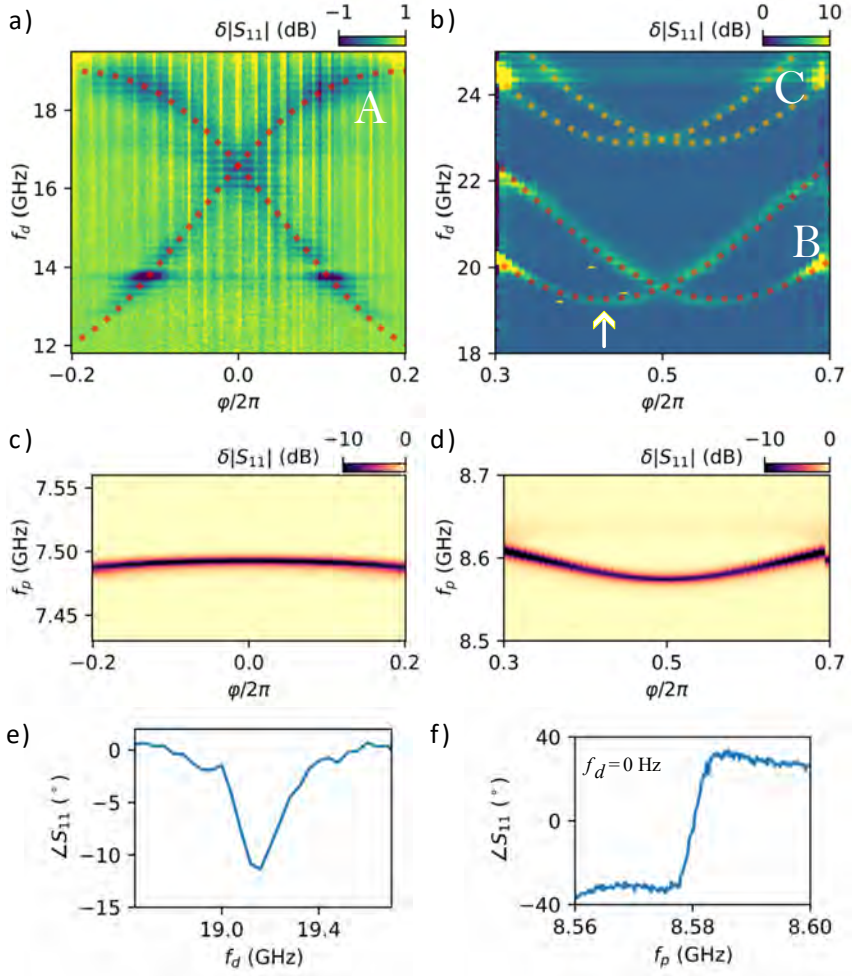


**Figure 3.9:** Single-quasiparticle transition (SQPT) spectroscopy measurements of Devices 2 and 3. Two-tone spectra acquired for Device 3 at $V_g = 1.498$ V (**a**, **c**) and for Device 2 at $V_g = 2.44$ V (**b**, **d**). In the two-tone measurements (**a**, **b**), distinct bundles of SQPTs are observed, exhibiting crossings at the degeneracy points. The extracted SQPT frequencies are indicated by the dotted lines and labelled A, B, and C; the corresponding fit parameters are summarised in Table 3.4. Panels (**c**, **d**) show the associated single-tone spectra recorded under identical gate conditions. Panel (**e**) displays the phase of the reflected signal as a function of drive frequency measured at the minimum of the lower SQPT (white arrow in **b**), highlighting the dispersive response. Panel (**f**) shows the bare resonator response in the absence of two-tone excitation.

white arrow. The phase shift induced by this transition is $\delta(\angle S_{11}) \approx 10°$. Based on the corresponding resonance line shape of a non-excited system (Fig. 3.9f), we convert

the phase shift to the resonator frequency shift $\delta f_r^{SQPT} \approx 770$ kHz from Eq. 2.13:

$$\Theta(f+\delta f) = \Theta(f) + \delta\Theta \tag{3.50}$$

$$\approx \Theta(f) + \frac{\partial\Theta(f)}{\partial f}\delta f_r^{SQPT} \tag{3.51}$$

$$= \Theta(f) - \frac{4Q_l(\varphi)}{f_r\left[4Q_l^2(\varphi)\left(1-\frac{f}{f_r}\right)^2+1\right]}\delta f_r^{SQPT}\ . \tag{3.52}$$

From here, we extract the coupling rate by Eq. 3.41 to a second-order approximation [32]. In turn, we extract the spin-photon coupling $g_c/2\pi \approx 77$ MHz. This value is comparable to the recently reported strong coupling between a high-impedance resonator and a singlet-triplet spin qubit [285] and to the previously reported spin-photon coupling in InAs nanowire weak links [32]. We note that a more rigorous assessment of the coupling requires measurements of parity-switching dynamics in the system, which was not done here. If the non-equilibrium quasiparticles poisoning is weak, the system resides in an odd-parity state [37, 264, 267, 286] for only a small fraction of time, during which a SQPT can be excited. This can reduce the signal obtained in the spectroscopy of spin-orbit split ABSs.

In our experiment, we repeatedly observed that only spin-conserving SQPTs are clearly visible in the spectra. This is in agreement with the general selection rules: in the presence of transverse symmetry in the nanowire, spin-flipping transitions should be suppressed. However, previous studies showed that spin-flipping transitions can still be excited at elevated drive powers in a realistic non-ideal device [32, 32]. For example, the gate drive violates transverse symmetry and unlock spin-flipping transitions [257, 264, 287]. Although we used the gate drive in our set-up, we did not observe spin-flipping SQPTs. This is most likely because we had to operate at sufficiently low drive powers, so that the thin film resonator is not driven into a non-linear regime.

**Summary**

In conclusion, this Chapter demonstrated the spectroscopy of Andreev bound states inductively coupled to high-impedance, differentially driven CPS resonators. Devices with $Z_{r,\mathrm{diff}} \approx 12.76\ \mathrm{k}\Omega$ and $f_r \approx 7.5$–$8.6$ GHz yield large zero-point flux fluctuations, $\Phi_{\mathrm{zpf}} \approx (0.015\text{–}0.03)\Phi_0$, enabling strong coupling to nanowire weak links of length 250–450 nm. The resonators exhibit internal quality factors $Q_i \approx 3800$ off-resonance, decreasing to $\sim 1000$ near $\varphi = \pi$ due to hybridisation-induced dissipation.
Gate control enables full pinch-off and the emergence of pronounced avoided crossings, providing evidence of photon-ABS strong coupling. Two-tone spectroscopy identifies pair transitions with fitted parameters $\Delta'/h \sim 10$–$25$ GHz and $\tau \sim 0.95$–$0.999$, indicating near-ballistic transport in the shortest junctions. Furthermore, extracted pair transition coupling strengths reach $g_c/2\pi \approx 2$ GHz, placing the system at the onset of the ultrastrong-coupling regime. In this limit, deviations from perturbative behaviour are observed as a misalignment between the RWA-based model and the data. Single-tone measurements show flux-dependent coupling rates up to 500 MHz, and are consistent with a small number of ABS channels with intermediate to high transmission. Finally, single-quasiparticle transitions are observed with a spin-photon

coupling $g_c/2\pi \approx 77$ MHz. These results establish high-impedance CPS resonators as a scalable platform for achieving strong to ultrastrong inductive coupling to ABS, with direct relevance for hybrid quantum circuits and Andreev-based qubit architectures.

# Chapter 4

# Towards hybrid superconductor-magnetic quantum systems

*"It is a capital mistake to theorise before one has data. Insensibly one begins to twist facts to suit theories, instead of theories to suit facts."*
— Arthur Conan Doyle, *A scandal in Bohemia*

In this chapter, the focus is on our results on the epitaxial ferrimagnetic insulator thulium iron garnet ($Tm_3Fe_5O_{12}$, TmIG) integrated with platinum to form the stack Pt/TmIG/GGG. This heterostructure of a metal, magnet insulator and paramagnetic substrate is particularly attractive for spin–orbit torque (SOT) studies because the full charge current remains confined to the Pt layer, while the magnetic volume (set by the TmIG thickness) is small. These effects reduce the SOT switching current threshold and mitigate Joule heating. A defining property enabling SOT switching in TmIG/Pt is the strain-induced perpendicular magnetic anisotropy (PMA) that emerges in TmIG grown on GGG(111). In the sputtered films, PMA is evidenced by square out-of-plane hysteresis from SQUID magnetometry, together with hard-axis behaviour in in-plane field scans [41]. The out-of-plane saturation magnetisation is generally in the range of $M_s \approx 100$ kA/m for high-quality films.Besides TmIG, Pt as the metallic layer is well-founded. A thin interfacial region in the inherently non-magnetic transition metal acquires an induced magnetic moment via exchange with the magnetic insulating layer, the strength governed by the Stoner criterion. For such structures, specifically the metal itself, it is often appropriate to view magnetism as an instability of an electron gas: a spontaneous spin polarisation of the individual electron bands when the density of states is reduced below a particular value. This is exactly what is formalised in the Stoner criterion: the competition between the kinetic-energy cost of splitting spin-up and spin-down bands, and gain from a parallel spin configuration to the exchange-energy yields a rigid criterion for induced ferro/ferrimagnetism in metals [288]. This is formalised as $I \cdot N(E_F) > 1$, where $I$ is the intra-atomic exchange integral and $N(E_F)$ the density of states at the Fermi energy [289, 290]. If the criterion is fulfilled, the metal lowers its energy by creating an imbalance in the number of up and down spins, thereby becoming (ferro/ferri)magnetic. Due to the high spin-orbit coupling of bare Pt, it nearly fulfills this criterion and relatively weak perturbations in the electronic

structure lead to induced magnetism, e.g. by coupling to a magnetic insulator.

This combination of strong spin-orbit coupling in Pt and low-damping ferrimagnetism in TmIG makes the Pt/TmIG platform particularly attractive for hybrid quantum architectures. In addition to enabling efficient electrical control of magnetisation via spin-orbit torques, the ferrimagnetic nature of TmIG supports coherent magnon excitations, which act as information carriers in the microwave regime. Owing to their bosonic character and long coherence lengths, magnons in low-damping garnets provide a natural interface between magnetic and superconducting degrees of freedom. Coupling such magnonic excitations to superconducting microwave resonators opens a pathway towards hybrid quantum systems, where information can be coherently transferred between spin, charge, and photonic subsystems. In this context, the ultrathin geometry and tunable magnetic properties of TmIG are particularly advantageous, as they allow for integration with superconducting circuits while maintaining compatibility with electrostatic control and magnetic field environments. The Pt/TmIG/GGG heterostructure thus represents a promising platform for exploring magnon-photon coupling and for realising next-generation quantum information processing schemes based on hybrid superconductor-magnetic systems [39, 291–293].

## 4.1 Room-temperature characterisation

### 4.1.1 Uniformity characterisation

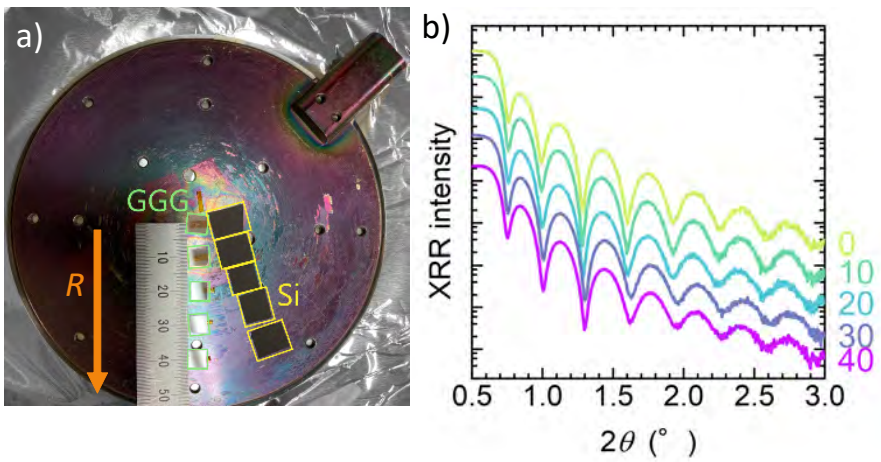


**Figure 4.1: a)** Photograph of a sample holder and pieces of GGG and Si substrates. **b)** XRR patterns of TmIG/Si samples at multiple positions where R from 0 to 40 mm. The data was shifted in y-direction for the visibility. The oscillation periods are identical among these samples. Figures are reproduced with permission of N. Yamashita

The scalability of rare-earth iron garnet films is an important requirement for hybrid quantum devices, where reproducibility across large substrates directly impacts device yield and integration with superconducting circuits. A central processing challenge is controlling stoichiometry and strain. On-axis RF magnetron sputtering produces

high-quality films when the growth position and gas conditions are optimised, but the composition may vary across the sample holder. In the case of TmIG, because sputtered Tm and Fe exhibit different angular distributions, this leads to position-dependent Tm/Fe. Consequently, there are position-dependent magnetic properties. Rotating substrate-holder strategies have therefore been developed to average out spatial variations and enable larger-area fabrication.

To establish the viability of a new large scale sputtering technique, we systematically evaluated the structural and magnetic uniformity of *on-axis* sputtered TmIG films across an 80 mm diameter wafer, using both interspaced GGG and Si substrates at radial positions $R = 0, 10, 20, 30$, and 40 mm, as shown in Figure 4.1a. To investigate the influence on electrical transport properties, Hall cross devices are fabricated by *ex-situ* depositing Pt on (only) the TmIG/GGG set of chips and subsequently defining the Hall structures via $Ar^+$ ion milling. The Si samples serve as a reference for film thickness measured by X-ray reflectivity measurements (XRR).

Across multiple devices and wafer positions, the TmIG films showed remarkably uniform magnetic behaviour. All Hall crosses exhibited essentially identical anomalous Hall loop shapes and switching thresholds (within experimental error), implying homogeneous thickness, strain, and interface quality. The low device-to-device variation underscores the effectiveness of on-axis sputtering for large-area, uniform garnet film growth.

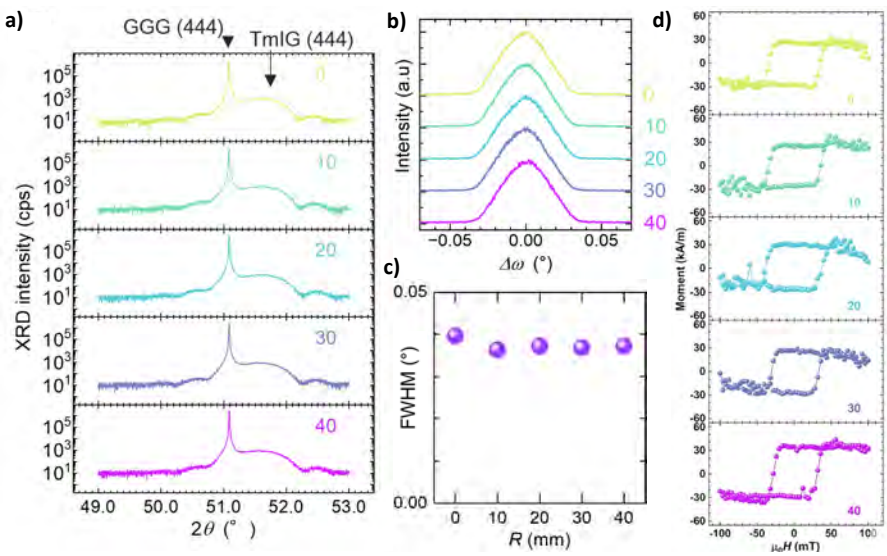


**Figure 4.2:** **a)** XRD patterns of the TmIG/GGG sputtered at multiple positions where R ranges from 0 to 40 mm. Both the peak of GGG and TmIG are indicated. **b)** X-ray Rocking curves of the TmIG (444) peaks of the samples where R ranges from 0 to 40 mm. **c)** R-dependence of the full-width-half-maximum of the curves in b), showcasing the uniformity. **d)** Uniformity of the saturation magnetic moment and the coercivity of TmIG/GGG films in an out-of-plane field at 300 K, where R ranges from 0 to 40 mm. Figures are reproduced with permission of N. Yamashita.

We examine the uniformity of the TmIG deposition by studying the thickness/deposition

rate using XRR on dummy Si substrates positioned at radial distances $R = 0$-40 mm from the centre of the rotating substrate holder; results are shown in Figure 4.1b. All samples exhibited identical oscillation periods in the XRR spectra, corresponding to a thickness of approximately 24 nm for this set of samples. The absence of measurable variation in oscillation spacing demonstrates a uniform deposition rate across the entire investigated radii. This result confirms that the optimised sputtering parameters (working pressure 3.0 Pa, 23 sccm Ar flow, post-annealing at 800°C in $O_2$) effectively suppress radial non-uniformities that are typically associated with compositional drift in composite garnet targets [40]. This is essential in enabling industry compatible TmIG or REIG deposition without sacrificing magnetic or spin-orbit torque performance. On-axis sputtering is more scalable than off-axis sputtering (or pulsed-layer deposition) because it uses the standard magnetron tools employed in industrial thin-film fabrication labs, enabling wafer-scale deposition limited only by target size. In contrast, off-axis sputtering relies on a non-standard substrate placement outside the plasma axis to reduce ion bombardment, which intrinsically limits deposition area, uniformity, and throughput. As a further test of the uniformity, we performed scanning transmission electron microscopy and energy dispersive X-ray measurements of the sample, shown in Figure 4.3, solidifying our arguments.

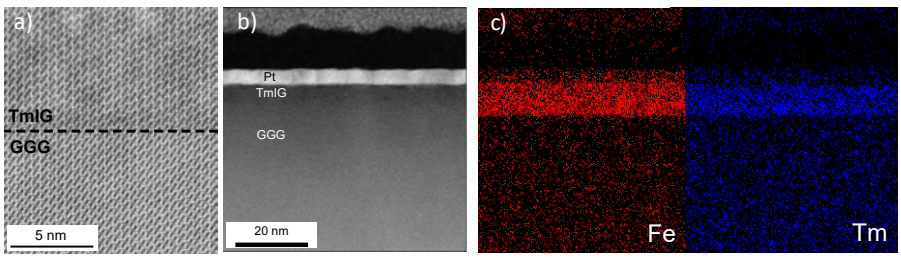


**Figure 4.3:** Further measurements of the uniformity of (thin-film Pt on) TmIG.
**a)** High-resolution scanning transmission electron microscopy of the interface between GGG substrate and TmIG film.
**b)** Scanning transmission electron microscope image of the heterostructure.
**c)** Energy dispersive X-ray spectrum of TmIG to determine the elemental composition of the TmIG layer. Figure reproduced with consent of N. Yamashita.

The out-of-plane lattice parameter was evaluated by $2\theta$-$\omega$ scans of the TmIG(444) reflection on GGG substrates shown in Figure 4.2a. Clear and well-defined GGG(444) and TmIG(444) peaks were observed at respectively 51.09° and 51.56°, respectively, confirming the strained cubic garnet phase with an out-of-plane lattice constant a(111) = 1.2275 nm; the lattice constant of bulk TmIG is 1.232 nm. No systematic radial peak shift occur within experimental resolution. This demonstrates that the epitaxial strain, which is directly linked to the perpendicular magnetic anisotropy via inverse magnetostriction, remains constant across the wafer-scale deposition. The structural homogeneity is particularly relevant for TmIG, where even small variations in lattice mismatch strongly modify the magnetic anisotropy energy and coercive field. The observed invariance of the (444) peak position therefore implies a spatially uniform magnetoelastic contribution to the anisotropy.

X-ray rocking curve (XRC, Figure 4.2b and c) measurements of the TmIG(444) reflection further confirm the structural uniformity and the epitaxial nature. The full width

at half maximum (FWHM) of the rocking curves ranges between 0.036° and 0.040° across the entire diameter. No systematic radial dependence is observed. These values are comparable to previously reported high-quality epitaxial TmIG films [294] and demonstrate uniform mosaicity and crystalline coherence. The combined XRR, XRD and XRC analysis thus establishes that the film is epitaxial up to a few millidegrees and that the thickness, lattice constant, and crystalline quality are homogeneous across the wafer within experimental uncertainty. This structural uniformity is reflected in SQUID magnetometer (Quantum design MPMS-3) measurements shown in Figure 4.2d using an out-of-plane magnetic field at room temperature. Both the saturation magnetisation $M_s$ and the coercivity exhibit low variance over the entire radial distribution; the samples show that $M_s \approx 30$ kA/m which is significantly smaller than those in the previous studies [295]. This smaller $M_s$ is beneficial for the operation of domain wall and skyrmionics devices for high-speed spintronic operations.

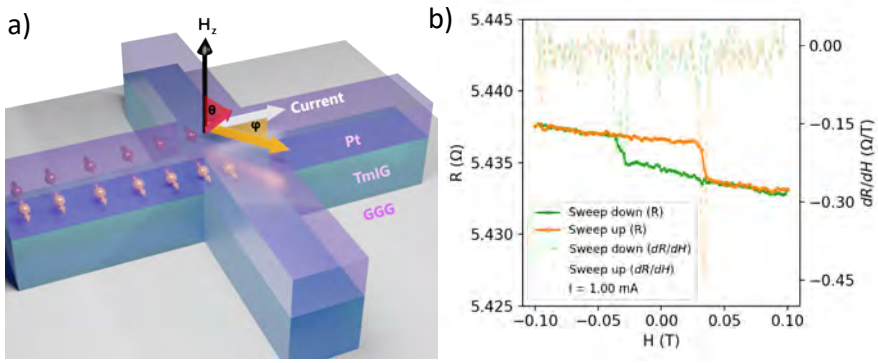


**Figure 4.4: a)** Device design of the cross-Hall bar samples. Indicated are the applied current-direction (white), the in-plane magnetic field angle $\varphi$ (orange) and the out-of-plane magnetic field angle $\theta$ (red). Voltage is measured using the perpendicular arms transverse to the current direction. **b)** Unprocessed AHE data for device $R = 00$ mm, taken at 1.0 mA applied current and showing the derivative signal superimposed on the AHE signal.

To investigate the influence of the wafer-scale deposition on the electrical transport properties, Pt/TmIG/GGG Hall crosses (width 8 $\mu$m) were fabricated on the multiple radial position-based chips and characterised via anomalous Hall effect (AHE) measurements at room temperature. The AHE signal, at this temperature originating from spin Hall magnetoresistance and interfacial spin-dependent scattering in the Pt layer, serves as a sensitive probe of the perpendicular magnetisation of TmIG. The device structure and an exemplary AHE plot are shown in Figure 4.4. The linear ordinary hall effect is extracted from the data by first extracting the coercive field (field at maximal divergence of $\frac{\mathrm{d}R}{\mathrm{d}(\mu_0 H)}$) and fitting a linear relation to the high-field edges of the data; the error is twice the field-measurement increment.

We performed both an applied-current dependence of one chip, as well as a radial dependence of current-averaged characteristics in Figure 4.5. The left panel presents measurements performed on a single Hall bar (at $R = 0$ mm) while varying the applied current between 0.25 and 1.5 mA. While the magnitude of $\Delta R_{\mathrm{AHE}}$ shows moderate variation with current, which may arise from Joule heating or small changes in the spin Hall magnetoresistance contribution, the coercive field remains essentially constant at

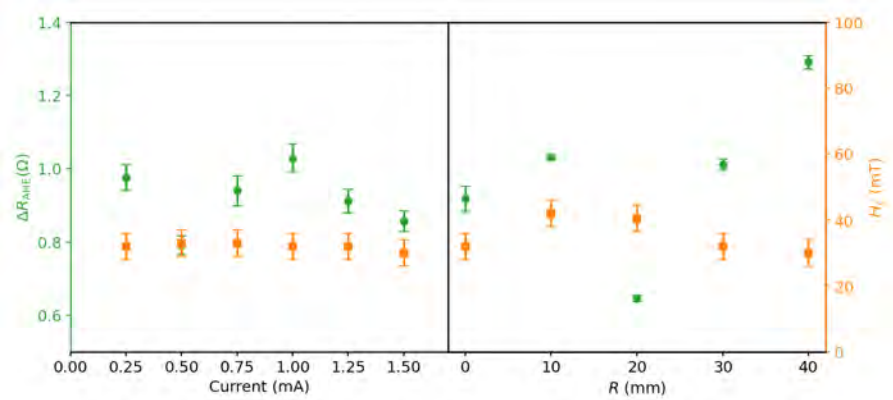


**Figure 4.5:** Dependence of the anomalous Hall resistance amplitude $\Delta R_{\mathrm{AHE}}$ and coercive field $H_{\mathrm{c}}$ on the applied current (**left**) and radial position on the wafer (**right**).

$H_{\mathrm{c}} \approx 30$–$33$ mT within experimental uncertainty. The right panel shows measurements obtained from Hall bars located at different radial positions of the wafer-scale deposition. The coercive field again remains nearly constant across the wafer, indicating that the perpendicular magnetic anisotropy and switching characteristics of the TmIG layer are spatially homogeneous. In contrast, $\Delta R_{\mathrm{AHE}}$ exhibits a somewhat larger spread between devices. Since the anomalous Hall signal originates from the Pt/TmIG interface via spin Hall magnetoresistance mechanisms at room temperature, such variations are likely dominated by small differences in interface quality, device geometry, or contact resistance rather than intrinsic variations in the magnetic properties of the TmIG film. Across all measured positions, the Hall resistance loops exhibit essentially identical square hysteresis, consistent coercive fields, and comparable saturation amplitudes. Overall, the nearly constant coercive field across both measurement series demonstrates a high degree of magnetic uniformity of the TmIG layer over the wafer. Such uniformity is essential for reproducible device behaviour in spin–orbit torque experiments and for the integration of ferrimagnetic insulators in hybrid magnonic and superconducting quantum circuits.

This uniformity demonstrates that: (i) the perpendicular magnetic anisotropy is homogeneous across the wafer and (ii) the Pt/TmIG interfacial quality does not degrade significantly with radial position. In conclusion, the absence of radial variation of large-area on-axis sputtered fabrication in both structural and magnetic metrics provides a strong foundation for scalable hybrid quantum architectures based on TmIG. For hybrid superconducting-magnonic circuits, this is particularly interesting because variations in anisotropy or magnetisation would translate into spatial fluctuations in magnon resonance frequency and spin-orbit torque efficiency.

### 4.1.2 Second-harmonic Hall measurements

Following uniformity characterisation, we measure the room temperature characteristics of the $R = 0$ mm chip. A spin–orbit torque (SOT) arising from strong spin–orbit coupling in heavy metals has enabled electrical control of magnetisation in thin ferromagnetic metals. When a longitudinal charge accumulation (e.g. a current) accrues in a

heavy metal (HM) of a HM/ferrimagnet bilayer, with the HM having strong spin-orbit coupling like Pt, a transversal spin current appears. This is the spin Hall effect (SHE), that injects a flow of spin angular momentum into an adjacent magnetic layer and exert torques on its magnetisation [296]; the SOT. The efficiency of this process is governed by a dimensionless material(stack) parameter, the effective (damping-like) spin Hall angle (or: torque efficiency) $\theta_{\mathrm{SHE}}^{\mathrm{DL}}$. This is a crucial measurement for determining the efficiency for general spintronic applications [297, 298]. We quantify the SOT efficiency in Pt(3nm)/TmIG(6nm)/GGG Hall crosses using second-harmonic Hall measurements ($2\omega$-Hall). An ac lock-in current is applied to Pt and the first and second harmonic Hall voltages are measured while sweeping an in-plane magnetic field. In the Pt/TmIG system, the dominant contributions at room temperature to the Hall response originate from SMR and an SMR-induced anomalous Hall component [299]. The damping-like torque efficiency is obtained from Eq. 4.1:

$$\theta_{\mathrm{SHE}}^{\mathrm{DL}} = \frac{2e}{\hbar}\left(\frac{H_{\mathrm{DL}}}{J_{\mathrm{c}}}\right) M_{\mathrm{s}}\, t_{\mathrm{FM}}, \tag{4.1}$$

Where $J_{\mathrm{c}}$ is the Pt-confined charge-current density and $t_{\mathrm{FM}}$ is the TmIG thickness. Furthermore, the damping-like effective field $H_{\mathrm{DL}}$ is extracted from second-harmonic Hall measurements with an in-plane field, scaling linearly with the current density. For Pt(3 nm)/TmIG(6 nm)/GGG devices, the resulting effective damping-like spin Hall angle is $\theta_{\mathrm{SHE}}^{\mathrm{DL}} = 0.030 = 3.0\%$. This corresponds to a damping-like effective field of $\sim 2.0$ Oe per $10^{10}$ A/m$^2$, indicating efficient charge-to-spin conversion and strong torque transfer across the Pt/TmIG interface.

### 4.1.3 Current-induced magnetisation switching

In metal-ferromagnet heterostructures, the SOTs efficiently switch the perpendicular magnetisation of the heterostructure via current-pulse induced switching (sometimes with an added interfacial effects between the HM and REIG such as the Rashba-Edelstein contribution) [300,301]. A key requirement for deterministic SOT (one-way) switching in a single perpendicular magnet is breaking the symmetry of the torques. This is typically achieved by applying a small in-plane magnetic field $H_x$ along or opposite to the current direction, designing structural asymmetry or ferroelectric gating, ensuring the spin torque favours one switched state over the other. Generally, the lower the necessary assisting field, the better for most applications as it imposes constraints on device scalability [302]. As no charge flows through the insulator, all the applied current contributes to spin current in the heavy metal (i.e. no shunting through the magnet), making the process energetically efficient. Conversely, spin currents propagate in the TmIG to flip its magnetisation, despite the zero charge flow. Unlocking this mechanism for magnetic insulators was an important milestone as it enables ultra-low dissipation switching in principle, and allows for the future development of fast, low-loss magneto-electrical elements.

The experimental platform for SOT switching in TmIG are the bilayer Hall cross devices consisting of an insulating TmIG film (typically in the range of $3-100$ nm thick) with a thin heavy-metal capping layer such as Pt (3–8 nm). Lithographically patterned Hall structures of the Pt layer serve both to carry current and to sense the magnetisation electrically, as shown in Figure 4.6a. The protocol for SOT switching

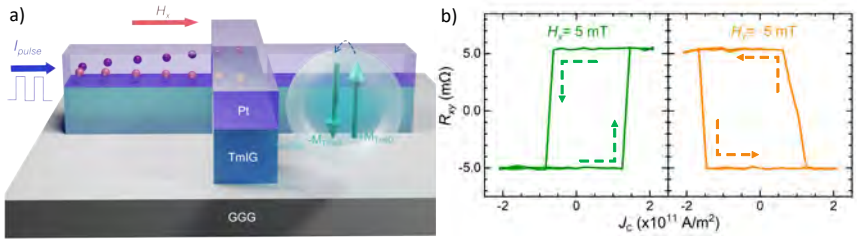


**Figure 4.6:** Device and measurement schematic for SOT switching in TmIG/Pt.**a)** A heavy-metal (Pt) Hall cross is fabricated on a TmIG film grown on a (111)GGG substrate. Pulsed currents $I_{\text{pulse}}$ along the in-plane horizontal direction in Pt generate spin currents (via the spin Hall effect) injected into TmIG (spin polarisation out-of-plane). A small in-plane magnetic field $H_x$ is applied collinear with current to break symmetry and define a deterministically preferred switching direction.**b)** Typical SOT-induced magnetisation switching loops, measured as the transverse Hall resistance $R_{xy}$ versus applied current density $J$ under $+5$ mT and $-5$ mT fields. The loops reverse when the field is reversed, indicating deterministic bipolar switching.

measurements is as follows. First and foremost we perform a standard dc AHE magnetisation switching measurement as a reference:

1. The magnetic layer is saturated into a known state (say 'up', or positive field above the coercive field $H_{c,+}$) using an external magnetic field out-of-plane at a given temperature. This is done at a well-defined reading current; in our experiments, it was 500 $\mu$A, much lower than the final switching current, on the order of 3 mA. A full magnetic trace is taken. The final configuration has the field as it was initialised, $H_z > H_{c,+}$, ramping back to zero.

2. Then, due to constraints in the set-up, the sample is rotated 90 degrees in the zenith axis so that an applied field would be in-plane. The reading current is turned off during this step. If necessary, also the azimuthal angle is rotated so that the external field is along the current direction. A small assisting field $|H_x| \lesssim \pm\frac{1}{3}H_c$ is applied to ensure deterministic switching.

3. A pulsed current of set amplitude/duration is then stepped carefully to attempt switching. At low current, the magnetisation remains in its initial state and $R_{xy}$ stays roughly constant. While pulsing mitigates continuous heating by its very nature, a too high sample temperature causes device breakage and thus small current pulse amplitude increments are the best strategy. After the pulse, we wait briefly (approximately 100 ms) to ensure magnetisation stability. Then, the same sensing current as for the magnetic AHE spectrum is used to read out the magnetic state by comparison. A small further delay is then incorporated (on the order of 1 s) to further mitigate heating effects. As the current density reaches a critical value, the spin–orbit torque on the magnetisation becomes strong enough to destabilise the orientation of spins in the magnetic layer. The magnetisation suddenly flips to the opposite out-of-plane direction, observed as an abrupt jump in the Hall resistance to the new level corresponding to the switched state. This threshold behaviour is analogous to the hysteretic switching transition with magnetic field of step 1: increasing current triggers reversal, and if the current is reduced back below a threshold of opposite polarity, the magnet switches back to the original state, forming a hysteresis loop when plotting $R_{xy}$ versus current.

4. This can be repeated in the three-dimensional order space of pulse amplitude, pulse width and assisting field. One then maps out the conditions under which switching succeeds. Often, multiple measurements are averaged [303]. Applying an opposite polarity of $H_x$ causes a likewise opposite switching direction, seen in Figure 4.6b.

These pulsed measurements are especially useful for studying the dynamics of switching. During the brief pulse, a large spin Hall torque is exerted on the magnetisation. They allow the extraction of switching probability as a function of pulse length or amplitude, revealing the stochasticity (if any) of the process. Depending on the exact experimental conditions (assisting field chiefly), the HM/FiM layer enters a metastable interstate without full polarisation. Hence, the reproducibility of these measurements is paramount. For example, by applying many identical pulses and measuring the fraction of successful switches, one can construct a switching phase diagram in current versus $H_x$ or versus pulse duration (see e.g. [296, 303]). The critical switching current density in SOT devices is relatively low and with high success rates; for example, in Pt/TmIG heterostructures the magnetisation reverses typically at $J_c \sim 10^{11}$ A/m$^2$ under a few mT in-plane field at room temperature, comparable to or lower than all-metallic spintronic stacks [304, 305], partially due to the high spin transparency at the Pt/TmIG interface. This low current threshold is directly attributed to the absence of current shunting in the magnetic insulator and the efficient spin-torque coupling at the Pt/TmIG interface. Overall, the use of current pulses confirms that the magnetisation switching is a fast, dynamic process initiated by SOT, often occurring on even sub-nanosecond timescales [302]. To further establish industrial feasibility of *on-axis* sputtered TmIG, we performed state-selective measurements under consecutive pulse currents (from 5 to 5.5 mA in the positive polarity, and from -5.5 to -5 mA in the negative polarity). These results, shown in Figure 4.7, show robust and deterministic switching establishing the material stack as an attractive candidate for spintronics.

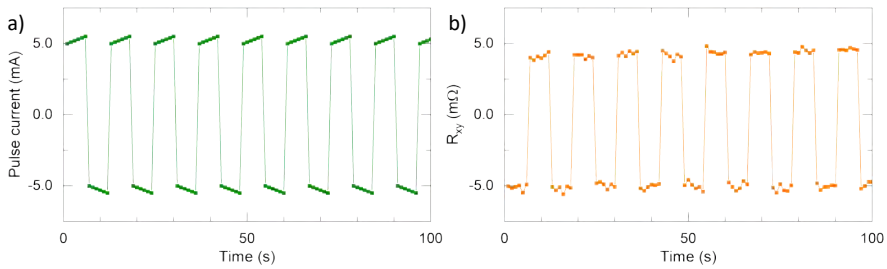


**Figure 4.7:** Spin-orbit torque magnetisation switching under an in-plane field of -5 mT. **a)** The temporal pulse spectrum of consecutive applications of the 50 $\mu$s width-pulse currents. We iterated the amplitude from between |5.0| and |5.5| mA. **b)** The Hall voltage was measured and plotted by applying 500 $\mu$A, 100ms after each pulse current application.

As seen in Figure 4.6b, the direction of magnetisation switching is determined by the current polarity and the sign of the in-plane field. Reversing the current direction (or equivalently reversing the small in-plane assist field) causes the opposite flip of magnetisation. In other words, the switching polarity inverts when either the current or the field's sign is reversed, as the spin Hall torque is $\propto J(\mathbf{M} \times \mathbf{m})$. Here, it is the non-equilibrium spin density $\mathbf{m}$ that changes sign [306]. If this is fulfilled, it

confirms the origin of the effect is not thermal. The asymmetry in the switching current density between $J_{sw,+}$ and $J_{sw,-}$ is a general phenomenon if the assisting field is not exactly collinear with the electric current pulse direction, and is attributed to a transverse SOT field [301]. For large mismatch, this effect increases $J_{sw}$ up to an order of magnitude. The critical switching current density is found to be $J_{\mathrm{sw}} \approx$ (7-15) $\times 10^{10}$ A/m$^2$, placing the Pt(3)/TmIG(6) devices among the lowest-threshold garnet-based SOT heterostructures reported to date. Pulse repetition measurements (50 $\mu$s pulses) confirm that switching is robust and reproducible, with minimal device-to-device variability under comparable biasing conditions [41]. The extracted $\theta_{\mathrm{SHE}}^{\mathrm{DL}}$ from Section 4.1.2 and switching amplitude thresholds $J_{\mathrm{sw}}$ are thus comparable to or improvements on previously reported Pt/TmIG systems fabricated by PLD or off-axis sputtering, implying that the industry-compatible on-axis sputtering route does not introduce a detrimental reduction of SOT efficiency. To quantify this, and to tie back to the uniformity measurements of Sec. 4.1.1, we compare the results obtained from similar HM/TmIG/GGG structures in literature. The results are shown in Table 4.1. Most of the variations can be attributed to the Pt/TmIG interface, the thickness of the TmIG and the corresponding internal stress and the quality of the Pt thin film. A useful scaling relation for interpreting these comparative results of the both current density threshold and spin-hall torque efficiency for a current-perpendicular-to-plane geometry is

$$J_{\mathrm{sw}} = \alpha \frac{2e}{\hbar} \frac{M_s t_{\mathrm{FM}}}{\theta_{\mathrm{SHE}}^{\mathrm{DL}}} \left( H_{K,\mathrm{ip}} + \frac{N_d M_s}{2} \right) \tag{4.2}$$

where $\alpha$ is the damping constant, $H_{K,\mathrm{ip}}$ is the in-plane magnetic anisotropy field and $N_d$ the demagnetisation factor; a dimensionless quantity that quantifies the internal magnetic field opposing the external magnetic field. Upon simplification, noticing that a similar structure is valid for current-parallel-to-plane geometries and for small $H_x \ll H_{K,eff} = H_{K,perp.} - N_d M_s$, this becomes:

$$J_{\mathrm{sw}} = \frac{2e}{\hbar} \frac{M_s t_{\mathrm{FM}}}{\theta_{\mathrm{SHE}}^{\mathrm{DL}}} \left( \frac{H_{K,eff}}{2} - \frac{H_x}{\sqrt{2}} \right). \tag{4.3}$$

This expression captures why the thin-magnet limit (here $t_{\mathrm{FM}} = 6$ nm) is advantageous for lowering $J_{\mathrm{sw}}$, while maintaining PMA is essential to preserve well-defined up/down states for reliable memory operation [307, 308]. Physically, the thickness is a defining factor for the total volume of the magnetic material (and hence the total amount of spins) that has to be flipped for a certain current density. For a thin-film NM/REIG heterostructure, the Pt layer influences the resulting switching current via $\theta_{\mathrm{SHE}}^{\mathrm{DL}}$. Near a magnetic compensation temperature, $M_s$ will decrease (or becomes negligible), while the effective perpendicular magnetic anisotropy field will substantially increase [309], leading to a larger critical switching current density.

Summarising, using pulsed charge currents in the Pt overlayer, we achieved deterministic SOT switching of the TmIG magnetisation at 300 K. Under a small in-plane bias ($\approx$5 mT), the perpendicular magnetisation could be reversibly toggled by $\pm$ current pulses. The switching polarity reverses when the field is reversed, confirming that the SOT mechanism is underlying the physics. The critical switching current density $J_{sw}$ was consistent in the range of 0.7 to 1.5 $\times 10^{11}$ A/m$^2$, among the lowest reported for garnet-based heterostructures. Notably, the switching curves were highly reproducible and showed only slight asymmetry, indicating uniform magnetic anisotropy and well-aligned device fields. These results demonstrate robust, energy-efficient magnetisation reversal in the sputtered Pt/TmIG devices at room temperature.

| Heterostructure(/GGG) | $\theta_{\mathrm{SHE}}^{DL}$ (%) | $J_{sw}$ (GA/m$^2$) | $\mu_0 H_x$ (mT) | Growth | Method | Ref. |
|---|---|---|---|---|---|---|
| Pt(3)/TmIG(6) | 1.5 | 70–150 | 5 | † | 2$\omega$-HE | [41] |
| Pt(5)/TmIG(8) | 1.5–2 | 170 | 50 | ∗ | 2$\omega$-HE | [296] |
| Pt(4)/TmIG(9.6) | 3 | 60 | 3.5 | ∗ | 2$\omega$-HE | [303] |
| Pt(3.2)/TmIG(9) | 8 | 25 | 0.5 | ‡ | 2$\omega$-HE | [310] |
| $CuO_x$(3)/Pt(1)/TmIG(6.5) | 1 | 170 | 2.5 | ∗ | $\chi_z$, $\beta$-scan | [311] |

**TABLE 4.1:** LIST OF SPIN-ORBIT TORQUE EFFICIENCY MEASURED IN PT/TMIG SYSTEMS. LEGEND:
†: MAGNETRON SPUTTERING, ∗: PLD, ‡: OFF-AXIS SPUTTERING
2$\omega$-HE: SECOND HARMONIC HALL MEASUREMENT AT LOW MAGNETIC FIELD.
$\beta$-SCAN: ANGLE DEPENDENCE OF THE SPIN HALL MAGNETORESISTANCE.
$\chi$: HYSTERESIS LOOP SHIFT UNDER BIAS CURRENT AND QUADRUPOLE FIELD.

## 4.2 Temperature-dependent results

Ferrimagnetic materials often consist of two (or more) magnetic sublattices. TmIG, for example, consists of three coupled magnetic sublattices: $Fe^{3+}$-ions occupy two octahedral and three tetrahedral sites, resp. a- and d-sites, and $Tm^{3+}$-ions reside on dodecahedral c-sites [312]. The antiferromagnetic superexchange coupling [313, 314] between the $Fe^{3+}$-ions of the a- and d-sites via the oxygen atoms is generally the strongest. Similarly, the a-sites are also parallel to the d-sites via exchange-enhanced paramagnetic coupling: the RE-ions are affected by an external field with superimposed Curie-Weiss law behaviour with a strong temperature dependence [312]. In total the rare-earth sublattice antiferromagnetically couples with the net Fe-sublattice magnetisation [315–318]. At high temperature, the strong superexchange interactions between the $Fe^{3+}$-ions dominates, but at low temperatures due to strong spin-orbit coupling and anisotropy effects the Tm sublattice magnetic moment increases significantly [319, 320]. Consequently, these sublattices have different magnetic moments and temperature dependencies, and a magnetisation compensation temperature (typically denoted $T_{\mathrm{comp}}$) can exist; here, the opposing sublattice magnetisations lead to a minimal net magnetisation which can become negligibly small [321]. Separately, there may also be an angular momentum compensation temperature ($T_{\mathrm{A}}$), where the net spin angular momentum cancels or is minimised [322]. These two temperatures do not necessarily coincide due to differences in the gyromagnetic ratio ($g$-factors) of the constituent rare-earth ions [323–325]. Physically, at $T_{\mathrm{comp}}$, the sublattice magnetisations balance, whereas $T_{\mathrm{A}}$ occurs when the spin densities (magnetic moments weighted by g-factors) equalise. Some REIGs like bulk TmIG lack an accessible $T_{\mathrm{comp}}$ entirely [319], while others, such as GdIG, exhibit well-defined compensation points near room temperature [309]. These temperatures are not set: tuning composition or strain shifts them significantly. In this Section, we will discuss our results on the discovery of a double polarity switch of the AHE sign in ultrathin-film TmIG grown on (111)GGG and capped with the thin-film heavy metal Pt [326]. Furthermore, we show early results on temperature-dependent switching measurements.

The main appeal of compensated ferrimagnets in spintronics is their ability to combine antiferromagnetic-like dynamics with ferromagnetic-like readout. Pure antiferromagnets (AFMs) offer ultrafast dynamics, low stray fields [327], and robustness against perturbation by external fields, but are difficult to manipulate directly [328, 329]. By contrast, compensated ferrimagnets retain a measurable sublattice magnetisation and can be electrically or optically probed, yet approach the ultrafast, efficient behaviour

of AFMs near $T_{comp}$ [321, 322]. Approaching $T_{comp}$ affects coercivity, current-induced switching, and domain wall (DW) dynamics. First, coercivity typically increases sharply as the net moment decreases, due to a diverging anisotropy field [330]. In kagome ferrimagnets near $T_{comp}$, coercive fields exceeding 14 T have been observed. In garnet films, similar trends occur, with switching becoming increasingly difficult due to stronger pinning and reduced susceptibility. Secondly, the polarity of SOT switching inverts when crossing $T_{comp}$ [309]. In REIG systems at room temperature, the anomalous Hall signal is attributed to magnetic proximity coupling between Fe 3*d* and Pt 5*d* orbitals [299]. Thus, at these elevated temperatures, the Fe sublattice dominates spin–orbit coupling and magnetic spin transport, allowing for electric characterisation techniques such as the spin Hall magnetoresistance or anomalous Hall signals. At lower temperatures, below $T_{comp}$, the total net magnetisation flips, and thus the direction in which spin current favours magnetisation reversal also reverses, analogous to the results of flipping the assisting field polarity in Section 4.1.3. This has been demonstrated in GdIG/Pt heterostructures, where SOT switching at 294 K and 301 K required opposite current polarities [309]. Third, and most significantly for device applications, domain wall velocities are maximised near the $T_A$. At this point, the inertia of the DW vanishes and the effective damping becomes very large, allowing extremely rapid response to torques. In REIG films such as GdIG and $(Tm,Gd,Bi)_3(Fe,Ga)_5O_{12}$, DW velocities of the order of km/s have been reported near $T_A$ [322, 331, 332], surpassing those in metallic systems potentially owing to the divergence of the Gilbert damping constant [333–337]. These speeds are enabled by low intrinsic damping, efficient torque transfer, and vanishing spin angular momentum. Thus, the compensation temperature, and related the angular compensation temperature are critical parameters in HM/REIG spintronic heterostructures. Near $T_{comp}$, such materials combine AFM-like speed and stability with FM-like detection and scalability.

A material that has $T_{comp}$ near room temperature further enables real-world spintronic applications without the need for (cryogenic) cooling. GdIG films offer a $T_{comp}$ around 280–300 K, alongside a Curie temperature over 500 K, making them ideal for ambient-condition devices. Operating near $T_{comp}$ allows for some key applications: racetrack memories [338], the study of chiral spin textures [332], energy efficient switching [339, 340], (spin-wave driven) domain wall logic [325], and ultrastrong magnon coupling [341] all while retaining electrical readout via SMR or Hall signals. In particular, only insulating ferrimagnets offer such energy-efficient operations with minimal Joule heating. In light of our studies, we have already confirmed deterministic SOT switching and high repeatability in device stacks compatible with industrial fabrication, demonstrating the potential for implementing these materials in further studies, specifically TmIG.
In summary, the compensation temperature in heavy-metal/rare-earth iron garnet heterostructures represents a critical point where the material transitions to an AFM-like state without losing the possibilities enabled by its partially ferromagnetic nature. Exploiting $T_{comp}$, ideally situated near room temperature, allows for spintronic devices that are faster, more energy-efficient, and more robust than their conventional ferromagnetic counterparts. The fundamental physics of zero net magnetisation and angular momentum underpins novel switching phenomena and domain wall dynamics, while the presence of a robust readout signal eliminates the primary drawback of using antiferromagnets.

In this Section, we show our measurements on both the coercive field and AHE signal (Sec. 4.2.1). We find a double polarity change in the anomalous Hall resistance, one of them exhibiting a divergence of the coercive field, and one not. We explain our results using and determine which physical effects could be underlying. Furthermore, we show our temperature-dependent switching data, and provide both an overview of other literature and why the measurements failed for us in Section 4.2.2.

### 4.2.1 Coercive field and anomalous Hall signal

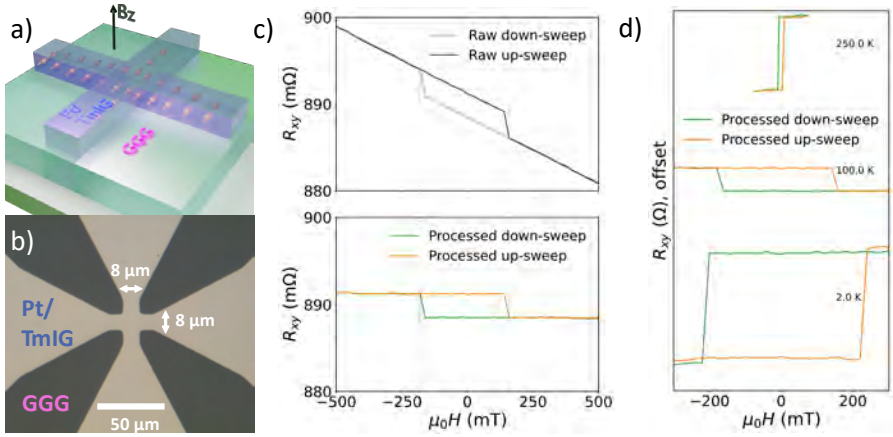


**Figure 4.8: a)** Schematic stack of the sample structure. The Pt is sputtered on TmIG, grown using on-axis sputtering on GGG. **b)** Microscope image of the Hall-bar used for the measurements, with channels of width 8 $\mu$m. Light grey is Pt on top of TmIG, dark grey is the underlying GGG layer. **c)** Representative Anomalous Hall Effect (AHE) measurement at 100 K. Both the raw data (grey) and the processed data after subtraction of the ordinary Hall effect-contribution as described in text are shown. The data is split up in down-sweep (from maximum field to minimum field) and up-sweep. **d)** AHE measurements at three different temperatures $T = 2.0, 100, 250$ K, offset from each other. The linear OHE component has been removed. The sweep direction from positive (negative) field to negative (positive) field is indicated as down (up)-sweep.

We carry out electrical transport measurements in a Quantum Design physical property measurement system (PPMS) using the built-in current and voltage sources. Here, we use a similar sample as to characterised in the room temperature SOT switching measurements with stack structure Pt(3nm)/TmIG(6nm)/(111)GGG. We reiterate that the Hall cross devices have arm widths and lengths of 8 $\mu$m, as shown in Fig. 4.8a and b. At each temperature, we sweep the out-of-plane magnetic field between positive and negative values, letting the magnetisation exceed the saturation magnetisation $M_s$, which yields AHE hysteresis loops for both sweep directions. Figure 4.8c shows representative raw and processed Hall resistance data at $T = 100$ K. Because the Pt layer is metallic, in addition to the AHE, the transversal voltage signal contains a (linear) background arising from the ordinary Hall effect (OHE). To isolate the anomalous Hall contribution, we remove the OHE signal by fitting a linear function $R_{OHE} = aR_{xy} + b$ to the low-field region around 0 T (averaging between up- and down-sweep), where aberrant multi-ordered Hall contributions are negligible to first order. We then extract the coercive fields $H_{c,+}$ and $H_{c,-}$ from the extrema of the numerical derivative of the Hall resistance with respect to field, and we define the mean

coercive field $|H_C|$ as the half-width of the major hysteresis loop. Finally, the AHE resistance, $\Delta R_{AHE} = \frac{1}{2}(R_{+H\to-H} - R_{-H\to+H})$, is defined as the half-difference between the two resistance plateaus. We repeat this analysis for the entire series of temperatures.

One of our key results is the observation of two distinct polarity reversals in the temperature dependence of $\Delta R_{AHE}$. The magnetic properties of TmIG are highly strain-sensitive. Films grown on Nd:GGG and SGGG substrates have exhibited true magnetic compensation points, as demonstrated in Refs. [342, 343]. In contrast, no such compensation point has been observed for TmIG on GGG substrates to date. Although high-temperature annealing can induce a compensation-like polarity reversal without a reversal of the Fe sublattice magnetisation, a true magnetic compensation temperature remains elusive for this specific material [318]. A divergence in $|H_C|$ is often used as a proxy for identifying a magnetic compensation point [343–345]. However, this criterion is not definitive: Soares *et al.* and Wang *et al.*'s data showed that $|H_C|$ can diverge even when a residual net magnetisation remains, indicating only a compensation-like transition, even when $\Delta R_{AHE} = 0$ [312, 318], while Pandey *et al.* talked about a compensation-temperature without total vanishing of net magnetisation [346]. Similarly, Ding *et al.* [299] reported that in the absence of a divergence of $|H_C|$, no true magnetic compensation occurs. Thus, our observed polarity reversals do not necessarily correspond to a definite compensation temperature; in literature, there is clearly some obfuscation of the term and "compensation-temperature" and "compensation-like" temperature are used alike. Here, we define $T_{comp}$ as a temperature with vanishing $\Delta R_{AHE}$ signal, *and* corresponding vanishing magnetisation; the latter prerequisite does not occur for $T_{comp-like}$.

In Fig. 4.8d, we plot the transversal resistance $R_{xy}$ as a function of the applied magnetic field $\mu_0 H$ for three representative temperatures, highlighting the observed polarity reversals after subtraction of the linear OHE background. The corresponding temperature dependent $|H_C|$ is plotted in Fig. 4.9. The error bars represent the uncertainty in determining $|H_C|$ due to the finite magnetic field step size used in the hysteresis measurements, and are defined as twice the field increment step. The temperature evolution of $|H_C|$ and $\Delta R_{AHE}$ observed in our devices more closely resembles that reported for W(5nm)/TbIG(6nm)/Nd:GGG heterostructures [342] than that of Pt(5nm)/TmIG(20nm)/GGG studied by Ding *et al.* [299]. This highlights that the magnetic properties of TmIG depend sensitively on film thickness, and the ultra-thin films investigated experience significantly lower epitaxial strain than those studied previously [299, 318, 347].

Three distinct temperature regimes are identified in the evolution of the coercivity indicated by the fits. At room temperature, the coercive field is small ($|H_C| \approx 5$ mT) and increases exponentially upon cooling. This regime is characterised by small domains [331]: in magnetic samples, interaction between magnetic domain walls and material imperfections exists. Different kinds of wall-pinning traps (material defects) coexist in the material, and each of them is active in a certain temperature region on a corresponding temperature/energy scale $T_0$, associated with a thermally activated magnetisation reversal processes and governed by the interplay between domain-wall motion and pinning [348, 349]. Hence, we fit this regime with an exponential phenomenological form of Eq. 4.4:

$$|H_C| = A \exp(-T/T_0) + C\,. \tag{4.4}$$

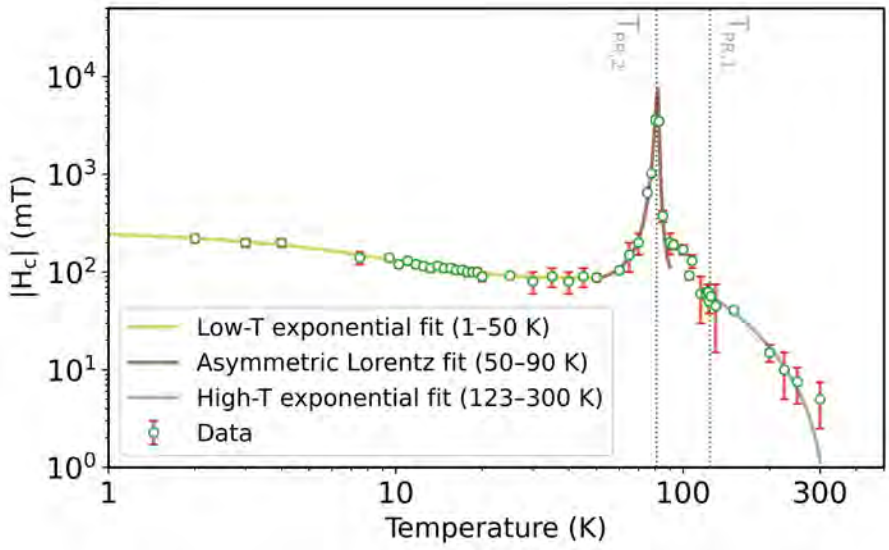


**Figure 4.9:** Mean coercive field $|H_C|$ as a function of temperature, extracted from the anomalous Hall hysteresis loops. Error bars reflect the uncertainty arising from the finite magnetic field step size. A pronounced divergence of $|H_C|$ is observed in the vicinity of $T_{PR,2}$, whereas no such divergence occurs near $T_{PR,1}$. The data are fitted in three temperature intervals (see text) using exponential or asymmetric Lorentzian functions to guide the eye.

However, we note that an Arrhenius-type of thermal activation behaviour would also adequately fit the data. In any model that is used, a correlation between the anisotropy and $H_c$ is assumed, with further modifications due to grains, impurities; in essence, the growth conditions of the Pt/TmIG heterostructure [350, 351]. The fit yields a characteristic temperature scale of $T_0 = 70.8 \pm 26.5$ K for the high-temperature regime. As the temperature approaches the first polarity-reversal temperature $T_{PR,1} \approx 124$ K, the coercive field increases smoothly to approximately 58 mT. At this temperature, the $\Delta R_{AHE}$-signal changes polarity for the first time, as indicated by the zero crossing in Fig. 4.10a), while no pronounced anomaly (in a $\pm 1$ K range) is observed in $|H_C|$. Upon further cooling, the coercivity increases sharply and reaches a maximum value of approximately 3.5 T in the temperature interval between $T_{PR,1}$ and the second polarity-reversal temperature $T_{PR,2} \approx 81$ K. To quantitatively capture the asymmetric shape of this coercivity peak, we fit the data in this temperature interval using a phenomenological asymmetric Lorentzian function of Equation 4.5, in this case used to capture a general asymmetric peak:

$$|H_C(T)| = \frac{A}{1 + \left(\frac{T - T_c}{w_{L,R}}\right)^2} + C\,, \tag{4.5}$$

where $A$ denotes the peak amplitude, $T_c$ the temperature at which $|H_C|$ is maximal, and $w_L$ and $w_R$ describe the widths of the low- and high-temperature flanks, respectively. The extracted widths differ significantly ($w_L = 3.0 \pm 0.7$ K and $w_R = 0.84 \pm 0.08$ K), indicating a much sharper decrease of $|H_C|$ above $T_{PR,2}$ than below. This asymmetry reflects the distinct thermal evolution of the rare-earth and iron sublattice magnetisations [318] and has been demonstrated in several ferrimagnetic systems, although the

relative asymmetry can be inverted depending on the material system and exact heterostructure design [203, 342, 345, 352]. The fit furthermore yields $T_c = 82.3 \pm 0.4$ K,

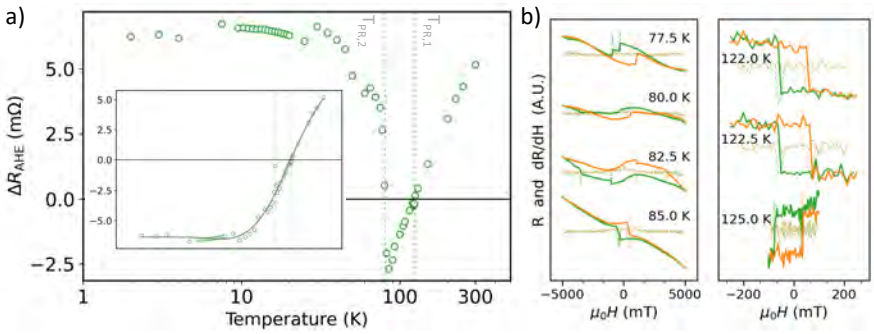


**Figure 4.10:** Temperature dependent $\Delta R_{AHE}$ and aberrant switching curves near $H_{PR,1}$ and $H_{PR,1}$. **a)** Half-difference of the anomalous Hall resistance plateaus, $\Delta R_{AHE}$, as a function of temperature for a Pt/TmIG/GGG heterostructure. This quantity serves as a proxy for the net magnetisation sensed by the proximitised Pt layer. Two zero crossings are observed at $T_{PR,2} \approx 81$ K and $T_{PR,1} \approx 124$ K (vertical dotted lines), where $\Delta R_{AHE}$ changes polarity, indicating two distinct polarity reversals of the anomalous Hall signal. *Inset:* $\Delta R_{AHE}$ data for $T < T_{PR,2}$ plotted with inverted sign, together with a guide-to-the-eye fit using a double n function (cf. Eq. 4.6) with fixed $J_1 = \frac{5}{2}$ and $J_2 = 6$, corresponding to the total angular momenta of the Fe and Tm sublattices, respectively.
**b)** Anomalous Hall effect data of a field sweep going down (green) and going up (orange), with corresponding numerically derivative data, shifted with respect to each other and scaled for visibility. *Left:* around $T_{PR,1}$ and *right:* around $T_{PR,2}$, showcasing multiple transitions.

in excellent agreement with $T_{PR,2}$. Moreover, as illustrated in the inset of Fig. 4.10a, numerically inverting the $\Delta R_{AHE}$ data for $T < T_{PR,2}$ renders the transition smooth rather than abrupt. This behaviour is consistent with a reversal of the magnetisation of one of the sublattices [203, 353, 354]. Indeed, magnetic phase diagrams of REIGs have shown that around $T_{PR,2}$, the Fe and Tm sublattices reorient themselves and the $Fe^{3+}$ (Re-ion $^{3+}$) sublattice aligns antiparallel (parallel) to the external field [346]. A similar behaviour is expected for TmIG: given the antiferromagnetic exchange coupling between the Tm and Fe sublattices across the full temperature range, a reversal of either sublattice's magnetisation naturally leads to the observed polarity change in $\Delta R_{AHE}$, and the smooth transition upon sign change. We fit the evolution over the entire temperature range using a two-component Brillouin-function fit (Eq. 4.6) to further illustrates the smooth character of the response. This function assumes that in first order, the Hall signal is related to the evolution of saturation magnetisation [351, 355]

$$\Delta R_{xy}(T) = \sum_{i=1,2} \pm A_i B_{J_i}(J_i a_i / T) + C, \tag{4.6}$$

where $B_J$ denotes the Brillouin function. The parameters $A_i$, $a_i$, and $C$ are free fitting parameters representing the amplitude, phenomenological temperature scaling, and a small residual offset such as imperfect linear background subtraction, respectively. In first order, this matches the linear magnetisation curve used by Wang *et al.* [347] to describe the evolution of the saturation magnetisation of doped TmIG in temperature. The prefactor $\pm A_i$ converts the magnetisation contribution of each sublattice into the corresponding anomalous Hall response; by convention, the Fe contribution is taken as positive, while the Tm contribution is taken as negative. Finally, $J_i$ is treated as a fixed shape parameter rather than as a strict microscopic angular-momentum quantum

number.

Finally, to elucidate the mechanism underlying the polarity reversals, we compare the behaviour of the AHE curves around both $T_{PR,1}$ and $T_{PR,2}$ in Figure 4.10b. While there is clear, uniquely-defined switching around $T_{PR,1}$, multiple transitions are present at $T_{PR,2}$. This indicates either the presence of multiple sublattice configurations and thus multiple switching events due to lattice reorientation, or the presence of a canted phase [356, 357]. Thus, in this intermediate regime multiple configurations are favoured since the total magnetisation is, to first order, the linear sum of the antiferromagnetically coupled sublattice magnetisations [357]. In the Pt/TmIG heterostructure, there can be regions with slightly differing compensation(-like) temperatures because of spatial inhomogeneities in strain (from film roughness or substrate defects) or composition (from O-vacancies) that produce local variations in the sublattice exchange coupling. The effect is a (small) spatial redistribution of the compensation temperature. Thus, while a region could have compensatory behaviour at $T_{PR,2}$, the interaction with neighbouring magnetic regions with a displaced compensation temperature lead to a net remaining magnetisation [315]. However, in other rare-earth iron garnet systems such as GdIG and HoIG, studies have shown that these features originate instead from the interaction between domains associated with different sublattices and their distinct switching dynamics [357, 358]. The multi-switching behaviour then arises from the coexistence of multiple sublattice configurations that stabilise near the compensation-like temperature. Furthermore, multi-domain signatures and corresponding multiple switching events can be induced by the fabrication of the Pt/TmIG heterostructure. Constrictions due to the edge of the Hall cross induce the formation of domains [359]. In our samples, the TmIG is uniform and epitaxial as shown by the transmission electron microscope and energy dispersive X-ray spectra in Figure 4.3. Additionally, single domain measurements on other REIGs have shown that the polarity reversal would exhibit multiple peaks in the temperature dependence of $H_c$ [317, 360] which are absent for our data. Thus the second multi-domain explanation is more consistent. We note that the multiple switching events are absent for the transition at $T_{PR,1}$, where there is a unique transition.

For temperatures below $T_{PR,2}$ (the lowest-temperature range), the coercive field initially decreases and reaches a nearly constant baseline value of $\sim 87$ mT between 20 and 50 K. Upon further cooling below approximately 20 K, the coercive field increases exponentially with decreasing temperature, following Eq. 4.4, with a characteristic temperature scale of $T_0 = 7.2 \pm 1.1$ K, and reaches a maximum value of approximately 220 mT at 2 K. While this local stable minimum has been attributed to the MPE becoming the dominant exchange mechanism, we do not believe it to be the case for our data [342] due to the reasons given below.

We propose that the two observed polarity reversals of the AHE in strained ultra-thin TmIG on GGG originate from distinct physical mechanisms. The higher-temperature transition at $T_{PR,1}$, in the absence of a divergence of $|H_C|$, can be understood in terms of a crossover in the dominant contribution to the AHE [299, 312, 342]. In ferrimagnet/heavy-metal heterostructures, the AHE arises from multiple mechanisms whose relative strengths are temperature dependent, including spin Hall magnetoresistance, which typically decreases upon cooling, and the magnetic proximity effect, which tends to increase at lower temperatures due to enhanced exchange coupling

between the $Fe^{3+}$ $3d$ orbitals and the Pt $5d$ orbitals once thermal fluctuations are suppressed. Depending on temperature, either contribution dominates the measured Hall response. This scenario is consistent with our observations and supported by the non-vanishing of $\Delta R_{\mathrm{AHE}}$, and thus net magnetisation, observed at $T_{\mathrm{PR},1}$.

In contrast, the polarity reversal at $T_{\mathrm{PR},2}$ likely reflects a change in the magnetic sublattice behaviour, rather than a change in the transport mechanism within interfacial TmIG/Pt layer. The Fe and Tm sublattice magnetisations exhibit distinct temperature dependences which results at the intersection $T_{\mathrm{PR},2}$ (where their combined contributions to the total magnetisation minimises) in a minimal or even negligible net magnetisation. As shown in the inset of Fig. 4.10, the apparent discontinuity in $\Delta R_{\mathrm{AHE}}$ becomes nearly continuous when the signal is numerically inverted for $T < T_{\mathrm{PR},2}$. This symmetry operation does not alter the physical content of the data but highlights the continuity of the underlying magnetisation evolution. This behaviour indicates that at $T_{\mathrm{PR},2}$, there is a full magnetisation reversal of the entire sublattice over a range of $\pm 3$ K, which is our data resolution. Due to the antiferromagnetic exchange between the Fe and Tm sublattices, a reversal in the magnetisation of one sublattice enforces an opposite change in the other. As the magnetisation of the Tm sublattice grows with decreasing temperature, we expect that the resulting $R_{\mathrm{AHE}}$ signal is parallel to the magnetisation of the Tm-ions for $T \ll T_{\mathrm{PR},2}$ [357, 361–363]. To review and re-summarise the characteristics at this transition under an out-of-plane magnetic field: a divergence of the coercive field; an (abrupt) change of the polarity of the $\Delta R_{\mathrm{AHE}}$, which becomes smooth when flipping the sign below $T_{\mathrm{PR},2}$ and multi-transitional behaviour in the AHE. We reiterate that at a true magnetic compensation point, the Fe sublattice magnetisation is expected to reverse and become antiparallel to the applied magnetic field, whereas at a compensation-like temperature the Fe magnetisation remains parallel to the field. In total, we could come up with six distinct physical mechanisms that could be responsible for a transition akin to $T_{\mathrm{PR},2}$ in TmIG:

(i) Compensation-like transition
The simplest explanation could be that the transition is compensation-like, where the net magnetisation remains finite. Most notably, we did not perform direct magnetometry (e.g., SQUID or VSM) to reveal a vanishing of the net magnetisation across $T_{\mathrm{comp},2}$. The anomalous Hall signal, although reversing sign, remains finite and smooth under flipping, and the polarisation reversal is not accompanied by measured abrupt changes in magnetic anisotropy or damping that typically accompany a full compensation state. Furthermore, the system is physically complex, and potentially a similar mechanism as is valid for $T_{\mathrm{PR},1}$ is present here due to a local reduction of MPE or SHE. These considerations, consistent with observations in literature of Pt/TmIG and Pt/GdIG structures [299, 318], suggest that $T_{\mathrm{comp},2}$ could mark a second crossover in interfacial dominance, rather than a strict zeroing of the total ferrimagnetic moment. The term compensation-like would therefore be more appropriate.

(ii) Additional rare-earth ion coupling term to the AHE
The $4f$ electrons of the rare-earth ions (Tm) may begin to contribute more strongly to the AHE via interfacial proximity exchange as temperature decreases. If the sign of the proximity-induced AHE from Tm opposes that of

the Fe contribution, the total AHE signal may reverse sign without a true compensation of bulk magnetisation [364]. This mechanism is consistent with the interfacial nature of AHE in HM/MI heterostructures [299].

(iii) Phase mixture of sublattices or compositions
The TmIG film may contain spatially mixed or compositionally distinct regions, such as Tm-rich and Fe-rich garnet phases. If these phases have different temperature dependencies of their sublattice magnetisations, then the apparent compensation point may reflect the crossover between dominant contributions, rather than true sublattice cancellation [363,365]. In this case, the magnetisation is due to a temperature-dependent composition gradient, with two sublattices attributing to the net magnetisation side-by-side, and independently, which approaches equilibrium before reversing across the compensation point [318].

(iv) Topological singularity in the electronic band structure
For the ferromagnet $SrRuO_3$ and HM/ferrimagnet heterostructure Pt/TbFeO, a Berry-phase-based explanation for AHE sign reversals has been proposed [356]. There, the sign change in AHE with temperature was attributed to the Fermi level crossing a topological singularity in the band structure; specifically, a Berry curvature monopole near an avoided crossing [366]. This mechanism is mostly observed in itinerant ferromagnets or semimetals, where spin–orbit-coupled bands near the Fermi level exhibits such momentum-space anomalies.

(v) Magnon-mode competition in compensated ferrimagnets
In systems like GdIG or DyIG, the spin Seebeck effect and other spin-transport signatures exhibit temperature-driven sign reversals due to the competition between distinct magnon modes [367, 368]. Near compensation, acoustic-like and optical-like magnon branches with opposite spin polarisation may dominate at different temperatures. If spin angular momentum is carried by these magnons into the metal, the resulting interfacial AHE (via spin-to-charge conversion) may also exhibit polarity reversal. This effect depends sensitively on interfacial magnon transmission and magnetic sublattice orientation, and could, in principle, contribute to a coercive-field divergence if the dominant mode crosses zero angular momentum.

(vi) True magnetisation compensation
The most conventional interpretation is that $T_{\mathrm{PR},2}$ represents a true magnetisation compensation point, where the net magnetisation of the ferrimagnet vanishes due to antiparallel sublattice moments of equal magnitude. This yields an infinite magnetic susceptibility and thus a divergence in coercivity. Experimental confirmation would require observing the vanishing of net magnetic moment in SQUID or vibrating sample magnetometry alongside a divergence in $H_{\mathrm{c}}$.

We shall consider these explanations one by one. The compensation-like explanation (i) of the transition is unlikely. Given that the present TmIG/GGG heterostructure employs the same GGG substrate as used by Soares *et al.* [318], a compensation-like scenario - where the Fe magnetisation remains parallel to the field - does appear plausible at first glance. However, this interpretation fails to account for the observed polarity reversal of the anomalous Hall effect in the Pt layer. Additionally, from the data shown

in Figures 4.9 and 4.10, the coercive behaviour is distinct between $T_{\mathrm{PR},1}$ and $T_{\mathrm{PR},2}$. If the transition would be a compensation-like transition, there is no adequate explanation of the divergence of $H_c$. Furthermore, due to the similarities in materials, we determine from the magnetometry results of Soares *et al.* [318] via an order-of-magnitude estimate what is the remaining magnetisation of our Pt/TmIG-sample at $T_{\mathrm{PR},2}$. Here, we use the inverse scaling of the coercive field with magnetisation near a compensation point: $H_{\mathrm{C}} \sim \frac{1}{M}$. Furthermore, we assume that $\Delta R_{\mathrm{AHE}}$ relates linearly to the magnetisation $M$ [369], which is valid if the effect of MPE is low compared to the effect of the SHE [355]; generally, if only a single magnetic sublattice would dominate the magnetisation effects, a $T^{\frac{3}{2}}$ law would be expected [350]. Relating the results of Soares *et al.* ($M_{300\mathrm{K}} = 2\ \mu_B$/ f.u., $M_{\mathrm{T_{comp-like}}} \approx 0.5\mu_B$/f.u.) to ours, we obtain a remaining magnetisation at $T_{\mathrm{PR},2}$ of $M_{\mathrm{PR},2} \approx 6 \times 10^{-6}\ \mu_B$/f.u, which is negligibly low and indicates that $T_{\mathrm{PR},2}$ is likely a true compensation temperature. This estimate relies on the assumption that $H_{\mathrm{C}} \sim 1/M$ scales identically between our 6 nm strained films and the 30 nm films of Ref. [318]. Deviations from this scaling due to inhomogeneous strain could alter this estimate by an order of magnitude, yet do not change the general conclusion that the transition is likely a true compensation temperature.

What then, if we just assume an additional contribution to the AHE sign as in (ii), originating from the $Tm^{3+}$-ions? Since the Pt-AHE is widely attributed to magnetic proximity coupling between Fe 3*d* and Pt 5*d* orbitals [299], a compensation scenario would require an additional proximity-induced contribution from the Tm 4*f* electrons to explain the polarity reversal [364]. That is, at $T_{\mathrm{PR},2}$, the Tm magnetisation has become the dominating factor of the net magnetisation. Consequently, for $T < T_{\mathrm{PR},2}$, the signal would follow the Pt-Tm coupling compared to the Pt-Fe coupling, leading to non-monotonous behaviour in the inset of Fig. 4.10. This is not observed. Conversely, if one assumes that the Pt magnetic proximity effect is dominated by interaction with Fe 3*d* electrons, the observed AHE polarity change implies a reversal of the Fe sublattice magnetisation, consistent with the realisation of a true magnetic compensation point in the Pt/TmIG/GGG system. Third, we consider whether the transition is due to TmIG existing as a phase mixture. In favour is the multi-domain behaviour. However, in this case, we would observe specific "humps" in the AHE spectrum over a wide temperature range that mimic the topological Hall effect, separate from the multi-domain behaviour [363]. Additionally, from the EDX characterisation in Figure 4.3, the Tm and Fe ions are uniformly distributed, and no Gaussian density profile is present, although this data was taken at room temperature only. This is strengthened by the analysis of Figure 4.2 showing clear, distinct peaks in the XRD pattern. Explanation (iv) is a topological singularity in the electronic band structure of TmIG. Also this explanation is unlikely to apply to our Pt/TmIG systems. TmIG is a ferrimagnetic insulator with the Fermi level in a wide band gap [370] and the contribution of bulk electronic bands is thus suppressed; its electronic structure does not have the Fermi level near any low-energy band crossings within the garnet. Since charge carriers do not propagate through the TmIG, their contribution to the total AHE signal can only be limited. Consequently, we reject this explanation.

Another proposed possibility is the competition between opposite-handed magnons, discovered via the spin Seebeck effect under an in-plane magnetic field (v). However, as far as we know, there has not been conclusively shown that (a) a compensation temperature with an out-of-plane field leads to the same compensation temperature using an in-plane field and (b) a simultaneous spin Seebeck and AHE measurement, showcasing the divergence of the coercive field at the transition temperature. Addi-

tionally, Cramer *et al.* showed that the potential equivalent $T_{PR,2}$ in their samples did not depend on the HM layer material, in direct contradiction to more relatable AHE results of Shao *et al.* [342].
Rejecting one more potential explanation of polarity change using liquid ionic gating (absent for us) [371], the only remaining realistic possibility is (vi): that the transition is a true compensation temperature. Thus, based on the pronounced $|H_C|$ divergence (reaching 3.5 T), the sign inversion of $\Delta R_{AHE}$ producing smooth behaviour after numerical flipping (Fig. 4.10a inset), the small remnant magnetisation when comparing to literature values and the multi-domain switching behaviour (Fig. 4.10b), we interpret $T_{PR,2}$ as a temperature where the Fe and Tm sublattice magnetisations cancel. In other words, $T_{PR,2}$ exhibits all the hallmarks of a magnetisation compensation point. Strain and finite-size effects in the ultra-thin films are expected to enhance these differences in sublattice magnetisation and thereby sharpen the compensation behaviour.

| Material stack (HM/ REIG/ sub.) Thickness (nm) | $T_{PR}$(K) | | Strain | Measurement method | Reference |
|---|---|---|---|---|---|
| | with $H_C$ div. | w/o $H_C$ div. | | | |
| Pt (3) / TmIG (6) / GGG | 81 | 121 | 0.42% | AHE | [41] |
| - / TmIG / GGG | 46 | - | 1.31% | *M* | [318, 372] |
| W (5) / TmIG (6) / Nd:GGG | 75 | 45 | 1.44%† | AHE | [342, 373] |
| Pt (5) / TmIG (6) / Nd:GGG | 82 | - | 1.44%† | AHE | |
| Pt (5) / TmIG (20) / GGG | - | 80 | 0.48%† | AHE, *M* | [299] |
| Pt (5) / Cu (2) / TmIG (20) / GGG | - | - | 0.48%† | AHE | |
| Pt(10) / BiGa:TmIG (1410) / GGG | 135 | 60 | 1.31% | AHE | [347] |
| Pt (6) / TmIG (6) / 2-Graphene / SGGG | 150 | 15 | -2% | AHE | [343] |
| Pt (6) / TmIG (6) / SGGG | - | 50 | -1.25% | AHE | |

**TABLE 4.2:** REPORTED OR EXTRACTED (VISUALLY ESTIMATED) COMPENSATION AND COMPENSATION-LIKE TEMPERATURES IN TMIG THIN FILMS CAPPED WITH HEAVY METALS ON DIFFERING SUBSTRATES. MEASUREMENT METHODS INCLUDE ANOMALOUS HALL EFFECT (AHE) AND MAGNETISATION *M* (SQUID MAGNETOMETRY [318] AND VIBRATING SAMPLE MAGNETOMETRY [299]). ONLY WE REPORT TWO POLARITY REVERSALS WITHIN A SINGLE UNIFORM PT/TMIG FILM.
† ESTIMATED FROM UNSTRAINED LATTICE CONSTANT VALUES.

However, true compensation in TmIG has not been observed before, nor has the observation of two distinct polarity-reversal temperatures in a uniform ultra-thin Pt/TmIG/(111)GGG heterostructure been previously reported or explained in the literature, particularly in heterostructures with relatively small epitaxial strain. We therefore summarise the results on TmIG-based heterostructures in Table 4.2, indicating the temperatures of polarity reversal and the presence or absence of a divergence of $|H_C|$. The lattice strain in our films is approximately a third of that reported in earlier studies on Nd:GGG substrates [342] and the TmIG thickness investigated here is nearly five times smaller than that in Ref. [318]. This ultrathin film structure may facilitate the emergence of a true compensation point, in line with recent observations by Yu *et al.*, who demonstrated thickness-dependent shifts of the compensation temperature in TmIG films grown on SGGG substrates [343]. We therefore suggest that a similar thickness-driven effect may occur even on GGG substrates with modest strain.
In the end, the exact nature of the transition thus remains indefinite since confirming the sublattice magnetisations requires element-specific probes. We therefore conservatively refer to this point as compensation-like to acknowledge the ambiguity in its

precise magnetic nature. Ultimately a definitive distinction requires element-specific measurements of the sublattice magnetisations, for instance, by X-ray magnetic circular dichroism (XMCD) which were unattainable at this time. Until such measurements are performed, the exact magnetic configuration below $T_{\mathrm{PR},2}$ remains unresolved.

Summarising, this Section described the temperature-dependent anomalous Hall response of Pt (3 nm)/TmIG (6 nm)/GGG(111) heterostructures and demonstrate the presence of two distinct polarity reversals. The higher-temperature polarity reversal at $T_{\mathrm{PR},1} \approx 124$ K is not accompanied by a divergence of the coercive field $|H_{\mathrm{C}}|$ or other signatures of vanishing net magnetisation. This behaviour suggests that $T_{\mathrm{PR},1}$ arises from purely interfacial transport effects, such as the temperature-dependent competition between spin Hall magnetoresistance and the magnetic proximity effect, rather than from a competition between the magnetisation of the ferrimagnetic sublattices. In contrast, the lower-temperature transition at $T_{\mathrm{PR},2} \approx 81$ K is accompanied by a pronounced divergence of the coercive field and signatures of multi-domain switching. This is consistent with established ferrimagnetic compensation physics and highlights the strong influence of strain and finite-size effects on the balance of sublattice magnetisations in ultrathin TmIG films. However, because of the lack of element-specific magnetic measurements, we cannot definitively confirm whether this represents a true compensation temperature or a near-cancellation of sublattice magnetisations.

**Ordinary Hall effect-component**

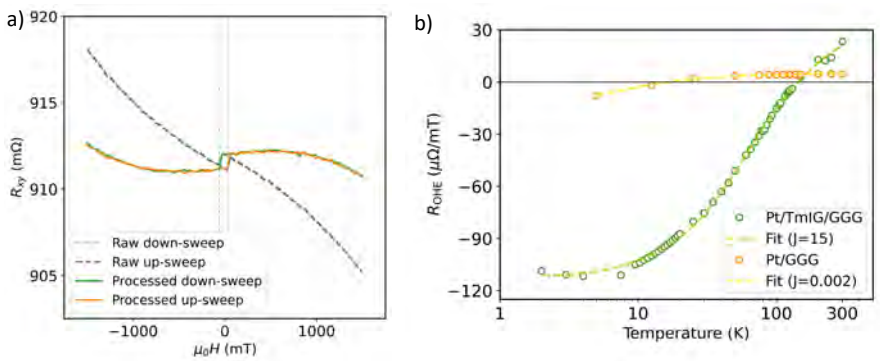


**Figure 4.11: a)** Anomalies in the ordinary Hall effect (OHE) coefficient for Pt/TmIG/GGG at high fields of the anomalous Hall effect (AHE) data taken at $T = 130$ K. **b)** Extracted OHE coefficient $R_{OHE}$ from the AHE data. The polarity-switching of the OHE linear coefficient occurs at $T \approx 140$ K and $T \approx 16$ K for respectively the Pt/TmIG/(111)GGG and Pt/(111)GGG samples.

From the $\Delta R_{\mathrm{AHE}}$ data in the previous Section, we could extract the OHE data following the detailed procedure. Figure 4.11a showcases the high-field non-linear Hall component of the OHE at 130 K. At higher magnetic fields ($\gtrsim 1.5$ T), we observe such additional anomalous contribution to the OHE. As we extract only the low-field, linear component of the OHE for data rectification, we neglect this effect that originates from multiple bands of the Pt contributing to the signal [289, 364, 374]. Besides multiband ordinary Hall physics, recent work has shown that strong spin–orbit metals like Pt host spin-Hall–Hanle transverse voltages arising from boundary spin accumulation and

spin precession, producing a non-linear Hall-like signal even without any magnetic interface. In the weak-precession regime this contribution can appear linear in $\mu_0 H$ and is practically indistinguishable from the "normal" OHE; at high spin precession, it would be quadratic which is not observed in our data [375].

Figure 4.11b compares the temperature dependence of the extracted ordinary Hall coefficient $R_{\mathrm{OHE}}(T)$ in a Pt(3 nm)/TmIG(6 nm)/(111)GGG Hall cross device with that of a reference Pt(3 nm)/(111)GGG device. In each respective case, $R_{\mathrm{OHE}}$ is extracted as described in the main text for the Pt/TmIG/GGG sample or from a linear fit over the entire field range for the Pt/GGG device, as no non-linearities are observed in the latter sample (up to $\pm 1$ T). Between the two stacks, the resulting $T$-dependence differs qualitatively both in magnitude as in value.
For Pt/TmIG/GGG, $R_{\mathrm{OHE}}$ is large and strongly non-linear, evolving from approximately $-11 \times 10^2\,\mu\Omega/\mathrm{mT}$ at low temperature to a positive value of roughly $25\,\mu\Omega/\mathrm{mT}$ at room temperature. The magnitude therefore varies by nearly an order of magnitude and changes polarity at $\approx 140$ K. We interpret this as arising from temperature-dependent exchange-enhanced paramagnetism in the Pt layer induced by the TmIG rare-earth sublattice. Unlike the AHE, which is sensitive to interfacial magnetisation direction, the OHE responds to the total scattering asymmetry of majority and minority carriers. The sign reflects the relative weighting of electron-like and hole-like contributions, which depend on both carrier densities and mobilities, and changes with temperature even if the underlying band topology does not literally switch from electron-dominated to hole-dominated; still, the sign change at 140 K could reflect a crossover in the dominant charge carrier type in Pt as the proximity-induced exchange splitting evolves with temperature. Temperature-dependent sign changes of the effective OHE in ultrathin Pt adjacent to a ferrimagnetic insulator have been reported previously in Pt/YIG, where the effect strengthens strongly below 4 nm Pt and is absent for Pt on non-magnetic substrates, pointing to an interfacial modification of Pt transport [289]. Proximity-induced magnetism in heavy metals on FiM is typically confined to a short interfacial region (on the order of nm) and depends on which sublattice supplies the effective exchange coupling (in our case, Fe or TmIG). A resonant X-ray study of Pt layered with Re:HM ferrimagnets finds a proximity-induced Pt moment confined to about a 2-nm interfacial region and aligned with the HM-sublattice and aligned parallel to the transition-metal moments, irrespective of the direction of the net magnetisation [376].

In contrast, the Pt/GGG control sample only exhibits a small, monotonic evolution of $R_{\mathrm{OHE}}$ from about $-7.5$ to $4.5\mu\Omega/\mathrm{mT}$, with a smooth crossover point of $\approx 16$ K. Such crossover is indicative of the paramagnetism induced in the Pt-layer, as a temperature dependence is (nearly) absent in Pt/Si samples [377]. To quantify the curvature, both data sets were fitted using a single Brillouin-type model of Equation 4.6.
For Pt/TmIG/GGG, scanning $J$ and comparing the fits via the Akaike information criterion reveals a best-fit with an effective Brillouin index of $J_{eff} = 15.00 \pm 0.01$. Although the curve follows the data well at temperatures larger than $\sim 30$ K, the low temperature behaviour is not well caught, likely because the temperature dependence of $J_{eff}$ in TmIG was not taken into account or due to the interaction between induced magnetic moments that become an important factor [371, 378, 379]. The corresponding curve with $J_{eff} = 15$ reproduces both the steep low-temperature rise and the high-temperature saturation of $R_{\mathrm{OHE}}$ with good fidelity. We stress that the

Brillouin fit with effective $J_{eff} = 15$, although curious it is exactly an integer, should not be interpreted as an intrinsic ionic angular momentum of $Tm^{3+}$ (which is $J = 6$ for the $^3H_6$ ground state [319, 380]). Instead, it reflects the temperature dependence of the exchange-enhanced Tm moment in the presence of Fe-Tm antiferromagnetic coupling in strained TmIG films. Because $B_J$ depends on both $J$ and the scaling parameter $a$, there is a trade-off: different ($J$,$a$) pairs produce very similar curves over a limited temperature window. We scanned $J$ in the range 0-50 and used the AIC maximum as the decider; yet, these parameters remain phenomenological. However, bulk studies demonstrated that the projected Tm contribution in TmIG is strongly reduced and highly anisotropic, with substantial canting and crystal-field effects, producing magnetisation curves that deviate significantly from a simple $J = 6$ Brillouin form [319]. Speculating, the large effective $J \approx 15$ signifies that the Pt layer senses a strongly magnetisation-driven evolution of the internal field dominated by the TmIG rare-earth sublattice. The large $J_{eff}$ captures this collective behaviour phenomenologically.

The fact that $T_{\mathrm{PR,OHE}} \neq T_{\mathrm{PR},,1} \neq T_{\mathrm{PR},,2}$ demonstrates that different observables probe distinct aspects of the multi-sublattice magnetisation dynamics. The OHE is most sensitive to the Pt band structure [364], the AHE at $T_{\mathrm{PR},1}$ reflects Pt interfacial spin transport mechanisms, and the AHE at $T_{\mathrm{PR},2}$ directly probes net magnetisation compensation. This multi-probe approach provides a more complete picture than single-method characterisation. For the Pt/GGG reference sample, the same Brillouin analysis yields a best fit with $J_{eff} \approx 0$, effectively reducing the model to a smooth crossover. This result aligns with the absence of a magnetic rare-earth iron garnet layer: GGG hosts diluted $Gd^{3+}$ moments with frustrated antiferromagnetic nearest-neighbour exchange interactions and no long-range order in the measured temperature and field range [381, 382]. Instead it supports regimes of short-range correlations while field-induced order appears under applied field [383,384]. Consequently, the interfacial magnetisation sensed by Pt remains small and only weakly temperature dependent.

Summarising, the pronounced Brillouin-like dependence and polarity reversal of $R_{\mathrm{OHE}}(T)$ in Pt/TmIG/GGG is not an intrinsic property of Pt, but arises from its coupling to the magnetisation of ultrathin TmIG. The Pt/GGG control provides a baseline without ferrimagnet elements, while the Pt/TmIG/GGG data show that the ordinary Hall response of Pt serves as an additional probe of rare-earth sublattice magnetisation.

### 4.2.2 Current-induced magnetisation switching

While the room temperature SOT switching presented in Section 4.1.3 is robust and reproducible, maintaining this behaviour over a wide temperature range proves considerably more challenging. As shown in the preceding section, cooling TmIG leads to pronounced changes in both the anomalous Hall response and the coercive field, reflecting the increasing role of its ferrimagnetic sublattice structure. Although current-induced switching in Pt/TmIG heterostructures is well established at room temperature, its evolution at lower temperatures (particularly in the vicinity of a compensation point) remains comparatively unexplored. In this section, we investigate this switching behaviour with temperature. Experimentally, we observe a clear degradation of deterministic switching upon cooling. Full magnetisation reversal is readily achieved at room temperature, whereas below approximately 100 K switching

becomes incomplete, stochastic, or entirely absent. This persists even at high current densities that could potentially damage the device, and later indeed do. The temperature evolution of this behaviour is shown in Fig. 4.12.

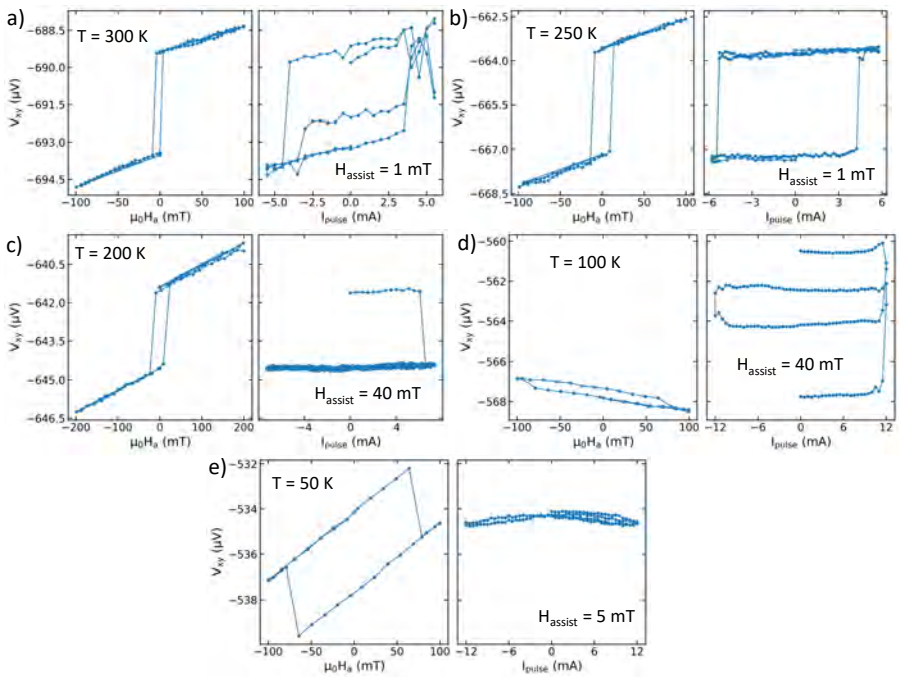


**Figure 4.12:** Temperature dependence of SOT switching in Pt/TmIG devices. **a**) 300 K, $\mu_0 H_a = 1$ mT. **b**) 250 K, $\mu_0 H_a = 1$ mT. **c**) 200 K, $\mu_0 H_a = 40$ mT, showing partial switching. **d**) 100 K, $\mu_0 H_a = 40$ mT, showing no switching. **e**) 50 K, $\mu_0 H_a = 5$ mT. The device broke after this measurement.

This behaviour is understood in the broader context of compensated ferrimagnets. In TmIG, the net magnetisation arises from multiple antiferromagnetically coupled sublattices with distinct temperature dependences. As the temperature approaches the magnetic compensation temperature $T_{\mathrm{comp}}$, the net magnetisation decreases and may vanish entirely. Concomitantly, the coercive and anisotropy fields increase, leading to a substantial modification of the magnetic energy landscape and a higher energy barrier for magnetisation reversal. As a result, the spin–orbit torque generated in the adjacent heavy metal layer increases significantly or may not even longer be sufficient to drive deterministic switching. Similar trends have been reported in other compensated ferrimagnets, including insulating systems such as GdIG [309] and TbIG [385], as well as metallic alloys such as CoTb [386] and GdCo [332]. Across these systems, the suppression of SOT switching at low temperature is consistently attributed not to reduced spin current generation, but to the rapid increase of the magnetic energy barrier near compensation. To describe this behaviour quantitatively, the conventional macrospin picture used for ferromagnets (i.e. exhibiting coherent rotation and switching) must be extended to account for the multi-sublattice nature of ferrimagnetic insulators [307, 309, 386]. Rare-earth iron garnets crystallise in a cubic structure in which the tetrahedral ($d$) and octahedral ($a$) sites are occupied by $Fe^{3+}$ ions. These iron moments form a strongly exchange-coupled heavy metal

(transition-metal) sublattice. The dodecahedral ($c$) sites are occupied by rare-earth (Re) ions, which couple antiferromagnetically to the iron moments through superexchange interactions mediated by oxygen ligands. Because the $4f$ orbitals of the Re ions are strongly localised and well shielded, the exchange interaction between the Re and HM sublattices ($J_{\mathrm{Re-HM}}$) is substantially weaker than the internal coupling between the iron sites ($J_{ad}$). As a result, the temperature dependence of the Re and HM sublattice magnetisations differs significantly. The macroscopic magnetisation of the ferrimagnet is therefore given by the difference between the two opposing sublattices, as utilised also in Equation 4.6,

$$M_{\mathrm{net}}(T) = \left| M_{\mathrm{HM}}(T) - M_{\mathrm{Re}}(T) \right|, \tag{4.7}$$

which vanishes at $T_{\mathrm{comp}}$.
Approaching this point leads to a strong increase in the coercive field. For a uniaxial magnetic system, $H_c$ is approximated as [387, 388]

$$H_c \approx \frac{2K_{\mathrm{eff}}}{\mu_0 M_{\mathrm{net}}}, \tag{4.8}$$

where $K_{\mathrm{eff}}$ is the effective magnetic anisotropy. The coercive field thus diverges as $M_{\mathrm{net}} \to 0$. This behaviour is observed experimentally (Fig. 4.9) and directly reflects an increasing energy barrier for reversal. This strong enhancement of coercivity near the compensation temperature is widely observed in compensated ferrimagnetic systems. Within heavy-metal/ferrimagnet heterostructures such as Pt/TmIG, at room temperature, magnetisation switching is driven primarily by the damping-like spin–orbit torque generated by the spin Hall effect in the heavy metal layer. The injected spin current exerts a torque on the magnetic moments of the ferrimagnet, which relates directly to the necessary switching current defined in Equation 4.3; it expresses that $J_{\mathrm{sw}} \propto M_s t_{\mathrm{fm}} H_K \cdot (-H_x) \propto H_{\mathrm{DL}}$ and inversely proportional to the damping-like torque efficiency of Equation 4.1. In this simplified picture, the damping-like spin-orbit torque field (the effective magnetic field generated by an in-plane electric current which directly manipulates the magnetisation of an adjacent magnetic layer) $H_{\mathrm{DL}} \propto \frac{1}{Ms}$ suggesting that the switching current should decrease as $M_s \to 0$. While experiments indeed show an enhancement of the effective torque efficiency near compensation [309, 386, 389, 390], they consistently demonstrate the opposite trend for switching: deterministic reversal becomes more difficult and requires larger current densities. For example, Li *et al.* performed harmonic Hall measurements on epitaxial GdIG/Pt heterostructures and observed a pronounced enhancement of the damping-like torque efficiency near the magnetisation compensation temperature ($T_{\mathrm{comp}} \approx 297$ K) [309]. By analysing the first- and second-harmonic Hall signals under a rotating in-plane magnetic field, they extracted the effective torque efficiency and showed that it increases strongly as the net magnetisation decreases, consistent with the expected $1/M_s$ scaling.A similar enhancement of the SOT efficiency near compensation has also been reported in metallic ferrimagnetic alloys such as CoTb and GdFeCo [386, 389, 390]. In these systems, harmonic Hall and spin–torque measurements demonstrate that the effective torque generated by a given current becomes significantly larger close to the compensation point in compensated ferrimagnets compared to conventional ferromagnets, while not leading to easier magnetisation switching. We compare some of these results in Table 4.3

To explain this phenomenon, we look at the basic physical mechanisms behind SOT switching. Current-induced SOT switching in ultrathin PMA layers occurs through

| Structure | Source | $T_{\text{comp}}$ | $H_{DL}$ | $J_{\text{sw}}$ | Ref. |
|---|---|---|---|---|---|
| **GdIG / Pt** | SHE | $\sim 297$ K | Diverges | Large | [309] |
| **TbIG / W** | SHE | $\sim 355$ K | Diverges | - | [385] |
| **GdFeCo / Pt** | SHE | Alloy dependent | $\sim 1/M_s$ | Large | [389] |
| **CoTb / Ta** | SHE | Alloy dependent | $\sim 1/M_s$ | Large | [386, 391] |
| **TmIG / Pt** | SHE | 81K | Unknown | T-dependent | This thesis |

**TABLE 4.3:** COMPARATIVE SUMMARY OF SPIN-ORBIT TORQUE SWITCHING PARAMETERS AND THERMODYNAMIC SCALING BEHAVIOUR ACROSS DISTINCT COMPENSATED FERRIMAGNETIC HETEROSTRUCTURES. BOTH THE SOT FIELD $H_{\text{DL}}$'S AND SWITCHING CURRENT $J_{\text{sw}}$'S EVOLUTION ARE GIVEN NEAR $T_{\text{comp}}$. THE $J_{\text{sw}}$ OF TBIG / W IS OBSCURED BY HEATING

(i) nucleation of a reversed domain and (ii) rapid propagation of a domain walls across the device. This is well established in time-resolved experiments, which identify an intrinsic short-pulse regime and a thermally assisted long-pulse regime; in both cases, the observed reversal is consistent with nucleation and fast domain propagation and does not follow a single-domain macrospin picture [392]: SOT magnetisation reversal in ultra-thin ferrimagnetic films with PMA does not occur via uniform coherent rotation. Thus, while the effective torque increases, the energy barrier for domain nucleation and propagation increases more rapidly. As a result, the switching current does not vanish near $T_{\text{comp}}$, but instead remains large or even increases. In Pt/TmIG, the interfacial Dzyaloshinskii–Moriya interaction stabilises Néel-type domain walls [332, 393, 394]. The thermodynamic activation energy barrier $E_A$ required to nucleate a stable, reversed domain of critical volume $V_n$ is dictated by the competition between the domain wall surface energy penalty (first term) and the Zeeman-like volume energy $E_z$ supplied by the injected SOT (second term):

$$E_A = \sigma_{DW} A_n - \mu_0 M_s H_{\text{DL}} V_n, \tag{4.9}$$

with $\sigma_{DW} \sim \sqrt{K_{\text{eff}}}$ represents the domain wall surface energy density which thus scales with the effective uniaxial anisotropy $K_{eff}$, and $A_n$, the surface area of the newly nucleated domain boundary. Then, we substitute the definition of $H_{DL}$ (Eq. 4.1) into the Zeeman energy term [395, 396]. This damping-like field to the torque acts orthogonally to the local magnetisation vector:

$$E_Z = \frac{\hbar}{2e} \frac{\theta_{SH}^{DL} J_e}{t_{FM}} V_n, \tag{4.10}$$

such that the explicit dependence on $M_s$ cancels. The driving energy is therefore largely independent of the macroscopic magnetisation [389], other effects notwithstanding, and gives an intuitive picture of the observed behaviour. Near compensation, the increasing anisotropy and coercivity dominate, leading to a larger domain wall energy penalty $\sigma_{DW}$ and, consequently, higher switching currents.

In addition to these intrinsic effects, Joule heating plays an important role in current-induced switching. The large current densities required for SOT switching ($J_e \sim 10^{11}$ A m$^{-2}$) generate significant power dissipation in the heavy-metal layer with electrical resistivity $\rho_{\text{HM}}$

$$P = J_e^2 \rho_{\text{HM}}, \tag{4.11}$$

which substantially raises the local device temperature. For pulse durations in the millisecond regime, the system approaches a quasi-steady thermal state, resulting

in temperature increases of several hundred kelvin [385]. In W/TbIG, this leads to switching occurring in a high-temperature phase, even when the base temperature is well below $T_{\mathrm{comp}}$. Such heat-assisted switching obscures the intrinsic temperature de-

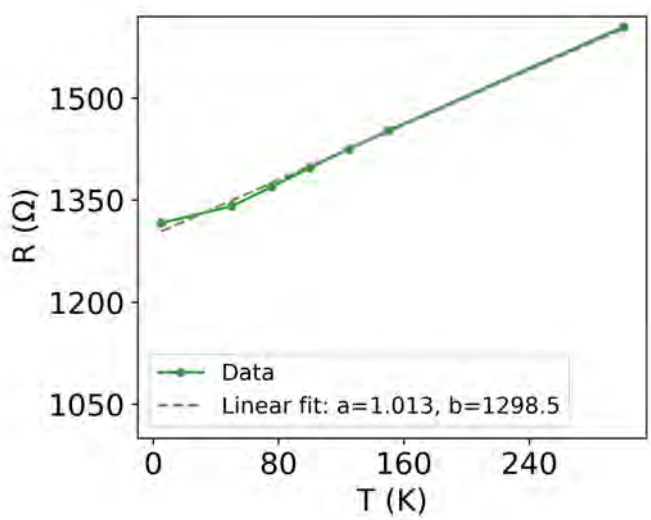


**Figure 4.13:** Temperature dependence of $R_{xx}$ in Pt/TmIG/GGG.

pendence. This contrasts with experiments using short pulses ($\sim$ 100 ns), where Joule heating is minimised and the intrinsic switching behaviour is recovered [309, 397].

In the present Pt/TmIG devices, however, the suppression of switching below $\sim$ 200 K cannot be fully explained by compensation or Joule heating alone. As discussed in Section 4.2.1, a well-defined compensation temperature is not observed, and instead a compensation-like transition occurs around 124 K, likely influenced by interfacial effects. At high temperatures, the SOT is primarily driven by the SHE in Pt. The efficiency of this charge-to-spin conversion is again characterised by the spin Hall angle $\theta_{SH}$, that depends on both intrinsic band-structure contributions and extrinsic scattering processes [398]. Because phonon scattering decreases strongly at low temperatures, the longitudinal resistivity $\rho_{xx}$ of platinum decreases accordingly, as shown in Figure 4.13, modifying the balance between these contributions and potentially reducing the effective spin Hall angle. Experimental studies in Pt/YIG report a reduction from $\sim$ 0.11 at room temperature to $\sim$ 0.075 at low temperature [399]. Simultaneously, the efficiency of spin transfer across the interface is reduced, while the magnetic proximity effect becomes increasingly dominant. In the present devices, this crossover occurs near 124 K and coincides with a reversal of the Hall polarity. The combined effect of reduced spin Hall efficiency, diminished interfacial spin transparency, and increasing MPE leads to a reduction in the effective torque. Under these conditions, the available SOT is insufficient to overcome the enhanced coercive field, resulting in the observed suppression of deterministic switching at low temperature.

## 4.3 Integration of TmIG with a superconducting waveguide

Finally, we present initial measurements of TmIG integrated with a superconducting waveguide. These experiments constitute the first implementation of such a hybrid platform in our laboratory and remain ongoing at the time of writing; the results shown here should therefore be regarded as preliminary. All measurements were performed in a dilution refrigerator equipped with a (1,1,9)-vector magnet. For simplicity, the microwave response was measured in transmission through a coplanar waveguide, and not a resonator, to simplify physics and to check whether magnons could be observed. We fabricated this device on GGG/TmIG(20nm) substrates, as grown by the Spin Lab at Kyushu University. On this, we sputtered $\sim$ 100 nm of NbTiN using cold deposition as to not overheat the sample, giving a kinetic inductance $L_k \approx 1$ pH/□. Devices were simulated using Sonnet, and the final geometry is shown in the inset of Figure 4.14; the parameters of the device are $W = 6\ \mu$m and $G = 22\ \mu$m, giving an impedance of $\sim 50\ \Omega$. The microwave simulations showed no resonances up to 25 GHz using sapphire as a dielectric, which has a similar relative permittivity as GGG [400, 401], although it is unclear how the latter scales with temperature. Future device iterations will incorporate field-resilient resonator designs, as discussed in previous chapters. We remind that at 2 K, the coercive out-of-plane field of TmIG is 220 mT.

For magnon-measurements, the general equation describing the dynamics is the Landau-Lifshitz-Gilbert equation. The magnetic moment $\mu$ of an atom in a solid with total angular momentum $J$ is given by

$$\mu = -\gamma J, \tag{4.12}$$

where $\gamma = \frac{g\mu_B}{\hbar}$ is the gyromagnetic ratio. It consists of the Landé g-factor $g$, and the Bohr magneton $\mu_B$. Due to this relation between the angular momentum and the magnetisation. the effective field experienced $H_{\text{eff}}$ by the sample exerts a torque $\tau$ on the magnetisation $M$. This leads to the Landau-Lifshitz equation [402, 403]:

$$\frac{\mathrm{d}M}{\mathrm{d}T} = -\gamma M \times \mu_0 H_{\text{eff}}\ . \tag{4.13}$$

This effective field is all the fields that lead to a reorientation of the magnetic moments. It is a combination of the magnetocrystalline anisotropy, uniaxial anisotropy ($H_u$, defined akin to Eq. 4.8), the applied external field $H_a$ and a demagnetisation field due to shape anisotropy. The latter can be seen intuitively as the magnetic analogue of surface tension; on the surface of the material, "north" and "south" poles exist of the magnetic material. They lead to a stray field outside, and a demagnetisation field inside the magnetic volume. Equation 4.13 is for the ideal, unattenuated case and leads to a precession of the magnetic moment around the effective field. However, various relaxation mechanisms, such as magnon-phonon relaxation and inter-magnon scattering require the inclusion of a damping term $\alpha$ to fully capture the dynamics. It was Gilbert who introduced this term [404,405], and hence the Landau-Lifshitz-Gilbert equation becomes

$$\frac{\mathrm{d}M}{\mathrm{d}t} = -\gamma M \times \mu_0 H_{\text{eff}} + \frac{\alpha}{M_s} M \times \frac{\mathrm{d}M}{\mathrm{d}t}\ , \tag{4.14}$$

where $\alpha$ is rescaled with the saturation magnetisation $M_s$. This is where the usefulness of TmIG comes in for magnonics; it possesses a low damping constant in the range of

$10 \times 10^{-3}$ [310, 406] which benefits, among others, long-range spin wave propagation (scaling as $\sim \frac{1}{\alpha}$). With the inclusion of the damping term, the system is analogous to a damped harmonic oscillator in classical mechanics. If an external driving field is applied, the dynamics change further, and it leads to the Kittel equation of ferromagnetic resonance, and the corresponding existence of a resonance field $H_{\text{res}}$ and a resonance frequency $f_r$. In the case for a thin film, it becomes [407]:

$$H_{\text{res}} = \begin{cases} M_s - H_u + \dfrac{2\pi f}{\gamma\mu_0}, & \text{out-of-plane } H_a, \\ -(\dfrac{1}{2}M_s + H_u) + \sqrt{\left(\dfrac{2\pi f}{\gamma\mu_0}\right)^2 + \left(\dfrac{M_s}{2}\right)^2}, & \text{in-plane } H_a. \end{cases} \tag{4.15}$$

From these sets of equations, one extracts the gyromagnetic ratio, and the damping parameter from $\frac{\gamma}{\omega_{FMR}}$ [408]. Finally, when coupling to a resonator, also the magnon-phonon coupling rate is extracted, analogous to Chapter 3.

As discussed above, the measurements were performed using a CPW geometry without a well-defined resonant mode. Consequently, no avoided crossings between a magnon mode and a cavity mode are expected a priori. Measurements were carried out with the magnetic field applied along the three cardinal directions. The results are shown in Fig. 4.14, corresponding respectively to an out-of-plane field, an in-plane field parallel to the central conductor, and an in-plane field perpendicular to the conductor (panels **a–c**, respectively). The data shown represent the numerical derivative of the microwave phase with respect to magnetic field, which suppresses sample-independent background contributions. From these maps, the resonance frequency was extracted using a local tracking algorithm. Starting from an initial resonance guess, the algorithm follows the largest second derivative in phase to identify the dominant resonance feature. However, fitting the extracted dispersion using Eq. 4.15 did not yield physically meaningful parameters. At the time of writing, we emphasise that these measurements and the associated analysis remain preliminary.

Nevertheless, several possible explanations for the observed behaviour are considered. In a conventional ferromagnetic system, the Kittel mode is expected to increase monotonically with applied field. This trend is not observed here. Given the ferrimagnetic nature of TmIG and the proximity to compensation-like behaviour, we considered whether a left-handed antiferromagnetic-like mode could be present. Such modes have been used to explain sign reversals in the in-plane spin Seebeck effect near compensation temperatures [367, 368, 409], and can, in principle, exhibit a decreasing resonance frequency with increasing field [410–412]. However, this scenario would also imply the presence of a corresponding right-handed mode at higher frequencies with opposite dispersion [413], which was not observed in our measurements, up to 20 GHz. Finally, it is often reported that antiferromagnetic magnons appear in the $\sim$THz regime [414].

An alternative explanation is that the measured features are not dominated by intrinsic magnon modes of the TmIG layer, but rather by the electromagnetic response of the superconducting waveguide itself. In particular, we observe a second harmonic at approximately 2.06 times the fundamental frequency as would be expected for a $\frac{\lambda}{2}$-type resonator, and a small but finite hysteresis in the field sweeps. These observations

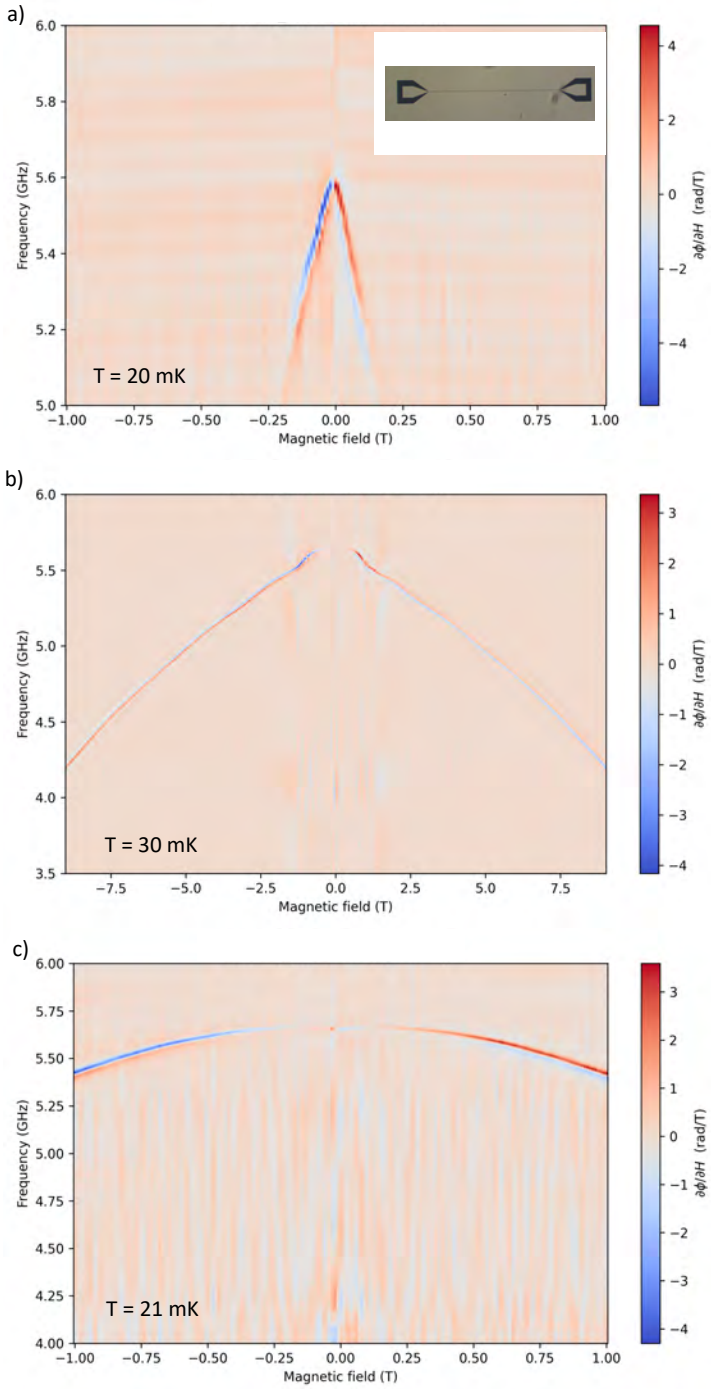


**Figure 4.14:** Microwave response under an applied magnetic field. The colour scale shows the derivative of the phase with respect to the applied field. **a**) An out-of-plane magnetic field, at base temperature ($T \approx 20$ mK). **b**) An in-plane magnetic field along the central conductor, at higher base temperature due to the magnet, $T \approx 30$ mK. **c**) An in-plane magnetic field perpendicular to the central conductor, at base temperature, $T \approx 21$ mK.

suggest that the signal may be influenced by anomalous resonances of the NbTiN waveguide, for instance due to slot modes or non-ideal current distributions. In the out-of-plane configuration (Fig. 4.14a), the static magnetic field $\vec{H}_a$ is applied perpendicular to the film, while the microwave magnetic field $\vec{h}_{\mathrm{rf}}$ remains predominantly in-plane. The dominant feature is a downward-pointing V-shaped structure, extending from approximately 5.6 GHz at zero field to 5.0 GHz at 175 mT, corresponding to a slope of $\mathrm{d}f_r/\mathrm{d}H_a \approx 3.4$ GHz/T. This feature weakens when extending the frequency range and is no longer visible below approximately 4.5 GHz. While tentative, we attribute this behaviour primarily to vortex-induced dissipation in the superconducting NbTiN film. Under an out-of-plane magnetic field, Abrikosov vortices penetrate the superconductor, and their motion under microwave excitation leads to enhanced dissipation that increases with both field and frequency [25].

The effect of the GGG can also not be neglected: operating in the millikelvin regime ($T \sim 20$ mK) introduces additional considerations that are negligible at higher temperatures. In particular, the GGG substrate, typically treated as a passive structure at room temperature, becomes an active magnetic element (frustrated antiferromagnet) that exhibits short-range order of its own [415, 416]. GGG is a geometrically frustrated paramagnet with a high density of $Gd^{3+}$ ions, each carrying a large magnetic moment ($S = 7/2$). At elevated temperatures, thermal fluctuations randomise these moments; however, at millikelvin temperatures the Zeeman energy can exceed the thermal energy, leading to alignment of the $Gd^{3+}$ spins with the external magnetic field [382, 383, 417]. As a result, even relatively small applied fields (on the order of a few hundred millitesla) are sufficient to drive the GGG substrate into a magnetised state. The substrate therefore generates a sizeable stray field $H_{\mathrm{GGG}}$ that penetrates the adjacent nanometre-thin TmIG layer. This stray field opposes the externally applied in-plane field, thereby reducing the effective internal field experienced by the magnetic system:

$$H_{\mathrm{int}} = H_{\mathrm{a}} - H_{\mathrm{GGG}}(T, H_{\mathrm{a}}). \tag{4.16}$$

Such effects have been reported to persist up to temperatures of order 10 K [418]. Consequently, the resonance frequency is shifted to lower values compared to the standard Kittel prediction, and a "baseline" that is independent in magnetic field is observed, corresponding to the data of Fig. 4.14b and c. At the lowest temperatures ($\lesssim 500$ mK), correlation effects between $Gd^{3+}$ spins become important, leading to a saturation of the stray field at values approaching $\sim 40$ mT near the sample centre [418]. Furthermore, the finite geometry of the substrate results in a spatially non-uniform stray field, which introduces an inhomogeneous broadening of the magnetic response. Taken together, these considerations indicate that the measured signal likely contains significant contributions from both the TmIG film and the underlying GGG substrate. In particular, the much larger volume of the GGG substrate compared to the ultrathin TmIG layer raises the possibility that the observed features are dominated by substrate-induced effects in this initial set of measurements.

The favourable magnonic properties of TmIG nevertheless make it a promising candidate for hybrid quantum magnonics, with applications in quantum information, communications and sensing [194, 419]. Recent experiments using diamond NV-centre magnetometry have demonstrated long-range spin-wave transport in TmIG thin films, with propagation lengths exceeding ten micrometres and wavelengths in the submicron regime [420]. These characteristics are well suited for integration with on-chip

quantum devices. In addition, hybrid structures combining TmIG with low-damping ferrimagnets such as YIG have exhibited strong magnon–magnon coupling, with cooperativities exceeding those typically observed in metallic systems [421]. Together, these results position TmIG as a versatile material platform, offering low magnetic damping, tunable anisotropy, and the potential for strong coherent coupling in future quantum information architectures. It will thus be an interesting and non-trivial scientific challenge to couple TmIG to resonators at cryogenic temperatures

**Summary**

In conclusion, this Chapter investigated Pt/TmIG/GGG heterostructures as a platform for hybrid superconductor–magnetic quantum systems. We first demonstrated that on-axis sputtering enables wafer-scale growth of epitaxial TmIG films with excellent structural and magnetic uniformity, providing a scalable and industry-compatible route for device integration. At room temperature, second-harmonic Hall measurements yield a damping-like spin Hall angle of $\theta_{\mathrm{SHE}}^{\mathrm{DL}} \approx 3\%$, enabling efficient spin–orbit torque switching with low critical current densities of $(0.7\text{–}1.5) \times 10^{11}$ A/m$^2$. These results confirm that sputtered TmIG maintains competitive spintronic performance.
In the temperature domain, we observe two distinct polarity reversals in the anomalous Hall signal at $T_{\mathrm{PR},1} \approx 124$ K and $T_{\mathrm{PR},2} \approx 81$ K. The higher-temperature transition is attributed to a crossover in interfacial transport mechanisms, whereas the lower-temperature transition is accompanied by a pronounced divergence in coercivity, consistent with compensation-like ferrimagnetic behaviour. Despite the expected enhancement of the effective torque in this regime, deterministic switching is suppressed due to the rapid increase in magnetic energy barriers.
Finally, preliminary integration with superconducting microwave circuits highlights both the potential of TmIG for hybrid magnonic systems and the experimental challenges associated with measurements at millikelvin temperatures. While clear magnon–photon coupling could not be unambiguously resolved, the results identify limitations arising from substrate and superconducting effects, providing important guidance for future device design. Overall, TmIG and TmIG-based heterostructures contain all the qualities for future devices that couple magnetic and superconducting degrees of freedom in next-generation quantum technologies, although further research is required.

# Chapter 5

# Future progress and conclusions

*"But [he] saw the world now with his companion's eyes, and saw the living splendour that was revealed about them in the silent, desolate land, as if by a power of enchantment surpassing any other, in every blade of the wind-bowed grass, every shadow, every stone. So when one stands in the cherished place for the last time before a voyage without return, he sees it all whole and real, and dear, as he has never seen it before and never will see it again."*
— Ursula K. Le Guin, *The farthest shore*

## How to continue from here?

Looking ahead, we identify several concrete directions to advance the hybrid architectures:

- **Coherence optimisation:** Improving coherence times by reducing loss and noise remains a central challenge across cQED. Near-term efforts include the use of ultra-low-loss substrates, deep-etching to minimise substrate losses, and further optimisation of dielectric layers and fabrication recipes. In the case of hybrid semiconductor-superconductors, alternative platforms such as InAs 2DEGs [422, 423] may also offer advantages in scalability and electrostatic control. In addition, quasiparticle traps, improved microwave filtering, and enhanced shielding against stray radiation and high-energy particles can help suppress spurious excitations. These refinements are relevant both for superconducting circuits and for hybrid qubit platforms, and underpin all future experiments.

- **Multi-qubit integration:** Extend the platform to multiple ABS-based qubits on a single chip. This includes fabricating arrays of gate-tunable nanowire junctions coupled either to individual CPS resonators or to a shared multimode resonator, together with on-chip flux-bias lines and multiplexed readout. A milestone will be the demonstration of coherent interactions between several ABS qubits and the simultaneous readout of multiple transitions.

- **Ultra-strong coupling:** Further increase the light–matter coupling strength by designing resonators with even higher impedance (e.g. longer, narrower

inductors or superinductors) and optimising junction capacitance. Reaching the ultrastrong coupling regime ($g/\omega_0 \gg 0.1$),and ultimately the deep-strong coupling regime will allow exploration of non-perturbative quantum dynamics and faster gate speeds.

- **Magnonic coupling for quantum information transfer:** Couple magnon modes in TmIG to the microwave cavity, and transferring state information to a nearby resonator. For example, embedding a patterned TmIG element at a magnetic field antinode of the resonator should enable cavity–magnon-polariton formation [424]. Demonstrating ultra strong magnon–photon interactions would allow storing quantum information in collective spin excitations and exploring non-linear spin dynamics.

Significant progress has already been made in these directions. Two distinct classes of strongly coupled Andreev-physics based qubits have been realised: Andreev-pair qubits and Andreev-spin qubits [33, 37]. Whereas prior research has primarily focused on the fundamental feasibility of ABS for quantum information processing, the field is now transitioning towards optimisation and architectural scalability. The next natural step is therefore the development of multi-qubit platforms based on ABS. In this thesis, high-impedance resonators were used because of their compact footprint and enhanced zero-point fluctuations. Complementary approaches, such as flip-chip integration, provide a promising pathway towards planar hybrid architectures. In this direction, gate- and flux-tunable ABS readout was demonstrated in a planar InAs/Al junction inductively coupled to a high-$Q$ flip-chip resonator [425]. This approach mitigates substrate-induced losses and points towards the possibility of densely integrating two-dimensional arrays of ABS junctions, each coupled either to individual resonators or to a shared bus.

In line with our results, the resonator design can be engineered to mediate strong qubit–qubit interactions across multiple ABS elements within a single device. Practically, scaling these systems will require implementation of on-chip flux-bias routing, multiplexed microwave readout, and potentially multi-mode resonator designs. A milestone will be the demonstration of coherent two-qubit gates between ABS qubits on the same chip, alongside simultaneous readout of multiple ABS transitions coupled to a single resonator. Analogous to the evolution of superconducting quantum computing, the implementation of tunable couplers that are induction-based [426] or gate-controlled [427] will be required to enable controllable interactions while minimising additional dissipation.

Initial experimental progress towards these goals has already been reported. Pita-Vidal *et al.* [428] demonstrated coherent coupling between two Andreev spin qubits separated by distances on the order of $\sim 25\ \mu$m via a shared cavity mode. The coupling strengths achieved in our work suggest a clear pathway towards faster remote-entanglement protocols [429, 430]. At the same time, high-impedance resonators involve clear trade-offs. While high impedance boosts $g_c$, it also generally increases the system's susceptibility to high-frequency environmental noise. There is an emerging realisation that this leads to an optimal impedance beyond which the gains in coupling are offset by an increase in the quasiparticle poisoning rate. Highly disordered films like NbTiN and grAl may host a higher density of subgap states, which can act as a source of decoherence. Future research must find the balance between maximising $Z_r$ for coupling

and minimising the material's internal loss and noise. At present, further progress in ABS-qubits is largely limited by materials optimisation [431].

Looking further ahead, the integration of Majorana zero modes (MZMs) within cQED architectures remains a major goal of hybrid devices [28, 432–434]. In particular, coupling a minimal Kitaev chain to a resonator in the USC regime offers a powerful spectroscopic probe of topological superconductivity [435]. In this regime, the resonator response becomes sensitive to the $4\pi$-periodic Josephson effect, as determined by Majorana physics. Even further in the future is the potential to implement MZM braiding operations [436], mediated by resonator-induced interactions. By coupling multiple Majorana-hosting Josephson junctions to a common (USC) microwave bus, one can engineer non-local interactions with intrinsic topological protection. Such an approach would combine the fast control enabled by ultrastrong light–matter coupling with the robustness of topological qubits, representing a significant paradigm shift in quantum computing architectures.

Finally, the characterisation of TmIG thin films presented here provides a basis for future magnon-photon hybrid systems, in which microwave photons in CPS resonators are coherently interfaced with spin-wave excitations. A magnonic quantum bus could enable the routing of quantum information between separated superconducting nodes without the dissipation associated with charge transport [437,438]. Future work should therefore focus on reaching the strong-coupling regime between magnon modes and superconducting resonator photons, enabling coherent state transfer between superconducting and magnetic subsystems. Such a platform would offer a promising route towards low-dissipation quantum information processing beyond purely electronic circuits.

# Conclusions

In this thesis, the standard workhorse of superconducting quantum circuits, the coplanar waveguide (CPW) resonator, was critically reassessed in the context of hybrid devices. While CPW designs have underpinned the success of transmon-based quantum computing architectures, they exhibit intrinsic limitations when operated in hybrid environments. In particular, the extended superconducting ground planes act as efficient traps for magnetic flux. Under applied magnetic fields, this leads to the formation of Abrikosov vortices, which introduce both excess dissipation and frequency instability. In addition, the continuous ground plane complicates the integration of the multiple electrostatic gate lines required for coupled semiconductor devices. This often results in parasitic microwave modes, increased crosstalk, and the emergence of slotline modes that are difficult to fully suppress. Together, these effects impose practical constraints on scalability and device performance in hybrid superconducting–semiconducting circuits. To address these limitations, this thesis developed superconducting high-impedance coplanar stripline (CPS) resonators as a versatile platform for hybrid quantum circuits. Based on thin-film NbTiN, these resonators exhibit low and geometrically dependent losses, $F\delta_{\mathrm{TLS}} \sim 10^{-5}$, and maintain stable resonance frequencies under in-plane magnetic fields up to 1 T and out-of-plane fields up to 250 mT. By eliminating the extended ground plane of a conventional CPW resonator, the CPS geometry enables independent electrostatic control of nearby

nanostructures without compromising microwave performance. In this way, the design balances electrostatic gateability, magnetic-field tolerance, and photon confinement in a waveguide, establishing CPS resonators as a robust interface for hybrid quantum devices.

In this platform, we demonstrated coherent coupling to Andreev bound states (ABS) in a near-ballistic proximitised semiconductor (InAs) nanowire. The CPS-based architecture leverages the high kinetic inductance of disordered NbTiN films to create resonators with differential impedances exceeding 12 kΩ. Such high-impedance environments amplify the zero-point flux fluctuations ($\Phi_{zpf}$), enabling the coupling between resonator and ABS to approach the ultrastrong coupling (USC) regime. Gate-dependent microwave spectroscopy revealed avoided level crossings when an ABS transition is tuned into resonance with the cavity mode, confirming that the Andreev excitations hybridise with the microwave photons. Given the small dipole moment of an Andreev pair, the measured coupling strength of pair transitions on the order of $\frac{g_c}{2\pi} = 1.95$ GHz is among the largest reported to date (Table 5.1), and demonstrates the potential of Andreev-based qubits in circuit QED. In addition to pair transitions, we observed single-quasiparticle transitions in devices with longer weak links, albeit with lower coupling strength. The gate tunability of the junction provided spectroscopic access to the ABS spectrum, and the combination of the high-impedance CPS resonator with the gate-tunable junction was essential in enabling this near-USC regime that is difficult to reach otherwise. These results help establish ABS-based Josephson junctions as electrically controllable quantum elements compatible with superconducting cavities.

| Platform | $l_{\mathrm{wl}}$ (nm)/ Width (nm) | Coupling $\frac{g}{2\pi}$ (MHz) | Reference |
|---|---|---|---|
| **Pair transitions (PT)** | | | |
| Planar Ge/Al | 350 / 150 | 3 | [425] |
| Ge-Si/Al nw | 33 | 47 | [439] |
| Al atomic contact | atomic scale | 74 | [262] |
| InAs/ Al (full-shell) | 550 | 92 | [257] |
| InAs/Al nw | 200 | 23 | [37] |
| InAs/Al nw, flip-chip | 90 | 78 | [440] |
| InAs/Al nw (Dev. 1) | 130 | ∼1950 | This work |
| **Single-quasiparticle transitions (SQPT)** | | | |
| InAs/Al nw | 250 | ∼30–50 | [249] |
| InAs/Al nw (full-shell) | ∼200 | 104 | [264] |
| InAs/Al nw | 300 | ∼ 200 | [441] |
| InAs/Al nw (Dev. 2) | 130 | 77 | This work |

**TABLE 5.1:** COMPARISON OF EXPERIMENTALLY REPORTED COUPLING STRENGTHS IN HYBRID ANDREEV BOUND STATE–RESONATOR SYSTEMS. PAIR-TRANSITION (PT) SPLITTINGS AND SINGLE-QUASIPARTICLE TRANSITION (SQPT) COUPLING RATES ARE LISTED SEPARATELY. THE WEAK-LINK LENGTH $l_{\mathrm{wl}}$ DENOTES THE EXPOSED SEMICONDUCTOR SECTION OF THE JUNCTION. ALL COUPLING STRENGTHS ARE GIVEN AS FREQUENCIES. "NANOWIRE" IS SHORTENED TO "NW". WE NOTE THAT THE MULTIPLE PLATFORMS DIFFER IN AL THICKNESS, RESONATOR STRUCTURES AND AL COVERING. UNLESS DIFFERENTLY NOTED, THE NANOWIRES COMPARED ARE HALF-SHELL IN THIS TABLE.

In parallel with the work on semiconducting hybrids, Chapter 4 investigated rare-earth iron garnet (ReIG) thin films grown by industrially viable sputtering techniques as potential low-loss media for collective spin excitations, or magnons. In particular, the objective was to probe the suitability of thulium iron garnet ($Tm_3Fe_5O_{12}$, TmIG) for integration with superconducting circuits, with a view towards magnonic quantum information transfer.

Electrical measurements revealed multiple anomalous Hall sign reversals near 81 K and 124 K . We analysed six potential physical mechanisms for these reversals, concluding that while the higher-temperature reversal ($\approx 124\ K$) is likely a crossover in interfacial transport dominance, the lower-temperature reversal ($\approx 81\ K$) represents a true magnetic compensation point. Near the lower reversal, the opposing sublattice magnetisations of $Fe^{3+}$ and $Tm^{3+}$ ions cancel, resulting in vanishing net magnetisation and a divergence of the coercive field. This "antiferromagnet-like" regime is ideal for hybrid devices, as it minimises magnetic back-action on superconducting resonators while supporting enhanced magnon-photon coupling.

Furthermore, we demonstrated robust and deterministic spin-orbit torque switching of TmIG at room temperature using current densities as low as $0.7 \times 10^{11}\ \frac{\mathrm{A}}{\mathrm{m}^2}$. However, our studies also revealed a degradation of switching efficiency at cryogenic temperatures, driven by the divergence of coercivity near the polarity reversals. Importantly, robust magnetic hysteresis persists at low temperature, and the spin-charge conversion (anomalous Hall effect) remains significant down to cryogenic temperatures. In other words, the garnet film retains strong magnetic order and efficient spin-current response at low temperatures, making it a viable component in a hybrid circuit. Finally, we showed early results on coupling these TmIG films to a superconducting resonator to explore their use for low-loss magnonic information transfer.

Taken together, these results demonstrate that the CPS resonator platform provides a powerful and adaptable interface for hybrid quantum devices, and allows for probing exotic ultra-strong coupling regime physics. By underscoring and advancing our understanding of the speed of superconducting circuits, the gate-tunability of semiconductors, and the low dissipation and temperature-dependent spin dynamics of magnetic insulators, the thesis contributes to the development of robust and versatile hybrid platforms for quantum science and for future scalable quantum technologies beyond the noisy intermediate-scale regime [442].

# Acknowledgments

I joined the Quantum Device Physics group at Chalmers as a PhD student in November 2019, and I've had the privilege of getting to meet so many interesting, fun, kind, and intelligent people. I think now - the day before printing the thesis - is the optimal time to thank these people.

Let's start with those that I have interacted with the longest: my parents and brother. Mama, papa en Youri, ik denk niet dat ik heel deze weg naar een doctoraat zou hebben kunnen afleggen zonder jullie hulp. Vanaf het begin (en eigenlijk al voordien) hebben jullie me op de weg geholpen en gesteund, zowel mentaal als financieel, in alles wat ik doe. Het was soms wat moeilijk, zeker met de verhuis naar het verre Zweden, maar ik heb er nooit aan getwijfeld dat jullie het beste voor me willen en mij willen zien slagen in het leven. Professioneel en persoonlijk. Dus ik denk dat het niet misplaatst is om het eerste, en grootste dankwoord aan jullie te richten.

Professionally, I have also gained a family by coming to Chalmers. My thanks go out to all current and old members of the Dungeon 1 group: the *PhD students* Nermin, Vittorio and Ankit, the *doctors* Bekmurat and Oleg, and ex-master students (or, as I am proud to say, current *PhD students*) Rodrigo and Theresa. Especially these first three I've had the pleasure to share the floor and lab with for this entire time. We have suffered at times, we have laughed by times, we were exasperated by times thinking of giving up, and we may have even enjoyed the road to our PhD's by times. But most of all, we started a lab together and I don't think I would have wanted to have done it with another group of ragtag scientific adventurers like yourselves. Without Nermin's everlasting musings, Vittorio's romantic notions and Ankit's ice-cold pragmatism, things likely would've turned out completely different. I would like to specifically thank Nermin for sharing an office with me this entire time, and to somehow manage to endure my peculiarities, critiques, jokes, and returning them in kind. Luckily, the four of us together were able to put our struggles in perspective, somehow. Not to mention the stimulating scientific discussions we had!

Furthermore, after the events of the first few years, I would like to thank the members of my new research group, the Spin and Quantum Technology group. That includes first and foremost my scientific supervisor Saroj, who helped me shift my entire research focus in a new direction; if I manage to finish, it will be in no small part thanks to him. But it also includes Prasanna, Divya, Himanshu, Lars, Roselle, Bogdan, Sameer, Anamul Md., Lalit, Bing (and Na). Related, I would like to thank anyone who I collaborated with over the years, including the Leuven-Liège team (Joris, Bart, Lukas and Julia), François J., Naoto Y. (head of the SPIN LAB at Kyushu University,

Japan), and the Copenhagen nanowire growth group.
Then, I would like to acknowledge those people who have contributed in various ways to my time in Sweden, both scientifically as well as personally. That includes my co-supervisor Thilo, but also others (which in essence are too many to name but I will try!): Ananthu P. S., Gustav A., Paul N., Munis K., Núria H., the people who have welcomed me in BTK Linné (Johan K., Joel, Alex, Simeon, Jens, Johan T., Mattias J., Lars R., but also everyone from the *styrelse*), the people of the Theatre of Menace and acting in general, all employees of ConScience AB, and everyone else I have interacted with along the way! I also thank all my best friends from Belgium, who for some reason never forgot about me, and supported me during this time. Thank you, Kristiaan, Giel, Thomas, Isaura, Stijn, Dagmar, Hendrik, Lars, Lukas, Miguelleke and Jelle.

Furthermore, some people deserve special recognition. Sumedh M. has helped me tremendously at the start, and I would not have gotten far with microwave physics without his help; Ragnar, who for me is the most happy and kind person that must have ever existed; Ariadna S., who is one of the most imposing scientists I know and will ever know; Dag Winkler, conversations with whom always somehow spiral out of control, but also was an amazing head of QDP who I always felt to be on my side; Marcus Rommel, whose support and sharing of his own story was invaluable for me to remain motivated; Niclas Lindvall, who you can always go to for help regarding EBL problems but also far, far beyond that, and Henrik Frederiksen, who is some sort of magician with everything thin-film related and has some of the best stories one can imagine.

Additionally, I'd like to thank all the so-called supportive personnel, including the cleanroom staff which are as important to me being able to finish (?) as all the rest above, if not more so. These are chiefly Annika, Ximena, Linda and Gilbert, Mattias F. and of course Lars Jönsson without whom the entire working of MC2 would collapse, I think. His contributions in fridge repair, sample box fabrication and all-around mechanical help has proven to be invaluable.

Last, but certainly not least, I want to thank my wife Anastasia for choosing me, for marrying me, and for becoming my best friend. I know that in you, I have my staunchest supporter, someone who will always be on my side, who shares my whimsicalness, and who reciprocates all the love I give in tenfold return. I know the past few months were difficult, but I love you, my little dinootje, now and forever! Thank you for everything, and thank you Oksana and Igor as well for their support and to welcome me in your part of the family.

Finally, if I forgot anyone, that's on me alone. But if I interacted with you, be certain I am grateful for it.

Ivo Cools
Göteborg, April 2026

# References


[1] J. H. Lee, J. Y. Kim, H.-J. Lee, S.-J. Choi, Y. J. Lee, and H. W. Jang, "Beyond the silicon plateau: A convergence of novel materials for transistor evolution," *Nano-Micro Letters*, vol. 18, Sept. 2025.

[2] A. Steane, "Quantum computing," *Reports on Progress in Physics*, vol. 61, pp. 117–173, Feb. 1998.

[3] S. P. Jordan, N. Shutty, M. Wootters, A. Zalcman, A. Schmidhuber, R. King, S. V. Isakov, T. Khattar, and R. Babbush, "Optimization by decoded quantum interferometry," *Nature*, vol. 646, pp. 831–836, Oct. 2025.

[4] G. Burkard, T. D. Ladd, A. Pan, J. M. Nichol, and J. R. Petta, "Semiconductor spin qubits," *Reviews of Modern Physics*, vol. 95, p. 025003, June 2023.

[5] S. Slussarenko and G. J. Pryde, "Photonic quantum information processing: A concise review," *Applied Physics Reviews*, vol. 6, Oct. 2019.

[6] A. Blais, A. L. Grimsmo, S. Girvin, and A. Wallraff, "Circuit quantum electrodynamics," *Reviews of Modern Physics*, vol. 93, p. 025005, May 2021.

[7] S. Bravyi, O. Dial, J. M. Gambetta, D. Gil, and Z. Nazario, "The future of quantum computing with superconducting qubits," *Journal of Applied Physics*, vol. 132, Oct. 2022.

[8] H. K. Onnes, *Communications from the Physical Laboratory at the University of Leiden*. No. 145-156, University of Leiden, 1922.

[9] B. Josephson, "Possible new effects in superconductive tunnelling," *Physics Letters*, vol. 1, pp. 251–253, July 1962.

[10] P. Krantz, M. Kjaergaard, F. Yan, T. P. Orlando, S. Gustavsson, and W. D. Oliver, "A quantum engineer's guide to superconducting qubits," *Applied Physics Reviews*, vol. 6, June 2019.

[11] A. Osman, *Scaling Superconducting Quantum Processors Coherence, Frequency Targeting and Crosstalk*. PhD thesis, Chalmers University of Technology, 2024.

[12] D. Castelvecchi, "IBM releases first-ever 1000-qubit quantum chip," *Nature*, vol. 624, pp. 238–238, Dec. 2023.

[13] R. Acharya *et al.*, "Quantum error correction below the surface code threshold," *Nature*, vol. 638, pp. 920–926, Dec. 2024.

[14] M. Mohseni *et al.*, "How to build a quantum supercomputer: Scaling from hundreds to millions of qubits," 2024.

[15] F. Volmer, I. Seidler, T. Bisswanger, J.-S. Tu, L. R. Schreiber, C. Stampfer, and B. Beschoten, "How to solve problems in micro- and nanofabrication caused by the emission of electrons and charged metal atoms during e-beam evaporation," *Journal of Physics D: Applied Physics*, vol. 54, p. 225304, Mar. 2021.

[16] R. Hanna, S. Ihssen, S. Geisert, U. Kocak, M. Arfini, A. Hertel, T. J. Smart, M. Schleenvoigt, T. Schmitt, J. Domnick, K. Underwood, A. R. Jalil, J. H. Bae, B. Bennemann, M. Féchant, M. Field, M. Spiecker, N. Zapata, C. Dickel, E. Berenschot, N. Tas, G. A. Steele, D. Grützmacher, I. M. Pop, and P. Schüffelgen, "On-chip stencil lithography for superconducting qubits," *Applied Physics Reviews*, vol. 13, Apr. 2026.

[17] S. A. Moiseev, K. I. Gerasimov, R. R. Latypov, N. S. Perminov, K. V. Petrovnin, and O. N. Sherstyukov, "Broadband multiresonator quantum memory-interface," *Scientific Reports*, vol. 8, Mar. 2018.

[18] J. Casanova, G. Romero, I. Lizuain, J. J. García-Ripoll, and E. Solano, "Deep strong coupling regime of the Jaynes-Cummings model," *Physical Review Letters*, vol. 105, p. 263603, Dec. 2010.

[19] A. Blais, R.-S. Huang, A. Wallraff, S. M. Girvin, and R. J. Schoelkopf, "Cavity quantum electrodynamics for superconducting electrical circuits: An architecture for quantum computation," *Physical Review A*, vol. 69, p. 062320, June 2004.

[20] M. Göppl, A. Fragner, M. Baur, R. Bianchetti, S. Filipp, J. M. Fink, P. J. Leek, G. Puebla, L. Steffen, and A. Wallraff, "Coplanar waveguide resonators for circuit quantum electrodynamics," *Journal of Applied Physics*, vol. 104, Dec. 2008.

[21] C. R. H. McRae, H. Wang, J. Gao, M. R. Vissers, T. Brecht, A. Dunsworth, D. P. Pappas, and J. Mutus, "Materials loss measurements using superconducting microwave resonators," *Review of Scientific Instruments*, vol. 91, p. 091101, Sept. 2020.

[22] D. Niepce, *Superinductance and Fluctuating Two-Level Systems: Loss and Noise in Disordered and Non-Disordered Superconducting Quantum Devices*. PhD thesis, Chalmers Tekniska Hogskola (Sweden), 2020.

[23] M. Janík, K. Roux, C. Borja-Espinosa, O. Sagi, A. Baghdadi, T. Adletzberger, S. Calcaterra, M. Botifoll, A. Garzón Manjón, J. Arbiol, D. Chrastina, G. Isella, I. M. Pop, and G. Katsaros, "Strong charge-photon coupling in planar germanium enabled by granular aluminium superinductors," *Nature Communications*, vol. 16, Mar. 2025.

[24] A. Wallraff, D. I. Schuster, A. Blais, L. Frunzio, R.-S. Huang, J. Majer, S. Kumar, S. M. Girvin, and R. J. Schoelkopf, "Strong coupling of a single photon to a superconducting qubit using circuit quantum electrodynamics," *Nature*, vol. 431, pp. 162–167, Sept. 2004.

[25] L. Nulens, N. Lejeune, J. Caeyers, S. Marinković, I. Cools, H. Dausy, S. Basov, B. Raes, M. J. Van Bael, A. Geresdi, A. V. Silhanek, and J. Van de Vondel, "Catastrophic magnetic flux avalanches in NbTiN superconducting resonators," *Communications Physics*, vol. 6, Sept. 2023.

[26] J. Baumgarten, N. Lejeune, L. Nulens, I. P. C. Cools, J. Van de Vondel, and A. V. Silhanek, "Magnetic landscape of NbTiN superconducting resonators under radio-frequency excitation," 2026.

[27] H. Zhang *et al.*, "Retraction note: Quantized majorana conductance," *Nature*, vol. 591, pp. E30–E30, Mar. 2021.

[28] M. Aghaee *et al.*, "Interferometric single-shot parity measurement in inas–al hybrid devices," *Nature*, vol. 638, pp. 651–655, Feb. 2025.

[29] W. Chang, S. M. Albrecht, T. S. Jespersen, F. Kuemmeth, P. Krogstrup, J. Nygård, and C. M. Marcus, "Hard gap in epitaxial semiconductor–superconductor nanowires," *Nature Nanotechnology*, vol. 10, pp. 232–236, Jan. 2015.

[30] C. W. J. Beenakker, "Universal limit of critical-current fluctuations in mesoscopic josephson junctions," *Physical Review Letters*, vol. 67, pp. 3836–3839, Dec. 1991.

[31] L. Bretheau, C. Girit, H. Pothier, D. Esteve, and C. Urbina, "Exciting Andreev pairs in a superconducting atomic contact," *Nature*, vol. 499, pp. 312–315, July 2013.

[32] M. Hays, V. Fatemi, K. Serniak, D. Bouman, S. Diamond, G. de Lange, P. Krogstrup, J. Nygård, A. Geresdi, and M. H. Devoret, "Continuous monitoring of a trapped superconducting spin," *Na*, vol. 16, pp. 1103–1107, Nov. 2020.

[33] M. Hays, V. Fatemi, D. Bouman, J. Cerrillo, S. Diamond, K. Serniak, T. Connolly, P. Krogstrup, J. Nygård, A. Levy Yeyati, A. Geresdi, and M. H. Devoret, "Coherent manipulation of an Andreev spin qubit," *Science*, vol. 373, pp. 430–433, July 2021.

[34] R. S. Souto, A. Martín-Rodero, and A. L. Yeyati, "Andreev bound states formation and quasiparticle trapping in quench dynamics revealed by time-dependent counting statistics," *Physical Review Letters*, vol. 117, p. 267701, Dec. 2016.

[35] I. P. C. Cools, R. M. López-Báez, V. Buccheri, O. Shvetsov, N. Trnjanin, E. Hogedal, and S. P. Dash, "Losses in magnetic field resilient coplanar stripline resonators," *Journal of Physics D: Applied Physics*, vol. 58, p. 255102, June 2025.

[36] O. O. Shvetsov, A. Khola, V. Buccheri, I. P. C. Cools, N. Trnjanin, A. Geresdi, T. Kanne, and J. Nygård, "Approaching the ultrastrong-coupling regime between an Andreev level and a microwave resonator," *Physical Review Applied*, vol. 24, Oct. 2025.

[37] M. Hays, G. de Lange, K. Serniak, D. van Woerkom, D. Bouman, P. Krogstrup, J. Nygård, A. Geresdi, and M. Devoret, "Direct microwave measurement of andreev-bound-state dynamics in a semiconductor-nanowire Josephson junction," *Physical Review Letters*, vol. 121, p. 047001, July 2018.

[38] P. Forn-Díaz, L. Lamata, E. Rico, J. Kono, and E. Solano, "Ultrastrong coupling regimes of light-matter interaction," *Reviews of Modern Physics*, vol. 91, p. 025005, June 2019.

[39] D. Lachance-Quirion, Y. Tabuchi, A. Gloppe, K. Usami, and Y. Nakamura, "Hybrid quantum systems based on magnonics," *Applied Physics Express*, vol. 12, p. 070101, June 2019.

[40] M. N. Agusutrisno, S. Obinata, T. Okumura, K. Kamataki, N. Itagaki, K. Koga, M. Shiratani, and N. Yamashita, "Large-scale fabrication of thulium iron garnet film with perpendicular magnetic anisotropy using rf magnetron sputtering," *Japanese Journal of Applied Physics*, vol. 63, p. 07SP06, July 2024.

[41] R. Ngaloy, N. Yamashita, B. Zhao, S. Kim, K. Yamashita, I. P. C. Cools, M. N. Agusutrisno, S. Lee, Y. Kurokawa, C.-Y. You, H. Yuasa, and S. P. Dash, "Deterministic spin-orbit torque switching of epitaxial ferrimagnetic insulator with perpendicular magnetic anisotropy fabricated by on-axis magnetron sputtering," *npj Spintronics*, vol. 3, Oct. 2025.

[42] H. Huebl *et al.*, "High cooperativity in coupled microwave resonator ferrimagnetic insulator hybrids," *Physical Review Letters*, vol. 111, p. 127003, Sept. 2013.

[43] Y. Tabuchi, S. Ishino, T. Ishikawa, R. Yamazaki, K. Usami, and Y. Nakamura, "Hybridizing ferromagnetic magnons and microwave photons in the quantum limit," *Physical Review Letters*, vol. 113, p. 083603, Aug. 2014.

[44] X. Zhang, C.-L. Zou, L. Jiang, and H. X. Tang, "Strongly coupled magnons and cavity microwave photons," *Physical Review Letters*, vol. 113, p. 156401, Oct. 2014.

[45] A. V. Kimel, A. Kirilyuk, A. Tsvetkov, R. V. Pisarev, and T. Rasing, "Laser-induced ultrafast spin reorientation in the antiferromagnet TmFeO3," *Nature*, vol. 429, pp. 850–853, June 2004.

[46] E. V. Gomonay and V. M. Loktev, "Spintronics of antiferromagnetic systems," *Low Temperature Physics*, vol. 40, pp. 17–35, Jan. 2014.

[47] W. Buckel and R. Kleiner, *Superconductivity: fundamentals and applications*. John Wiley & Sons, 2008.

[48] J. File and R. G. Mills, "Observation of persistent current in a superconducting solenoid," *Physical Review Letters*, vol. 10, pp. 93–96, Feb. 1963.

[49] W. Meissner and R. Ochsenfeld, "Ein neuer effekt bei eintritt der supraleitfähigkeit," *Naturwissenschaften*, vol. 21, no. 44, pp. 787–788, 1933.

[50] F. Cadiz and A. Couairon, *Classical Electrodynamics: Fundamentals and Applications*. Springer Nature Switzerland, 2025.

[51] J. Bardeen, L. N. Cooper, and J. R. Schrieffer, "Theory of superconductivity," *Physical Review*, vol. 108, pp. 1175–1204, Dec. 1957.

[52] X. Yang, L. You, L. Zhang, C. Lv, H. Li, X. Liu, H. Zhou, and Z. Wang, "Comparison of Superconducting Nanowire Single-Photon Detectors Made of NbTiN and NbN Thin Films," *IEEE Transactions on Applied Superconductivity*, vol. 28, pp. 1–6, Jan. 2018.

[53] J. Zichi, *NbTiN for improved superconducting detectors*. PhD thesis, KTH Royal Institute of Technology, 2019.

[54] D. J. Thoen, B. G. C. Bos, E. A. F. Haalebos, T. M. Klapwijk, J. J. A. Baselmans, and A. Endo, "Superconducting NbTiN thin films with highly uniform properties over a 100 mm wafer," *IEEE Transactions on Applied Superconductivity*, vol. 27, pp. 1–5, June 2017.

[55] A. A. Abrikosov, "On the magnetic properties of superconductors of the second group," *Soviet Physics-JETP*, vol. 5, pp. 1174–1182, 1957.

[56] M. Tinkham, *Introduction to Superconductivity: Second Edition*. Mineola, NY: Dover Publications, June 2004.

[57] R. Meservey and P. M. Tedrow, "Properties of very thin aluminum films," *Journal of Applied Physics*, vol. 42, pp. 51–53, Jan. 1971.

[58] N. R. Werthamer, E. Helfand, and P. C. Hohenberg, "Temperature and purity dependence of the superconducting critical field, III. Electron spin and spin-orbit effects," *Physical Review*, vol. 147, pp. 295–302, July 1966.

[59] E. Helfand and N. R. Werthamer, "Temperature and purity dependence of the superconducting critical field, Hc2. ii," *Physical Review*, vol. 147, pp. 288–294, July 1966.

[60] D. A. Mayoh, J. A. T. Barker, R. P. Singh, G. Balakrishnan, D. M. Paul, and M. R. Lees, "Superconducting and normal-state properties of the noncentrosymmetric superconductor Re6Zr," *Physical Review B*, vol. 96, p. 064521, Aug. 2017.

[61] V. Ginzburg and L. Landau, *On the Theory of Superconductivity*, pp. 546–568. Elsevier, 1965.

[62] C. Gorter, *The Two Fluid Model for Superconductors and Helium II*, pp. 1–16. Elsevier, 1955.

[63] F. London and H. London, "The electromagnetic equations of the supraconductor," *Proceedings of the Royal Society of London. Series A - Mathematical and Physical Sciences*, vol. 149, pp. 71–88, Mar. 1935.

[64] Y. Mawatari, "Kinetic inductance of superconducting nanostrips with turns," *Journal of Applied Physics*, vol. 133, May 2023.

[65] L. Yu, N. Newman, and J. Rowell, "Measurement of the coherence length of sputtered Nb0.62Ti0.38N thin films," *IEEE Transactions on Appiled Superconductivity*, vol. 12, pp. 1795–1798, June 2002.

[66] M. Sidorova, A. D. Semenov, H.-W. Hübers, S. Gyger, S. Steinhauer, X. Zhang, and A. Schilling, "Magnetoconductance and photoresponse properties of disordered NbTiN films," *Physical Review B*, vol. 104, p. 184514, Nov. 2021.

[67] Y. Lee, J. Yun, C. Lee, M. Sirena, J. Kim, and N. Haberkorn, "Penetration depth in dirty superconducting NbTiN thin films grown at room temperature," *Applied Physics A*, vol. 130, June 2024.

[68] J. F. Cochran and D. E. Mapother, "Superconducting transition in aluminum," *Physical Review*, vol. 111, pp. 132–142, July 1958.

[69] D. López-Núñez, A. Torras-Coloma, Q. Portell-Montserrat, E. Bertoldo, L. Cozzolino, G. A. Ummarino, A. Zaccone, G. Rius, M. Martínez, and P. Forn-Díaz, "Superconducting penetration depth of aluminum thin films," *Superconductor Science and Technology*, vol. 38, p. 095004, Sept. 2025.

[70] A. P. M. Place, L. V. H. Rodgers, P. Mundada, B. M. Smitham, M. Fitzpatrick, Z. Leng, A. Premkumar, J. Bryon, A. Vrajitoarea, S. Sussman, G. Cheng, T. Madhavan, H. K. Babla, X. H. Le, Y. Gang, B. Jäck, A. Gyenis, N. Yao, R. J. Cava, N. P. de Leon, and A. A. Houck, "New material platform for superconducting transmon qubits with coherence times exceeding 0.3 milliseconds," *Nature Communications*, vol. 12, Mar. 2021.

[71] X. Chen, C. Tang, L. Yao, Z. Cao, Y. Zhu, D. Zhang, and X. Kou, "Two-dimensional superconductivity of epitaxial tantalum films," *Physical Review B*, vol. 111, p. 184503, May 2025.

[72] P. C. J. J. Coumou, *Electrodynamics of strongly disordered superconductors*. PhD thesis, TU Delft, 2015.

[73] H. G. Leduc, B. Bumble, P. K. Day, B. H. Eom, J. Gao, S. Golwala, B. A. Mazin, S. McHugh, A. Merrill, D. C. Moore, O. Noroozian, A. D. Turner, and J. Zmuidzinas, "Titanium nitride films for ultrasensitive microresonator detectors," *Applied Physics Letters*, vol. 97, Sept. 2010.

[74] D. K. Finnemore, T. F. Stromberg, and C. A. Swenson, "Superconducting properties of high-purity niobium," *Physical Review*, vol. 149, pp. 231–243, Sept. 1966.

[75] A. I. Gubin, K. S. Il'in, S. A. Vitusevich, M. Siegel, and N. Klein, "Dependence of magnetic penetration depth on the thickness of superconducting Nb thin films," *Physical Review B*, vol. 72, p. 064503, Aug. 2005.

[76] M. C. Burton, M. R. Beebe, K. Yang, R. A. Lukaszew, A.-M. Valente-Feliciano, and C. Reece, "Superconducting NbTiN thin films for superconducting radio frequency accelerator cavity applications," *Journal of Vacuum Science and Technology A: Vacuum, Surfaces, and Films*, vol. 34, Feb. 2016.

[77] P. Pratap, L. Nanda, K. Senapati, R. P. Aloysius, and V. Achanta, "Optimization of the superconducting properties of NbTiN thin films by variation of the N2 partial pressure during sputter deposition," *Superconductor Science and Technology*, vol. 36, p. 085017, July 2023.

[78] W. Słysz, M. Guziewicz, M. Borysiewicz, J. Domagała, I. Pasternak, K. Hejduk, W. Rzodkiewicz, J. Ratajczak, J. Bar, M. Węgrzecki, P. Grabiec, R. Grodecki, I. Węgrzecka, and R. Sobolewski, "Ultrathin NbN films for superconducting single-photon detectors," *Acta Physica Polonica A*, vol. 120, pp. 200–203, July 2011.

[79] Y. Zhong, L. Zhang, J. Xie, Z. Zheng, M. Lu, H. Jin, L. Wu, W. Shi, H. Wang, W. Peng, L. Chen, and Z. Wang, "Inductance and penetration depth measurements of polycrystalline NbN films for all-NbN single flux quantum circuits," *Superconductor Science and Technology*, vol. 38, p. 015001, Nov. 2024.

[80] A. J. Annunziata, D. F. Santavicca, L. Frunzio, G. Catelani, M. J. Rooks, A. Frydman, and D. E. Prober, "Tunable superconducting nanoinductors," *Nanotechnology*, vol. 21, p. 445202, Oct. 2010.

[81] N. A. Masluk, I. M. Pop, A. Kamal, Z. K. Minev, and M. H. Devoret, "Microwave characterization of Josephson junction arrays: Implementing a low loss superinductance," *Physical Review Letters*, vol. 109, p. 137002, Sept. 2012.

[82] A. Ioffe and A. Regel, *Non-crystalline, amorphous, and liquid electronic semiconductors*, pp. 237–291. London: Heywood and Co., Ltd., 1960.

[83] P. W. Anderson, "Absence of diffusion in certain random lattices," *Physical Review*, vol. 109, pp. 1492–1505, Mar. 1958.

[84] M. P. A. Fisher, "Quantum phase transitions in disordered two-dimensional superconductors," *Physical Review Letters*, vol. 65, pp. 923–926, Aug. 1990.

[85] A. Ghosal, M. Randeria, and N. Trivedi, "Role of spatial amplitude fluctuations in highly disordered s-wave superconductors," *Physical Review Letters*, vol. 81, pp. 3940–3943, Nov. 1998.

[86] Y. Dubi, Y. Meir, and Y. Avishai, "Nature of the superconductor–insulator transition in disordered superconductors," *Nature*, vol. 449, pp. 876–880, Oct. 2007.

[87] A. Karpov, D. Miller, F. R. Rice, J. A. Stern, B. Bumble, H. G. LeDuc, and J. Zmuidzinas, "Low-noise SIS mixer for far-infrared radio astronomy," in *Millimeter and Submillimeter Detectors for Astronomy II* (J. Zmuidzinas, W. S. Holland, and S. Withington, eds.), vol. 5498, p. 616, SPIE, Oct. 2004.

[88] J. Kawamura, J. Chen, D. Miller, J. Kooi, J. Zmuidzinas, B. Bumble, H. G. LeDuc, and J. A. Stern, "Low-noise submillimeter-wave nbtin superconducting tunnel junction mixers," *Applied Physics Letters*, vol. 75, pp. 4013–4015, Dec. 1999.

[89] L. Nulens, D. A. Chaves, S. Reniers, R. Dillemans, I. P. Cools, K. Temst, B. Raes, M. J. Van Bael, and J. Van de Vondel, "Nonvolatile cryogenic phase-slip memory with single-shot readout," *Physical Review Applied*, vol. 24, Nov. 2025.

[90] Y. Tian, I. Grytsenko, A. Jennings, J. Wang, H. Ikegami, X. Zhou, S. Tamate, H. Terai, H. Kutsuma, D. Jin, M. Benito, and E. Kawakami, "NbTiN nanowire resonators and prospects for spin-photon coupling with electrons on solid Neon," *Physical Review Applied*, vol. 25, Feb. 2026.

[91] Y. Jo, A. Fasano, E. Won, M. Hattori, S. Honda, C. Otani, J. Suzuki, M. Peel, K. Karatsu, R. Genova-Santos, and M. Tsujii, "Groundbird telescope: Systematics modelization of MKID arrays response," *IEEE Transactions on Applied Superconductivity*, pp. 1–7, 2026.

[92] M. Yabuno, "A wide-strip superconducting photon detector," *JSAP Review*, vol. 2026, p. 260404, 2026.

[93] A. Chattaraj, A. k. Anbalagan, J. Cho, and M. Liu, "Materials studies of niobium thin films for quantum circuit applications: Progress and challenges," *Advanced Quantum Technologies*, vol. 9, Jan. 2026.

[94] H. Ge, Y.-R. Jin, and X.-H. Song, "High quality NbTiN films fabrication and rapid thermal annealing investigation," *Chinese Physics B*, vol. 28, p. 077402, July 2019.

[95] L. Yu, R. Singh, H. Liu, S. Wu, R. Hu, D. Durand, J. Bulman, J. Rowell, and N. Newman, "Fabrication of niobium titanium nitride thin films with high superconducting transition temperatures and short penetration lengths," *IEEE Transactions on Appiled Superconductivity*, vol. 15, pp. 44–48, Mar. 2005.

[96] C. Klein, S. Cohen, T. Descamps, A. Iovan, P. Zolotov, P. Vennéguès, I. Florea, F. Semond, and V. Zwiller, "Enhanced superconducting nanowire single photon detector performances using silicon capping," 2026.

[97] J. Krupka, K. Derzakowski, M. Tobar, J. Hartnett, and R. G. Geyer, "Complex permittivity of some ultralow loss dielectric crystals at cryogenic temperatures," *Measurement Science and Technology*, vol. 10, pp. 387–392, Jan. 1999.

[98] K. W. Kirby, *Processing of sapphire surfaces for semiconductor device applications*. Master's thesis, Penn State, 2008.

[99] T. Boehme, *Characterisation and optimisation of superconducting microwave resonators*. Master's thesis, Chalmers University of Technology, 2016.

[100] A. Somoroff, Q. Ficheux, R. A. Mencia, H. Xiong, R. Kuzmin, and V. E. Manucharyan, "Millisecond coherence in a superconducting qubit," *Physical Review Letters*, vol. 130, p. 267001, June 2023.

[101] J. M. Martinis and A. Megrant, "UCSB final report for the CSQ program: Review of decoherence and materials physics for superconducting qubits," 2014.

[102] S. S. Yeram, S. Bhakat, S. S. Dash, and A. Pal, "Structural transitions in superconducting NbTiN thin films," 2023.

[103] F. Joint, K. Rafsanjani Amin, I. P. C. Cools, and S. Gasparinetti, "Dynamics of gate-controlled superconducting Dayem bridges," *Applied Physics Letters*, vol. 125, Aug. 2024.

[104] S. Vervoort, L. Nulens, D. A. D. Chaves, H. Dausy, S. Reniers, M. Abouelela, I. P. C. Cools, A. V. Silhanek, M. J. Van Bael, B. Raes, and J. Van de Vondel, "DC-operated Josephson junction arrays as a cryogenic on-chip microwave measurement platform," *Communications Physics*, vol. 8, July 2025.

[105] B. A. Mazin, *Microwave Kinetic Inductance Detectors*. PhD thesis, California Institute of Technology, Aug. 2004.

[106] M. W. Olszewski, L. Kong, S. Reinhardt, D. Tong, X. Du, G. Di Gianluca, H. Lu, S. Roy, L. Zhang, A. B. Biedron, D. A. Muller, and V. Fatemi, "Krypton-sputtered tantalum films for scalable high-performance quantum devices," 2026.

[107] M. Müller, T. Luschmann, A. Faltermeier, S. Weichselbaumer, L. Koch, G. B. P. Huber, H. W. Schumacher, N. Ubbelohde, D. Reifert, T. Scheller, F. Deppe, A. Marx, S. Filipp, M. Althammer, R. Gross, and H. Huebl, "Magnetic field robust high quality factor NbTiN superconducting microwave resonators," *Materials for Quantum Technology*, vol. 2, Feb. 2022.

[108] N. Maleeva, L. Grünhaupt, T. Klein, F. Levy-Bertrand, O. Dupre, M. Calvo, F. Valenti, P. Winkel, F. Friedrich, W. Wernsdorfer, A. V. Ustinov, H. Rotzinger, A. Monfardini, M. V. Fistul, and I. M. Pop, "Circuit quantum electrodynamics of granular aluminum resonators," *Nature Communications*, vol. 9, Sept. 2018.

[109] C. T. Earnest, J. H. Béjanin, T. G. McConkey, E. A. Peters, A. Korinek, H. Yuan, and M. Mariantoni, "Substrate surface engineering for high-quality silicon/aluminum superconducting resonators," *Superconductor Science and Technology*, vol. 31, p. 125013, Nov. 2018.

[110] E. V. Zikiy, A. I. Ivanov, N. S. Smirnov, D. O. Moskalev, V. I. Polozov, A. R. Matanin, E. I. Malevannaya, V. V. Echeistov, T. G. Konstantinova, and I. A. Rodionov, "High-Q trenched aluminum coplanar resonators with an ultrasonic edge microcutting for superconducting quantum devices," *Scientific Reports*, vol. 13, Sept. 2023.

[111] K. D. Crowley, R. A. McLellan, A. Dutta, N. Shumiya, A. P. Place, X. H. Le, Y. Gang, T. Madhavan, M. P. Bland, R. Chang, N. Khedkar, Y. C. Feng, E. A. Umbarkar, X. Gui, L. V. Rodgers, Y. Jia, M. M. Feldman, S. A. Lyon, M. Liu, R. J. Cava, A. A. Houck, and N. P. de Leon, "Disentangling losses in tantalum superconducting circuits," *Physical Review X*, vol. 13, p. 041005, Oct. 2023.

[112] C. Wang, X. Li, H. Xu, Z. Li, J. Wang, Z. Yang, Z. Mi, X. Liang, T. Su, C. Yang, G. Wang, W. Wang, Y. Li, M. Chen, C. Li, K. Linghu, J. Han, Y. Zhang, Y. Feng, Y. Song, T. Ma, J. Zhang, R. Wang, P. Zhao, W. Liu, G. Xue, Y. Jin, and H. Yu, "Towards practical quantum computers: transmon qubit with a lifetime approaching 0.5 milliseconds," *npj Quantum Information*, vol. 8, Jan. 2022.

[113] R. Dhundhwal, H. Duan, L. Brauch, S. Arabi, D. Fuchs, A.-A. Haghighirad, A. Welle, F. Scharwaechter, S. Pal, M. Scheffler, J. Palomo, Z. Leghtas, A. Murani, H. Hahn, J. Aghassi-Hagmann, C. Kübel, W. Wulfhekel, I. M. Pop, and T. Reisinger, "High quality superconducting tantalum resonators with beta phase defects," 2025.

[114] J. B. Chang, M. R. Vissers, A. D. Córcoles, M. Sandberg, J. Gao, D. W. Abraham, J. M. Chow, J. M. Gambetta, M. Beth Rothwell, G. A. Keefe, M. Steffen, and D. P. Pappas, "Improved superconducting qubit coherence using titanium nitride," *Applied Physics Letters*, vol. 103, July 2013.

[115] L. Grünhaupt, N. Maleeva, S. T. Skacel, M. Calvo, F. Levy-Bertrand, A. V. Ustinov, H. Rotzinger, A. Monfardini, G. Catelani, and I. M. Pop, "Loss mechanisms and quasiparticle dynamics in superconducting microwave resonators made of thin-film granular aluminum," *Physical Review Letters*, vol. 121, p. 117001, Sept. 2018.

[116] R. W. Cohen and B. Abeles, "Superconductivity in granular aluminum films," *Physical Review*, vol. 168, pp. 444–450, Apr. 1968.

[117] B. Calmels, *Granular aluminium as a building block of superinductance*. PhD thesis, University Paris-Saclay, 2025.

[118] L. Grünhaupt, M. Spiecker, D. Gusenkova, N. Maleeva, S. T. Skacel, I. Takmakov, F. Valenti, P. Winkel, H. Rotzinger, W. Wernsdorfer, A. V. Ustinov, and I. M. Pop, "Granular aluminium as a superconducting material for high-impedance quantum circuits," *Nature Materials*, vol. 18, pp. 816–819, Apr. 2019.

[119] K. Borisov, D. Rieger, P. Winkel, F. Henriques, F. Valenti, A. Ionita, M. Wessbecher, M. Spiecker, D. Gusenkova, I. M. Pop, and W. Wernsdorfer, "Superconducting granular aluminum resonators resilient to magnetic fields up to 1 Tesla," *Applied Physics Letters*, vol. 117, Sept. 2020.

[120] M. Kudra, J. Biznárová, A. Fadavi Roudsari, J. J. Burnett, D. Niepce, S. Gasparinetti, B. Wickman, and P. Delsing, "High quality three-dimensional aluminum microwave cavities," *Applied Physics Letters*, vol. 117, p. 070601, Aug. 2020.

[121] J. Braumüller, *Quantum simulation experiments with superconducting circuits*. PhD thesis, Karlsruher Institut fur Technologie (KIT), 2018.

[122] C. Janvier, *Coherent manipulation of Andreev bound states in an atomic contact*. PhD thesis, Université Paris Saclay (COmUE), 2016.

[123] C. Müller, J. H. Cole, and J. Lisenfeld, "Towards understanding two-level-systems in amorphous solids: insights from quantum circuits," *Reports on Progress in Physics*, vol. 82, p. 124501, Oct. 2019.

[124] S. E. de Graaf, L. Faoro, J. Burnett, A. A. Adamyan, A. Y. Tzalenchuk, S. E. Kubatkin, T. Lindström, and A. V. Danilov, "Suppression of low-frequency charge noise in superconducting resonators by surface spin desorption," *Nature Communications*, vol. 9, p. 1143, Mar. 2018.

[125] D. P. Pappas, M. R. Vissers, D. S. Wisbey, J. S. Kline, and J. Gao, "Two Level System Loss in Superconducting Microwave Resonators," *IEEE Transactions on Applied Superconductivity*, vol. 21, pp. 871–874, June 2011.

[126] J. Burnett, L. Faoro, and T. Lindström, "Analysis of high quality superconducting resonators: consequences for TLS properties in amorphous oxides," *Superconductor Science and Technology*, vol. 29, p. 044008, Mar. 2016.

[127] J. Burnett, A. Bengtsson, D. Niepce, and J. Bylander, "Noise and loss of superconducting aluminium resonators at single photon energies," *Journal of Physics: Conference Series*, vol. 969, p. 012131, Mar. 2018.

[128] C.-C. Hung, T. Kohler, and K. D. Osborn, "Quantum defects from a single surface exhibit strong mutual interactions," *Physical Review Applied*, vol. 21, p. 044021, Apr. 2024.

[129] W. A. Phillips, "Tunneling states in amorphous solids," *Journal of Low Temperature Physics*, vol. 7, pp. 351–360, May 1972.

[130] W. A. Phillips, "Two-level states in glasses," *Reports on Progress in Physics*, vol. 50, p. 1657, Dec. 1987.

[131] I. Nsanzineza, *Vortices and quasiparticles in superconducting microwave resonators*. PhD thesis, Syracuse University, 2016.

[132] P. J. De Visser, *Quasiparticle dynamics in aluminium superconducting microwave resonators*. PhD thesis, TUDelft, 2014.

[133] D. M. Pozar, *Microwave Engineering*. Hoboken, NJ: Wiley, 4th edition ed., Nov. 2011.

[134] S. Probst, F. Song, P. A. Bushev, A. V. Ustinov, and M. Weides, "Efficient and robust analysis of complex scattering data under noise in microwave resonators," *Review of Scientific Instruments*, vol. 86, no. 2, p. 024706, 2015.

[135] P. G. Baity, C. Maclean, V. Seferai, J. Bronstein, Y. Shu, T. Hemakumara, and M. Weides, "Circle fit optimization for resonator quality factor measurements: Point redistribution for maximal accuracy," *Physical Review Research*, vol. 6, p. 013329, Mar. 2024.

[136] A. Bruno, G. De Lange, S. Asaad, K. Van Der Enden, N. Langford, and L. DiCarlo, "Reducing intrinsic loss in superconducting resonators by surface treatment and deep etching of silicon substrates," *Applied Physics Letters*, vol. 106, no. 18, p. 182601, 2015.

[137] A. Paquette, J. Griesmar, G. Lavoie, R. Albert, F. Blanchet, A. Grimm, U. Martel, and M. Hofheinz, "Absorptive filters for quantum circuits: Efficient fabrication and cryogenic power handling," *Applied Physics Letters*, vol. 121, Sept. 2022.

[138] J. Gao, M. Daal, A. Vayonakis, S. Kumar, J. Zmuidzinas, B. Sadoulet, B. A. Mazin, P. K. Day, and H. G. Leduc, "Experimental evidence for a surface distribution of two-level systems in superconducting lithographed microwave resonators," *Applied Physics Letters*, vol. 92, p. 152505, Apr. 2008.

[139] J. Gao, *The Physics of Superconducting Microwave Resonators*. PhD thesis, California Institute of Technology, 2008.

[140] K. R. Amin, C. Ladner, G. Jourdan, S. Hentz, N. Roch, and J. Renard, "Loss mechanisms in tin high impedance superconducting microwave circuits," *Applied Physics Letters*, vol. 120, Apr. 2022.

[141] M. Arzeo, F. Lombardi, and T. Bauch, "Microwave losses in MgO, LaAlO3, and (La0.3Sr0.7)(Al0.65Ta0.35)O3 dielectrics at low power and in the millikelvin temperature range," *Applied Physics Letters*, vol. 104, p. 212601, May 2014.

[142] C. R. H. McRae, J. H. Béjanin, C. T. Earnest, T. G. McConkey, J. R. Rinehart, C. Deimert, J. P. Thomas, Z. R. Wasilewski, and M. Mariantoni, "Thin film metrology and microwave loss characterization of indium and aluminum/indium superconducting planar resonators," *Journal of Applied Physics*, vol. 123, p. 205304, May 2018.

[143] J. Burnett, L. Faoro, I. Wisby, V. L. Gurtovoi, A. V. Chernykh, G. M. Mikhailov, V. A. Tulin, R. Shaikhaidarov, V. Antonov, P. J. Meeson, A. Y. Tzalenchuk, and T. Lindström, "Evidence for interacting two-level systems from the 1/f noise of a superconducting resonator," *Nature Communications*, vol. 5, June 2014.

[144] J. Wenner, R. Barends, R. C. Bialczak, Y. Chen, J. Kelly, E. Lucero, M. Mariantoni, A. Megrant, P. J. J. O'Malley, D. Sank, A. Vainsencher, H. Wang, T. C. White, Y. Yin, J. Zhao, A. N. Cleland, and J. M. Martinis, "Surface loss simulations of superconducting coplanar waveguide resonators," *Applied Physics Letters*, vol. 99, p. 113513, Sept. 2011.

[145] D. Niepce, J. J. Burnett, M. G. Latorre, and J. Bylander, "Geometric scaling of two-level-system loss in superconducting resonators," *Superconductor Science and Technology*, vol. 33, p. 025013, Jan. 2020.

[146] Sonnet, "Sonnet software." https://www.sonnetsoftware.com/, 2012.

[147] R. Simons, *Coplanar waveguide circuits, components, and systems*. No. v. 165 in Wiley Series in Microwave and Optical Engineering, New York: Wiley Interscience, 2001. Includes bibliographical references and index.

[148] J. Rautio, *Method of Moments Analysis of Structures Embedded in Shielded Layered Media*. Amazon, 2020.

[149] C. X. Yu, S. Zihlmann, G. Troncoso Fernández-Bada, J.-L. Thomassin, F. Gustavo, E. Dumur, and Romain, "Magnetic field resilient high kinetic inductance superconducting niobium nitride coplanar waveguide resonators," *Applied Physics Letters*, vol. 118, p. 054001, Feb. 2021.

[150] M. S. Khalil, M. Stoutimore, F. Wellstood, and K. Osborn, "An analysis method for asymmetric resonator transmission applied to superconducting devices," *Journal of Applied Physics*, vol. 111, no. 5, p. 054510, 2012.

[151] A. Megrant, C. Neill, R. Barends, B. Chiaro, Y. Chen, L. Feigl, J. Kelly, E. Lucero, M. Mariantoni, P. J. J. O'Malley, D. Sank, A. Vainsencher, J. Wenner, T. C. White, Y. Yin, J. Zhao, C. J. Palmstrøm, J. M. Martinis, and A. N. Cleland, "Planar superconducting resonators with internal quality factors above one million," *Applied Physics Letters*, vol. 100, Mar. 2012.

[152] C. Chen, D. Perello, S. Aghaeimeibodi, G. Marcaud, I. Jarrige, H. Lee, W. Fon, M. Matheny, and J. Gao, "Efficient methods for extracting superconducting resonator loss in the single-photon regime," *Journal of Applied Physics*, vol. 137, Jan. 2025.

[153] L. Ranzani, L. Spietz, Z. Popovic, and J. Aumentado, "Two-port microwave calibration at millikelvin temperatures," *Review of Scientific Instruments*, vol. 84, Mar. 2013.

[154] S. Simbierowicz, V. Y. Monarkha, S. Singh, N. Messaoudi, P. Krantz, and R. E. Lake, "Microwave calibration of qubit drive line components at millikelvin temperatures," *Applied Physics Letters*, vol. 120, Jan. 2022.

[155] H. Wang, S. Singh, C. R. H. McRae, J. C. Bardin, S.-X. Lin, N. Messaoudi, A. R. Castelli, Y. J. Rosen, E. T. Holland, D. P. Pappas, and J. Y. Mutus, "Cryogenic single-port calibration for superconducting microwave resonator measurements," *Quantum Science and Technology*, vol. 6, p. 035015, June 2021.

[156] N. Chernov and C. Lesort, "Least squares fitting of circles," *Journal of Mathematical Imaging and Vision*, vol. 23, pp. 239–252, Nov. 2005.

[157] H. Abdul-Rahman and N. Chernov, "Fast and numerically stable circle fit," *Journal of Mathematical Imaging and Vision*, vol. 49, pp. 289–295, Sept. 2013.

[158] S. Doyle, P. Mauskopf, J. Naylon, A. Porch, and C. Duncombe, "Lumped element kinetic inductance detectors," *Journal of Low Temperature Physics*, vol. 151, pp. 530–536, Apr. 2008.

[159] K. L. Geerlings, *Improving Coherence of Superconducting Qubits and Resonators*. PhD thesis, Yale University, Jan. 2013.

[160] U. Fano, "Effects of configuration interaction on intensities and phase shifts," *Physical Review*, vol. 124, pp. 1866–1878, Dec. 1961.

[161] M. E. Brinson and S. Jahn, "Qucs: A gpl software package for circuit simulation, compact device modelling and circuit macromodelling from dc to rf and beyond," *International Journal of Numerical Modelling: Electronic Networks, Devices and Fields*, vol. 22, pp. 297–319, Sept. 2008.

[162] C. Deng, M. Otto, and A. Lupascu, "An analysis method for transmission measurements of superconducting resonators with applications to quantum-regime dielectric-loss measurements," *Journal of Applied Physics*, vol. 114, Aug. 2013.

[163] D. Rieger, S. Günzler, M. Spiecker, A. Nambisan, W. Wernsdorfer, and I. Pop, "Fano interference in microwave resonator measurements," *Physical Review Applied*, vol. 20, p. 014059, July 2023.

[164] W. Kern, "The evolution of silicon wafer cleaning technology," *Journal of The Electrochemical Society*, vol. 137, pp. 1887–1892, June 1990.

[165] M. Yoshimoto, T. Maeda, T. Ohnishi, H. Koinuma, O. Ishiyama, M. Shinohara, M. Kubo, R. Miura, and A. Miyamoto, "Atomic-scale formation of ultrasmooth surfaces on sapphire substrates for high-quality thin-film fabrication," *Applied Physics Letters*, vol. 67, pp. 2615–2617, Oct. 1995.

[166] S. Mahashabde, E. Otto, D. Montemurro, S. de Graaf, S. Kubatkin, and A. Danilov, "Fast tunable high Q-factor superconducting microwave resonators," *Physical Review Applied*, vol. 14, p. 044040, Oct. 2020.

[167] F. Pobell, *Matter and methods at low temperatures*. Springer Science & Business Media, 2007.

[168] S. Krinner, S. Storz, P. Kurpiers, P. Magnard, J. Heinsoo, R. Keller, J. Luetolf, C. Eichler, and A. Wallraff, "Engineering cryogenic setups for 100-qubit scale superconducting circuit systems," *EPJ Quantum Technology*, vol. 6, no. 1, p. 2, 2019.

[169] P. Kurpiers, T. Walter, P. Magnard, Y. Salathe, and A. Wallraff, "Characterizing the attenuation of coaxial and rectangular microwave-frequency waveguides at cryogenic temperatures," *EPJ Quantum Technology*, vol. 4, pp. 1–15, Dec. 2017.

[170] R. Barends, J. Wenner, M. Lenander, Y. Chen, R. C. Bialczak, J. Kelly, E. Lucero, P. O'Malley, M. Mariantoni, D. Sank, H. Wang, T. C. White, Y. Yin, J. Zhao, A. N. Cleland, J. M. Martinis, and J. J. A. Baselmans, "Minimizing quasiparticle generation from stray infrared light in superconducting quantum circuits," *Applied Physics Letters*, vol. 99, p. 113507, Sept. 2011.

[171] F. P. Milliken, J. R. Rozen, G. A. Keefe, and R. H. Koch, "50 Ohm characteristic impedance low-pass metal powder filters," *Review of Scientific Instruments*, vol. 78, Feb. 2007.

[172] A. Lukashenko and A. V. Ustinov, "Improved powder filters for qubit measurements," *Review of Scientific Instruments*, vol. 79, p. 014701, Jan. 2008.

[173] A. I. Ivanov, V. I. Polozov, V. V. Echeistov, A. A. Samoylov, E. I. Malevannaya, A. R. Matanin, N. S. Smirnov, and I. A. Rodionov, "Robust cryogenic matched low-pass coaxial filters for quantum computing applications," *Applied Physics Letters*, vol. 123, Nov. 2023.

[174] A. Roitman, A. Shaulov, and Y. Yeshurun, "Characterization of YBa2Cu3O7 coplanar resonator for microwave kinetic inductance detectors," *Superconductor Science and Technology*, vol. 36, p. 015002, Nov. 2022.

[175] A. Roitman, L. Burlachkov, A. Sharoni, A. Shaulov, and Y. Yeshurun, "Suppression of magnetic vortex losses in submicron NbN coplanar waveguide resonators," *Scientific Reports*, vol. 14, Nov. 2024.

[176] G. Calusine, A. Melville, W. Woods, R. Das, C. Stull, V. Bolkhovsky, D. Braje, D. Hover, D. K. Kim, X. Miloshi, D. Rosenberg, A. Sevi, J. L. Yoder, E. Dauler, and W. D. Oliver, "Analysis and mitigation of interface losses in trenched superconducting coplanar waveguide resonators," *Applied Physics Letters*, vol. 112, Feb. 2018.

[177] C. Neill, A. Megrant, R. Barends, Y. Chen, B. Chiaro, J. Kelly, J. Y. Mutus, P. J. J. O'Malley, D. Sank, J. Wenner, T. C. White, Y. Yin, A. N. Cleland, and J. M. Martinis, "Fluctuations from edge defects in superconducting resonators," *Applied Physics Letters*, vol. 103, Aug. 2013.

[178] J. Biznárová, *Development of high-coherence superconducting devices for quantum computing: fabrication process development, materials analysis, and device characterization*. PhD thesis, Chalmers University of Technology, 2024.

[179] S. Ohya, B. Chiaro, A. Megrant, C. Neill, R. Barends, Y. Chen, J. Kelly, D. Low, J. Mutus, P. J. J. O'Malley, P. Roushan, D. Sank, A. Vainsencher, J. Wenner, T. C. White, Y. Yin, B. D. Schultz, C. J. Palmstrøm, B. A. Mazin, A. N. Cleland, and J. M. Martinis, "Room

temperature deposition of sputtered TiN films for superconducting coplanar waveguide resonators," *Superconductor Science and Technology*, vol. 27, Dec. 2013.

[180] J. Gorobez, B. Maack, and N. Nilius, "Growth of self-passivating oxide layers on aluminum—pressure and temperature dependence," *physica status solidi (b)*, vol. 258, Jan. 2021.

[181] A. Darlinski and J. Halbritter, "Angle-resolved XPS studies of oxides at NbN, NbC, and Nb surfaces," *Surface and Interface Analysis*, vol. 10, pp. 223–237, June 1987.

[182] I. Lindau and W. E. Spicer, "Oxidation of Nb as studied by the uv-photoemission technique," *Journal of Applied Physics*, vol. 45, pp. 3720–3725, Sept. 1974.

[183] X. Q. Jia, L. Kang, X. Y. Liu, Z. H. Wang, B. B. Jin, S. B. Mi, J. Chen, W. W. Xu, and P. H. Wu, "High performance ultra-thin niobium films for superconducting hot-electron devices," *IEEE Transactions on Applied Superconductivity*, vol. 23, pp. 2300704–2300704, June 2013.

[184] B. A. Mazin, "Microwave kinetic inductance detectors: The first decade," in *AIP Conference Proceedings*, vol. 1185, pp. 135–142, American Institute of Physics, 2009.

[185] D. Bothner, T. Gaber, M. Kemmler, D. Koelle, and R. Kleiner, "Improving the performance of superconducting microwave resonators in magnetic fields," *Applied Physics Letters*, vol. 98, p. 102504, Mar. 2011.

[186] J. M. Sage, V. Bolkhovsky, W. D. Oliver, B. Turek, and P. B. Welander, "Study of loss in superconducting coplanar waveguide resonators," *Journal of Applied Physics*, vol. 109, no. 6, p. 063915, 2011.

[187] J. Lee, H. Lee, W. Kim, J. Lee, and J. Kim, "Suppression of coupled-slotline mode on CPW using air-bridges measured by picosecond photoconductive sampling," *IEEE Microwave and Guided Wave Letters*, vol. 9, pp. 265–267, July 1999.

[188] F. Lange, L. Heunisch, H. Fehske, D. P. DiVincenzo, and M. J. Hartmann, "Crosstalk in superconducting qubit lattices with tunable couplers—comparing transmon and fluxonium architectures," *Quantum Science and Technology*, vol. 11, p. 015020, Dec. 2025.

[189] S. E. de Graaf, D. Davidovikj, A. Adamyan, S. E. Kubatkin, and A. V. Danilov, "Galvanically split superconducting microwave resonators for introducing internal voltage bias," *Applied Physics Letters*, vol. 104, p. 052601, Feb. 2014.

[190] S. Ganjam, Y. Wang, Y. Lu, A. Banerjee, C. U. Lei, L. Krayzman, K. Kisslinger, C. Zhou, R. Li, Y. Jia, M. Liu, L. Frunzio, and R. J. Schoelkopf, "Surpassing millisecond coherence in on chip superconducting quantum memories by optimizing materials and circuit design," *Nature Communications*, vol. 15, May 2024.

[191] G.-W. Deng, D. Wei, S.-X. Li, J. R. Johansson, W.-C. Kong, H.-O. Li, G. Cao, M. Xiao, G.-C. Guo, F. Nori, H.-W. Jiang, and G.-P. Guo, "Coupling two distant double quantum dots with a microwave resonator," *Nano Letters*, vol. 15, pp. 6620–6625, Oct. 2015.

[192] T. Frey, P. J. Leek, M. Beck, A. Blais, T. Ihn, K. Ensslin, and A. Wallraff, "Dipole coupling of a double quantum dot to a microwave resonator," *Physical Review Letters*, vol. 108, p. 046807, Jan. 2012.

[193] G. Burkard, M. J. Gullans, X. Mi, and J. R. Petta, "Superconductor–semiconductor hybrid-circuit quantum electrodynamics," *Nature Reviews Physics*, vol. 2, pp. 129–140, mar 2020.

[194] G. Kurizki, P. Bertet, Y. Kubo, K. Mølmer, D. Petrosyan, P. Rabl, and J. Schmiedmayer, "Quantum technologies with hybrid systems," *Proceedings of the National Academy of Sciences*, vol. 112, pp. 3866–3873, mar 2015.

[195] Z.-L. Xiang, S. Ashhab, J. You, and F. Nori, "Hybrid quantum circuits: Superconducting circuits interacting with other quantum systems," *Reviews of Modern Physics*, vol. 85, no. 2, p. 623, 2013.

[196] A. Zazunov, V. S. Shumeiko, E. N. Bratus, J. Lantz, and G. Wendin, "Andreev level qubit," *Physical Review Letters*, vol. 90, p. 087003, Feb. 2003.

[197] A. Shearrow, G. Koolstra, S. J. Whiteley, N. Earnest, P. S. Barry, F. J. Heremans, D. D. Awschalom, E. Shirokoff, and D. I. Schuster, "Atomic layer deposition of titanium nitride for quantum circuits," *Applied Physics Letters*, vol. 113, Nov. 2018.

[198] E. Zeldov, J. R. Clem, M. McElfresh, and M. Darwin, "Magnetization and transport currents in thin superconducting films," *Physical Review B*, vol. 49, pp. 9802–9822, Apr. 1994.

[199] J. Kroll, F. Borsoi, K. van der Enden, W. Uilhoorn, D. de Jong, M. Quintero-Pérez, D. van Woerkom, A. Bruno, S. Plissard, D. Car, E. Bakkers, M. Cassidy, and L. Kouwenhoven, "Magnetic-Field-Resilient Superconducting Coplanar-Waveguide Resonators for Hybrid Circuit Quantum Electrodynamics Experiments," *Physical Review Applied*, vol. 11, p. 064053, June 2019.

[200] C. P. Bean and J. D. Livingston, "Surface barrier in type-II superconductors," *Physical Review Letters*, vol. 12, pp. 14–16, Jan. 1964.

[201] A. V. Silhanek, L. Jiang, C. Xue, and B. Vanderheyden, "Impact of border defects on the magnetic flux penetration in superconducting films," *Applied Physics Reviews*, vol. 12, Dec. 2025.

[202] E. H. Brandt and M. Indenbom, "Type-II-superconductor strip with current in a perpendicular magnetic field," *Physical Review B*, vol. 48, pp. 12893–12906, Nov. 1993.

[203] H. Bai, H.-A. Zhou, W. Li, T. Xu, L. Wang, P. Gargiani, M. Valvidares, and W. Jiang, "4 f electron–mediated compensated magnetism in rare-earth-substituted iron garnet films with perpendicular magnetic anisotropy," *Physical Review Applied*, vol. 23, p. 044062, Apr. 2025.

[204] J. I. Vestgården, D. V. Shantsev, Y. M. Galperin, and T. H. Johansen, "Lightning in superconductors," *Scientific Reports*, vol. 2, Nov. 2012.

[205] C. Roy, S. Frasca, and P. Scarlino, "Magnetic-field-resilient high-impedance high-kinetic-inductance superconducting resonators," *Physical Review Applied*, vol. 25, Jan. 2026.

[206] D. Bothner, C. Clauss, E. Koroknay, M. Kemmler, T. Gaber, M. Jetter, M. Scheffler, P. Michler, M. Dressel, D. Koelle, and R. Kleiner, "Reducing vortex losses in superconducting microwave resonators with microsphere patterned antidot arrays," *Applied Physics Letters*, vol. 100, p. 012601, Jan. 2012.

[207] D. Bothner, T. Gaber, M. Kemmler, D. Koelle, R. Kleiner, S. Wünsch, and M. Siegel, "Magnetic hysteresis effects in superconducting coplanar microwave resonators," *Physical Review B*, vol. 86, p. 014517, July 2012.

[208] N. Samkharadze, A. Bruno, P. Scarlino, G. Zheng, D. DiVincenzo, L. DiCarlo, and L. Vandersypen, "High-Kinetic-Inductance Superconducting Nanowire Resonators for Circuit QED in a Magnetic Field," *Physical Review Applied*, vol. 5, p. 044004, Apr. 2016.

[209] I. Cools, "Basic mw analysis fitting and controlling software," Dec. 2022.

[210] S. J. Weber, K. W. Murch, D. H. Slichter, R. Vijay, and I. Siddiqi, "Single crystal silicon capacitors with low microwave loss in the single photon regime," *Applied Physics Letters*, vol. 98, p. 172510, Apr. 2011.

[211] B. Abdo, E. Segev, O. Shtempluck, and E. Buks, "Nonlinear dynamics in the resonance line shape of NbN superconducting resonators," *Physical Review B*, vol. 73, Apr. 2006.

[212] V. Lahtinen and M. Möttönen, "Effects of device geometry and material properties on dielectric losses in superconducting coplanar-waveguide resonators," *Journal of Physics: Condensed Matter*, vol. 32, p. 405702, July 2020.

[213] I. B. Vendik, M. N. Gubina, A. N. Deleniv, and D. V. Kholodnyak, "Distribution of current, surface impedance, and damping in superconductor coupled microstriplines," *Technical Physics*, vol. 42, pp. 196–201, Feb. 1997.

[214] A. Deleniv, M. Gubina, D. Kholodniak, and I. Vendik, "Model of high-temperature superconducting coupled microstrip lines on anisotropic sapphire substrate," *International Journal of RF and Microwave Computer-Aided Engineering*, vol. 8, no. 5, pp. 375–385, 1998.

[215] C. Kaiser, S. T. Skacel, S. Wünsch, R. Dolata, B. Mackrodt, A. Zorin, and M. Siegel, "Measurement of dielectric losses in amorphous thin films at gigahertz frequencies using superconducting resonators," *Superconductor Science and Technology*, vol. 23, p. 075008, June 2010.

[216] S. Clima, G. Pourtois, A. Hardy, S. Van Elshocht, M. K. Van Bael, S. De Gendt, D. J. Wouters, M. Heyns, and J. A. Kittl, "Dielectric response of Ta2O5, Nb2O5, and NbTaO5 from first-principles investigations," *Journal of The Electrochemical Society*, vol. 157, no. 1, p. G20, 2010.

[217] A. P. Read, B. J. Chapman, C. U. Lei, J. C. Curtis, S. Ganjam, L. Krayzman, L. Frunzio, and R. J. Schoelkopf, "Precision measurement of the microwave dielectric loss of sapphire in the quantum regime with parts-per-billion sensitivity," *Physical Review Applied*, vol. 19, p. 034064, Mar. 2023.

[218] A. Y. Mironov, D. M. Silevitch, T. Proslier, S. V. Postolova, M. V. Burdastyh, A. K. Gutakovskii, T. F. Rosenbaum, V. V. Vinokur, and T. I. Baturina, "Charge Berezinskii-Kosterlitz-Thouless transition in superconducting NbTiN films," *Scientific Reports*, vol. 8, Mar. 2018.

[219] J. Pearl, "Current distribution in superconducting films carrying quantized fluxoids," *Applied Physics Letters*, vol. 5, pp. 65–66, Aug. 1964.

[220] P. W. Anderson and J. M. Rowell, "Probable observation of the Josephson superconducting tunneling effect," *Physical Review Letters*, vol. 10, pp. 230–232, Mar. 1963.

[221] L. Flammia, L.-F. Zhang, L. Covaci, A. Perali, and M. V. Milošević, "Superconducting nanoribbon with a constriction: a quantum-confined Josephson junction," *Physical Review B*, vol. 97, p. 134514, Apr. 2018.

[222] H. Sickinger, A. Lipman, M. Weides, R. G. Mints, H. Kohlstedt, D. Koelle, R. Kleiner, and E. Goldobin, "Experimental evidence of a $\varphi$-Josephson junction," *Physical Review Letters*, vol. 109, p. 107002, Sept. 2012.

[223] R. Panghotra, B. Raes, C. C. de Souza Silva, I. Cools, W. Keijers, J. E. Scheerder, V. V. Moshchalkov, and J. Van de Vondel, "Giant fractional Shapiro steps in anisotropic Josephson junction arrays," *Communications Physics*, vol. 3, Mar. 2020.

[224] A. A. Golubov, M. Y. Kupriyanov, and E. Il'ichev, "The current-phase relation in Josephson junctions," *Reviews of Modern Physics*, vol. 76, pp. 411–469, Apr. 2004.

[225] K. K. Likharev, "Superconducting weak links," *Reviews of Modern Physics*, vol. 51, pp. 101–159, Jan. 1979.

[226] P. G. De Gennes, *Superconductivity of Metals and Alloys*. CRC Press, Mar. 2018.

[227] T. M. Klapwijk, "Proximity effect from an Andreev perspective," *Journal of Superconductivity*, vol. 17, pp. 593–611, Oct. 2004.

[228] A. F. Andreev, "Thermal conductivity of the intermediate state of superconductors," *Zh. Eksperim. i Teor. Fiz.*, vol. Vol: 46, 05 1964.

[229] M. Hays, *Realizing of an Andreev Spin Qubit: Exploration of Sub-gap Structure in Josephson Nanowires Using Circuit QED*. PhD thesis, Yale University, 2020.

[230] A. Furusaki and M. Tsukada, "Current-carrying states in Josephson junctions," *Physical Review B*, vol. 43, pp. 10164–10169, May 1991.

[231] C. W. J. Beenakker and H. van Houten, "Josephson current through a superconducting quantum point contact shorter than the coherence length," *Physical Review Letters*, vol. 66, pp. 3056–3059, June 1991.

[232] F. Nichele, E. Portolés, A. Fornieri, A. Whiticar, A. Drachmann, S. Gronin, T. Wang, G. Gardner, C. Thomas, A. Hatke, M. Manfra, and C. Marcus, "Relating Andreev bound states and supercurrents in hybrid Josephson junctions," *Physical Review Letters*, vol. 124, p. 226801, June 2020.

[233] A. Maiani, K. Flensberg, M. Leijnse, C. Schrade, S. Vaitiekėnas, and R. Seoane Souto, "Nonsinusoidal current-phase relations in semiconductor–superconductor– ferromagnetic insulator devices," *Physical Review B*, vol. 107, p. 245415, June 2023.

[234] P. Anderson, "Lectures on the many-body problem," *Academic Press, New York*, 1964.

[235] Y. V. Nazarov and Y. M. Blanter, *Quantum transport: introduction to nanoscience*. Cambridge university press, 2009.

[236] B. Dassonneville, A. Murani, M. Ferrier, S. Guéron, and H. Bouchiat, "Coherence-enhanced phase-dependent dissipation in long SNS Josephson junctions: Revealing Andreev bound state dynamics," *Physical Review B*, vol. 97, p. 184505, May 2018.

[237] I. O. Kulik, "Macroscopic quantization and the proximity effect in SNS junctions," *Soviet Journal of Experimental and Theoretical Physics*, vol. 30, p. 944, 1969.

[238] T. T. Heikkilä, J. Särkkä, and F. K. Wilhelm, "Supercurrent-carrying density of states in diffusive mesoscopic Josephson weak links," *Physical Review B*, vol. 66, p. 184513, Nov. 2002.

[239] S. Pinon, V. Kaladzhyan, and C. Bena, "Modeling long imperfect SNS junctions and Andreev bound states using two impurities and the T-matrix formalism," *Physical Review B*, vol. 101, May 2020.

[240] J. Cayao, A. M. Black-Schaffer, E. Prada, and R. Aguado, "Andreev spectrum and supercurrents in nanowire-based SNS junctions containing Majorana bound states," *Beilstein Journal of Nanotechnology*, vol. 9, pp. 1339–1357, May 2018.

[241] F. Chiodi, M. Ferrier, K. Tikhonov, P. Virtanen, T. T. Heikkilä, M. Feigelman, S. Guéron, and H. Bouchiat, "Probing the dynamics of Andreev states in a coherent normal/superconducting ring," *Scientific Reports*, vol. 1, June 2011.

[242] P. Krogstrup, N. L. B. Ziino, W. Chang, S. M. Albrecht, M. H. Madsen, E. Johnson, J. Nygård, C. Marcus, and T. S. Jespersen, "Epitaxy of semiconductor–superconductor nanowires," *Nature Materials*, vol. 14, pp. 400–406, Jan. 2015.

[243] A. E. Antipov, A. Bargerbos, G. W. Winkler, B. Bauer, E. Rossi, and R. M. Lutchyn, "Effects of gate-induced electric fields on semiconductor Majorana nanowires," *Physical Review X*, vol. 8, p. 031041, Aug. 2018.

[244] J. Zhao, A. Mazanik, D. Razmadze, Y. Liu, P. Krogstrup, F. Bergeret, and S. Vaitiekėnas, "Spin-split superconductivity in spin-orbit coupled hybrid nanowires with ferromagnetic barriers," *Physical Review Letters*, vol. 136, Feb. 2026.

[245] P. G. De Gennes and J. Matricon, "Collective modes of vortex lines in superconductors of the second kind," *Reviews of Modern Physics*, vol. 36, pp. 45–49, Jan. 1964.

[246] W. L. McMillan, "Transition temperature of strong-coupled superconductors," *Physical Review*, vol. 167, pp. 331–344, Mar. 1968.

[247] C. Blömers, T. Grap, M. I. Lepsa, J. Moers, S. Trellenkamp, D. Grützmacher, H. Lüth, and T. Schäpers, "Hall effect measurements on InAs nanowires," *Applied Physics Letters*, vol. 101, Oct. 2012.

[248] W. F. Schiela, P. Yu, and J. Shabani, "Progress in superconductor-semiconductor topological josephson junctions," *PRX Quantum*, vol. 5, p. 030102, Sept. 2024.

[249] L. Tosi, C. Metzger, M. Goffman, C. Urbina, H. Pothier, S. Park, A. L. Yeyati, J. Nygård, and P. Krogstrup, "Spin-orbit splitting of Andreev states revealed by microwave spectroscopy," *Physical Review X*, vol. 9, Jan. 2019.

[250] G. Dresselhaus, "Spin-orbit coupling effects in zinc blende structures," *Physical Review*, vol. 100, pp. 580–586, Oct. 1955.

[251] E. Rashba, "Properties of semiconductors with an extremum loop. I. cyclotron and combinational resonance in a magnetic field perpendicular to the plane of the loop," *Sov. Phys.-Solid State*, vol. 2, p. 1109, 1960.

[252] A. Manchon, H. C. Koo, J. Nitta, S. M. Frolov, and R. A. Duine, "New perspectives for rashba spin–orbit coupling," *Nature Materials*, vol. 14, pp. 871–882, Aug. 2015.

[253] S. D. Escribano, A. L. Yeyati, and E. Prada, "Improved effective equation for the Rashba spin-orbit coupling in semiconductor nanowires," *Physical Review Research*, vol. 2, p. 033264, Aug. 2020.

[254] N. Trnjanin, I. P. Cools, V. Buccheri, and T. Bauch, "Magnetic-field anisotropy of the Josephson diode effect in ferromagnetic hybrid nanowires," *Submitted to: Phys. Rev. B.*, 2026.

[255] S. Vaitiekėnas, M.-T. Deng, J. Nygård, P. Krogstrup, and C. Marcus, "Effective g factor of subgap states in hybrid nanowires," *Physical Review Letters*, vol. 121, p. 037703, July 2018.

[256] S. Park and A. L. Yeyati, "Andreev spin qubits in multichannel rashba nanowires," *Physical Review B*, vol. 96, p. 125416, Sept. 2017.

[257] C. Metzger, *Spin and charge effects in Andreev Bound States*. PhD thesis, université Paris-Saclay, 2022.

[258] E. Jaynes and F. Cummings, "Comparison of quantum and semiclassical radiation theories with application to the beam maser," *Proceedings of the IEEE*, vol. 51, no. 1, pp. 89–109, 1963.

[259] D. Zueco, G. M. Reuther, S. Kohler, and P. Hänggi, "Qubit-oscillator dynamics in the dispersive regime: Analytical theory beyond the rotating-wave approximation," *Physical Review A*, vol. 80, p. 033846, Sept. 2009.

[260] A. Vaaranta, M. Cattaneo, and P. Muratore-Ginanneschi, "Analytical solution of the open dispersive jaynes-cummings model and perturbative analytical solution of the open quantum rabi model," *Physical Review A*, vol. 111, p. 053717, May 2025.

[261] M. Boissonneault, J. M. Gambetta, and A. Blais, "Dispersive regime of circuit QED: Photon-dependent qubit dephasing and relaxation rates," *Physical Review A*, vol. 79, p. 013819, Jan. 2009.

[262] C. Janvier, L. Tosi, L. Bretheau, C. O. Girit, M. Stern, P. Bertet, P. Joyez, D. Vion, D. Esteve, M. F. Goffman, H. Pothier, and C. Urbina, "Coherent manipulation of Andreev states in superconducting atomic contacts," *Science*, vol. 349, pp. 1199–1202, Sept. 2015.

[263] L. Bretheau, *Localized excitations in superconducting atomic contacts: Probing the Andreev doublet*. PhD thesis, Ecole Polytechnique X, 2013.

[264] C. Metzger, S. Park, L. Tosi, C. Janvier, A. A. Reynoso, M. F. Goffman, C. Urbina, A. Levy Yeyati, and H. Pothier, "Circuit-QED with phase-biased Josephson weak links," *Physical Review Research*, vol. 3, Jan. 2021.

[265] S. Park, C. Metzger, L. Tosi, M. Goffman, C. Urbina, H. Pothier, and A. L. Yeyati, "From adiabatic to dispersive readout of quantum circuits," *Physical Review Letters*, vol. 125, Aug. 2020.

[266] P. D. Kurilovich, V. D. Kurilovich, V. Fatemi, M. H. Devoret, and L. I. Glazman, "Microwave response of an Andreev bound state," *Physical Review B*, vol. 104, p. 174517, Nov. 2021.

[267] V. Fatemi, P. Kurilovich, M. Hays, D. Bouman, T. Connolly, S. Diamond, N. Frattini, V. Kurilovich, P. Krogstrup, J. Nygård, A. Geresdi, L. Glazman, and M. Devoret, "Microwave susceptibility observation of interacting many-body Andreev states," *Physical Review Letters*, vol. 129, p. 227701, Nov. 2022.

[268] V. E. Manucharyan, *Superinductance*. PhD thesis, Yale University, 2012.

[269] T. Niemczyk, F. Deppe, H. Huebl, E. P. Menzel, F. Hocke, M. J. Schwarz, J. J. Garcia-Ripoll, D. Zueco, T. Hümmer, E. Solano, A. Marx, and R. Gross, "Circuit quantum electrodynamics in the ultrastrong-coupling regime," *Nature Physics*, vol. 6, pp. 772–776, July 2010.

[270] P. Forn-Díaz, J. Lisenfeld, D. Marcos, J. J. García-Ripoll, E. Solano, C. J. P. M. Harmans, and J. E. Mooij, "Observation of the bloch-siegert shift in a qubit-oscillator system in the ultrastrong coupling regime," *Physical Review Letters*, vol. 105, p. 237001, Nov. 2010.

[271] P. Gartner and V. Moldoveanu, "Effective hamiltonians in the quantum rabi problem," *Physical Review A*, vol. 105, p. 023704, Feb. 2022.

[272] I. D. Feranchuk, A. V. Leonov, and O. D. Skoromnik, "Physical background for parameters of the quantum Rabi model," *Journal of Physics A: Mathematical and Theoretical*, vol. 49, p. 454001, Oct. 2016.

[273] A. Frisk Kockum, A. Miranowicz, S. De Liberato, S. Savasta, and F. Nori, "Ultrastrong coupling between light and matter," *Nature Reviews Physics*, vol. 1, pp. 19–40, Jan. 2019.

[274] G. Romero, D. Ballester, Y. M. Wang, V. Scarani, and E. Solano, "Ultrafast quantum gates in circuit QED," *Physical Review Letters*, vol. 108, p. 120501, Mar. 2012.

[275] P. Nataf and C. Ciuti, "Protected quantum computation with multiple resonators in ultrastrong coupling circuit qed," *Physical Review Letters*, vol. 107, Nov. 2011.

[276] T. H. Kyaw, D. A. Herrera-Martí, E. Solano, G. Romero, and L.-C. Kwek, "Creation of quantum error correcting codes in the ultrastrong coupling regime," *Physical Review B*, vol. 91, p. 064503, Feb. 2015.

[277] R. Stassi and F. Nori, "Long-lasting quantum memories: Extending the coherence time of superconducting artificial atoms in the ultrastrong-coupling regime," *Physical Review A*, vol. 97, p. 033823, Mar. 2018.

[278] L. Garziano, V. Macrì, R. Stassi, O. Di Stefano, F. Nori, and S. Savasta, "One photon can simultaneously excite two or more atoms," *Physical Review Letters*, vol. 117, p. 043601, July 2016.

[279] C. Hotter, A. Miranowicz, and K. Gietka, "Quantum metrology in the ultrastrong coupling regime of light-matter interactions: Leveraging virtual excitations without extracting them," *Physical Review Letters*, vol. 135, Sept. 2025.

[280] S. Vaitiekėnas, G. W. Winkler, B. van Heck, T. Karzig, M.-T. Deng, K. Flensberg, L. I. Glazman, C. Nayak, P. Krogstrup, R. M. Lutchyn, and C. M. Marcus, "Flux-induced topological superconductivity in full-shell nanowires," *Science*, vol. 367, Mar. 2020.

[281] S. Vaitiekėnas, P. Krogstrup, and C. M. Marcus, "Anomalous metallic phase in tunable destructive superconductors," *Physical Review B*, vol. 101, p. 060507, Feb. 2020.

[282] J. E. Sestoft, M. Marnauza, D. Olsteins, T. Kanne, R. D. Schlosser, I.-J. Chen, K. Grove-Rasmussen, and J. Nygård, "Shadowed versus etched superconductor–semiconductor junctions in Al/InAs nanowires," *Nano Letters*, vol. 24, pp. 8394–8401, June 2024.

[283] P. Jung, S. Butz, S. V. Shitov, and A. V. Ustinov, "Low-loss tunable metamaterials using superconducting circuits with Josephson junctions," *Applied Physics Letters*, vol. 102, Feb. 2013.

[284] A. Paila, D. Gunnarsson, J. Sarkar, M. A. Sillanpää, and P. J. Hakonen, "Current-phase relation and Josephson inductance in a superconducting Cooper-pair transistor," *Physical Review B*, vol. 80, Oct. 2009.

[285] J. H. Ungerer, A. Pally, A. Kononov, S. Lehmann, J. Ridderbos, P. P. Potts, C. Thelander, K. A. Dick, V. F. Maisi, P. Scarlino, A. Baumgartner, and C. Schönenberger, "Strong coupling between a microwave photon and a singlet-triplet qubit," *Nature Communications*, vol. 15, Feb. 2024.

[286] M. R. Sahu, F. J. Matute-Cañadas, M. Benito, P. Krogstrup, J. Nygård, M. F. Goffman, C. Urbina, A. L. Yeyati, and H. Pothier, "Ground-state phase diagram and parity-flipping microwave transitions in a gate-tunable Josephson junction," *Physical Review B*, vol. 109, p. 134506, Apr. 2024.

[287] H. Lu, D. F. Bofill, Z. Sun, T. Kanne, J. Nygård, M. Kjaergaard, and V. Fatemi, "Andreev spin relaxation time in a shadow-evaporated inas weak link," *Physical Review Applied*, vol. 24, Aug. 2025.

[288] E. C. Stoner, "Collective electron ferromagnetism," *Proceedings of the Royal Society of London. Series A. Mathematical and Physical Sciences*, vol. 165, pp. 372–414, Apr. 1938.

[289] Y. M. Lu, Y. Choi, C. M. Ortega, X. M. Cheng, J. W. Cai, S. Y. Huang, L. Sun, and C. L. Chien, "Pt magnetic polarization on Y3Fe5O12 and magnetotransport characteristics," *Physical Review Letters*, vol. 110, p. 147207, Apr. 2013.

[290] Q. Sun, F. Mahfouzi, J. P. Velev, E. Y. Tsymbal, and N. Kioussis, "Ferroelectric-driven tunable magnetism in ultrathin platinum films," *Physical Review Materials*, vol. 4, p. 124401, Dec. 2020.

[291] X. Zhang, "A review of common materials for hybrid quantum magnonics," *Materials Today Electronics*, vol. 5, p. 100044, Sept. 2023.

[292] M. Song, T. Polakovic, J. Lim, T. W. Cecil, J. Pearson, R. Divan, W.-K. Kwok, U. Welp, A. Hoffmann, K.-J. Kim, V. Novosad, and Y. Li, "Single-shot magnon interference in a magnon-superconducting-resonator hybrid circuit," *Nature Communications*, vol. 16, Apr. 2025.

[293] X. Zheng, M. Wei, and Q. Guo, "Magnon blockade in a hybrid magnon-superconducting qubit system," *Annalen der Physik*, vol. 538, Mar. 2026.

[294] S. Husain, N. F. Prestes, O. Fayet, S. Collin, F. Godel, E. Jacquet, T. Denneulin, R. E. Dunin-Borkowski, A. Thiaville, M. Bibes, H. Jaffrès, N. Reyren, A. Fert, and J.-M. George, "Field-free switching of perpendicular magnetization in an ultrathin epitaxial magnetic insulator," *Nano Letters*, vol. 24, pp. 2743–2750, Feb. 2024.

[295] Y. Wang, P. Zhou, S. Liu, Y. Qi, and T. Zhang, "Ferromagnetic resonance and spin hall magnetoresistance of Tm3Fe5O12 films," 2025.

[296] C. O. Avci, A. Quindeau, C.-F. Pai, M. Mann, L. Caretta, A. S. Tang, M. C. Onbasli, C. A. Ross, and G. S. D. Beach, "Current-induced switching in a magnetic insulator," *Nature Materials*, vol. 16, pp. 309–314, Nov. 2016.

[297] A. Hoffmann, "Spin hall effects in metals," *IEEE Transactions on Magnetics*, vol. 49, pp. 5172–5193, Oct. 2013.

[298] M.-H. Nguyen, D. Ralph, and R. Buhrman, "Spin torque study of the spin hall conductivity and spin diffusion length in platinum thin films with varying resistivity," *Physical Review Letters*, vol. 116, p. 126601, Mar. 2016.

[299] S. Ding, Z. Liang, C. Yun, R. Wu, M. Xue, Z. Lin, A. Ross, S. Becker, W. Yang, X. Ma, D. Chen, K. Sun, G. Jakob, M. Kläui, and J. Yang, "Anomalous hall effect in magnetic insulator heterostructures: Contributions from spin-hall and magnetic-proximity effects," *Physical Review B*, vol. 104, p. 224410, Dec. 2021.

[300] Q. Shao, C. Tang, G. Yu, A. Navabi, H. Wu, C. He, J. Li, P. Upadhyaya, P. Zhang, S. A. Razavi, Q. L. He, Y. Liu, P. Yang, S. K. Kim, C. Zheng, Y. Liu, L. Pan, R. K. Lake, X. Han, Y. Tserkovnyak, J. Shi, and K. L. Wang, "Role of dimensional crossover on spin-orbit torque efficiency in magnetic insulator thin films," *Nature Communications*, vol. 9, Sept. 2018.

[301] W. Fan, J. Zhao, M. Tang, H. Chen, H. Yang, W. Lü, Z. Shi, and X. Qiu, "Asymmetric spin-orbit-torque-induced magnetization switching with a noncollinear in-plane assisting magnetic field," *Physical Review Applied*, vol. 11, p. 034018, Mar. 2019.

[302] S. Hu, J. Huang, C. Zheng, J. Ke, J. Cai, R. Evans, R. Chantrell, Z. Zhang, and Y. Liu, "Magnetocrystalline anisotropy enables field-free deterministic switching in Tm3Fe5O12/Pt bilayers: An atomistic spin dynamics study," *ACS Applied Materials and Interfaces*, vol. 18, pp. 5762–5770, Jan. 2026.

[303] C. O. Avci, E. Rosenberg, M. Baumgartner, L. Beran, A. Quindeau, P. Gambardella, C. A. Ross, and G. S. D. Beach, "Fast switching and signature of efficient domain wall motion driven by spin-orbit torques in a perpendicular anisotropy magnetic insulator/Pt bilayer," *Applied Physics Letters*, vol. 111, Aug. 2017.

[304] I. M. Miron, K. Garello, G. Gaudin, P.-J. Zermatten, M. V. Costache, S. Auffret, S. Bandiera, B. Rodmacq, A. Schuhl, and P. Gambardella, "Perpendicular switching of a single ferromagnetic layer induced by in-plane current injection," *Nature*, vol. 476, no. 7359, pp. 189–193, 2011.

[305] L. Liu, C.-F. Pai, Y. Li, H. Tseng, D. Ralph, and R. Buhrman, "Spin-torque switching with the giant spin hall effect of tantalum," *Science*, vol. 336, no. 6081, pp. 555–558, 2012.

[306] A. Manchon and S. Zhang, "Theory of spin torque due to spin-orbit coupling," *Physical Review B*, vol. 79, Mar. 2009.

[307] K.-S. Lee, S.-W. Lee, B.-C. Min, and K.-J. Lee, "Threshold current for switching of a perpendicular magnetic layer induced by spin hall effect," *Applied Physics Letters*, vol. 102, Mar. 2013.

[308] T. Xu, A. Tang, K. Wang, W. Wei, Y. Liu, and H. Du, "Orbital torque switching of perpendicular magnetization in Ti/ferrimagnet bilayers," *The Innovation Materials*, vol. 3, no. 4, p. 100158, 2025.

[309] Y. Li, D. Zheng, C. Liu, C. Zhang, B. Fang, A. Chen, Y. Ma, A. Manchon, and X. Zhang, "Current-induced magnetization switching across a nearly room-temperature compensation point in an insulating compensated ferrimagnet," *ACS Nano*, vol. 16, pp. 8181–8189, May 2022.

[310] C. N. Wu, C. C. Tseng, Y. T. Fanchiang, C. K. Cheng, K. Y. Lin, S. L. Yeh, S. R. Yang, C. T. Wu, T. Liu, M. Wu, M. Hong, and J. Kwo, "High-quality thulium iron garnet films with tunable perpendicular magnetic anisotropy by off-axis sputtering – correlation between magnetic properties and film strain," *Scientific Reports*, vol. 8, July 2018.

[311] S. Ding, A. Ross, D. Go, L. Baldrati, Z. Ren, F. Freimuth, S. Becker, F. Kammerbauer, J. Yang, G. Jakob, Y. Mokrousov, and M. Kläui, "Harnessing orbital-to-spin conversion of interfacial orbital currents for efficient spin-orbit torques," *Physical Review Letters*, vol. 125, p. 177201, Oct. 2020.

[312] S. Wang, G. Li, X. Huang, Y. Tian, J. Yu, L. Ren, H. Zhang, J. Wang, and K. Jin, "Preparation of thulium iron garnet ceramics and investigation of spin transport properties in thin films," *Ceramics International*, vol. 45, pp. 7649–7653, Apr. 2019.

[313] H. Kramers, "L'interaction entre les atomes magnétogènes dans un cristal paramagnétique," *Physica*, vol. 1, pp. 182–192, Jan. 1934.

[314] B. Barbara, "Louis néel: His multifaceted seminal work in magnetism," *Comptes Rendus. Physique*, vol. 20, pp. 631–649, Aug. 2019.

[315] K. P. Belov and W. H. Furry, *Magnetic Transitions*. State Publishing House for Physico-mathematical Literature, Moscow, 1959.

[316] K. P. Belov, "Ferrimagnets with a "weak" magnetic sublattice," *Physics-Uspekhi*, vol. 39, pp. 623–634, June 1996.

[317] B. Goransky and A. Zvezdin, "Temperature dependence of the coercive force of ferrimagnets near the compensation temperature," *Sov Phys Jetp*, vol. 30, no. 2, pp. 299–301, 1970.

[318] C. C. Soares, T. J. A. Mori, F. Béron, J. S. Moodera, J. C. Cezar, J. Brandão, and G. Vilela, "Compensation-like temperature and spin-flip switch in strained thulium iron garnet thin films: Tuning sublattice interactions for ferrimagnetic spintronics," *ACS Applied Nano Materials*, vol. 8, pp. 14567–14575, July 2025.

[319] S. Geller, J. P. Remeika, R. C. Sherwood, H. J. Williams, and G. P. Espinosa, "Magnetic study of the heavier rare-earth iron garnets," *Phys. Rev.*, vol. 137, pp. A1034–A1038, Feb 1965.

[320] T. Bayaraa, C. Xu, D. Campbell, and L. Bellaiche, "Tuning magnetization compensation and curie temperatures in epitaxial rare earth iron garnet films," *Physical Review B*, vol. 100, p. 214412, Dec. 2019.

[321] H.-A. Zhou, Y. Dong, T. Xu, K. Xu, L. Sánchez-Tejerina, L. Zhao, Y. Ba, P. Gargiani, M. Valvidares, Y. Zhao, M. Carpentieri, O. A. Tretiakov, X. Zhong, G. Finocchio, S. K. Kim, and W. Jiang, "Compensated magnetic insulators for extremely fast spin-orbitronics," 2019.

[322] L. Caretta and C. O. Avci, "Domain walls speed up in insulating ferrimagnetic garnets," *APL Materials*, vol. 12, Jan. 2024.

[323] A. Priyanshu, M. Nath, and A. Bandyopadhyay, "Rare earth based iron garnet – a survey on its magnetic properties," *IOP Conference Series: Materials Science and Engineering*, vol. 1291, p. 012028, Sept. 2023.

[324] M. J. Gross, T. Su, J. J. Bauer, and C. A. Ross, "Molecular-field-coefficient modeling of temperature-dependent ferrimagnetism in a complex oxide," *Physical Review Applied*, vol. 21, p. 014060, Jan. 2024.

[325] A. Janutka and C. A. Ross, "Spin-wave-driven motion of a domain wall in a compensated ferrimagnet nanostripe," *Journal of Applied Physics*, vol. 138, Aug. 2025.

[326] I. P. Cools, J. Xu, L. Yan, S. P. Dash, and N. Yamashita, "Observation of double anomalous hall polarity reversals with temperature in an ultrathin ferrimagnetic insulator," *Submitted to: APL Materials*, 2026.

[327] B. You, N. Hu, H. Zhu, Y. Liu, and C. Lu, "Enhanced low-field anisotropic magnetoresistance in the lightly hole-doped antiferromagnet Sr2IrO4," *Physical Review B*, vol. 112, Aug. 2025.

[328] T. Jungwirth, J. Sinova, A. Manchon, X. Marti, J. Wunderlich, and C. Felser, "The multiple directions of antiferromagnetic spintronics," *Nature Physics*, vol. 14, pp. 200–203, Mar. 2018.

[329] V. Baltz, A. Manchon, M. Tsoi, T. Moriyama, T. Ono, and Y. Tserkovnyak, "Antiferromagnetic spintronics," *Reviews of Modern Physics*, vol. 90, p. 015005, Feb. 2018.

[330] J. M. DeStefano, E. Rosenberg, G. Ren, Y. Lee, Z. Ning, O. Peek, K. Harrison, S. I. Khondaker, L. Ke, I. I. Mazin, J. C. Idrobo, and J.-H. Chu, "Giant coercivity and enhanced intrinsic anomalous hall effect at vanishing magnetization in a compensated kagome ferrimagnet," *Science Advances*, vol. 11, Aug. 2025.

[331] M. Logunov, S. Safonov, A. Fedorov, A. Danilova, N. Moiseev, A. Safin, S. Nikitov, and A. Kirilyuk, "Domain wall motion across magnetic and spin compensation points in magnetic garnets," *Physical Review Applied*, vol. 15, p. 064024, June 2021.

[332] L. Caretta, M. Mann, F. Büttner, K. Ueda, B. Pfau, C. M. Günther, P. Hessing, A. Churikova, C. Klose, M. Schneider, D. Engel, C. Marcus, D. Bono, K. Bagschik, S. Eisebitt, and G. S. D. Beach, "Fast current-driven domain walls and small skyrmions in a compensated ferrimagnet," *Nature Nanotechnology*, vol. 13, pp. 1154–1160, Sept. 2018.

[333] R. K. Wangsness, "Sublattice effects in magnetic resonance," *Physical Review*, vol. 91, pp. 1085–1091, Sept. 1953.

[334] C. D. Stanciu, A. V. Kimel, F. Hansteen, A. Tsukamoto, A. Itoh, A. Kirilyuk, and T. Rasing, "Ultrafast spin dynamics across compensation points in ferrimagnetic GdFeCo: The role of angular momentum compensation," *Physical Review B*, vol. 73, p. 220402, June 2006.

[335] M. Mansuripur, *The Physical Principles of Magneto-optical Recording*. Cambridge University Press, Apr. 1995.

[336] B. A. Calhoun, J. Overmeyer, and W. V. Smith, "Ferrimagnetic resonance in gadolinium iron garnet," *Physical Review*, vol. 107, pp. 993–994, Aug. 1957.

[337] R. C. LeCraw, J. P. Remeika, and H. Matthews, "Angular momentum compensation in narrow linewidth ferrimagnets," *Journal of Applied Physics*, vol. 36, pp. 901–905, Mar. 1965.

[338] S. Vélez, J. Schaab, M. S. Wörnle, M. Müller, E. Gradauskaite, P. Welter, C. Gutgsell, C. Nistor, C. L. Degen, M. Trassin, M. Fiebig, and P. Gambardella, "High-speed domain wall racetracks in a magnetic insulator," *Nature Communications*, vol. 10, Oct. 2019.

[339] T. Kobayashi, H. Hayashi, Y. Fujiwara, and S. Shiomi, "Damping parameter and wall velocity of RE-TM films," *IEEE Transactions on Magnetics*, vol. 41, pp. 2848–2850, Oct. 2005.

[340] M. Deb, P. Molho, B. Barbara, and J.-Y. Bigot, "Controlling laser-induced magnetization reversal dynamics in a rare-earth iron garnet across the magnetization compensation point," *Physical Review B*, vol. 97, p. 134419, Apr. 2018.

[341] L. Liensberger, A. Kamra, H. Maier-Flaig, S. Geprags, A. Erb, S. T. Goennenwein, R. Gross, W. Belzig, H. Huebl, and M. Weiler, "Exchange-enhanced ultrastrong magnon-magnon coupling in a compensated ferrimagnet," *Physical Review Letters*, vol. 123, Sept. 2019.

[342] Q. Shao, A. Grutter, Y. Liu, G. Yu, C.-Y. Yang, D. A. Gilbert, E. Arenholz, P. Shafer, X. Che, C. Tang, M. Aldosary, A. Navabi, Q. L. He, B. J. Kirby, J. Shi, and K. L. Wang, "Exploring interfacial exchange coupling and sublattice effect in heavy metal/ferrimagnetic insulator heterostructures using hall measurements, X-ray magnetic circular dichroism, and neutron reflectometry," *Physical Review B*, vol. 99, p. 104401, Mar. 2019.

[343] R. Yu, J. Cao, F. Zhu, X. Meng, Y. Wang, J. Li, and Y. Wang, "Tailoring unusual ferrimagnetism in rare-earth iron garnets via graphene interlayers," *Advanced Science*, vol. 12, Sept. 2025.

[344] E. R. Rosenberg, L. Beran, C. O. Avci, C. Zeledon, B. Song, C. Gonzalez-Fuentes, J. Mendil, P. Gambardella, M. Veis, C. Garcia, G. S. D. Beach, and C. A. Ross, "Magnetism and spin transport in rare-earth-rich epitaxial terbium and europium iron garnet films," *Physical Review Materials*, vol. 2, Sept. 2018.

[345] J. M. Liang, X. W. Zhao, Y. K. Liu, P. G. Li, S. M. Ng, H. F. Wong, W. F. Cheng, Y. Zhou, J. Y. Dai, C. L. Mak, and C. W. Leung, "The thickness effect on the compensation temperature of rare-earth garnet thin films," *Applied Physics Letters*, vol. 122, June 2023.

[346] S. Pandey, A. Barbier, A. Forget, B. Sarpi, F. Maccherozzi, R. Sant, N. B. Brookes, J.-B. Moussy, and P. V. B. Pinho, "Magnetic behavior and phase diagram of epitaxial Er3Fe5O12 thin films across the compensation temperature," 2025.

[347] Y. Wang, X. Wang, A. T. Clark, H. Chen, X. M. Cheng, J. W. Freeland, and J. Q. Xiao, "Probing exchange bias at the surface of a doped ferrimagnetic insulator," *Physical Review Materials*, vol. 5, p. 074409, July 2021.

[348] G. Vértesy and I. Tomas, "Survey of the dependence on temperature of the coercivity of garnet films," *Journal of Applied Physics*, vol. 77, pp. 6426–6431, June 1995.

[349] G. Vértesy, "Coercive properties of magnetic garnet films," *Crystals*, vol. 13, p. 946, June 2023.

[350] R. Kütterer, H.-R. Hilzinger, and H. Kronmüller, "The temperature dependence of the coercive field of Co5Sm magnets," *Journal of Magnetism and Magnetic Materials*, vol. 4, pp. 1–7, Jan. 1977.

[351] R. Grossinger, R. Krewenka, F. Haslinger, M. Sagawa, and H. Kirchmayr, "Temperature dependence of the coercivity and the anisotropy of Nd-Fe-B based magnets," *IEEE Transactions on Magnetics*, vol. 23, pp. 2114–2116, Sept. 1987.

[352] G. A. N. Connell, R. Allen, and M. Mansuripur, "Magneto-optical properties of amorphous terbium–iron alloys," *Journal of Applied Physics*, vol. 53, pp. 7759–7761, Nov. 1982.

[353] P. G. Li, J. M. Liang, S. M. Ng, H. F. Wong, Y. Zhou, L. J. Huang, K. W. Lin, Y. H. Tsang, C. L. Mak, and C. W. Leung, "Tunable compensation temperature through ferromagnetic coupling in perpendicular Tb3Fe5O12/Eu3Fe5O12 bilayer heterostructure," *Journal of Magnetism and Magnetic Materials*, vol. 592, Feb. 2024.

[354] Y. Li, X. Yang, H. Bai, M. Wang, D. Cheng, C. Song, Z. Yuan, Y. Liu, and Z. Shi, "Strain-tunable magnetic compensation temperature of epitaxial Tb3Fe5O12 thin films," *Physical Review B*, vol. 108, Nov. 2023.

[355] Y. Ohnuma, H. Adachi, E. Saitoh, and S. Maekawa, "Enhanced dc spin pumping into a fluctuating ferromagnet neartc," *Physical Review B*, vol. 89, p. 174417, May 2014.

[356] Y. Liu, H. Wong, K. Lam, K. Chan, C. Mak, and C. Leung, "Anomalous hall effect in Pt/Tb3Fe5O12 heterostructure: Effect of compensation point," *Journal of Magnetism and Magnetic Materials*, vol. 468, pp. 235–240, Dec. 2018.

[357] J. Bernasconi and D. Kuse, "Canted spin phase in gadolinium iron garnet," *Physical Review B*, vol. 3, pp. 811–815, Feb. 1971.

[358] A. M. Kalashnikova, V. V. Pavlov, A. V. Kimel, A. Kirilyuk, T. Rasing, and R. V. Pisarev, "Magneto-optical study of holmium iron garnet Ho3Fe5O12," *Low Temperature Physics*, vol. 38, pp. 863–869, Sept. 2012.

[359] B. Zhao, R. Ngaloy, L. Sjöström, and S. P. Dash, "Spin-texture spin-valve with a van der Waals magnet," 2025.

[360] M. Uemura, T. Yamagishi, S. Ebisu, S. Chikazawa, and S. Nagata, "A double peak of the coercive force near the compensation temperature in the rare earth iron garnets," *Philosophical Magazine*, vol. 88, pp. 209–228, Jan. 2008.

[361] Y. Ohnuma, H. Adachi, E. Saitoh, and S. Maekawa, "Spin seebeck effect in antiferromagnets and compensated ferrimagnets," *Physical Review B*, vol. 87, p. 014423, Jan. 2013.

[362] K. Ganzhorn, J. Barker, R. Schlitz, B. A. Piot, K. Ollefs, F. Guillou, F. Wilhelm, A. Rogalev, M. Opel, M. Althammer, S. Geprägs, H. Huebl, R. Gross, G. E. W. Bauer, and S. T. B. Goennenwein, "Spin hall magnetoresistance in a canted ferrimagnet," *Physical Review B*, vol. 94, p. 094401, Sept. 2016.

[363] T. Fu, S. Li, X. Feng, Y. Cui, J. Yao, B. Wang, J. Cao, Z. Shi, D. Xue, and X. Fan, "Complex anomalous hall effect of CoGd alloy near the magnetization compensation temperature," *Physical Review B*, vol. 103, p. 064432, Feb. 2021.

[364] Y. K. Liu, H. F. Wong, S. M. Ng, C. L. Mak, and C. W. Leung, "Interfacial Tm3+ moment-driven anomalous hall effect in Pt/Tm3Fe5O12 heterostructure," *Journal of Magnetism and Magnetic Materials*, vol. 501, p. 166454, May 2020.

[365] T. Shiino, M. Fettizio, S. Estandía, and C. O. Avci, "Tunable magnetism and intrinsic exchange bias in al-substituted terbium iron garnet," *Advanced Materials*, vol. 38, Sept. 2025.

[366] Z. Fang, N. Nagaosa, K. S. Takahashi, A. Asamitsu, R. Mathieu, T. Ogasawara, H. Yamada, M. Kawasaki, Y. Tokura, and K. Terakura, "The anomalous Hall effect and magnetic monopoles in momentum space," *Science*, vol. 302, pp. 92–95, Oct. 2003.

[367] S. Geprägs, A. Kehlberger, F. D. Coletta, Z. Qiu, E.-J. Guo, T. Schulz, C. Mix, S. Meyer, A. Kamra, M. Althammer, H. Huebl, G. Jakob, Y. Ohnuma, H. Adachi, J. Barker, S. Maekawa, G. E. W. Bauer, E. Saitoh, R. Gross, S. T. B. Goennenwein, and M. Kläui, "Origin of the spin Seebeck effect in compensated ferrimagnets," *Nature Communications*, vol. 7, Feb. 2016.

[368] J. Cramer, E.-J. Guo, S. Geprägs, A. Kehlberger, Y. P. Ivanov, K. Ganzhorn, F. Della Coletta, M. Althammer, H. Huebl, R. Gross, J. Kosel, M. Kläui, and S. T. B. Goennenwein, "Magnon mode selective spin transport in compensated ferrimagnets," *Nano Letters*, vol. 17, pp. 3334–3340, May 2017.

[369] N. Nagaosa, J. Sinova, S. Onoda, A. H. MacDonald, and N. P. Ong, "Anomalous hall effect," *Reviews of Modern Physics*, vol. 82, pp. 1539–1592, May 2010.

[370] A. Sharma, O. T. Ciubotariu, P. Matthes, S. Okano, V. Zviagin, J. Kalbáčová, S. Gemming, C. Himcinschi, M. Grundmann, D. R. T. Zahn, M. Albrecht, and G. Salvan, "Optical and magneto-optical properties of pulsed laser-deposited thulium iron garnet thin films," *Applied Research*, vol. 3, Aug. 2023.

[371] S. Shimizu, K. S. Takahashi, T. Hatano, M. Kawasaki, Y. Tokura, and Y. Iwasa, "Electrically tunable anomalous hall effect in Pt thin films," *Physical Review Letters*, vol. 111, p. 216803, Nov. 2013.

[372] G. Vilela, H. Chi, G. Stephen, C. Settens, P. Zhou, Y. Ou, D. Suri, D. Heiman, and J. S. Moodera, "Strain-tuned magnetic anisotropy in sputtered thulium iron garnet ultrathin films and TIG/Au/TIG valve structures," *Journal of Applied Physics*, vol. 127, Mar. 2020.

[373] Y. Kuwano, "Effective distribution coefficient of neodynium in Nd:Gd3Ga5O12 crystals grown by the Czochralski method," *Journal of Crystal Growth*, vol. 57, pp. 353–361, Apr. 1982.

[374] L. J. Riddiford, A. J. Grutter, T. Pillsbury, M. Stanley, D. Reifsnyder Hickey, P. Li, N. Alem, N. Samarth, and Y. Suzuki, "Understanding signatures of emergent magnetism in topological insulator/ferrite bilayers," *Physical Review Letters*, vol. 128, p. 126802, Mar. 2022.

[375] J. Li, A. H. Comstock, D. Sun, and X. Xu, "Comprehensive demonstration of spin hall hanle effects in epitaxial Pt thin films," *Physical Review B*, vol. 106, p. 184420, Nov. 2022.

[376] C. Swindells, B. Nicholson, O. Inyang, Y. Choi, T. Hase, and D. Atkinson, "Proximity-induced magnetism in pt layered with rare-earth–transition-metal ferrimagnetic alloys," *Physical Review Research*, vol. 2, p. 033280, Aug. 2020.

[377] S. Y. Huang, X. Fan, D. Qu, Y. P. Chen, W. G. Wang, J. Wu, T. Y. Chen, J. Q. Xiao, and C. L. Chien, "Transport magnetic proximity effects in platinum," *Physical Review Letters*, vol. 109, p. 107204, Sept. 2012.

[378] L. Caretta, E. Rosenberg, F. Büttner, T. Fakhrul, P. Gargiani, M. Valvidares, Z. Chen, P. Reddy, D. A. Muller, C. A. Ross, and G. S. D. Beach, "Interfacial dzyaloshinskii-moriya interaction arising from rare-earth orbital magnetism in insulating magnetic oxides," *Nature Communications*, vol. 11, Feb. 2020.

[379] A. Lehmann-Szweykowska, P. E. Wigen, L. Kowalewski, M. M. Kaczmarek, and T. B. Mitchell, "Orbital effects in magnetic dynamics of thulium iron garnets," *Physical Review B*, vol. 37, pp. 459–466, Jan. 1988.

[380] T. G. H. Blank, E. A. Mashkovich, K. A. Grishunin, C. F. Schippers, M. V. Logunov, B. Koopmans, A. K. Zvezdin, and A. V. Kimel, "Effective rectification of terahertz electromagnetic fields in a ferrimagnetic iron garnet," *Physical Review B*, vol. 108, p. 094439, Sept. 2023.

[381] Y. K. Tsui, N. Kalechofsky, C. A. Burns, and P. Schiffer, "Study of the low temperature thermal properties of the geometrically frustrated magnet: Gadolinium gallium garnet," *Journal of Applied Physics*, vol. 85, pp. 4512–4514, Apr. 1999.

[382] M. Ancliff, V. Sachnev, and N. d'Ambrumenil, "Model of the low temperature magnetic phases of gadolinium gallium garnet," *Journal of Physics: Condensed Matter*, vol. 33, p. 475801, Sept. 2021.

[383] P. Schiffer, A. P. Ramirez, D. A. Huse, and A. J. Valentino, "Investigation of the field induced antiferromagnetic phase transition in the frustrated magnet: Gadolinium gallium garnet," *Physical Review Letters*, vol. 73, pp. 2500–2503, Oct. 1994.

[384] O. Petrenko, D. Paul, C. Ritter, T. Zeiske, and M. Yethiraj, "Magnetic frustration and order in gadolinium gallium garnet," *Physica B: Condensed Matter*, vol. 266, pp. 41–48, May 1999.

[385] Z. Ren, K. Qian, M. Aldosary, Y. Liu, S. K. Cheung, I. Ng, J. Shi, and Q. Shao, "Strongly heat-assisted spin–orbit torque switching of a ferrimagnetic insulator," *APL Materials*, vol. 9, May 2021.

[386] J. Finley and L. Liu, "Spin-orbit-torque efficiency in compensated ferrimagnetic cobalt-terbium alloys," *Physical Review Applied*, vol. 6, p. 054001, Nov. 2016.

[387] E. C. Stoner and E. P. Wohlfarth, "A mechanism of magnetic hysteresis in heterogeneous alloys," *Philosophical Transactions of the Royal Society of London. Series A, Mathematical and Physical Sciences*, vol. 240, pp. 599–642, May 1948.

[388] R. E. Fayling, "Relationship between coercive force and anisotropy field for oriented barium ferrite tapes and magnets," *Journal of Applied Physics*, vol. 49, pp. 1823–1825, Mar. 1978.

[389] R. Mishra, J. Yu, X. Qiu, M. Motapothula, T. Venkatesan, and H. Yang, "Anomalous current-induced spin torques in ferrimagnets near compensation," *Physical Review Letters*, vol. 118, p. 167201, Apr. 2017.

[390] N. Roschewsky, C.-H. Lambert, and S. Salahuddin, "Spin-orbit torque switching of ultralarge-thickness ferrimagnetic GdFeCo," *Physical Review B*, vol. 96, p. 064406, Aug. 2017.

[391] K. Ueda, M. Mann, P. W. P. de Brouwer, D. Bono, and G. S. D. Beach, "Temperature dependence of spin-orbit torques across the magnetic compensation point in a ferrimagnetic TbCo alloy film," *Physical Review B*, vol. 96, p. 064410, Aug. 2017.

[392] K. Garello, C. O. Avci, I. M. Miron, M. Baumgartner, A. Ghosh, S. Auffret, O. Boulle, G. Gaudin, and P. Gambardella, "Ultrafast magnetization switching by spin-orbit torques," *Applied Physics Letters*, vol. 105, Nov. 2014.

[393] M. Mansuripur, "Magnetization reversal, coercivity, and the process of thermomagnetic recording in thin films of amorphous rare earth–transition metal alloys," *Journal of Applied Physics*, vol. 61, pp. 1580–1587, Feb. 1987.

[394] G. Sala and P. Gambardella, "Ferrimagnetic dynamics induced by spin-orbit torques," *Advanced Materials Interfaces*, vol. 9, Oct. 2022.

[395] H. Wang, P. Vallobra, Y. Xu, Z. Zhang, S. Peng, and W. Zhao, "Fieldlike torque driven switching in rare-earth transition-metal alloys," *Physical Review B*, vol. 110, p. 094413, Sept. 2024.

[396] M. H. Lee, S.-J. Kim, S. I. Yoon, J. K. Lee, H. S. Ko, G. Kim, S. Hong, K.-J. Lee, and Y. K. Kim, "Reduction of operating current by harnessing the field- and damping-like torque ratios in nonmagnet–ferromagnet heterojunctions," *Small Science*, vol. 4, Dec. 2023.

[397] H. Wu, Y. Xu, P. Deng, Q. Pan, S. A. Razavi, K. Wong, L. Huang, B. Dai, Q. Shao, G. Yu, X. Han, J. Rojas-Sánchez, S. Mangin, and K. L. Wang, "Spin-orbit torque switching of a nearly compensated ferrimagnet by topological surface states," *Advanced Materials*, vol. 31, July 2019.

[398] J. Sinova, S. O. Valenzuela, J. Wunderlich, C. Back, and T. Jungwirth, "Spin hall effects," *Reviews of Modern Physics*, vol. 87, pp. 1213–1260, Oct. 2015.

[399] S. Meyer, M. Althammer, S. Geprägs, M. Opel, R. Gross, and S. T. B. Goennenwein, "Temperature dependent spin transport properties of platinum inferred from spin hall magnetoresistance measurements," *Applied Physics Letters*, vol. 104, June 2014.

[400] A. R. Bedyukh, V. V. Danilov, A. Y. Nechiporuk, and V. F. Romanyuk, "Resonant magnetic properties of gadolinium–gallium garnet single crystals," *Low Temperature Physics*, vol. 25, pp. 182–183, Mar. 1999.

[401] D. A. Connelly, H. R. O. Aquino, M. Robbins, G. H. Bernstein, A. Orlov, W. Porod, and J. Chisum, "Complex permittivity of gadolinium gallium garnet from 8.2 to 12.4 ghz," *IEEE Magnetics Letters*, vol. 12, pp. 1–4, 2021.

[402] L. Landau and E. Lifshitz, "On the theory of the dispersion of magnetic permeability in ferromagnetic bodies," *Phys. Z. Sowjet.*, no. 8, 1935.

[403] L. Landau and E. Lifshitz, *On the theory of the dispersion of magnetic permeability in ferromagnetic bodies*, pp. 51–65. Elsevier, 1992.

[404] T. L. Gilbert, *Formulation, Foundations and Applications of the Phenomenological Theory of Ferromagnetism*. PhD thesis, Illinois institute of technology, 1956.

[405] T. Gilbert, "Classics in magnetics: A phenomenological theory of damping in ferromagnetic materials," *IEEE Transactions on Magnetics*, vol. 40, pp. 3443–3449, Nov. 2004.

[406] Z. Li, T. Zhang, Q. Wang, Q. Zhao, F. Li, Y. Fan, C. Zhao, J. Wang, Q. Liu, G. Yu, and J. Wei, "Controlling perpendicular magnetic anisotropy and damping in thulium iron garnet films by strain engineering," *Journal of Magnetism and Magnetic Materials*, vol. 632, Nov. 2025.

[407] M. Müller, *Coupling Phenomena in Magnonic Hybrid Heterostructures*. PhD thesis, Walther-Meissner-institut, 2023.

[408] C. W. Zollitsch, S. Khan, V. T. T. Nam, I. A. Verzhbitskiy, D. Sagkovits, J. O'Sullivan, O. W. Kennedy, M. Strungaru, E. J. G. Santos, J. J. L. Morton, G. Eda, and H. Kurebayashi, "Probing spin dynamics of ultra-thin van der Waals magnets via photon-magnon coupling," *Nature Communications*, vol. 14, May 2023.

[409] A. B. Cahaya, "Spin current compensation from competing magnon modes in ferrimagnets," *Journal of Physics D: Applied Physics*, vol. 58, p. 345002, Aug. 2025.

[410] M. Hagiwara, K. Katsumata, H. Yamaguchi, M. Tokunaga, I. Yamada, M. Gross, and P. Goy, "A complete frequency-field chart for the antiferromagnetic resonance in MnF2," *International Journal of Infrared and Millimeter Waves*, vol. 20, pp. 617–622, Apr. 1999.

[411] J. Hernández, A. Eberharter, M. Schuler, J. Lass, D. Mazzone, R. Sibille, S. Raymond, K. Krämer, B. Normand, B. Roessli, A. Läuchli, and M. Kenzelmann, "Field-induced magnon decay, magnon shadows, and rotonlike excitations in the honeycomb antiferromagnet YbBr3," *Physical Review Letters*, vol. 135, Oct. 2025.

[412] Y. Shiota, T. Taniguchi, D. Hayashi, H. Narita, S. Karube, R. Hisatomi, T. Moriyama, and T. Ono, "Handedness manipulation of propagating antiferromagnetic magnons," *Nature Communications*, vol. 15, Nov. 2024.

[413] A. L. Melendez, S. Das, F. A. Rodriguez, I.-H. Kao, W. Liu, A. J. Williams, B. Lv, J. Goldberger, S. Chatterjee, S. Singh, and P. C. Hammel, "Quantum sensing of broadband spin dynamics and magnon transport in antiferromagnets," *Science Advances*, vol. 11, June 2025.

[414] S. M. Rezende, A. Azevedo, and R. L. Rodríguez-Suárez, "Introduction to antiferromagnetic magnons," *Journal of Applied Physics*, vol. 126, Oct. 2019.

[415] P. Schiffer, A. P. Ramirez, D. A. Huse, P. L. Gammel, U. Yaron, D. J. Bishop, and A. J. Valentino, "Frustration induced spin freezing in a site-ordered magnet: Gadolinium gallium garnet," *Physical Review Letters*, vol. 74, pp. 2379–2382, Mar. 1995.

[416] S. M. Wu, J. E. Pearson, and A. Bhattacharya, "Paramagnetic spin seebeck effect," *Physical Review Letters*, vol. 114, p. 186602, May 2015.

[417] P. P. Deen, O. Florea, E. Lhotel, and H. Jacobsen, "Updating the phase diagram of the archetypal frustrated magnet Gd3Ga5O12," *Physical Review B*, vol. 91, p. 014419, Jan. 2015.

[418] R. O. Serha, A. A. Voronov, D. Schmoll, R. Verba, K. O. Levchenko, S. Koraltan, K. Davídková, B. Budinská, Q. Wang, O. V. Dobrovolskiy, M. Urbánek, M. Lindner, T. Reimann, C. Dubs, C. Gonzalez-Ballestero, C. Abert, D. Suess, D. A. Bozhko, S. Knauer, and A. V. Chumak, "Magnetic anisotropy and GGG substrate stray field in YIG films down to millikelvin temperatures," *npj Spintronics*, vol. 2, July 2024.

[419] Y. Li, W. Zhang, V. Tyberkevych, W.-K. Kwok, A. Hoffmann, and V. Novosad, "Hybrid magnonics: Physics, circuits, and applications for coherent information processing," *Journal of Applied Physics*, vol. 128, Oct. 2020.

[420] R. Timalsina, H. Wang, B. Giri, A. Erickson, X. Xu, and A. Laraoui, "Mapping of spin-wave transport in thulium iron garnet thin films using diamond quantum microscopy," *Advanced Electronic Materials*, vol. 10, Dec. 2023.

[421] J. Liu, Y. Xiong, J. Liang, X. Wu, C. Liu, S. K. Cheung, Z. Ren, R. Liu, A. Christy, Z. Chen, Y. Liu, F. P. Nugraha, X.-X. Zhang, D. C. W. Leung, W. Zhang, and Q. Shao, "Strong magnon-magnon coupling and low dissipation rate in an all-magnetic-insulator heterostructure," *Physical Review Applied*, vol. 22, Sept. 2024.

[422] M. Suto, *Transport and superconducting properties of a near-surface InAs two-dimensional electron gas*. PhD thesis, Budapest University of Technology and Economics, 2025.

[423] Z. Scherübl, M. Sütő, D. Kóti, E. Tóvári, C. Horváth, T. Kalmár, B. Vasas, M. Berke, M. Kirti, G. Biasiol, S. Csonka, P. Makk, and G. Fülöp, "Determination of the current-phase relation of an InAs 2DEG josephson junction with a microwave resonator," *Physical Review Research*, vol. 7, p. 023173, May 2025.

[424] R.-C. Shen, J. Li, Y.-M. Sun, W.-J. Wu, X. Zuo, Y.-P. Wang, S.-Y. Zhu, and J. Q. You, "Cavity-magnon polaritons strongly coupled to phonons," *Nature Communications*, vol. 16, July 2025.

[425] M. Hinderling, S. C. ten Kate, M. Coraiola, D. Haxell, M. Stiefel, M. Mergenthaler, S. Paredes, S. Bedell, D. Sabonis, and F. Nichele, "Direct microwave spectroscopy of andreev bound states in planar Ge Josephson junctions," *PRX Quantum*, vol. 5, p. 030357, Sept. 2024.

[426] H. Zhang, C. Ding, D. Weiss, Z. Huang, Y. Ma, C. Guinn, S. Sussman, S. P. Chitta, D. Chen, A. A. Houck, J. Koch, and D. I. Schuster, "Tunable inductive coupler for high-fidelity gates between fluxonium qubits," *PRX Quantum*, vol. 5, p. 020326, May 2024.

[427] A. D. Bendersky, S. S. Gomez, and R. H. Romero, "Quantum gates in coupled quantum dots controlled by coupling modulation," *Quantum Science and Technology*, vol. 11, p. 015053, Feb. 2026.

[428] M. Pita-Vidal, J. J. Wesdorp, L. J. Splitthoff, A. Bargerbos, Y. Liu, L. P. Kouwenhoven, and C. K. Andersen, "Strong tunable coupling between two distant superconducting spin qubits," *Nature Physics*, vol. 20, pp. 1158–1163, May 2024.

[429] M. Jakob, K. Laubscher, P. Del Vecchio, A. Chatterjee, V. Fatemi, and S. Bosco, "Fast readout of quantum dot spin qubits via Andreev spins," 2025.

[430] J. Dijkema, X. Xue, P. Harvey-Collard, M. Rimbach-Russ, S. L. de Snoo, G. Zheng, A. Sammak, G. Scappucci, and L. M. K. Vandersypen, "Cavity-mediated iswap oscillations between distant spins," *Nature Physics*, vol. 21, pp. 168–174, Dec. 2024.

[431] G. Wendin and V. Shumeiko, "Coherent manipulation of a spin qubit," *Science*, vol. 373, pp. 390–391, July 2021.

[432] L. Fu and C. L. Kane, "Superconducting proximity effect and Majorana fermions at the surface of a topological insulator," *Physical Review Letters*, vol. 100, p. 096407, Mar. 2008.

[433] R. M. Lutchyn, J. D. Sau, and S. Das Sarma, "Majorana fermions and a topological phase transition in semiconductor-superconductor heterostructures," *Physical Review Letters*, vol. 105, p. 077001, Aug. 2010.

[434] S. D. Sarma, M. Freedman, and C. Nayak, "Majorana zero modes and topological quantum computation," *npj Quantum Information*, vol. 1, Oct. 2015.

[435] N. van Loo, F. Zatelli, G. O. Steffensen, B. Roovers, G. Wang, T. Van Caekenberghe, A. Bordin, D. van Driel, Y. Zhang, W. D. Huisman, G. Badawy, E. P. A. M. Bakkers, G. P. Mazur, R. Aguado, and L. P. Kouwenhoven, "Single-shot parity readout of a minimal kitaev chain," *Nature*, vol. 650, pp. 334–339, Feb. 2026.

[436] P. Frey, T. Hodge, E. Mascot, and S. Rachel, "Majorana braiding simulations with projective measurements," *Physical Review B*, vol. 113, Mar. 2026.

[437] C. C. Rusconi, M. J. A. Schuetz, J. Gieseler, M. D. Lukin, and O. Romero-Isart, "Hybrid architecture for engineering magnonic quantum networks," *Physical Review A*, vol. 100, p. 022343, Aug. 2019.

[438] R. O. Serha, C. Dubs, and A. V. Chumak, "Magnetic materials for quantum magnonics," 2025.

[439] H. Zheng, *Superconducting quantum devices with germanium nanowires*. PhD thesis, Universitet Basel, 2024.

[440] P. Zellekens, R. S. Deacon, P. Perla, D. Grützmacher, M. I. Lepsa, T. Schäpers, and K. Ishibashi, "Microwave spectroscopy of Andreev states in InAs nanowire-based hybrid junctions using a flip-chip layout," *Communications Physics*, vol. 5, Oct. 2022.

[441] J. Wesdorp, *Spinful Andreev States in Superconducting Circuits*. PhD thesis, Delft University of Technology, 2024.

[442] S. Chen, J. Cotler, H.-Y. Huang, and J. Li, "The complexity of NISQ," *Nature Communications*, vol. 14, Sept. 2023.

# Appendix A

# Higher frequency data for Andreev state spectra

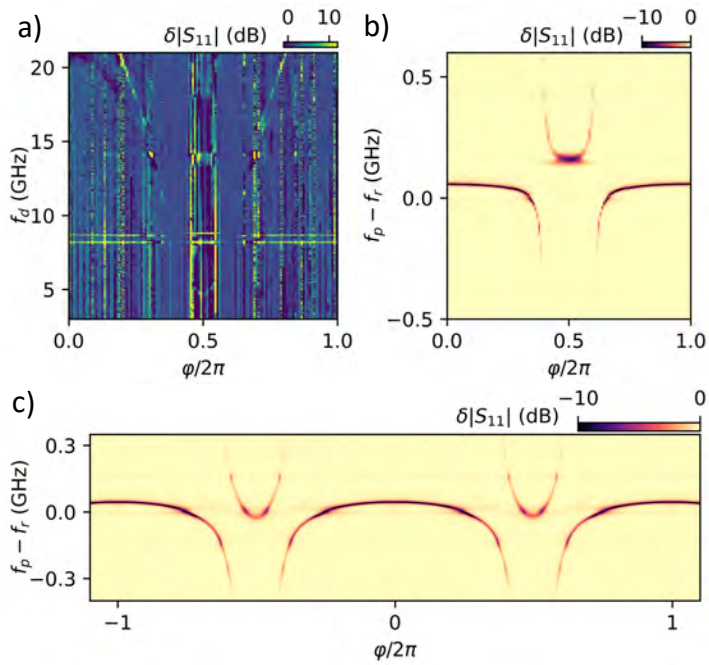


**Figure A.1:** Supplement to Fig. 3.8a,b. (a) Two-tone spectrum measured in Device 2 at $V_g = 3.39$ V. No higher energy transitions are observed, which validates the single-channel model used in the fits. (b) Corresponding single-tone spectrum. (c) Single-tone spectrum at $V_g = 3.07\ V$ demonstrates periodicity.

Fig. A.1 is a supplement to Figure 3.8a,b. Here, the full data is shown, up to 21 GHZ. The two-tone spectrum in **a** demonstrates the absence of higher-energy transitions, which justifies the single-channel approximation used in the fit in Fig.3.8b. Panel **b** shows the corresponding single-tone spectrum, over the full $0 \rightarrow 2\pi$-range. The wide range spectrum at $V_g = 3.07\ V$ in **c** confirms the periodicity and serves as a way to go from $\Phi$, or applied coil current $I$, to $\phi$.

Fig. A.2 is a supplement to Figure 3.8c,d. The two-tone spectrum in (a) shows the lack of contributions from other higher-energy transitions, which justifies the use of the single-channel approximation in the fit in Figure 3.8. The wide-range single-tone spectrum in Fig. A.2(b) confirms the periodicity.

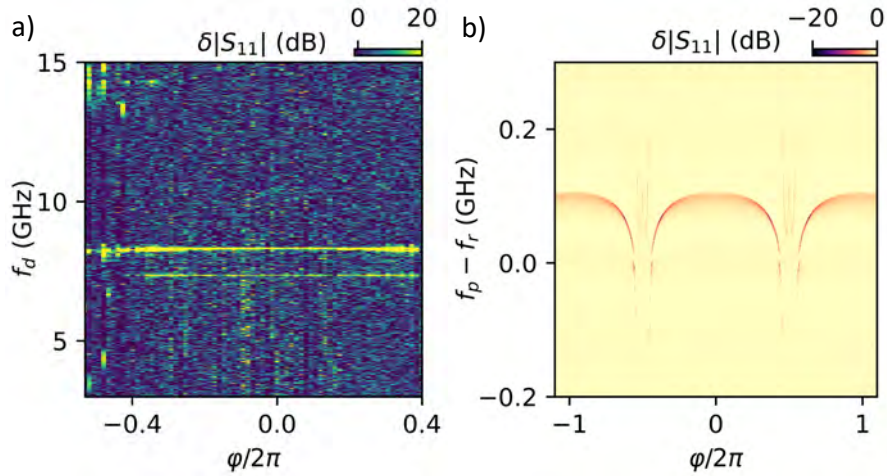


**Figure A.2:** Supplement to Fig. 3.8c,d. (a) Two-tone spectrum measured in Device 1 at $V_g = 14.5$ V. (b) Single-tone spectrum in a wide range of phase verifies the periodicity. The dashed rectangle denotes the range where (a) was measured.

# Appendix B

# Temperature-dependent magnetic properties of TmIG: fit results

The full fit results and uncertainties for the phenomenological fits to the coercive field and the Brillouin-function fits to the Hall signals, respectively in Tables B.1 and B.2. For each dataset, we list the fixed angular momentum quantum numbers used in the model, the fitted amplitudes and characteristic temperature scales, as well as standard goodness-of-fit metrics. Uncertainties correspond to $1\sigma$ errors obtained from the covariance matrix of the non-linear least-squares fit, and are expressed as relative percentages to facilitate comparison between parameters of different magnitudes. Table B.1 shows that the temperature dependence of the average coercive field $|H_C|$ is well described by simple exponential and asymmetric Lorentzian models in the relevant temperature ranges. The extracted parameters are well constrained, with relative uncertainties typically below 10%, confirming that the observed divergence of $|H_C|$ near $T_{PR,2}$ is statistically robust and not dominated by fitting ambiguity

| Temp. range (K) | Model | $A$ | $T_c$ | $w_L$ | $w_R$ | $R^2$ |
|---|---|---|---|---|---|---|
| 1–50 | Eq. 4.4 | $1.8\times10^2$ (12%) | 7.2 (16%) | – | – | 0.98 |
| 50–90 | Eq. 4.5 | $7.4\times10^3$ (7.7%) | 81.8 (0.1%) | 1.7 (6.4%) | 0.67 (13%) | 0.999 |
| 123–300 | Eq. 4.4 | $3.5\times10^2$ (52%) | 71 (37%) | – | – | 0.95 |

**TABLE B.1:** SUMMARY OF PHENOMENOLOGICAL FITS TO THE TEMPERATURE DEPENDENCE OF THE COERCIVE FIELD $|H_C|$ TO EQUATIONS 4.4 AND 4.5 OF THE MAIN TEXT. UNCERTAINTIES ARE $1\sigma$; PERCENTAGES GIVE THE RELATIVE UNCERTAINTY $100\times\sigma/|p|$.

Table B.2 compares single- and double-Brillouin descriptions of the temperature dependence of anomalous Hall signal $\Delta R_{AHE}$ and the the ordinary Hall effect (OHE). For the OHE in both Pt/TmIG/GGG and Pt/GGG, a single Brillouin function with fixed $J$ yields excellent agreement with the data, reflected by near-unity $R^2$ values and small

| Fit | Fixed $J$ | $A_1$ | $a_1$ | $A_2$ | $a_2$ | $C$ | $R^2$ | AIC |
|---|---|---|---|---|---|---|---|---|
| $\Delta R_{\mathrm{AHE}}$ (single $J$) | 6 | $-1.8\times10^{-2}$ (4.2%) | 44 (5.5%) | – | – | $1.1\times10^{-2}$ (7.0%) | 0.983 | -766 |
| $\Delta R_{\mathrm{AHE}}$ (double $J$) | $J_1 = 2.5$ $J_2 = 6$ | $-3.0\times10^{-2}$ (30%) | 74 (22%) | $1.4\times10^{-2}$ (68%) | 37 (58%) | $9.6\times10^{-3}$ (8.8%) | 0.987 | -777 |
| Pt/TmIG/GGG (OHE) | 15 | $-1.5\times10^{-4}$ (0.7%) | 7.5 (1.7%) | – | – | $4.1\times10^{-5}$ (2.7%) | 0.999 | -1337 |
| Pt/GGG (OHE) | $2\times10^{-3}$ | $-1.5\times10^{-5}$ (3.8%) | 17 (6.7%) | – | – | $5.2\times10^{-6}$ (1.3%) | 0.999 | -434 |

**TABLE B.2:** SUMMARY OF BRILLOUIN-FUNCTION FITS TO EQUATION 4.6. LISTED UNCERTAINTIES ARE $1\sigma$ FROM THE COVARIANCE MATRIX; PERCENTAGES GIVE THE RELATIVE UNCERTAINTY $100\times\sigma/|p|$.

relative parameter uncertainties. This indicates that the OHE is governed by a single dominant temperature-dependent contribution. A robust fit quality is obtained for the Pt/GGG reference sample with a near zero extracted effective angular momentum, consistent with a weak, nearly paramagnetic response. In contrast, $\Delta R_{\mathrm{AHE}}$ is better described by a double-Brillouin model. While the single-$J$ fit already captures the overall trend, the double-Brillouin model consistently improves the fit quality, yielding a higher $R^2$ and a lower Akaike information criterion (AIC). The larger relative uncertainties of individual parameters in the double-Brillouin fit reflect increased parameter correlations inherent to multi-component models rather than poor fit quality. The improved information-theoretic metrics therefore indicate that the additional Brillouin term is justified, supporting the presence of multiple temperature-dependent contributions to the anomalous Hall response.